

BULGARIAN CHEMICAL COMMUNICATIONS

2018 Volume 50 / Number 2

*Journal of the Chemical Institutes
of the Bulgarian Academy of Sciences
and of the Union of Chemists in Bulgaria*

Waste waters of milk and cheese processing as an efficient promoter for the synthesis of 1,8-dioxo-octahydroxanthenes

S. Fiorito, F. Epifano*, F. Preziuso, V. A. Taddeo, S. Genovese

Department of Pharmacy, University "G. D'Annunzio" of Chieti-Pescara, Via dei Vestini 31, 66100 Chieti Scalo (CH), Italy.

Received May 17, 2017, Accepted December 20, 2017

Waste waters of agricultural and industrial processing have been recently employed to effectively promote numerous "classic" and innovative processes of synthetic organic chemistry. Such a green chemical approach allowed to bypass the use of toxic, polluting, and hazardous chemicals and in the meantime led to an increase of the commercial values of such byproducts. Xanthenes are a group of natural and semi-synthetic compounds with great pharmacological potentialities, also used for several other applications. In this paper we described a new and improved methodology for the synthesis of the title compounds using waste waters of milk and cheese processing as a solvent. 1,8-Dioxo-octahydroxanthenes were obtained in very good yields (94 – 98 %) from differently substituted aromatic aldehydes and dimedone as substrates. Although several reports about the synthesis of 1,8-dioxo-octahydroxanthenes have been published in recent years, this is the first report about the use of waste waters of agricultural and industrial processing to this aim. The findings depicted herein underline once again the great usefulness of agricultural and food industry byproducts to perform green chemical processes.

Keywords: Aromatic aldehydes, Dimedone, Green chemistry, Waste waters, Xanthenes

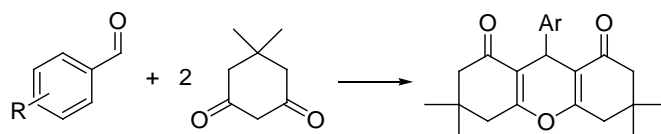
INTRODUCTION

Modern tendencies of synthetic organic chemistry involve the use and development of greener and more eco-friendly methodologies as an alternative to toxic, hazardous, polluting, and expensive substrates, reagents, and solvents. Recent reports from the literature indicate that numerous organic processes have been accomplished in water, as a safe and inexpensive solvent [1]. In the meantime the use of waste waters derived from agricultural and industrial processing has gained more and more interest of several research teams. Waste waters are in fact able to effectively play the role of promoters and solvents; they have environmentally beneficial features, are non-hazardous, non-toxic, non-polluting, largely available, and in general cheap. Examples of organic reactions employing waste waters include the Knoevenagel condensation [2], the Biginelli reaction [3], the preparation of amides [4], the reduction of carbonyls, the hydrolysis of esters and amides [5] and several others, most of which have been recently extensively reviewed [6]. The xanthene core is found in several natural products. Furthermore, xanthenes semisynthetic derivatives exert also a wide array of promising pharmacological activities as anti-inflammatory [7], anti-depressant, and anti-malarial agents [8]. They are also used as dyes and fluorescent probes [9, 10]. Reported methodologies for the synthesis of title compounds typically include the condensation of

aromatic aldehydes and 5,5-dimethyl-1,3-cyclohexanedione, commonly known as dimedone, in the presence of different catalysts like ZnCl_2 /choline chloride [11], $\text{ZnO}/\text{CH}_3\text{COCl}$ [12], Amberlyst-15 [13], ZrOCl_2 hydrate [14], trichloroisocyanuric acid [15], silica sulfuric acid [16], nanosized MCM-41- SO_3H [17], Fe_3O_4 nanoparticles [18], ionic liquids like [bmim][HSO_4] [19, 20] [hmim]TFA [21] [TMPSA][HSO_4] [22], [DDPA][HSO_4] [23], $[\text{Et}_3\text{N}-\text{SO}_3\text{H}]\text{Cl}$ [24], [Hbim] BF_4 [25], tetramethylguanidium trifluoroacetate [26], [BPy][HSO_4] [27], ammonium hydrogen sulphate based ionic liquid immobilized on Na^+ -montmorillonite [28], CuCl_2 [29] titanium aminophosphonates [30], cesium phosphotungstate [31] and natural phosphates [32]. However, the majority of methodologies for the synthesis of 1,8-dioxo-octahydroxanthenes is featured by several drawbacks and disadvantages like low yields (often strictly depending on the structures of the starting materials), long reaction times, high temperatures, use of hazardous and expensive catalysts, tedious work-up procedures, non recyclability of catalysts and solvents. Thus, development and set up of greener protocols to provide 1,8-dioxo-octahydroxanthenes can be still considered a challenging field of research in synthetic organic chemistry. As a continuation of our studies aimed at settling easy to handle methods to obtain synthons and compounds of biological interest using a green technology, we report herein that 1,8-dioxo-octahydroxanthenes can be efficiently and

* To whom all correspondence should be sent.

E-mail: fepifano@unich.it



Scheme 1. Synthetic route to 1,8-dioxo-octahydroxanthenes

selectively obtained by coupling of dimedone and different functionalized benzaldehydes using waste waters derived from milk and cheese processing (Scheme 1).

EXPERIMENTAL

Waste waters of milk processing have been obtained by local farmers.

General procedure: Benzaldehyde (1.0 mmol) and dimedone (1.01 mmol) were suspended in an aqueous medium (3 mL). The resulting mixture was let to react at 50 °C overnight. The precipitate so formed was filtrated under vacuum. Structural assignments (NMR) were made by comparison of the recorded analytical data with those of commercially available samples or those already reported for the same compounds.

Coumarin-3-carboxylic acid (entry 1): white solid (m.p.: 189-191 °C). Analytical data were in full agreement with those recorded for a pure commercial sample.

7-(Diethylamino)coumarin-3-carboxylic acid (entry 2): yellowish solid (m.p.: 221-223 °C). Analytical data were in full agreement with those recorded for a pure commercial sample.

7-Nitrocoumarin-3-carboxylic acid (entry 3): reddish solid (m.p.: 233-235 °C). Analytical data were in full agreement with those already reported in the literature for the same compound [33].

6-Bromocoumarin-3-carboxylic acid (entry 4): reddish solid (m.p.: 214-215 °C). Analytical data were in full agreement with those already reported in the literature for the same compound [16].

6-Hydroxycoumarin-3-carboxylic acid (entry 5): white solid (m.p.: 280-282 °C). Analytical data were in full agreement with those already reported in the literature for the same compound [16].

4-Methyl-6-nitrocoumarin-3-carboxylic acid (entry 6): reddish solid (m.p.: 244-247 °C). Anal. Calc. for C₁₁H₇NO₆: C 53.02, H 2.83, N 5.62, O 38.52; Found: C 53.09, H 2.77, N 5.60, O 38.44. ¹H NMR (200 MHz, CDCl₃) δ 2.31 (s, 3H), 6.05 (s, 1H), 7.74-8.23 (m, 3H); ¹³C NMR (50 MHz, CDCl₃) δ 18.9, 111.6, 118.5, 125.9, 127.9, 133.7, 138.6, 154.4, 156.5, 160.2.

6-Chloro-4-methylcoumarin-3-carboxylic acid (entry 7): brownish solid (m.p.: 223-247 °C). Analytical data were in full agreement with those already reported in the literature for the same compound.[16]

7-Methoxy-4-methylcoumarin-3-carboxylic acid (entry 8): yellowish solid (m.p.: 183-185 °C). Analytical data were in full agreement with those recorded for a pure commercial sample.

6-Hydroxy-4-methylcoumarin-3-carboxylic acid (entry 9): pale yellow solid (m.p.: 201-202 °C). Analytical data were in full agreement with those recorded for a pure commercial sample.

6,8-Dihydroxy-4-methylcoumarin-3-carboxylic acid (entry 10): pale yellow solid (m.p.: 246-248 °C). Anal. Calc. for C₁₁H₈O₆: C 55.94, H 3.41, O 40.65; Found: C 55.99, H 3.35, O 40.64. ¹H NMR (200 MHz, CDCl₃) δ 2.40 (s, 3H), 5.85 (s, 1H), 6.23 (s, 1H), 6.89 (s, 1H); ¹³C NMR (50 MHz, CDCl₃) δ 18.9, 100.4, 106.7, 112.2, 124.9, 132.9, 144.1, 155.0, 156.0, 160.9.

4-Methylcoumarin-3-carboxylic acid (entry 11): white solid (m.p.: 161-162 °C). Analytical data were in full agreement with those recorded for a pure commercial sample.

RESULTS AND DISCUSSION

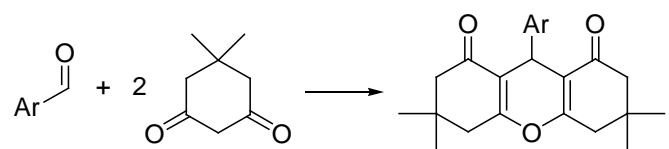
Preliminary assays to optimize reaction conditions were performed using commercially available benzaldehyde and dimedone as starting materials. Both were suspended in different aqueous media represented by waste waters derived from milk/cheese processing. This solvent was the same we recently used to successfully accomplish the synthesis of cinnamic and coumarin-3-carboxylic acids [35]. Reactions were initially carried out over a period of 18 h under magnetic stirring at room temperature and monitored by thin layer chromatography (TLC). Employing the above depicted experimental conditions, low conversions (<15%) into the desired 1,8-dioxo-octahydroxanthenes were achieved. Thus we decided to increase the temperature up to 50 °C and follow the progress of reactions over the same period. This was seen to be the best medium in promoting the conversion of benzaldehyde and dimedone to the condensed adduct. In fact 1,8(2*H*)-dione,3,4,5,6,7,9-hexahydro-3,3,6,6-tetramethyl-9-phenyl-1*H*-xanthene was obtained as a yellow solid after filtration under vacuum in 97 % yield without the need of any other purification. It is noteworthy to underline that a blank experiment using distilled water alone as the solvent applying temperatures in the range of 30 °C– 90 °C led to virtually no progress of the reaction. Handling these excellent

results, we decided to use waste waters of milk/cheese processing and 50 °C as the optimized reaction conditions to validate the protocol and apply it to the condensation of different substituted aromatic aldehydes with dimedone. Results are reported in Table 1. Substrates with electron donating or electron withdrawing groups reacted to the same extent providing the desired 1,8-dioxo-octahydroxanthenes in very high yields. For all entries, final products were simply collected as solids after filtration under vacuum from the reaction media without the need of any chromatographic purifications. Waste waters were recovered as filtrates from every synthetic step, recycled and re-used to carry out other condensations without appreciable loss of effectiveness in terms of yields of the desired xanthene derivative. For example, reactions leading to 1,8(2*H*)-dione,3,4,5,6,7,9-hexahydro-3,3,6,6-tetramethyl-9-(4'-methoxy)phenyl-1*H*-xanthene (entry 2) and 1,8(2*H*)-dione,3,4,5,6,7,9-hexahydro-3,3,6,6-tetramethyl-9-(4'-methoxy) phenyl-1*H*-xanthene (entry 5) were accomplished four successive times each and provided adducts with yield values ranging from 93 % to 96 %. To rationalize the efficiency of waste waters of milk processing as promoters of the title condensation process, we may hypothesize that this medium has a suitable acidic pH value (due the presence of organic acids like pyruvic and lactic ones) to promptly boost the reaction between aromatic aldehydes and dimedone. Indeed, pH measurement

for the employed waste waters recorded a value of 4.62. Although we previously found that application of ultrasound was seen to be an efficient means for the condensation of differently substituted acetophenones and benzaldehydes to provide coumarin-3-carboxylic and cinnamic acids in high yields in 5 – 15 min, the same protocol was not equally effective for the synthesis of 1,8-dioxo-octahydroxanthenes.

As a conclusion, in this paper we showed that safe, non polluting, cheap, and easy to obtain and handle waste waters derived from milk and cheese processing represent a powerful means to promote an efficient and high-yielding condensation reaction of differently substituted aromatic aldehydes with dimedone leading to 1,8-dioxo-octahydroxanthenes. Favourable features of our method include a simple work-up, mild conditions and very good yields. Furthermore, although numerous methodologies for the synthesis of the title compounds appeared in the literature during the last two decades, this is the first time that waste waters are employed to promote the process. Thus, the reaction described herein can be viewed as an additional and alternative example in the field of 1,8-dioxo-octahydroxanthenes synthesis. The use of water residues of industrial processing can be considered as an example of useful waste management and recycling. Further investigations to extend the scope and applicability of waste waters and related solvents are now in progress in our laboratories and will be reported in due course.

Table 1. Synthesis of 1,8-dioxo-octahydroxanthenes from waste waters of milk processing



Entry	Ar	Yield (%) ^a
1	C ₆ H ₅	97
2	4-CH ₃ O-C ₆ H ₄	98
3	4-CH ₃ -C ₆ H ₄	95
4	4-OH-C ₆ H ₄	96
5	4-F-C ₆ H ₄	96
6	4-NO ₂ -C ₆ H ₄	97
7	4-Cl-C ₆ H ₄	98
8	4-Br-C ₆ H ₄	98
9	4-OH-3-CH ₃ O-C ₆ H ₃	95
10	3-NO ₂ -C ₆ H ₄	94
11	3-CH ₃ O-C ₆ H ₄	95
12	2-Cl-C ₆ H ₄	94
13	2,4-Cl ₂ -C ₆ H ₃	98
14	2-OH-C ₆ H ₄	96
15	C ₆ H ₅ -CH=CH	97

^aYields of pure isolated products, characterized by ¹H NMR, ¹³C NMR, elemental analysis, and melting point. Analytical data of all adducts exactly matched those already reported for the same compounds [14, 15, 19, 20, 24, 27].

REFERENCES

1. C.J. Li, L. Chen, *Chem. Soc. Rev.*, **35**, 68 (2006).
2. M.B. Deshmukh, S.S. Patil, S.D. Jadhav, P.B. Pawar, *Synth. Commun.*, **42**, 1177 (2012).
3. S. Patil, S. Jadhav, M.B. Deshmukh, *Arch. Appl. Sci. Res.*, **3**, 203 (2011).
4. K. Mote, S. Pore, G. Rashinkar, S. Kambale, A. Kumbhar, R. Salunkhe, *Arch. Appl. Sci. Res.*, **2**, 74 (2010).
5. A.M. Fonseca, F.J. Monte, M.C.F. Oliveira, M.C.M. Mattos, G.A. Cordell, R. Braz-Filho, T.L.G. Lemos, *J. Mol. Catal. B.: Enzyme*, **57**, 78 (2009).
6. R. Pal, *Open J. Org. Chem.*, **1**, 47, (2013).
7. J.P. Poupelin, G. Saint-Rut, O. Fussard-Blanpin, G. Narcisse, G. Uchida-Ernoff, R. Lacroix, *Eur. J. Med. Chem.*, **13**, 67, (1978).
8. K. Chibale, M. Visser, D.V. Schalkwyk, P.J. Smith, A. Saravanamuthu, A.H. Fairlamb, *Tetrahedron*, **59**, 2289 (2003).
9. A. Banerjee, A.K. Mukherjee, *Stain Technol.*, **56**, 83 (1981).
10. C.G. Knight, T. Stephens, *Biochem. J.*, **258**, 683 (1989).
11. N. Azizi, S. Dezfooli, M.M. Hashemi, *Chimie*, **16**, 997, (2013).
12. M.T. Maghsoodlou, S.M. Habibi-Khorassani, Z. Shankarami, N. Maleki, M. Rostamizadeh, *Chin. Chem. Lett.*, **21**, 686 (2010).
13. B. Das, P. Thirupathi, I. Mahender, V.S. Reddy, Y.K. Rao, *J. Mol. Catal. A: Chem.*, **247**, 233 (2006).
14. H. Lu, J. Li, Z. Zhang, *Z. Appl. Organometall. Chem.* **23**, 165 (2009).
15. M.A. Bigdeli, F. Nemati, G.H. Mahdavinia, H. Doostmohammadi, *Chin. Chem. Lett.*, **20**, 1275 (2009).
16. M. Seyyedhamzeh, P. Mirzaei, A. Bazgir, *Dyes Pigments*, **76**, 836 (2008).
17. A. Rostamizadeh, A.M. Amani, G.H. Mahdavinia, G. Amiri, H. Sepehrian, *Ultrason. Sonochem.*, **17**, 306, (2010).
18. B. Karami, S.J. Hosein, K. Eskandari, A. Ghasemi, H. Nasrabadi, *Catal. Sci. Technol.* **2**, 331, (2012).
19. J. Ma, C. Wang, Q. Wu, R. Tang, H. Liu, Q. Li, *Heteroatom. Chem.* **19**, 609, (2008).
20. K. Niknam, M. Damya, *J. Chin. Chem. Soc.* **56**, 659, (2009).
21. M. Dabiri, M. Baghbanmzadeh, E. Arzroomchilar, *Catal. Commun.*, **9**, 939, (2008).
22. D. Fang, K. Gong, Z. Liu, *J. Heterocyclic Chem.*, **48**, 468, (2011).
23. D. Fang, J. Yang, Z. Liu, *Catal. Lett.*, **127**, 291, (2009).
24. A. Zare, A.R. Moosavi-Zare, M. Merajoddin, M.A. Zolfigol, T. Hekmat-Zadeh, A. Hasaninejad, A. Khazaei, M. Mokhlesi, V. Khakyzadeh, F. Derakshan-Panah, M.H. Beyzavi, E. Rostami, A. Arghoon, R. Roohandeh, *J. Mol. Liq.* **167**, 69, (2012).
25. K. Venkatesan, S.S. Pujari, R.J. Lahoti, K.V. Srinivasan, *Ultrason. Sonochem.*, **15**, 548, (2008).
26. A. Rahmati, *Chin. Chem. Lett.*, **21**, 761, (2010).
27. L. Han, L. Zhang, Z. Zhou, *Heterocyclic Lett.*, **6**, 23, (2016).
28. S.S. Beigbaghlou, K. Marjani, A. Habibi, S.V. Atghia, *RSC Adv.*, **6**, 20306, (2016).
29. D.L. Ronibala, C.L. Vartima, C.I. Harimala, S.O. Mukherjee, *As. J. Chem.* **7**, 1528, (2016).
30. A. Rajini, C. Suman, A. Ajay Kumar, S. Suresh, N. Venkatathri, *Synth. Commun.*, **46**, 1671, (2016).
31. A. Thakur, A. Sharma, A. Sharma, *Synth. Commun.*, **46**, 1766, (2016).
32. A. Fallah, M. Tajbakhsh, H. Vahedi, A. Bekhradnia, *Res. Chem. Intermediat.*, **43**, 29, (2017).
33. M.M. Heravi, S. Sadjadi, H.A. Oskooie, R.H. Shoar, F.F. Bamoharram, *Catalysis Commun.*, **9**, 470, (2007).
34. S. Fiorito, V.A. Taddeo, S. Genovese, F. Epifano, *Tetrahedron Lett.*, **57**, 4795, (2016).

ОТПАДЪЧНИ ВОДИ ОТ ПРОИЗВОДСТВОТО НА МЛЯКО И СИРЕНЕ КАТО ЕФЕКТИВЕН ПРОМОТОР ЗА СИНТЕЗА НА 1,8-ДИОКСО-ОКТАХИДРОКСАНТЕНИ

С. Фиорито, Ф. Епифано*, Ф. Прециузо, В. А. Тадео, С. Дженовезе

*Департамент по фармация, Университет „Г. Д'Анунцио” на Киети-Пескара, Виа дей Вестини 31, 66100
Киети Скало (СН), Италия*

Постъпила на 17 май, 2017 г.; Приета на 20 декември, 2017 г.

(Резюме)

Отпадни води от селскостопански и промишлени производства се използват в последно време за подпомагане на голям брой класически и иновативни процеси в синтетичната органична химия. Такъв „зелен” химичен подход позволява да се избегне използването на токсични, замърсяващи и опасни химикали, като същевременно води до повишаване на търговската стойност на такива странични продукти. Ксантените са група природни и полусинтетични съединения с голям фармакологичен потенциал и редица други приложения. В настоящата статия е описана нова, подобрена методология за синтез на 1,8-диоксо-октахидрооксантени чрез използване на отпадна вода от производството на мляко и сирене като разтворител. 1,8-Диоксо-октахидрооксантените са получени с много добри добиви (94 – 98 %) от различно-заместени ароматни алдехиди и димедон като субстрати. Въпреки публикуването на редица статии върху синтеза на 1,8-диоксо-октахидрооксантени през последните години, настоящото съобщение е първото, в което за целта се използва отпадна вода от селскостопанско и промишлено производство. Това подчертава още веднъж ползата от страничните продукти на селскостопански и промишлени производства за осъществяването на „зелени” химични процеси.

One-pot three-component synthesis of 3-[(aryl)-arylsulfanyl-methyl]-4-hydroxy-6-methylpyran-2-one

M. Khaleghdadi, A. Hassanabadi*

Department of Chemistry, Zahedan Branch, Islamic Azad University, PO Box 98135-978, Zahedan, Iran

Received February 26, 2017; Accepted December 18, 2017

A good yield in the synthesis of 3-[(aryl)-arylsulfanyl-methyl]-4-hydroxy-6-methylpyran-2-one is described involving the reaction of 4-hydroxy-6-methyl-2H-pyran-2-one with aromatic aldehydes and thiols in the presence of *p*-toluene sulfonic acid (*p*-TSA) under reflux conditions.

Keywords: 4-Hydroxy-6-methyl-2H-pyran-2-one, *p*-Toluene sulfonic acid, Thiols, Aromatic aldehydes, Multicomponent reactions

INTRODUCTION

Multicomponent reactions (MCRs), by virtue of their convergence, provide a single purification step, higher yields than stepwise procedure, use of simple and diverse precursors to construct complex molecules and use of only a single promoter or catalyst [1-3]. Multicomponent reactions are useful and efficient methods in organic synthesis. Thus, the development of new multicomponent reactions is a popular area of research in organic chemistry from a green chemistry point of view [4-6].

The reaction of 4-hydroxy-6-methyl-2H-pyran-2-one with aromatic aldehydes and thiol has already been reported [7-9], but there are many limitations, such as long reaction times, hazardous organic solvents and reagents, and low yields. Hence, we have used a novel method to synthesize another class of this derivatives *via* three-component condensation reaction of 4-hydroxy-6-methyl-2H-pyran-2-one with aromatic aldehydes and thiols in the presence of *p*-toluene sulfonic acid (*p*-TSA). We have developed a mild one-pot method, characterized by excellent yield, simple work-up, fast reaction, and employment of the cheap catalyst *p*-TSA.

As part of our current studies on the development of new routes in organic synthesis [10-13], we report the reaction of 4-hydroxy-6-methyl-2H-pyran-2-one with aromatic aldehydes and thiols in the presence of *p*-toluene sulfonic acid.

EXPERIMENTAL

Instruments

Elemental analyses were performed using a Heraeus CHN-O-Rapid analyzer. Mass spectra were

recorded on a FINNIGAN-MAT 8430 mass spectrometer operating at an ionization potential of 70 eV. IR spectra were recorded on a Shimadzu IR-470 spectrometer. ¹H and ¹³C NMR spectra were recorded on a Bruker DRX-250 Avance spectrometer in DMSO solution using TMS as internal standard. The chemicals used in this work were purchased from Fluka (Buchs, Switzerland) and were used without further purification.

General experimental procedure

To a mixture of 4-hydroxy-6-methyl-2H-pyran-2-one (1 mmol) and aromatic aldehyde (1 mmol) in acetone (10 mL) in the presence of *p*-toluene sulfonic acid (0.1 mmol) as the catalyst, 1 mmol thiol was added under reflux.

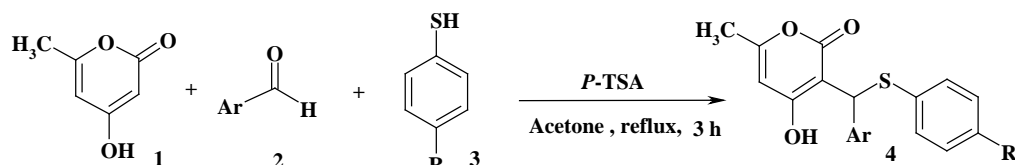
The reaction progress was controlled by TLC (*n*-hexane:ethyl acetate=1:1). After 3 h, the reaction was completed and the solvent was removed under reduced pressure, the precipitated product was filtered off, washed with water (5 mL) and crystallised from ethanol.

RESULTS AND DISCUSSION

Reaction between 4-hydroxy-6-methyl-2H-pyran-2-one **1** with aromatic aldehydes **2** and thiols **3** in the presence of *p*-toluene sulfonic acid under reflux conditions affords 3-[(aryl)-arylsulfanyl-methyl]-4-hydroxy-6-methylpyran-2-one **4** in good yields. (Scheme 1).

The compounds **4a-d** were characterized by ¹H, ¹³C-NMR and IR spectroscopy and elemental analyses [5-7]. Compounds **4e-n** were new and their structures were deduced by elemental and spectral analysis. The structure of the other products was proved on the basis of ¹H, ¹³C-NMR and IR spectroscopy and elemental analyses. The mass spectra of compounds **4a-n** were fairly similar and displayed molecular ion peaks. For example, the

* To whom all correspondence should be sent.
E-mail: ar_hasanabadi@yahoo.com



4	Ar	R	%Yield*	4	Ar	R	%Yield*
a	C ₆ H ₅	H	78	h	2-Cl C ₆ H ₄	H	85
b	4-NO ₂ C ₆ H ₄	H	91	i	2-FC ₆ H ₄	H	87
c	4-Cl C ₆ H ₄	H	86	j	2-O ₂ N C ₆ H ₄	H	90
d	4-CH ₃ O C ₆ H ₄	H	75	k	4-NO ₂ C ₆ H ₄	CH ₃	87
e	4-Br C ₆ H ₄	H	84	l	4-Cl C ₆ H ₄	CH ₃	83
f	4-FC ₆ H ₄	H	80	m	4-CH ₃ O C ₆ H ₄	CH ₃	72
g	4-CH ₃ C ₆ H ₄	H	75	n	2-Cl C ₆ H ₄	CH ₃	82

*Isolated yields

Scheme 1

mass spectrum of compound **4e** showing a molecular ion peak at 403 m/z confirmed that compound **4e** is a triadduct of 4-hydroxy-6-methyl-2H-pyran-2-one, 4-bromobenzaldehyde and thiol. The ¹H-NMR spectrum of compound **4e** displayed a sharp single signal at δ = 5.82 ppm for methine proton, along with characteristic signals at δ = 6.81–7.80 ppm for aromatic protons. A singlet was observed at δ = 9.93 ppm for OH proton, disappeared by addition of D₂O. ¹³C NMR spectrum of compound **4e** showed 15 distinct signals in agreement with the proposed structure.

A mechanism of reasonable possibility is presented in scheme 2. As can be seen, firstly, Knoevenagel condensation between 4-hydroxy-6-methyl-2H-pyran-2-one **1** and aromatic aldehydes **2** in the presence of *p*-toluene sulfonic acid occurs and intermediate **5** is formed. Intermediate **5** reacts with thiols *via* conjugate addition to form product **4**.

In summary, we have developed a mild, one-pot three-component reaction between 4-hydroxy-6-methyl-2H-pyran-2-one, aromatic aldehydes and thiols in the presence of *p*-toluene sulfonic acid under reflux conditions, characterized by excellent

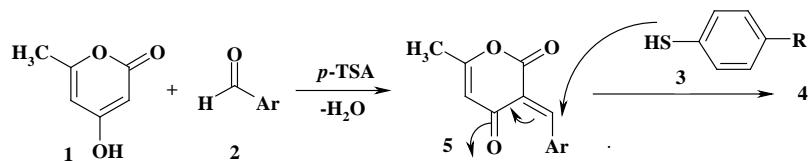
yield, simple work-up, fast reaction, and employment of the cheap catalyst *p*-TSA.

3-[(4-Bromophenyl)-phenylsulfanyl-methyl]-4-hydroxy-6-methylpyran-2-one (4e).

Brown powder, m.p. 83–85 °C, IR (KBr) (ν_{max} cm⁻¹): 3113 (OH), 1684 (C=O). Analyses: Calcd. for C₁₉H₁₅BrO₃S: C, 56.59; H, 3.75%. Found: C, 56.45; H, 3.90. MS (m/z, %): 403 (5). ¹H NMR (250 MHz, d₆-DMSO): δ 2.13 (3H, s, CH₃), 5.82 (1H, s, CH), 6.07 (1H, s, =CH), 6.81–7.80 (9H, m, arom), 9.93 (1H, s br, OH) ppm. ¹³C NMR (62.9 MHz, d₆-DMSO): δ 19.51 (CH₃), 34.48 (CH), 100.40, 101.58, 119.06, 127.05, 129.11, 129.48, 131.20, 131.63, 132.68, 140.03, 161.70, 164.23, 168.29 ppm.

3-[(4-Fluorophenyl)-phenylsulfanyl-methyl]-4-hydroxy-6-methylpyran-2-one (4f).

Yellow powder, m.p. 118–120 °C, IR (KBr) (ν_{max} cm⁻¹): 3427 (OH), 1684 (C=O). Analyses: Calcd. for C₁₉H₁₅FO₃S: C, 66.65; H, 4.42%. Found: C, 66.54; H, 4.58. MS (m/z, %): 342 (3). ¹H NMR (250 MHz, d₆-DMSO): δ 2.28 (3H, s, CH₃), 5.75 (1H, s, CH), 6.07 (1H, s, =CH), 6.96–7.52 (9H, m, arom), 10.90 (1H, s br, OH) ppm. ¹³C NMR (62.9 MHz, d₆-DMSO): δ 19.62 (CH₃), 34.20 (CH), 103.19, 115.48, 127.17, 127.53, 128.14, 129.06, 130.32, 131.10, 137.00, 159.66, 161.83, 163.56, 169.60 ppm.



Scheme 2

3-[(4-methylphenyl)-phenylsulfanyl-methyl]-4-hydroxy-6-methylpyran-2-one (4g).

Brown powder, m.p. 183–185 °C, IR (KBr) (ν_{\max} cm^{-1}): 3125 (OH), 1693 (C=O). Analyses: Calcd. for $\text{C}_{20}\text{H}_{18}\text{O}_3\text{S}$: C, 70.98; H, 5.36%. Found: C, 80.13; H, 5.21. MS (m/z, %): 338 (4). ^1H NMR (250 MHz, d_6 -DMSO): δ 1.70 (3H, s, CH_3), 2.21 (3H, s, CH_3), 5.68 (1H, s, CH), 6.11 (1H, s, =CH), 7.13–7.90 (9H, m, arom), 11.18 (1H, s br, OH) ppm. ^{13}C NMR (62.9 MHz, d_6 -DMSO): δ 19.57 (CH_3), 23.36 (CH_3), 35.76 (CH), 100.21, 101.40, 119.15, 123.53, 124.46, 127.17, 127.85, 131.55, 129.32, 143.10, 161.43, 165.61, 167.75 ppm.

3-[(2-Chlorophenyl)-phenylsulfanyl-methyl]-4-hydroxy-6-methylpyran-2-one (4h).

Brown powder, m.p. 161–163 °C, IR (KBr) (ν_{\max} cm^{-1}): 3115 (OH), 1696 (C=O). Analyses: Calcd. for $\text{C}_{19}\text{H}_{15}\text{ClO}_3\text{S}$: C, 63.60; H, 4.21%. Found: C, 63.75; H, 4.012. MS (m/z, %): 358 (5). ^1H NMR (250 MHz, d_6 -DMSO): δ 2.19 (3H, s, CH_3), 5.73 (1H, s, CH), 6.04 (1H, s, =CH), 7.11–7.84 (9H, m, arom), 11.52 (1H, s br, OH) ppm. ^{13}C NMR (62.9 MHz, d_6 -DMSO): δ 19.48 (CH_3), 34.46 (CH), 100.37, 101.71, 125.77, 127.17, 127.88, 128.31, 128.90, 130.48, 131.14, 133.08, 140.35, 143.27, 161.82, 164.37, 166.52 ppm.

3-[(2-Fluorophenyl)-phenylsulfanyl-methyl]-4-hydroxy-6-methylpyran-2-one (4i).

Yellow powder, m.p. 103–105 °C, IR (KBr) (ν_{\max} cm^{-1}): 3432 (OH), 1691 (C=O). Analyses: Calcd. for $\text{C}_{19}\text{H}_{15}\text{FO}_3\text{S}$: C, 66.65; H, 4.42%. Found: C, 66.50; H, 4.60. MS (m/z, %): 342 (5). ^1H NMR (250 MHz, d_6 -DMSO): δ 2.24 (3H, s, CH_3), 5.86 (1H, s, CH), 6.13 (1H, s, =CH), 7.03–7.65 (9H, m, arom), 10.96 (1H, s br, OH) ppm. ^{13}C NMR (62.9 MHz, d_6 -DMSO): δ 19.50 (CH_3), 34.27 (CH), 103.34 115.62, 127.13, 127.67, 128.19, 129.12, 130.45, 131.17, 133.15, 137.06, 140.28, 159.52, 161.77, 163.50, 169.43 ppm.

3-[(2-nitrophenyl)-phenylsulfanyl-methyl]-4-hydroxy-6-methylpyran-2-one (4j).

Brown powder, m.p. 201–203 °C, IR (KBr) (ν_{\max} cm^{-1}): 3418 (OH), 1688 (C=O), 1524 and 1355 (NO_2). Analyses: Calcd. for $\text{C}_{19}\text{H}_{15}\text{NO}_5\text{S}$: C, 61.78; H, 4.09; N, 3.79%. Found: C, 61.63; H, 4.27; N, 3.92. MS (m/z, %): 369 (8). ^1H NMR (250 MHz, d_6 -DMSO): δ 2.26 (3H, s, CH_3), 5.74 (1H, s, CH), 6.13 (1H, s, =CH), 7.15–8.46 (9H, m, arom), 11.50 (1H, s br, OH) ppm. ^{13}C NMR (62.9 MHz, d_6 -DMSO): δ 19.57 (CH_3), 35.80 (CH), 100.46, 101.22, 121.20, 122.14, 124.33, 127.13, 127.72, 128.76, 130.55, 133.06, 146.03, 148.71, 161.58, 165.60, 167.43 ppm.

3-[(4-nitrophenyl)(p-tolylsulfanyl)-methyl]-4-hydroxy-6-methylpyran-2-one (4k).

Brown powder, m.p. 211–213 °C, IR (KBr) (ν_{\max} cm^{-1}): 3403 (OH), 1681 (C=O), 1526 and 1345 (NO_2). Analyses: Calcd. for $\text{C}_{20}\text{H}_{17}\text{NO}_5\text{S}$: C, 62.65; H, 4.47; N, 3.65%. Found: C, 62.71; H, 4.35; N, 3.80. MS (m/z, %): 383 (8). ^1H NMR (250 MHz, d_6 -DMSO): δ 2.10 (3H, s, CH_3), 2.38 (3H, s, CH_3), 5.72 (1H, s, CH), 6.13 (1H, s, =CH), 7.35–8.28 (8H, m, arom), 11.42 (1H, s br, OH) ppm. ^{13}C NMR (62.9 MHz, d_6 -DMSO): δ 19.43 (CH_3), 21.66 (CH_3), 35.80 (CH), 100.52, 101.22, 123.43, 124.39, 127.07, 127.64, 128.72, 129.26, 146.18, 149.82, 161.73, 165.51 and 168.18 ppm.

3-[(4-Chlorophenyl)(p-tolylsulfanyl)-methyl]-4-hydroxy-6-methylpyran-2-one (4l).

Brown powder, m.p. 125–127 °C, IR (KBr) (ν_{\max} cm^{-1}): 3267 (OH), 1693 (C=O). Analyses: Calcd. for $\text{C}_{20}\text{H}_{17}\text{ClO}_3\text{S}$: C, 64.42; H, 4.60%. Found: C, 64.55; H, 4.49. MS (m/z, %): 372 (4). ^1H NMR (250 MHz, d_6 -DMSO): δ 2.18 (3H, s, CH_3), 2.35 (3H, s, CH_3), 5.81 (1H, s, CH), 6.14 (1H, s, =CH), 7.08–7.95 (8H, m, arom), 11.36 (1H, s br, OH) ppm. ^{13}C NMR (62.9 MHz, d_6 -DMSO): δ 19.47 (CH_3), 21.50 (CH_3), 34.46 (CH), 100.42, 101.73, 124.85, 127.16, 127.64, 128.21, 129.10, 130.77, 139.43, 141.32, 161.87, 164.20 and 166.75 ppm.

3-[(4-methoxyphenyl)(p-tolylsulfanyl)-methyl]-4-hydroxy-6-methylpyran-2-one (4m).

Brown powder, m.p. 173–175 °C, IR (KBr) (ν_{\max} cm^{-1}): 3156 (OH), 1681 (C=O). Analyses: Calcd. for $\text{C}_{21}\text{H}_{20}\text{O}_4\text{S}$: C, 68.46; H, 5.47%. Found: C, 68.62; H, 5.33. MS (m/z, %): 368 (3). ^1H NMR (250 MHz, d_6 -DMSO): δ 2.22 (3H, s, CH_3), 2.30 (3H, s, CH_3), 3.68 (3H, s, OCH_3), 5.72 (1H, s, CH), 6.15 (1H, s, =CH), 7.11–7.88 (8H, m, arom), 11.21 (1H, s br, OH) ppm. ^{13}C NMR (62.9 MHz, d_6 -DMSO): δ 19.48 (CH_3), 21.52 (CH_3), 35.77 (CH), 56.43 (OCH_3), 100.16, 101.52, 119.22, 123.58, 124.63, 127.16, 127.80, 131.63, 129.35, 143.24, 161.50, 165.39 and 167.52 ppm.

3-[(2-Chlorophenyl)(p-tolylsulfanyl)-methyl]-4-hydroxy-6-methylpyran-2-one (4n).

Brown powder, m.p. 150–152 °C, IR (KBr) (ν_{\max} cm^{-1}): 3293 (OH), 1690 (C=O). Analyses: Calcd. for $\text{C}_{20}\text{H}_{17}\text{ClO}_3\text{S}$: C, 64.42; H, 4.60%. Found: C, 64.58; H, 4.43. MS (m/z, %): 372 (7). ^1H NMR (250 MHz, d_6 -DMSO): δ 2.27 (3H, s, CH_3), 2.30 (3H, s, CH_3), 5.66 (1H, s, CH), 6.09 (1H, s, =CH), 7.08–7.92 (8H, m, arom), 11.33 (1H, s br, OH) ppm. ^{13}C NMR (62.9 MHz, d_6 -DMSO): δ 19.50 (CH_3), 21.62 (CH_3), 34.37 (CH), 100.28, 101.69, 125.71, 127.25, 127.76, 128.39, 128.95, 130.53, 131.22, 133.11, 140.30, 143.37, 161.75, 164.34, 166.72 ppm.

REFERENCES

1. A. Domling, I. Ugi, *Angew. Chem.*, **112**, 3300 (2000).
2. D. J. Ramon, M. Yus, *Angew. Chem.*, **117**, 1628 (2005).
3. A. Ulaczyk-Lesankom, D. G. Hall, *Curr. Opin. Chem. Biol.*, **9**, 266 (2005).
4. I. Ugi, *Angew. Chem. Int. Ed.*, **21**, 810 (1982).
5. A. Dömling, I. Ugi, *Angew. Chem. Int. Ed.*, **39**, 3169 (2000).
6. A. Dömling, *Chem. Rev.*, **106**, 17 (2006).
7. P. De March, M. Moreno-Manas, R. Pi, A. Trius, *J. Heterocycl. Chem.*, **19**, 335 (1982).
8. M. Moreno-Manas, R. Pleixats, *Synthesis*, **5**, 430 (1984).
9. O. S. Darwish, K. A. Granum, Q. Tan, R. P. Hsung, *Tetrahedron Lett.*, **42**, 3283 (2001).
10. N. Bizhanpoor, A. Hassanabadi, *J. Chem. Res.*, **40**, 38 (2016).
11. E. Hashemzaei, A. Hassanabadi, *J. Chem. Res.*, **39**, 421 (2015).
12. A. Hassanabadi, *J. Chem. Res.*, **37**, 152 (2013).
13. M. Anary-Abbasinejad, M. Akhavan, A. Hassanabadi, *J. Chem. Res.*, **33**, 143 (2009).

ЕДНОСТАДИЕН ТРИКОМПОНЕНТЕН СИНТЕЗ НА 3-[(АРИЛ)-АРИЛСУЛФАНИЛ-МЕТИЛ]-4-ХИДРОКСИ-6-МЕТИЛПИРАН-2-ОН

М. Калегеди, А. Хасанабади*

Департамент по химия, Захедански клон на Ислямски Азад университет, п.к. 98135-978, Захедан, Иран

Постъпила на 26 февруари, 2017 г.; Приета на 18 декември, 2017 г.

(Резюме)

Описан е синтезът на 3-[(арил)-арилсулфанил-метил]-4-хидрокси-6-метилпиран-2-он с добър добив посредством реакция на 4-хидрокси-6-метил-2*H*-пиран-2-он с ароматни алдехиди и тиоли в присъствие на *p*-толуенсулфонова киселина при температура на кипене.

Detection limit and electrochemical behavior of maleic acid on a platinum electrode

H. M. Rageh¹, M. M. Abou-Krishna^{1,2,*}, A. M. Abo-Bakr¹, M. Abd-Elsabour¹

¹Department of Chemistry, South Valley University, Qena, 83523, Egypt

²College of Science, Chemistry Department, Al Imam Mohammad Ibn Saud Islamic University (IMSIU), Riyadh 11623, KSA

Received September 30, 2017; Revised January 9, 2018

The electrochemical behavior of maleic acid (MA) on a platinum electrode was studied using cyclic voltammetric, linear sweep voltammetric and chronoamperometric techniques. The results showed that the reduction of MA on a Pt electrode is a quasi-reversible process as a result of the diffusion and the reductive potential of MA at -0.62 V (vs. Ag/AgCl). The detection limit of MA on a Pt electrode was calculated to be 1.6×10^{-5} M. The anodic and cathodic current peaks of MA increased with increasing the concentration of MA from 5.00×10^{-3} to 8.89×10^{-3} M at a scan rate ranging from 20-200 mV/s. The diffusion coefficient of MA was determined to be 0.815×10^{-7} cm².s⁻¹. The mechanism of the produced succinic acid by electrochemical reduction of MA was discussed.

Keywords: Maleic acid; Succinic acid; Cyclic voltammetry; Linear sweep voltammetry; Chronoamperometric measurements.

INTRODUCTION

The electrochemical behavior of maleic acid (HOOC-CH=CH-COOH) in oxidation is of great interest because this molecule is the hinge between cyclic and linear structures. So the oxidation of MA on born doped diamond electrode (BDDE) has been studied. The reduction of MA in acidic media on a Pb cathode in electrolytic solution of Co, Ni, Cu, and Mn citrate complexes has been also studied [1]. Reduction of MA on Ti/ceramicTiO₂ under galvanostatic and cyclic voltammetric conditions has been examined [2]. Also, the behavior of MA had previously been studied using Au, (BDD), glassy carbon (GC) and lead electrodes [3-5].

Maleic acid can be easily reduced to succinic acid, both chemically and electrochemically, the electrochemical synthesis having numerous advantages such as high yield, high purity, mild reaction conditions, low environmental pollution and zero-emission process *via* filtrate recycling [6-9].

Succinic acid as a product of the electrochemical reduction of MA is of great marketable rank as an important chemical material. It finds extensive applications in different areas such as radiation dosimetry, agriculture, electroplating, medicine, photography, waste-gas scrubbing, surfactants, foods, textiles, cosmetics and is used in the food and drink industry, mainly as acidity regulator [10-15].

The current study targets to inspect the electrochemical behavior of MA on a Pt electrode by

using cyclic voltammetry to elucidate the mechanism of the reduction process. The effects of concentration of MA and scan rate on the current peaks were studied as well. The electrochemical synthesis of succinic acid from MA using linear sweep voltammetry was studied. The detection limit of MA on a Pt electrode was a part in this work.

EXPERIMENTAL

Reagents and solutions

All solutions used in the present investigation were freshly prepared from Analar grade chemicals used without further purification. 0.1M Sodium phosphate monohydrate Na₂HPO₄ used as a supporting electrolyte was prepared by dissolving 3.55 g in 250 mL of double-distilled water. A stock solution of 0.01M MA (dihydrate) was prepared by dissolving 0.315 g in 250 mL of double-distilled water. Other concentrations of MA were obtained by dilution from the stock solution.

Electrochemical equipment

The device used in these experiments was EG&G Princeton Applied Research potentiostat/galvanostat model 263. The cell contains three electrodes (model K0264 micro-cell), an Ag/AgCl (saturated KCl) -model K0265 electrode was used as the reference electrode, while the working and counter-model K0266-electrodes were of high purity platinum wire. All measurements were carried out at room temperature in duplicate and the reproducibility of these measurements was found to be satisfactory.

* To whom all correspondence should be sent.

E-mail: abou_krishna@yahoo.com

Techniques used

The electrochemical behavior of maleic acid was studied in Na_2HPO_4 solutions on a platinum electrode using cyclic voltammetry (CV). The voltammetric parameters were as follows: initial potential was 1 V; vertex potential was -1 V and final potential was 1 V vs. Ag/AgCl in presence of different concentrations of maleic acid at different scan rates. Another technique used was cathodic linear sweep voltammetry (CLSV) of 8.57×10^{-3} M maleic acid in 0.1 M Na_2HPO_4 from 1 V to -1 V (vs. Ag/AgCl) at a scan rate of 100 mV/s. The third technique used was chronoamperometry (CA) of 3.33 mM to 8.33 mM of MA in 0.1 M Na_2HPO_4 as a supporting electrolyte, setting the working electrode at 0.00 mV (first potential step) and at -1.00 mV (second potential step) at time 5 s.

RESULTS AND DISCUSSION

Supporting electrolyte selection

In the current study, many supporting electrolytes (e. g.: sodium sulfate, silver nitrate, sodium chloride and phosphate monohydrate) have been used to test the behaviour of the MA on a Pt electrode. It has been found that the phosphate monohydrate is the most appropriate.

Figure 1 shows the cyclic voltammogram of 0.1M Na_2HPO_4 as supporting electrolyte from 1 V to -1 V at a scan rate 50 mV/s on a Pt electrode. It is seen that there is one reduction peak at - 0.9 V and one oxidation peak at - 0.6 V.

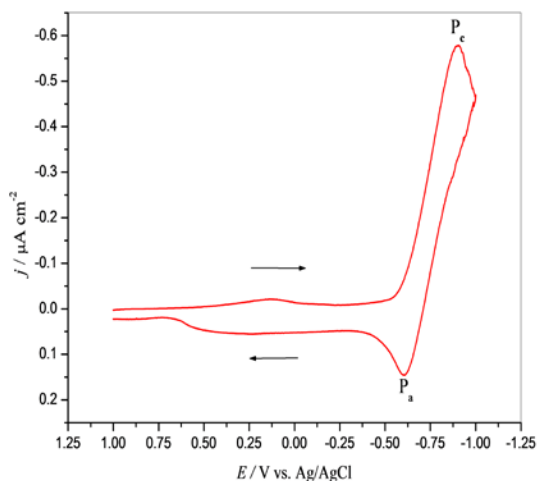


Fig. 1. Cyclic voltammogram of a Pt electrode in 0.1M Na_2HPO_4 at a scan rate of 50 mV/s.

Different volumes of 0.01M maleic acid were added to other different volumes of 0.1M sodium phosphate monohydrate to study the cyclic voltammetry of MA in this supporting electrolyte.

But there are no peaks of MA observed from concentrations 5.00×10^{-5} M to 3.33×10^{-3} M, as illustrated in Figure 2.

Also the cathodic and anodic current peaks of supporting electrolyte (Na_2HPO_4) decreased with increasing in the concentration of MA, as observed in Figure 2.

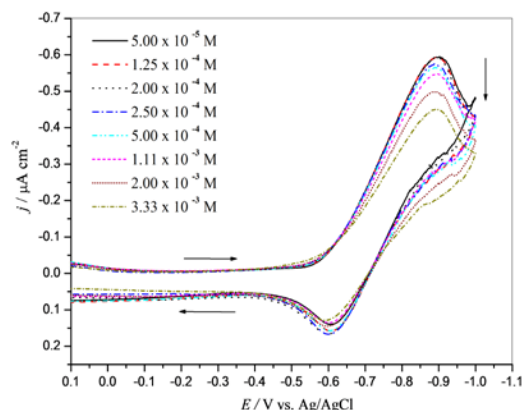


Fig. 2. Cyclic voltammograms of different concentrations of maleic acid in 0.1 M Na_2HPO_4 , at a scan rate 50 mV/s.

At a concentration of 8.57×10^{-3} M, the best cathodic peak (P_{C1}) at -0.62 V appears which corresponds to the reduction of MA to succinic acid and the anodic peak (P_{A1}) at -0.33 V. P_{C2} and P_{A2} belong to Na_2HPO_4 , as follows from Figure 3.

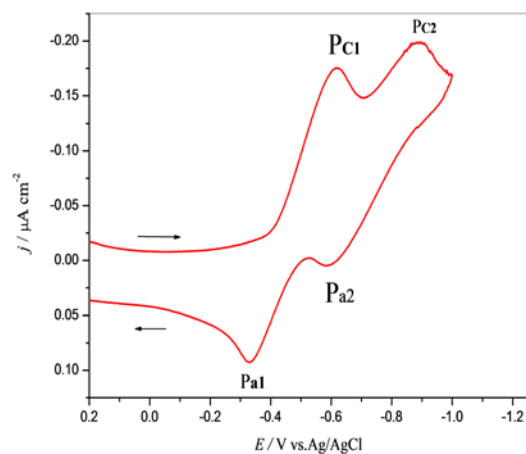


Fig. 3. Cyclic voltammograms of 8.57×10^{-3} M maleic acid in 0.1 M Na_2HPO_4 , at a scan rate of 50 mV/s.

From the anodic and cathodic peaks the potential difference was calculated as equation (1):

$$\Delta E = E_c - E_a = -0.62 - (-0.33) = -0.29V \quad (1)$$

A quasi-reversible process controlled by diffusion represents the electrochemical reduction of maleic acid on a Pt electrode [16,17], where the

potential difference (-0.29 V) refers to a quasi-reversible process controlled by diffusion.

Effect of maleic acid concentration

Figure 4 shows the effect of various concentrations of MA on the cathodic and the anodic peaks. The cathodic peak of MA increases with the increase in MA concentrations from 5.00×10^{-3} M to 8.89×10^{-3} M, and also the cathodic peak potential shifted to more negative values.

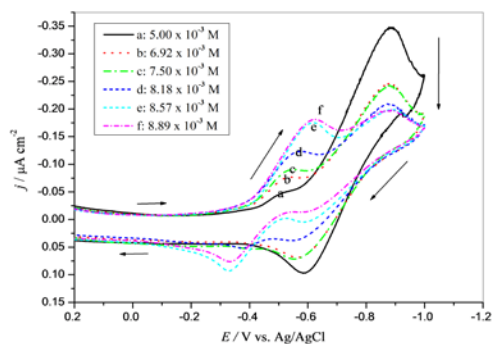


Fig. 4. Cyclic voltammograms of different concentrations of maleic acid in 0.1 M Na₂HPO₄, at a scan rate of 50 mV/s.

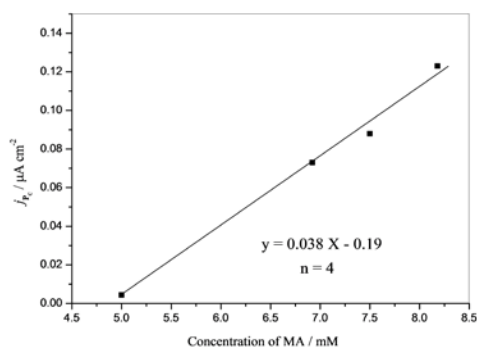


Fig. 5. Calibration graph of maleic acid in 0.1 M Na₂HPO₄ using a Pt electrode at a scan rate of 50 mV/s.

On the other side, the anodic peak started to appear at a concentration of 8.18 mM of MA and its oxidation current increased with the increase in the concentration of maleic acid up to 8.57×10^{-3} M and then decreased with the increase in concentration (8.89×10^{-3} M). This supports the idea that the electrochemical reduction of maleic acid on a Pt electrode is a quasi-reversible process controlled by diffusion.

The calibration graph of MA in different concentrations was obtained by using a Pt electrode, as shown in Figure 5. A linear response was achieved in the concentration range (5.00 - 8.18 mM) of MA at a sensitivity response of 0.19 μA/mM. Table 1 displays the data used to estimate the value of SD (standard deviation) of the mean current applying on Figure 5.

Table 1. Data used to calculate the value of SD taken from figure 5

I _j	i _j	X
0.00	0.002	5.00
0.073	0.074	6.92
0.095	0.093	7.50
0.121	0.123	8.18

The SD value can be calculated according to Miller equation (2):

$$SD = 1/(n-2) \sum (i_j - I_j)^2 \quad (2)$$

where, n is the number of MA concentrations used (n = 4), i_j is the experimental value of the experiment number j and I_j is the corresponding recalculated value, at the same concentration using the regression line equation (3):

$$j_{pc} (\mu A/cm^2) = 0.038C (mM) - 0.190 \quad (3)$$

The calculated SD was used to determine the detection limit of MA at the platinum electrode [17] (DL, 3 × SD / slope), which was calculated as 1.6×10^{-5} M.

Effect of scan rate

The effect of a varying scan rate of the oxidation-reduction process of MA was studied. Cyclic voltammograms of 8.57×10^{-3} M MA in 0.1M Na₂HPO₄ supporting electrolyte using a Pt electrode were obtained for a scan rate ranging from 20-200 mV/s (Figure 6).

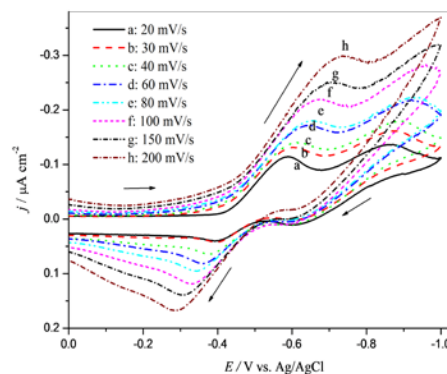


Fig. 6. Cyclic voltammograms of 8.57×10^{-3} M maleic acid in 0.1M Na₂HPO₄, at different scan rates.

As shown in Figure 6, the cathodic and anodic peak currents of MA increased with increasing the scan rate at the Pt electrode. Furthermore, the cathodic peak potential shifted to lower negative values and the anodic peak potential shifted to higher positive values with increasing the scan rate. This is because of the accumulation of the MA molecules on the Pt electrode.

Good linearity between the cathodic and the anodic peak currents with the square root of scan rate (Figures 7, 8) was obtained by:

$$j_{pc}(\mu A/cm^2)=0.0189^{0.5}(mV/s)^{0.5}+0.085 \quad (4)$$

$$j_{pa}(\mu A/cm^2)=0.0135^{0.5}(mV/s)^{0.5}+0.019 \quad (5)$$

This supports the idea that the electrode reactions of maleic acid were under diffusion control, referring to [17].

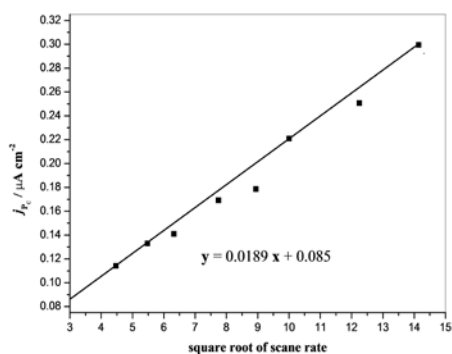


Fig. 7. Plot of cathodic peak current *versus* square root of scan rate of 8.57×10^{-3} M maleic acid in 0.1M Na_2HPO_4 .

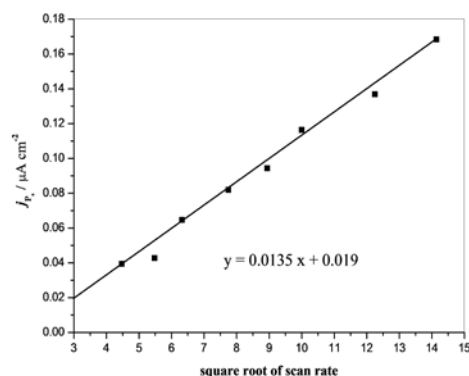


Fig. 8. Plot of anodic peak current *versus* square root of scan rate of 8.57×10^{-3} M maleic acid in 0.1M Na_2HPO_4 .

Cathodic linear sweep voltammetry

Cathodic linear sweep voltammetry can be used as an electrosynthesis process because it is a simple, quick and accurate technique. So succinic acid can be electrosynthesized from maleic acid by this technique.

Cathodic linear sweep voltammetry of 8.57×10^{-3} M MA at a scan rate of 100 mV/s displays two cathodic peaks in a cathodic scan. The P_c at -0.68 V may be referred to the reduction of maleic acid into succinic acid. The second P_c at -0.96 V belongs to Na_2HPO_4 as a supporting electrolyte (Figure 9).

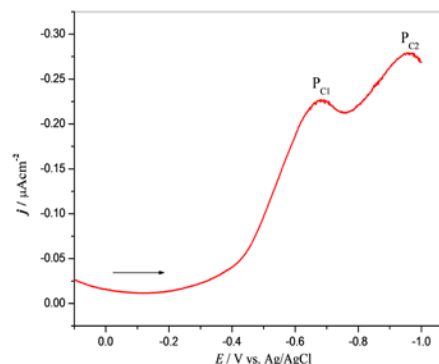


Fig. 9. Cathodic linear sweep voltammogram of 8.57×10^{-3} M maleic acid in 0.1 M Na_2HPO_4 , at a scan rate of 100 mV/s, in cathodic scan.

Chronoamperometric method

Chronoamperometry was used as a revealing method and also to investigate the electrode process [18-22]. Figure 10 displays the chronoamperometric measurements of MA by adjusting the working electrode at 0.00 mV (first potential step) and at -1.00 mV (second potential step) vs. Ag/AgCl which shows increased current when MA concentrations were changed from 3.33 to 8.33 mM in 0.1M Na_2HPO_4 as a supporting electrolyte.

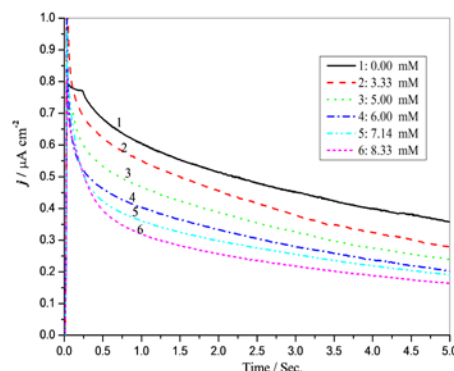


Fig. 10. Chronoamperograms in the absence and presence of different concentrations of maleic acid in 0.1 M Na_2HPO_4 supporting electrolyte; first and second potential steps were 0.00 and -1.00 V vs. Ag/AgCl, respectively.

The current of the electrochemical reaction (Figure 11, under mass transport control) of an electroactive material with a diffusion coefficient is expressed by Cottrell equation (6) [21-23]:

$$I(t)=nFAC(D/\pi t)^{1/2} \quad (6)$$

where, D is the diffusion coefficient ($cm^2 s^{-1}$), C - bulk concentration (mM), n - number of electrons, F - Faraday's constant and A - electrode surface area.

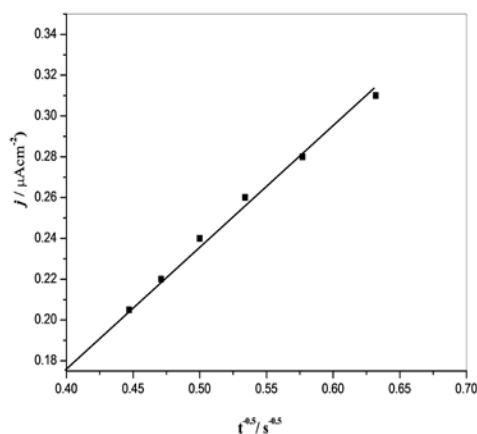


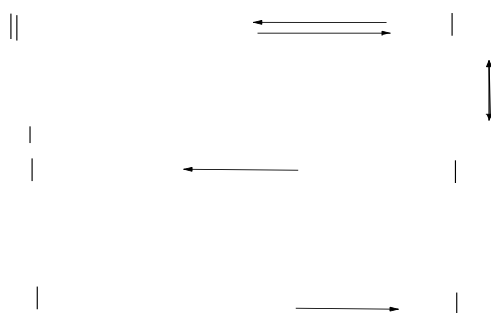
Fig. 11. Cottrell plot for potential step chronoamperometry of 6 mM maleic acid in 0.1 M Na_2HPO_4 .

Figure 11 reveals that the plot of I vs. $t^{-0.5}$ is a linear relationship from which we can obtain the value of D . According to the Cottrell equation, the diffusion coefficient of MA (D) was found to be $0.815 \times 10^{-7} \text{ cm}^2 \text{ s}^{-1}$. The obtained value is comparable with the relevant previous studies [17].

Mechanism of the reduction reaction

From the results it is known that during the electroreduction process of MA the gain of electron leads to the formation of an anion-radical intermediate. Then this intermediate accepted one proton from the aqueous media and formed succinic radical. At the end, the succinic radical accepted one electron and one proton to form succinic acid.

The reduction mechanism of MA to succinic acid may be expressed as follows [24-26]:



CONCLUSION

The results indicated that the reduction of MA on a Pt electrode is a quasi-reversible process controlled by diffusion. The cathodic and anodic peak currents of MA increased with an increase in concentration of MA from $5.00 \times 10^{-3} \text{ M}$ to $8.89 \times 10^{-3} \text{ M}$ at a scan rate ranging from 20-200 mV/s vs. Ag/AgCl. From chronoamperometric measurements, the diffusion

coefficient of maleic acid was found to be $0.815 \times 10^{-7} \text{ cm}^2 \cdot \text{s}^{-1}$. Maleic acid can be electrochemically reduced to succinic acid using cathodic linear voltammetry using a simple, quick, accurate, and sensitive technique.

REFERENCES

1. S. Swann, C. Y. Chen, H. D. Kerfman, *J. Electrochem. Soc.*, **99**, 460 (1952).
2. R. Kanakam, M. S. V. Pathy, H. V. K. Udupa, *Electrochim. Acta*, **12**, 329 (1967).
3. O. Chailapakul, E. Popa, H. Tai, B. V. Sarada, D. A. Tryk, A. Fujishima, *J. Electrochem. Commun.*, **2**, 422 (2000).
4. M. Avramov-Ivic, V. Jovanovic, G. Vlajnic, J. Popic, *J. Electroanal. Chem.*, **423**, 119 (1997).
5. S. Heng, G. Yong-Ping, H. Hui, Wen-Kui, *J. Acta Phys-Chim. Sin.*, **24**, 1264 (2008).
6. C. J. Kennedy, A. J. Rethinam, *J. Appl. Electrochem.*, **33**, 832 (2003).
7. D. Vasudevan, *Russ. J. Electrochem.*, **45**, 1310 (2009).
8. Daobao Chu, Mai Xu, Jia Lu, Peng Zheng, Guoxu Qin, Ximei Yuan, *J. Electrochem. Commun.*, **10**, 350 (2008).
9. S. S. Vaghela, A. D. Jethva, M. S. Gohil, G. Ramachandran, P. K. Ghosh, D. Vasudevan, *J. Bulletin Electrochem.*, **18**, 237 (2002).
10. H. Song, S. Y. Lee, *Enzyme Microb. Tech.*, **39**, 352 (2006).
11. I. Krik, D. F. Othmer, *Encyclopedia of Chemical Technology*, Wiley & Sons, New York, 1997.
12. M. M. Baizer, H. Lund, *Organic Chemistry: an Introduction and a Guide*, Marcel Dekker, New York, 1983.
13. E. Scholten, T. Renz, J. Thomas, *Biotechnol. Lett.*, **31**, 1949 (2009).
14. K. X. Xu, *Handbook of Fine Organic Chemical Materials and Intermediates*, Chemical Industry Press, Beijing: 2002.
15. J. G. Zeikus, M. K. Jain, P. Elankovan, *J. Appl. Microbiobiol. Biotechn.*, **51**, 545 (1999).
16. C. Shengpei, L. Qiaoqi, C. Yanxin, S. Shigang, *J. Chem. Ind. Eng.*, **59**, 25 (2008).
17. F. Manea, C. Radovan, I. Corb, A. Pop, G. Burtica, P. Malchev, S. Picken, J. Schoonman, *J. Sensor.*, **7**, 615 (2007).
18. M. Vidotti, S. I. Cordoba de Torresi, L. T. Kubota, *J. Sensor Actuator B: Chem.*, **135**, 245 (2008).
19. Z. Taleat, M. M. Ardakant, H. Naeimi, H. Bettollahi, M. Nejati, H. R. Zare, *J. Anal. Sci.*, **24**, 1039 (2008).
20. M. M. Ardakani, P. E. Karami, P. Rahimi, H. R. Zare, H. Naeimi, *Electrochim. Acta*, **52**, 6118 (2007).
21. A. J. Bard, L. R. Faulkner, *Electrochemical Methods, Fundamentals and Applications*, 2nd ed., John Wiley and Sons, New York, 2001.
22. M. M. Ardakani, Z. Akrami, H. Kazemian, H. R. Zare, *J. Electroanal. Chem.*, **586**, 31 (2006).
23. S. Swann, C. Y. Chen, H. D. Kerfman, *J. Electrochem. Soc.*, **99**, 460 (1952).

24. A. V. Muzumdar, S. B. Sawant, V. G. Pangarkar, *J. Org. Process Res. Dev.*, **4**, 685 (2004).
25. V. V. Chernyi, Y. B. Vasiliev, *Soviet Electrochem.*, **12**, 812 (1976).
26. S. S. Khidirov, O. A. Khazova, V. N. Andreev, *Soviet Electrochem.*, **13**, 1089 (1977)

ГРАНИЦА НА ОТКРИВАНЕ И ЕЛЕКТРОХИМИЧНО ОТНАСЯНЕ НА МАЛЕИНОВА КИСЕЛИНА ВЪРХУ ПЛАТИНОВ ЕЛЕКТРОД

Х.М. Радех¹, М. М. Абу-Криша^{1,2*}, А. М. Або-Бакр¹, М. Абд-Елсабур¹

¹ Департамент по химия, Саут Вали Университет, Кена, 83523, Египет

² Научен колеж, Департамент по химия, Ал Имам Мохамад Ибн Сауд Ислямски университет, Риад, 11623, Саудитска Арабия

Постъпила на 30 септември 2018 г.; коригирана на 9 януари 2018 г.

(Резюме)

Електрохимичното отнасяне на малеинова киселина (МК) върху платинов електрод е изучено чрез циклична волтамметрия, линейна волтамметрия и хроноамперометрия. Установено е, че редукцията на МК върху Pt електрод е квазиобратим процес в резултат на дифузията и на редукционния потенциал на МК при -0.62 V (спрямо Ag/AgCl). Изчислената граница на откриване на МК върху Pt електрод е $1.6 \times 10^{-5}\text{ M}$. Анодните и катодните токови пикове на МК нарастват с увеличаване на концентрацията на малеинова киселина от 5.00×10^{-3} to $8.89 \times 10^{-3}\text{ M}$ при скорост на сканиране в интервала от 20 до 200 mV/s. Дифузионният коефициент на МК е $0.815 \times 10^{-7}\text{ cm}^2\cdot\text{s}^{-1}$. Дискутиран е механизъмът на получаване на сукцинова киселина чрез електрохимична редукция на МК.

Chemical analysis of components in burned and unburned propellant powders

İ. Kara^{1,2}

¹Department of Engineering Physics, Faculty of Engineering, Ankara University, Ankara, Turkey:

²Department of Ballistics, Ankara Criminal Police Laboratory, Ankara, Turkey.

Received August 11, 2017, Accepted January 9, 2018

After firing a shot, gunshot residue (GSR) compounds containing burned and partially unburned particles are dispersed in the environment. The partially unburned GSR compounds contain elements that are ready to explode in appropriate circumstances. This can lead to serious safety problems, especially in indoor shooting ranges. In this study, the GSR compounds collected from Machine Chemistry Institute brand 9×19 mm parabellum shells were analyzed using gas chromatography/mass spectrometry (GC-MS) method. As a result of the analysis, nitroglycerin, dimethyl phthalate, 2,4-dinitrotoluene, diphenylamine, n-diphenylamine, trimethyl, 2,4-methypropyl and dibutyl phthalate compounds were detected in the GSR compounds. The changes in the amounts of these compounds depending on the number of shots were discussed.

Keywords: Chemical analysis, Gas chromatography-mass spectrometry (GC-MS), Propellant powder, GSR (Gunshot residue).

INTRODUCTION

When a firearm is used, gunshot residues (GSR) are formed following the combustion that takes place inside the chamber, and these residues spread into the gun, especially in the vicinity of the firing bed. Some of them exit the barrel and disperse in burned and partially unburned form [1,2]. GSR analysis is one of the most important tests in forensic sciences [3,4]. This analysis is of great importance in identifying the shooter, as well as for clarification of the origin (i.e., suicide, murder, accident) of the incidence [5].

The shooting range is widely used in comparison with suspect firearms in forensic investigations, in sports, military or police training [6,7]. As a result of the intense shooting, GSR compounds spread in the environment. The scattered GSR compounds contain elements that are ready to explode in appropriate circumstances [8-10]. Unless necessary measures are taken, there may be accidents that can cause death, especially in indoor shooting ranges.

The GC-MS method is a technique used in GSR analysis since it yields robust results with high sensitivity and authenticity for the appropriate analyte classes (Fig. 1). Inorganic and organic gunshot residues (Table 1) were analyzed in the studies carried out with the methods of liquid or gas chromatography [11,12].

The objective of this study was to use GC-MS method to investigate the change in amounts of GSR compounds identified after firing MKE brand

9×19 mm parabellum, depending on the number of shots.

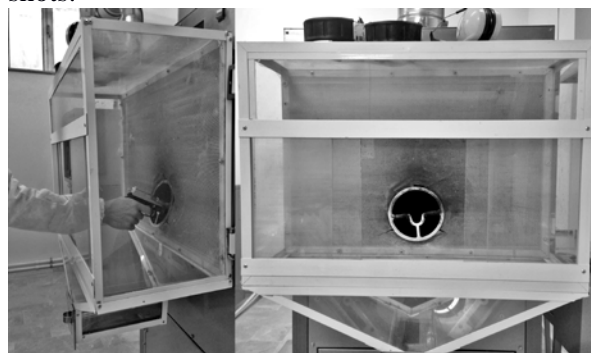


Fig. 1. The shooting tank and its front chamber.

EXPERIMENTAL

Samples

This experimental study was carried out at the directorate department of the Ankara Criminal Police Laboratory (in Turkish: KPL). All of the tests were carried out in the KPL shooting room. In test shooting, we used a Sarsilmaz brand Mega 2000 Kilinc model semi-automatic 9×19 mm parabellum pistol {Machine Chemistry Institute (MKE)} with a 2010 gun cartridge. Propellant powders from one ammunition type [9×19 mm parabellum type MKE brand cartridge were of 38% lead styphnate (TNR Pb), 6% tetracene (TRZN), 34% barium nitrate Ba(NO₃), 15% antimony sulfide Sb₂S₃, 4% pentrite (PETN), and 3% aluminum powder [4], full metal jacket (Turkey)} were supplied by the Turkish National Police.

* To whom all correspondence should be sent.
E-mail: ilkerkara06@hotmail.com

Table 1. Characteristic organic and inorganic gunshot residue components.

Compound	Abbreviation	Usage
Resorcinol	Rs	Stabilizer
2,4-Dinitrotoluene	24-DNT Flash	inhibitor
2,6-Dinitrotoluene	26-DNT Flash	inhibitor
2,3-Dinitrotoluene	23-DNT Flash	inhibitor
Dimethyl phthalate	MF	Plasticizer
Diethyl phthalate	EF	Plasticizer
Dibutyl phthalate	BF	Plasticizer
Diphenylamine	DPA	Stabilizer
Methyl centralite	MC	Stabilizer
Ethyl centralite	EC	Stabilizer
Antimony	Sb	Fuel
Calcium	Ca	Fuel
Magnesium	Mg	Fuel
Aluminum	Al	Fuel
Nickel	Ni	Bullet material
Zinc	Zn	Bullet material
Copper	Cu	Bullet material
Iron	Fe	Bullet material
Barium	Ba	Oxidizing agent
Lead	Pb	Explosive (lead styphnate)

The chemical compounds of gunshot residues in this list do not represent a comprehensive study [5].

Sample preparation

In the experiment, the barrel of the firearm was cleaned before firing each shot.

The cleaning process began with mechanical cleaning. Then, the barrel was washed in deionized water in an ultrasonic bath. Finally, the barrel was dried with dry nitrogen gas. Before applying the method to real samples, it was necessary to find the best sampling conditions. GSR compounds scattered around after firing were collected by a paper screening (by coating the inside) placed in the front chamber of the shooting tank (Fig. 1). The samples were collected under the same conditions since the physical conditions and method of collection may have an effect on the sampling procedure.

RESULTS

Sample analysis and chromatographic conditions

The samples were dissolved in 25 ml of acetone and were mixed with a vortex mixer for 30 min. Each was filtered with a syringe and 0.45 µm nylon

filter. The results were analyzed using an AOC-20i auto-sampler and chromatograph interfaced to a mass spectrometer (Model: QP2010 PLUS Shimadzu, Japan).

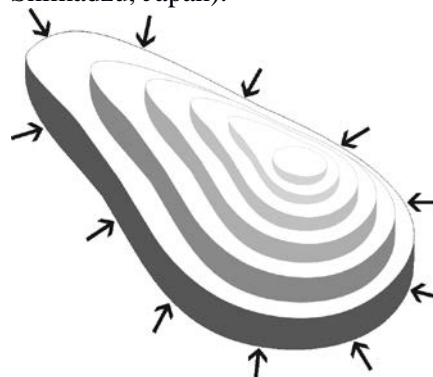


Fig. 2. Gunpowder particle, emerged layers, and combustion process.

The instrument was equipped with a VF 5 ms fused silica capillary column of 30 m length, 0.25 mm diameter and 0.25 µm film thickness. The temperatures employed were: column oven temperature 70°C, injection temperature 170°C, pressure of 108.0 kPa, with total flow and column flow of 6.20 ml/min and 1.15 ml/min, respectively.

The linear velocity was 46.3 cm/sec and the purge flow was 3.0 ml/min. The GC ion source and interface temperature were 150°C and 290°C, respectively with solvent cut time of 3.50 min. The MS program starting time was 3.00 min, which ended at 30.0 min with event time of 0.50 sec, scan speed of 1666 μ l/sec, scan range 40-8 00 u (split ratio 10:1). The total running time of GC-MS was 30 min. The relative percentage of the extract was expressed as a percentage with peak area normalization.

DISCUSSION

Each explosive can be burned by using processed gunpowder and a sufficient amount of oxygen molecules. The energy required for combustion is initially provided externally (spark or flame), and combustion is maintained as it reaches to layers of gunpowder. Gunpowder particles burn starting from the outer surface inward in parallel layers (Fig. 2) [4].

The powder gases formed during the combustion process increase continuously with rising temperature, pressure, and combustion speed [4,13]. The pressure wave, which occurs as a result of the energy released during this event, causes disintegration of explosives at a constant rate [6]. This pressure wave can be obtained by impact or friction; hence, cartridges include a primer capsule to achieve this. If the primer capsule or firing pin's hit is weak, then the pressure wave will not be sufficient to achieve complete combustion (causing unburned particles).

To achieve complete combustion, the average kinetic energy resulted from the pressure wave caused by the collision of molecules should be greater than the critical energy required for the breakdown of the molecules. Accordingly, mechanical effects, in addition to thermal effects of the gases, also play a major role in combustion. Here, these two factors prepare the necessary environment for detonation and provide the required activation energy.

As the manufacture of gunpowder progressed, it was observed that the main part of the gunpowder, which consists of cellulose, glycerin, and nitrates, lost its characteristics as a result of successive solving, evaporation, drying, hot pressing, and final forming processes, and it was concluded that it would be possible to eliminate these problems with various agents. In addition, the lowest priced gunpowder is preferred, which complies with the production specifications. These products burn quickly and pollute internal parts of the gun as well as the environment [1].

The combustion rates of gunpowder vary by ammunition brand. However, no gunpowder burns completely [14]. Partially unburned GSR compounds can be detected correctly by using GS-MS method with high precision (Fig. 3).

In Figure 3, the mean peak areas of the GSR compounds obtained from MKE brand 9 \times 19 mm parabellum indicate nitroglycerin, dimethyl phthalate, 2,4-dinitrotoluene, diphenylamine, n-diphenylamine, trimethyl, 2,4 methypropyl, and dibutyl phthalate compounds. Although these compounds are unique to the selected type of ammunition, they are consistent with Table 1. The change in the amount of the detected compounds depending on the number of shots was investigated. Therefore, the GSR samples were collected after firing 10, 50, and 100 shots. The results found were combined in a single graphic to compare, as shown in Figure 3. As can be seen, peaks of all compounds increase with increasing number of shots.

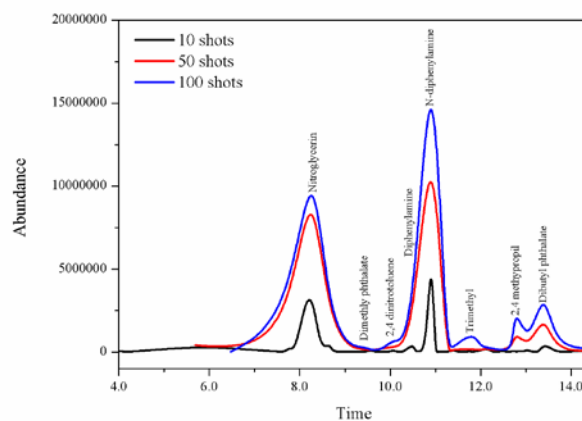


Fig. 3. Changes in the amounts of GSR compounds obtained from MKE brand 9 \times 19 mm parabellum for 10, 50, and 100 shots, according to GC-MS analysis.

CONCLUSIONS

The gas chromatographic (GC-MS) technique selected for interpreting the GSR compounds formed after firing shots is very suitable to analyze different properties, compared to other methods. The selected MKE brand cartridges have contaminated the shooter's firearm and surroundings extremely. In the examination of these GSR compounds, it was observed that they contain elements that are ready to explode in appropriate conditions. The amount of these compounds increased depending on the number of the shots fired.

This result leads to serious problems in the areas of intense shooting. Therefore, the area in front of the shooting range should be cleaned regularly, and unburned GSR compounds must be collected and

disposed to prevent possible accidents. As a rare contribution to the literature, this study shows the danger of compounds of gunshot residues formed after firing a shot according to type of cartridge selected; however, repeated studies are necessary utilizing more samples (employing a variety of cartridge brands).

REFERENCES

1. I. Kara, O. Yalcinkaya, *Bulg. Chem. Commun.*, **49**, 101 (2017).
2. Z. Brožek-Mucha, *XraySpectrom.* **36**, 398 (2007).
3. O. Dalby, D. Butler, J.W. Burkett, *J. Forensic Sci.*, **55**, 924 (2010).
4. I. Kara, Y. Sarikavak, S.B. Lisesivdin, M. Kasap, *Environmental Forensics*, **17**, 68 (2016).
5. C. Cruces-Blanco, L. Gámiz-Gracia, A.M. Garcia-Campana, *Trends in Analytical Chemistry*, **26**, 215 (2007).
6. K.H. Chang, P.T. Jayaprakash, C.H. Yew, A.F.L. Abdullah, *Australian Forensic Science*, **45**, 23 (2013).
7. N.F. Fidan, B. İzgi, *Bulg. Chem. Commun.*, **41**, 404 (2009).
8. O. Dalby, D. Butler, J.W. Birkett, *Journal of Chromatography A*, **1217**, 7183 (2010).
9. O. Cascio, M. Trettene, F. Bortolotti, G. Milana, F. Tagliaro, *Electrophoresis*, **25**, 1543 (2004).
10. C. de Perre, I. Corbin, M. Blas, B.R. McCord, *J. Chromatogr., A* **1267**, 259 (2012).
11. H. Meng, B. Caddy, Gunshot Residue analysis - a review, *J. Forensic Sci.*, **42**, 553 (1997).
12. E.B. Morales, A.L.R. Vázquez, *J. Chromatography A.*, **106**, 225(2004).
13. F.S. Romolo, P. Margot, *Forensic Sci. Int.*, **119**, 195 (2001).
14. J.L. Thomas, D. Lincoln, B.R. McCord, *J. Forensic Sci.*, **58**, 609 (2013).

Химичен анализ на компонентите в изгорели и недоизгорели горивни прахове

И. Кара^{1,2}

¹ Департамент по инженерна физика, Инженерен факултет, Анкарски университет, Анкара, Турция

² Департамент по балистика, Криминална полицейска лаборатория, Анкара, Турция

Постъпила на 11 август, 2017 г.; приета на 9 януари, 2018 г.

(Резюме)

След произвеждане на изстрел, остатъци от стрелбата (ОС), съдържащи изгорели и недоизгорели частици се разпръскват в околната среда. Частично недоизгорелите ОС съединения съдържат елементи, които са готови да експлодират при подходящи условия. Това може да доведе до сериозни проблеми с безопасността, особено при стрелба в затворени помещения. В настоящата статия, ОС съединения, събрани от гилзи от парабел тип 9×19 mm са анализирани чрез газова хроматография/маспектрометрия (GC-MS). От получените резултати следва, че ОС съединения съдържат нитроглицерин, диметилфталат, 2,4-динитротолуен, дифениламин, п-дифениламин, триметил-, 2,4-метилпропил- и дибутилфосфат. Дискутирани са промените в количествата на тези съединения в зависимост от броя изстрели.

New chelation products of thorium(IV) and cerium(III) with diclofenac and paracetamol analgesic drugs: Synthesis, spectroscopic, thermal stability, antimicrobial activities investigations

F.A.I. Al-Khodir

College of Science, Princess Nourah bint Abdulrahman University, Department of Chemistry, KSA

Received, November, 26, 2017; Revised, December, 21, 2017

Four new complexes of thorium(IV) and cerium(III) with two analgesic drugs, diclofenac sodium (*diclo*) and paracetamol (*para*): $[\text{Ce}(\text{diclo})_3] \cdot 2\text{H}_2\text{O}$ (1), $[\text{Th}(\text{diclo})_2(\text{OH})_2] \cdot 4\text{H}_2\text{O}$ (2), $[\text{Ce}(\text{para})_3(\text{H}_2\text{O})_3]$ (3), and $[\text{Th}(\text{para})_4(\text{H}_2\text{O})_2]$ (4), were synthesized and characterized using elemental analysis, thermal analysis and FT-IR, $^1\text{H-NMR}$, and UV-VIS spectroscopy. The micro-analytical elemental measurements confirmed the ratio metal ions:drug for the synthesized complexes as 1:3 for complexes 1 and 3, 1:4 for complex 2, and 1:2 for complex 4. The FT-IR spectra of the *para* ligand $\nu_s(\text{O-H})$ stretching vibration of $-\text{OH}$ disappeared in the spectra of the complexes proving the involvement of the oxygen atom of the $-\text{OH}$ group in the complexation after deprotonation. In case of *diclo* complexes, the $\nu(\text{C=O})$ stretching vibrations of the carboxylic group were shifted in the spectra of the complexes, confirming the involvement of the $-\text{COOH}$ group in the complexation with covalent bonding as bidentate chelation. The geometry of the Ce^{3+} and Th^{4+} ions was six-coordinated with those of both drug complexes. The nano-structured form was investigated using transmittance electron microscope (TEM). The antimicrobial activities of the newly synthesized complexes were determined against some kinds of bacteria and fungi. All these complexes showed antimicrobial results.

Keywords: Thorium(IV); Cerium(III); TEM; Nanoscale; Diclofenac; Paracetamol; IR.

INTRODUCTION

Diclofenac sodium (*diclo*, Fig. 1) is a sodium salt of aminophenyl acetic acid and is a well-known representative of non-steroidal anti-inflammatory drugs (NSAIDs) [1,2]. Like other NSAIDs diclofenac sodium is clinically prescribed as an antipyretic, analgesic and anti-inflammatory agent [3-5]. Knowledge of the structure of *diclo* molecule is essential to understand its pharmaceutical action. The *diclo* is a potent inhibitor of cyclo-oxygenase *in vitro* and *in vivo*, therapy decreasing the synthesis of prostaglandins, prostacyclin, and thromboxane products. Lanthanide ion probe spectrofluorometry (LIPS) introduced by Horrocks and Sundick [6] employs this technique for determination of diclofenac sodium. The structure of diclofenac consists of phenylacetic acid group, secondary amino group, phenyl ring, both *ortho* position of which are occupied by chlorine atom. The secondary amino group precipitates in bifurcate intramolecular hydrogen bond interacting with the adjacent acceptor chlorine atom [7-9]. The interaction of diclofenac with cyclodextrin has been reported [9,10]. The nature of the inclusion complex in the solid state was studied by X-ray crystallography, IR, and NMR spectroscopy.

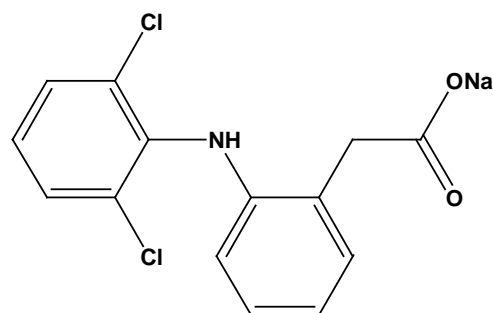


Fig. 1. Chemical structure of diclofenac sodium (*diclo*).

Paracetamol (*para*, Fig. 2) is a well-known drug that has application in pharmaceutical industries as a popular analgesic and antipyretic medication that is readily absorbed after administration and little toxic when used in recommended dose [11-17].

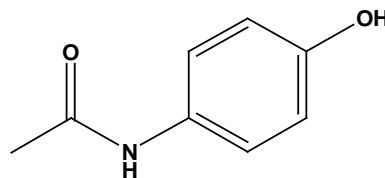


Fig. 2. Chemical structure of paracetamol (*para*).

Paracetamol in pharmaceutical preparations can be determined by different methods such as fluorimetry [18], chemiluminescence [19], electrochemical method [20], nuclear magnetic resonance, mass spectroscopy [21], and liquid chromatography [22]. Paracetamol has high therapeutic value; it is also used as an intermediate

* To whom all correspondence should be sent.
E-mail: fatimaalkhodir@yahoo.com

for pharmaceuticals (as a precursor of penicillin) and azo dye, stabilizer for hydrogen peroxide, photographic chemical [23]. Paracetamol is also known to be hepatotoxic in man and various experimental animals upon overdose [24]. Paracetamol is also oxidized by cytochrome P450 into the reactive intermediate N-acetyl-p-benzoquinone imine [25]. Several different approaches have previously been utilized in an attempt to achieve rapidly absorbed solid dose paracetamol formulations. These include enhancing tablet disintegration rate [26], addition of alkali metal salt or antiacid [27] to paracetamol tablets.

In the present work, we focused on raising the efficiency of the drug by the addition of a special metal ion like Ce^{3+} and Th^{4+} and formation of new complexes, to be proven using thermal and spectroscopic characterizations. These complexes were structurally characterized in the solid state by IR, 1H -NMR, conductivity measurement, thermal studies and biological evaluation. The nanoscale range of drug complexes was investigated using transmission electron microscopy (TEM).

EXPERIMENTAL

Chemicals and reagents

The analgesic drugs diclofenac sodium (*diclo*) and paracetamol (*para*) were purchased from Merck, all the other used reagents and solvents were analytical grade products. Hydrated salts of both $Th(NO_3)_4$ and $CeCl_3$ were obtained from Aldrich Company.

Synthesis of Ce^{3+} and Th^{4+} complexes

Ce(III) and Th(IV) complexes of diclo drug. The mentioned complexes were prepared as follows, employing a molar ratio (metal:drug) of 1:3 and 1:4 for Ce(III) and Th (IV) complexes, respectively. The resulting solutions were stirred and refluxed on a hot plate at 60-70°C for 3 h. The volume of the obtained solution was reduced to one-half by evaporation one day later, the precipitates were settled down, filtered off and washed several times by small amounts of hot CH_3OH and dried under *vacuum* over anhydrous $CaCl_2$. The data from the elemental analysis (Table 1) were in good agreement with those corresponding to the formula.

Ce(III) and Th(IV) complexes of para drug. $Th(IV)$ nitrate or $Ce(III)$ chloride (1 mmol) were dissolved in 20 mL of distilled water and then were added to 20 mL of methanolic solution containing 4 mmol of *para* under magnetic stirring. The pH of solution was adjusted to neutral using ammonium hydroxide solution. The resulting mixture was heated to 60 °C and left to evaporate slowly at room

temperature. The precipitate was filtered off, washed with hot methanol and dried at 60 °C. $Ce(III)$ chloride was added to the solution of *para* at a stoichiometric ratio of 1:3 and was synthesized by the same procedure.

Instruments

The elemental analyses of %C, %H and %N contents were performed by a microanalysis unit using a Perkin Elmer CHN 2400 analyzer. The molar conductivity of a freshly prepared 10^{-3} mol/ cm^3 dimethylsulfoxide (DMSO) solution of the dissolved complexes was measured using a Jenway 4010 conductivity meter. The electronic spectra were measured on UV-3101 PC Shimadzu UV-Vis spectrophotometer. The infrared spectra with KBr discs were recorded on a Bruker FT-IR spectrophotometer (4000–400 cm^{-1}). 1H -NMR spectra were scanned using a Varian Gemini 200 MHz spectrometer. The solvent used was DMSO. The thermal study TG/DTG-50H was carried out on a Shimadzu thermogravimetric analyzer under nitrogen atmosphere till 800 °C. The transmission electron microscopy images were recorded using a JEOL 100s microscope. Magnetic measurements were carried out on a Sherwood scientific magnetic balance in the micro analytical laboratory using Gouy method.

Antimicrobial effects

The biological activity of Ce^{3+} and Th^{4+} complexes of *diclo* and *para* drugs were tested against bacteria and fungi. In testing the antibacterial activity of these complexes, we used more than one test organism. The organisms used in the present investigation included two bacteria *B. subtilis* (Gram +), *E. coli* (Gram –) and two fungi *Aspergillus niger* and *Aspergillus flavus*. The results of the bactericidal and fungicidal screening of the synthesized complexes were collected.

RESULTS AND DISCUSSION

Microanalytical and conductance data

Selected physical properties and characteristic data of the synthesized metal complexes of *diclo* and *para* are listed in Table 1. The four new isolated solid complexes are formulated as $[Ce(diclo)_3] \cdot 2H_2O$, $[Th(diclo)_2(OH)_2] \cdot 4H_2O$, $[Ce(para)_3(H_2O)_3]$ and $[Th(para)_4(H_2O)_2]$. The complexes are air-stable, with high melting points. The metal complexes are insoluble in common organic solvents but are soluble in DMSO. The molar conductivity of 10^{-3} mol/ dm^3 solutions of the complexes in DMSO (Table 1) indicates that all synthesized complexes are non-electrolytes [28].

Table 1. Elemental analysis and physical data of *diclo* and *para* complexes with Ce(III) and Th(IV) metal ions.

Complexes	%C		%H		%N		%M		Δ (Ω^{-1} . cm ² .mol ⁻¹)
	Found	Calcd.	Found	Calcd.	Found	Calcd.	Found	Calcd.	
[Ce(<i>diclo</i>) ₃].2H ₂ O 1	47.44	47.52	3.20	3.23	3.90	3.96	13.16	13.20	15
[Th(<i>diclo</i>) ₂ (OH) ₂].4H ₂ O 2	36.12	36.22	3.21	3.26	2.98	3.02	24.90	24.99	19
[Ce(<i>para</i>) ₃ (H ₂ O) ₃] 3	44.56	44.72	4.58	4.69	6.44	6.50	21.65	21.74	21
[Th(<i>para</i>) ₄ (H ₂ O) ₂] 4	44.21	44.24	4.12	4.18	6.42	6.45	26.55	26.71	17

The synthesized complexes according to elemental analysis, IR, ¹H-NMR, UV-Vis and thermogravimetric data confirm that the complexes have monodentate and bidentate chelation for the *para* and *diclo* chelator, respectively. These data matched with the calculated elemental analysis revealing that no Cl⁻ ions were detected by addition of AgNO₃ reagent to the solution of the mentioned complexes.

Infrared spectra

The IR data of *diclo* and its Ce(III) and Th(IV) complexes are shown in Table 2 and Fig. 3. The IR spectra of these complexes were compared with those of the free *diclo* ligand in order to determine the coordination sites involved in chelation. It was observed in the IR spectra that there are no large shifts for ν (NH) and δ (NH) bands in the spectra of all complexes compared to those of the ligand, which indicates that there is no interaction between the -NH group and the metal ions. The difference between the bands of $\nu_{as}(\text{COO})$ and $\nu_s(\text{COO})$ characterized the carboxylate ligation. The $\nu_{as}(\text{COO})$ and $\nu_s(\text{COO})$ bands of the *diclo* complexes are at 1581-1546 and 1445-1423 cm⁻¹, respectively. The difference ($\Delta = \nu_{as}\text{COO} - \nu_s\text{COO}$) of 136-123 cm⁻¹ is

less than the ionic value of sodium diclofenac (the Δ value is 170 cm⁻¹), as expected for the bidentate bridging mode of carboxylate. Diclofenac complexes exhibit bands at 3782 and 3594 cm⁻¹ attributed to the presence of coordinated and lattice water [29]. The weak band at 570-528 cm⁻¹ of the complexes was assigned to the $\nu(\text{M-O})$ stretching vibration motion. The IR data of *para* and its Ce(III) and Th(IV) complexes are shown in Table 3 and Fig. 4. From the comparison of the IR spectra of *para* and its complexes, it follows that:

- The absorption bands at 3300 cm⁻¹ and 3200 cm⁻¹ of free *para* were assigned to -OH and -NH stretching vibration motions. These bands were shifted in the spectra of the metal complexes due to coordination.
- The strong absorption band at 680 cm⁻¹ in the spectra of the metal complexes which does not appear in the free *para* was tentatively assigned to [M-OH] stretch band of metal complex.
- The blue shift of stretching band and in-plane bend band of hydroxyl group, with respect to phenyl moiety at 1260-1100 cm⁻¹ is an evidence for the contribution of the hydroxyl oxygen atom to chelation with the metal ion.

Table 2. IR spectra of *diclo* and its Ce(III) and Th(IV) complexes

Compound	$\nu(\text{NH})$ and $\nu(\text{OH})$	$\delta(\text{NH})$	$\nu(\text{COO})$ (as)	$\nu(\text{COO})$ (s)	$\nu(\text{M-O})$ (COO)	Δ	$\nu(\text{M-O})$ (H ₂ O)
<i>Diclo</i>	3359	1500	1572	1402	--	170	--
1	3776 3594 3250	1504	1546	1423	533	123	570
2	3782 3598 3321	1503	1581	1445	452	136	528

Table 3. IR frequencies (4000-400 cm⁻¹) of *para* and its Ce(III) and Th(IV) complexes.

Compound	$\nu(\text{OH}) + \nu(\text{NH})$	$\nu(\text{C=O})$	$\delta(\text{CNH})$ amide group	$\nu(\text{C-O})$ phenyl group	$\nu(\text{M-O})$
<i>Para</i>	3300 3200	1650	1560	1260	--
3	3389	1620	1538	1200	509
4	3322 3160	1654	1560	1240	508

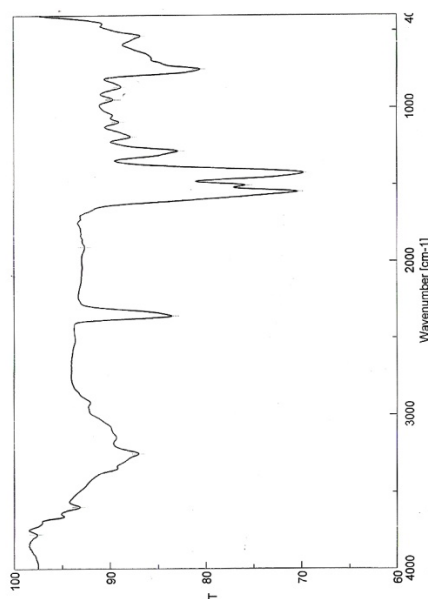


Fig. 3a. FT-IR spectrum of *diclo*/Ce³⁺ complex

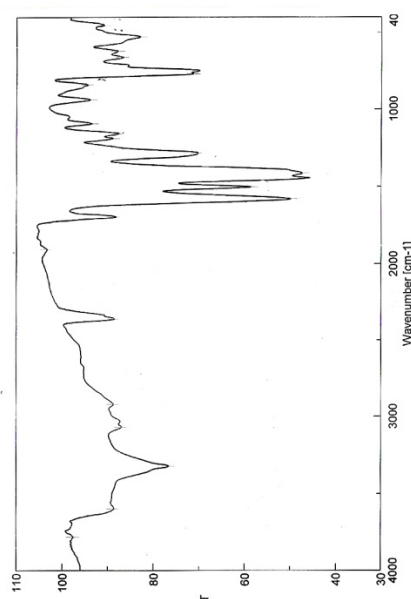


Fig. 3b. FT-IR spectrum of *diclo*/Th⁴⁺ complex

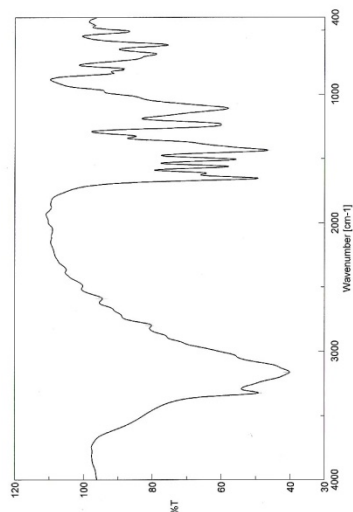


Fig. 4a. FT-IR spectrum of *para*/Ce³⁺ complex

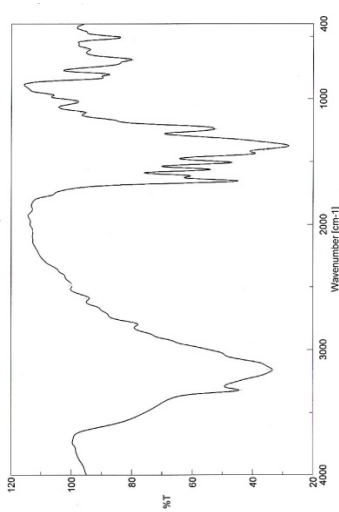


Fig. 4b. FT-IR spectrum of *para*/Th⁴⁺ complex

¹H-NMR spectra

The ¹H-NMR spectral data of *diclo* and its Th(IV) complex are presented in Table 4 and Fig. 5. The ¹H-NMR spectrum of the Th(IV) complex shows that the signals of the protons of the aromatic CH₂ and CH are unshifted at δ = 3.50 ppm as a broad singlet which refers to CH₂ of acetate group and proton of uncoordinated water. The multiplet peaks at 6.2-7.5 ppm were attributed to the protons of phenyl group

of two *diclo* molecules, in the prepared complex. The protons of both NH and OH of coordinated chelate appeared as a broad singlet at δ = 8.6 ppm in the spectrum of the Th⁴⁺ complex, thus, the upfield shift of the complex would mean coordination with a cleaved metal ion. The association is due to intermolecular hydrogen bond with respect to the pure salt [30-32].

Table 4. ¹H-NMR spectral data of *diclo* and its Th(IV) complex

Compound	δ(ppm) of protons			
	2H; H ₂ O	H; CH ₂	H; ArH	H; NH
<i>Diclo</i>	--	3.410	6.23-7.47	10.51
2	2.503	3.504	6.2-7.52	8.6

Table 5. $^1\text{H-NMR}$ spectral data of *diclo* and its Th(IV) complex.

Compound	δ ppm of hydrogen				
	H; CH_3	H; H_2O	H; ArH	H; NH	H; OH
<i>Para</i>	1.9	--	6.57-7.28	9.37	10
4	1.96	2.5	6.6-7.22	9.6	--

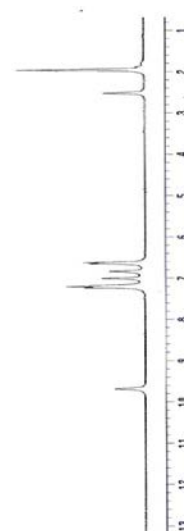
**Fig. 5.** $^1\text{H-NMR}$ spectrum of *diclo*/Th $^{4+}$ complex.

$^1\text{H-NMR}$ spectrum of *para* (Table 5) displays the signals $\delta = 9.37$ and 10.00 ppm which are due to the proton of the amide and hydroxyl groups, respectively. The disappearance of the signal $\delta = 10.00$ ppm of the hydroxyl hydrogen atom in the $^1\text{H-NMR}$ spectrum of the Th(IV) complex of *para* (Fig. 6) confirms the consumption of hydroxyl hydrogen atom in the complexation between *para* and metal ion. The persistence of the signal of the proton of the amide hydrogen atom in the $^1\text{H-NMR}$ spectrum of the complex confirms that amide proton does not participate in the complexation.

Magnetic measurements and UV-Vis spectra

The molar susceptibilities of thorium(IV) complexes (**2** and **4**) are diamagnetic, which agrees with the similar properties of other thorium(IV) complexes reported earlier [33,34]. The molecular weight data of the complexes also support this fact. Magnetic moment data show that lanthanum(III) nitrate complexes are essentially diamagnetic in nature while all other complexes are paramagnetic due to the presence of 4f-electrons which are effectively shielded by $5s^2p^2$ electrons [35]. This shows that 4f-electrons do not participate in the bond formation [36]. Magnetic moment data of the Ce(III) complexes of **1** and **3** are 2.77 and 2.84 B.M.

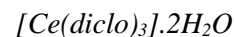
The formation of the metal complexes was also confirmed by UV-Vis spectra. The electronic spectra of the metal complexes in DMSO were scanned within the range of 200-600 nm. The free *diclo* drug has two essential bands; the first band at 275 nm may

**Fig. 6.** $^1\text{H-NMR}$ spectrum of *para*/Th $^{4+}$ complex

be attributed to $\pi-\pi^*$ transition of the aromatic ring and the second observed band at 350 nm - to $n-\pi^*$ electronic transition. In case of the spectra of metal complexes, the two bands are bathochemically shifted, suggesting that the ligand is coordinated to the metal ion through carboxylic group. It can be seen that free *para* has two distinct absorption bands. The first one at 300 nm may be attributed to $\pi-\pi^*$ intra-ligand transition of the aromatic ring. The second band observed at 390 nm was attributed to $n-\pi^*$ electronic transition. These bands are shifted after complexation.

Thermogravimetric analysis

Thermogravimetric analysis of the *diclo* complexes was performed and weight loss was measured from ambient temperature up to 1000°C . The decomposition behavior is shown in Fig. 7.



The thermal decomposition of this complex occur in four steps. The 1st step takes place in the range $60-170^\circ\text{C}$ and corresponds to the loss of $2\text{H}_2\text{O}$, with weight loss of 3.90% and its calculated value is 3.39%. The second step takes place in the range of $170-290^\circ\text{C}$ corresponding to the loss of two terminal Cl_2 molecules with weight loss of 6.83% and its calculated value is 6.69%. The third and fourth decomposition steps occur in the range of $290-900^\circ\text{C}$ and correspond to the loss of organic molecules. $\frac{1}{2}\text{Ce}_2\text{O}_3$ contaminated with residual carbon is the final product.

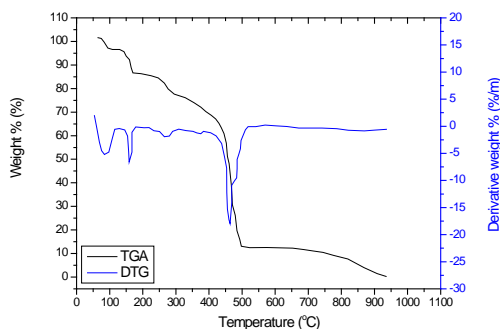


Fig. 7a. TG-DTG curves of *diclo*/ Ce^{3+} complex.

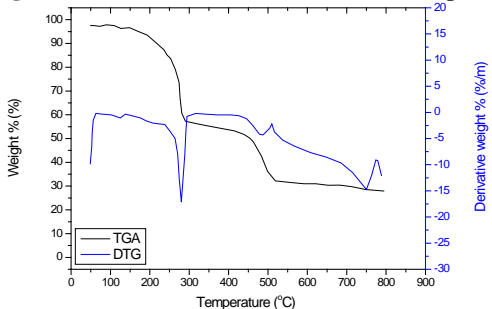
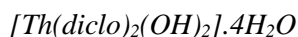
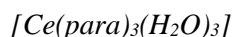


Fig. 7b. TG-DTG curves of *diclo*/ Th^{4+} complex.



The thermal decomposition of this complex occurs in four steps. The first decomposition step takes place in the range of 120-190°C and corresponds to the loss of 2H₂O molecules representing a weight loss of 2.50% and its calculated value is 1.94%. The 2nd step occurs in the range of 190-340°C, corresponding to the loss of two water molecules and decomposition of the organic moiety, representing a weight loss of 39.30% and its calculated value is 40%. The 3rd step takes place in the range of 340-490°C. It corresponds to the loss of the remaining organic molecules, representing a weight loss of 33.90% and its calculated value is 33.80%. The fourth step corresponds to the loss of organic molecules. The final product is ThO₂ oxide.

In case of *para* complexes, the heating rate was controlled at 10°C/min under nitrogen atmosphere and the weight loss was measured from ambient temperature up to \approx 1000 °C. The weight losses for each chelate was calculated within the corresponding temperature ranges (see Fig. 8).



The mentioned complex was decomposed in two essential steps: the first step occurs at 50-250°C and corresponds to the loss of 3H₂O and part of the organic molecules. The mass loss due to this step was 19.79% (obs.) and 20.21% (calcd.). The second step occurs at 250-600°C and corresponds to the loss of the remaining organic molecules with weight loss of 50.60% (obs.) and 50.88% (calcd.). The final product obtained at 800°C contained ½Ce₂O₃ and organic moiety.

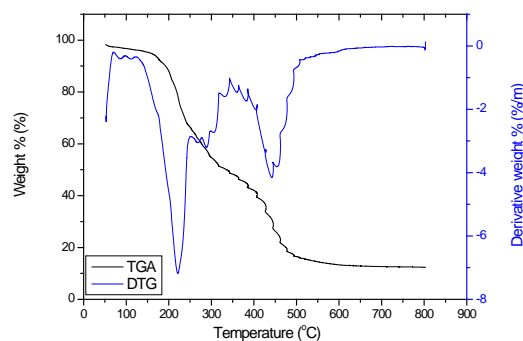


Fig. 8a. TG-DTG curves of *para*/ Ce^{3+} complex.

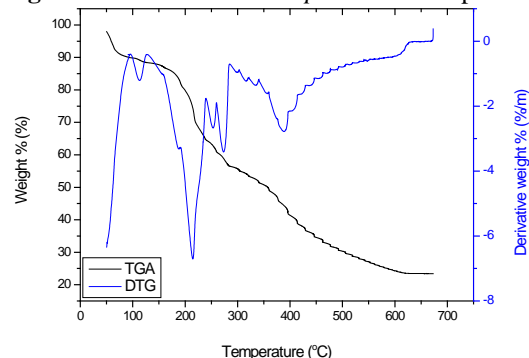
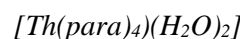


Fig. 8b. TG-DTG curves of *para*/ Th^{4+} complex.



The [Th(*para*)₄(H₂O)₂] complex was decomposed in three main steps. The first step takes place at 50-155°C and corresponds to the loss of 2H₂O molecules, representing a weight loss of 4.50% (obs.) and 4.14% (calcd.). The second step takes place within the temperature range 155-379°C and can be assigned to the loss of organic molecules of *para*, the mass loss due to this step was 31.90% (obs.) and 31.40% (calcd.). The third step occurs at 379-650°C and corresponds to the loss organic molecules of *para*, the mass loss due to this step was 53.00% (obs.) and 52.70% (calcd.). The final product at 750°C is ThO₂.

Kinetic thermodynamic calculations

The calculated thermodynamic parameters from TG and DTG are listed in Table 6. The thermodynamic activation parameters of the decomposition processes of the complexes, namely, activation energy (ΔE^*), enthalpy (ΔH^*), entropy (ΔS^*) and Gibbs free energy change of the decomposition (ΔG^*) were evaluated graphically (Figs. 7, 8) by employing the Coats-Redfern and Horowitz – Metzger relations [37, 38]. In order to access the influence of the structural properties of the ligand and the type of the metal on the thermal behavior of the complexes, the order, *n*, and the heat of activation *E* of the various decomposition stages were determined from the TG and DTG thermograms.

Table 6. Kinetic parameters using the Coats–Redfern (CR) equations for the complexes 1-4.

Complex	Step	Kinetic Parameters					
		E (Jmol ⁻¹)	A (S ⁻¹)	Δ S (Jmol ⁻¹ K ⁻¹)	Δ H (Jmol ⁻¹)	Δ G (Jmol ⁻¹)	r
1	1 st	9.40E+04	7.34E+11	-1.90E+01	9.08E+04	9.65E +04	0.97104
2	1 st	4.66E+04	5.00E+04	-1.52E+02	4.36E+04	1.00E +05	0.97315
3	1 st	6.87E+04	1.30E+07	-1.20E+02	6.45E+04	1.20E +05	0.97021
4	1 st	5.15E+04	2.02E+05	-1.40E+02	4.70E+04	1.01E+ 05	0.97423

Coats – Redfern equation. The equations are as follows:

$$\ln \left[\frac{1 - (1 - \alpha)^{1-n}}{(1-n)T^2} \right] = \frac{M}{T} + B \quad \text{for } n \neq 1 \quad (1)$$

$$\ln \left[\frac{-\ln(1 - \alpha)}{T^2} \right] = \frac{M}{T} + B \quad \text{for } n=1 \quad (2)$$

where $M = -E/R$ and $B = \ln AR/\Phi E$; E , R , A , and Φ are the heat of activation, the universal gas constant, pre-exponential factor and heating rate, respectively. The correlation coefficient, r , was computed using the least square method for different values of n , by plotting the left-hand side of Eqs. (1) or (2) versus $1000/T$.

Horowitz – Metzger equation. The relations derived are as follows:

$$\ln [-\ln(1 - \alpha)] = \frac{E}{RT_m} \Theta \quad (3)$$

where α , is the fraction of the sample decomposed at time t and $\Theta = T - T_m$.

The plot of $\ln [-\ln(1-\alpha)]$ against Θ was found to be linear, from the slope of which E was calculated and Z can be deduced from the relation:

$$Z = \frac{E\phi}{RT_m^2} \exp\left(\frac{E}{RT_m}\right) \quad (4)$$

where ϕ is the linear heating rate, the order of reaction, n , can be calculated from the relation:

$$n = 33.64758 - 182.295\alpha_m + 435.9073\alpha_m^2 - 551.157\alpha_m^3 + 357.3703\alpha_m^4 - 93.4828\alpha_m^5$$

The n value which gave the best fit ($r \approx 1$) was chosen as the order parameter for the decomposition stage of interest. From the intercept and linear slope of such stage, the A and E values were determined. The other kinetic parameters, ΔH , ΔS and ΔG were computed using the relationships; $\Delta H = E - RT$, $\Delta S = R[\ln(Ah/kT) - 1]$ and $\Delta G = \Delta H - T\Delta S$, where k is the Boltzmann constant and h is the Planck constant. The following remarks can be pointed out: (i) all complexes decomposition stages show a best fit for ($n = 1$) indicating a first-order decomposition in all cases. Other n values (e.g. 0, 0.3 and 0.7) did not lead to better correlations [39,40]; (ii) the negative values

of activation entropies ΔS indicate a more ordered activated complex than the reactants and/or slow reactions [41]; (iii) the positive values of ΔH mean that the decomposition processes are endothermic.

Transmission electron microscopy

The surface morphology and particle size of all *diclo* and *para* complexes were obtained from transmission electron micrography (TEM) (Fig. 9a-d). It is clear that these complexes have uniform matrix and homogeneity. The surface morphology of the TEM micrograph reveals the well sintered nature of the complexes with varying grain sizes and shapes. Clear large grains are obtained with agglomerates for all complexes. The distribution of the grain size is homogeneous except that medium to small particles of size about 200 nm-0.5 μm are obtained.

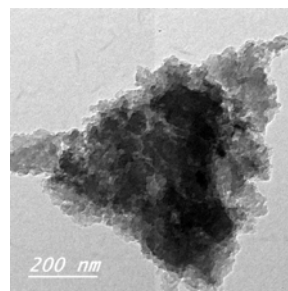


Fig. 9a. TEM image of *diclo*/Ce³⁺ complex.

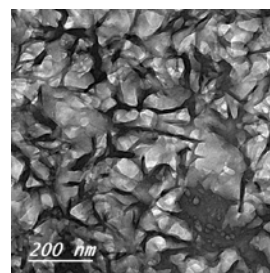


Fig. 9b. TEM image of *diclo*/Th⁴⁺ complex.

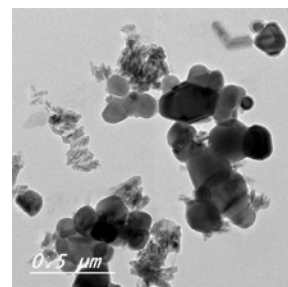


Fig. 9c. TEM image of *para*/Ce³⁺ complex.

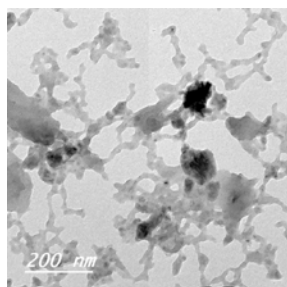


Fig. 9d. TEM image of *para*/Th⁴⁺ complex.

3-8-Antimicrobial activity

Antibacterial and antifungal activity of the *diclo* ligand and its complexes are carried out against two kind of bacteria, *B. subtilis* (Gram +ve), *Escherichia coli* (Gram -ve) and fungal (*Aspergillus niger*, *Aspergillus flavus*) in Fig. (10) and Table 7. The antimicrobial activity estimated based on the size of inhibition zone around dishes. The complexes are found to have high activity against *Aspergillus niger* and *flavus*.

Antibacterial and antifungal activities of *para* complexes were studied against bacteria (Gram-) as *Escherichia coli*, (Gram +) as *Bacillus subtilis* and

fungi (*Aspergillus niger* and *Aspergillus flavus*). The antimicrobial activity was estimated based on the size of the inhibition zone in the dishes. Th(IV) complex was found to have high activity against bacteria and the two kinds of fungi. The data are shown Table 8 and Fig. 10.

Suggested structures of Ce(III) and Th(IV) complexes

The structures of the complexes of *diclo* and *para* drugs with Ce(III) and Th(IV) metal ions were confirmed by elemental analysis, IR, molar conductance, UV-Vis, ¹H-NMR and thermal analysis data.

Thus, from ¹H-NMR and IR spectra, it was concluded that *diclo* chelated in a bidentate fashion but *para* behave as monodentate ligand coordinated to the metal ion *via* the oxygen of the phenolic group. From the molar conductance data, it was found that all complexes seem to be non-electrolytes. So, the investigated complexes have the structures shown in Fig. 11.

Table 7. Antimicrobial effect of *diclo* complexes.

	Diameter of inhibition zone (cm)			
	<i>B. subtilis</i>	<i>E. coli</i>	<i>Aspergillus niger</i>	<i>Aspergillus flavus</i>
Control	0	0	0	0
<i>Diclo</i> /Ce	2	1.2	2.2	2.3
<i>Diclo</i> /Th	1.8	1	2.2	2.2

Table 8. Antimicrobial effect of *para* complexes.

	Diameter of inhibition zone (cm)			
	<i>B. subtilis</i>	<i>E. coli</i>	<i>Aspergillus niger</i>	<i>Aspergillus flavus</i>
Control	0	0	0	0
Ce(III) complex	1.3	1.1	2.6	1.8
Th(IV) complex	1.7	1.2	1.7	3.1

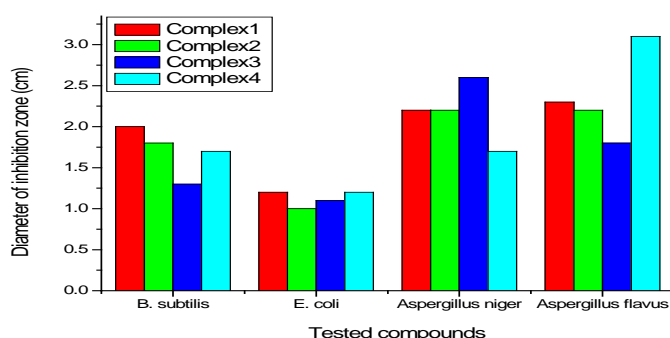
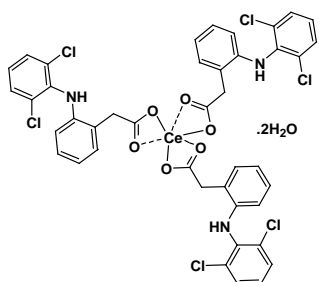
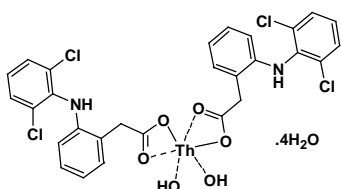


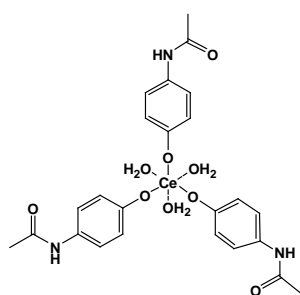
Fig. 10: Statistical representation of the biological activity of complexes 1-4.



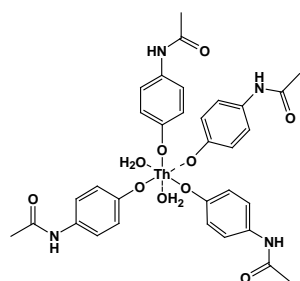
Complex 1



Complex 2



Complex 3



Complex 4

Fig. 11. Structure of the investigated complexes.

REFERENCES

- M. Tuncay, S. Calis, H.S. Kas, M.T. Ercan, I. Peksoy, A.A. Hincal, *Int. J. Pharm.*, **195**, 179 (2000).
- D. Kovala-Demertzi, D. Mentzafos, A. Terzis, *Polyhedron*, **12**, 1361(1993).
- M.E. Abdel-Hamid, L. Novotony, H. Hamza, J. *Pharm. Biomed. Anal.*, **24**, 587 (2001).
- P.A. Todd, E.M. Sorkin, *Drugs*, **35**, 244 (1988).
- P. Moser, A. Sallmann, I. Wiesenberg, *J. Med. Chem.*, **33**, 2358 (1990).
- W.D. Horrocks. D.R. Sundnick, *J. Am. Soc.*, **101** 334 (1979).
- J. R. Vane, R.M. Botting, *Inflamm. Res.*, **1** (1995).
- C. Castellari, S. Ottani, *Acta. Crystallogr.*, **53** 794 (1997).
- M.R. Caira, V.J. Griggith, L.R. Outshoorn Massimbeni, *J. Chem Soc., Chem Commun.*, **9** 1061 (1994).
- I. Bratu, S. Astilean, C. Lonesc, J.P. Indrea, J.P. Huvenne P. Legrand, *Spectrosc. Acta Part A*, **54** 191 (1998).
- M.A. Jan Mens, *Best Pract. Res. Clin. Rheumat.*, **19**, 609 (2005).
- E. Dic, A. Ozdemir, D. Baleanu, *Talanta*, **65** 36 (2005).
- A.B. Moreira, H.B.M. Oliveira, T.D.Z. Atvars, L.L.T. Dias, G.O. Neto, E.A.G. Zagatto, L.T. Kubota, *Anal. Chim. Acta*, **539**, 257 (2005).
- B.B. Ivanova, *J. Mol. Struct.*, **738**, 233 (2005).
- C. Xu, B. Li, *Spectrochim. Acta A*, **60**, 1861 (2004).
- L.G. Binev, Y.I. Vassileva-Boyardjieva, J. Binev, *Mol. Struct.*, **447** 235 (1998).
- A.M. MacConnachie, *Intensive Crit. Care Nuts*, **13**, 238 (1997).
- J.L. Vilchez, R. Blance, R. Avidad, A. Navalon, J. *Pharm. Biomed.* **13** (1995) 119.
- D. Easwaramoorthy, Y. Yu, H. Huang, *Anal. Chim. Acta*, **439**, 95 (2001).
- H. Tanka, P.K. Dasgupta, J. Huang, *J. Anal. Chem.*, **72**, 4713 (2000).
- J.P. Shockcor, S.E. Linger, I.D. Wilson, *Anal. Chem.*, **68**, 4431 (1996).
- S. Murray, A.R. Boobis, *J. Chromatogr.*, **33**, 355 (1991).
- A.K. Singh, R. Negi, Y. Katre, S.P. Singh, *Journal of Molecular Catalysis A: Chemical*, **302**, 36 (2009).
- L.F. Prescott, Paracetamol overdose. Pharmacological consideration and clinical management, *Drugs*, **25**, 290 (1983).
- P.J. Harvison, F.P. Guengerich, *Chem. Res. Toxicol.*, **1**, 47 (1988).
- L. Chavkin, H. Merkle, US Patent (1979).
- F.J. Strenbenz, L. Weintraub, G.L. Cohen, UK Patent, Application GB 2103 87A, 1983.
- W.J. Geary, *Coord. Chem. Rev.*, **7**, 81 (1971).
- K. Nakamoto, *Infrared and Raman Spectra of Inorganic and Coordination Compounds: Part B*, 5th ed., Wiley, New York, 1997.
- D. Kovala-Demertzi, S.K. Hadjikakou, M.A. Demertzis, Y. Deligiannakis, *Journal of Inorganic Biochemistry*, **69**, 223 (1998).
- D. Kovala-Demertzi, A. Theodorou, M.A. Demertzis, C.P. Raptopoulou, A. Terzis, *Journal of Inorganic Biochemistry*, **65**, 151 (1997).
- D. Kovala-Demertzi, D. Mentzafos, A. Terzis, *Polyhedron*, **12** 1361 (1993).
- B.B. Misra, S.R. Mohanty, N.V.V.S. Murti, S. Roychowdhury, *Inorg. Chim. Acta*, **28**, 275 (1978).
- E.D. Eastman, L. Brawar, L.A. Bromby, P.W. Gilles, N.L. Lofgren, *J. Am. Chem. Soc.*, **72**, 4019 (1950).
- R.K. Agarwal, Himanshu Agarwal, *Synth React Inorg Met Org Chem.*, **31**, 263 (2001).
- P. Indersenan, Raj N. K. Kala, *J. Indian Chem. Soc.*, **77**, 259 (2000).

37. A. W. Coats, J. P. Redfern, *Nature*, **201**, 68 (1964).
38. H. W. Horowitz, G. Metzger, *Anal. Chem.*, **35** 1464 (1963)
39. P.B. Maravalli, T.R. Goudar, *Thermochim. Acta*, **325**, 35 (1999).
40. K.K.M. Yusuff, R. Sreekala, *Thermochim. Acta*, **159**, 357 (1990).
41. A.A. Frost, R.G. Pearson, *Kinetics and Mechanisms*, Wiley, New York, 1961.

НОВИ ХЕЛАТНИ ПРОДУКТИ НА ТОРИЙ(IV) И ЦЕРИЙ(III) С АНАЛГЕТИЧНИТЕ ЛЕКАРСТВА ДИКЛОФЕНАК И ПАРАЦЕТАМОЛ: СИНТЕЗ И ИЗСЛЕДВАНЕ НА СПЕКТРОСКОПСКИТЕ ХАРАКТЕРИСТИКИ, ТЕРМИЧНАТА СТАБИЛНОСТ И АНТИМИКРОБИАЛНАТА АКТИВНОСТ

Ф.А.И. Ал-Кодир

Департамент по химия, Научен колеж, Университет Принцеса Нора Бинт Абдул Рахман

Постъпила на 26 ноември, 2017 г.; Коригирана на 21 декември 2017 г.

(Резюме)

Четири нови комплекса на торий(IV) и церий(III) с две аналгетични лекарства, натриев диклофенак (*diclo*) и парацетамол (*para*): $[\text{Ce}(\text{diclo})_3] \cdot 2\text{H}_2\text{O}$ (1), $[\text{Th}(\text{diclo})_2(\text{OH})_2] \cdot 4\text{H}_2\text{O}$ (2), $[\text{Ce}(\text{para})_3(\text{H}_2\text{O})_3]$ (3), и $[\text{Th}(\text{para})_4(\text{H}_2\text{O})_2]$ (4), са синтезирани и охарактеризирани чрез елементен анализ, термичен анализ, FT-IR, $^1\text{H-NMR}$ и UV-VIS спектроскопия. Микроаналитичното определяне на елементите показва, че съотношението метал:лекарство за синтезираните комплекси е съответно 1:3 за комплексите 1 и 3, 1:4 за комплекс 2 и 1:2 за комплекс 4. Вибрациите на разтягане $\nu_s(\text{O-H})$ на -OH във FT-IR спектрите на *para* лиганда изчезват в спектрите на комплексите, което доказва включването на кислорода от -OH групата в комплексообразуването след депротониране. При *diclo* комплексите, вибрациите на разтягане $\nu(\text{C=O})$ на карбоксилната група се изместват в спектрите на комплексите, което потвърждава включването на -COOH групата в комплексообразуването с ковалентно свързване като бидентатно хелатообразуване. Геометрията на Ce^{3+} и Th^{4+} йони в комплексите с лекарствата е шест-координирана. Наноструктурните форми са изследвани с помощта на трансмисионна електронна микроскопия. Антимикробни свойства на новосинтезираните комплекси са определени спрямо някои видове бактерии и гъбички. Всички синтезирани комплекси притежават антимикробна активност.

A new green protocol for the synthesis of 2-substituted perimidines from hydrazones under catalyst- and solvent-free conditions

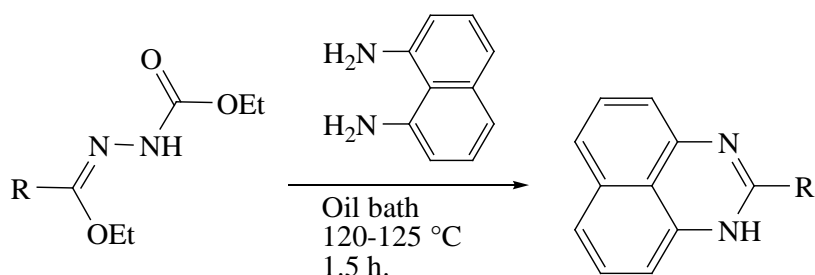
E. Menteşe^{1*}, F. Yılmaz², B. Kahveci³

¹Department of Chemistry, Art and Science Faculty, Recep Tayyip Erdoğan University, 53100, Rize, Turkey

²Department of Chemistry and Chemical Process Technology, Vocational School of Technical Studies, Recep Tayyip Erdoğan University, 53100, Rize, Turkey

³Department of Nutrition and Dietetics, Faculty of Health Sciences, Karadeniz Technical University, 61080, Trabzon, Turkey

Received September 19, 2016; Accepted December 18, 2017



A new green protocol was developed for the synthesis of 2-substituted perimidines. The protocol involves a reaction of ethoxy carbonylhydrazone with 1,8-diaminonaphthalene under solvent- and catalyst-free conditions. Simple workup procedure, economical and environmentally benign are the most advantages of the present method.

Keywords: Perimidine, Hydrazone, Green synthesis, 1,8-Diaminonaphthalene, Catalyst-free conditions

INTRODUCTION

Perimidines, also called 1*H*-benzo[d,e]quinazolines or perinaphthimidazoles, are an interesting heterocyclic system because they include both an excess and a deficiency of π electrons [1-3] and these systems show amphoteric chemical properties [1, 2]. Their derivatives have been used in industry for dyeing of various fibres, as additives to liquid crystal displays, as sources of carbene ligands [4]. They exhibit reversible photochromic and thermochromic properties and are thus used in molecular switches, and photochemical memory devices [5-7]. Recently, the biological activity of perimidines has attracted the attention of organic chemists. Various perimidine derivatives have been found effective as neurotropic preparations

[8]. Also, some synthetic perimidine derivatives are found which have anticancer [9], cytostatic [10], antimicrobial [11] and antifungal activities [12].

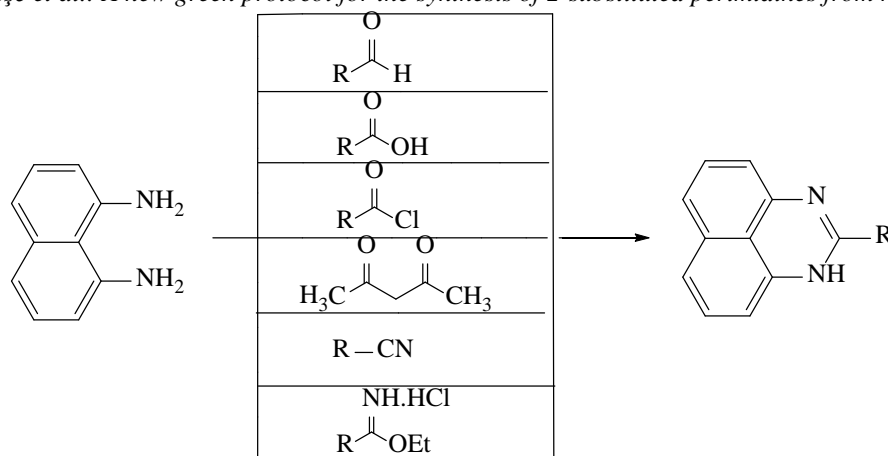
Literature surveys reveal that there are many protocols for the synthesis of perimidine derivatives. Many methods provide the

condensation of 1,8-diaminonaphthalene and carboxylic acids or their derivatives such as aldehydes, acylhalides, anhydrides, nitriles and imidates [12-17] (Scheme 1). However, these methods generally require a catalyst, long reaction time and difficult purification steps. Also, the yield is low due to side reactions. Therefore, there is a need for an easy and efficient method for the synthesis of perimidine derivatives.

The increasing need for environmental protection has led our researches to develop chemical processes with maximum yield and minimum cost while using nontoxic reagents, solvents and catalysts. For this propose, a new method was developed for the synthesis of perimidine derivatives, which is environmentally benign, simple and economical by condensation of 1,8-diaminonaphthalene and 2-[(alkyl/aryl)(ethoxy)methylidene]hydrazinecarboxylates. This is the first synthesis of perimidine derivatives from ethoxy carbonylhydrazones and 1,8-diaminonaphthalene. This reaction requires neither solvents nor harmful reagents.

* To whom all correspondence should be sent.

E-mail: emre.mentese@erdogan.edu.tr



Scheme 1. The synthetic approach for perimidines

EXPERIMENTAL

All chemicals were supplied from Merck (Darmstadt, Germany), Aldrich and Fluka (Buchs SG, Switzerland). Melting points were determined in capillary tubes on a Büchi oil-heated melting point apparatus (Essen, Germany) and uncorrected. ¹H-NMR spectra were recorded on the Varian-Mercury 400 MHz spectrometer (Varian, Darmstadt, Germany) in DMSO-*d*₆ using TMS as internal standard. Mass spectra were recorded on a Thermo Scientific Quantum Access max LC-MS spectrometer. The elemental compositions were determined on a Carlo Erba 1106 CHN analyzer (Heraeus, Hanau, Germany); the experimental values were in agreement (± 0.4 %) with the calculated ones. All reactions were monitored by TLC using precoated aluminum sheets (silica gel 60 F 2.54, 0.2 mm thickness).

Synthesis of compounds 3-14

The corresponding ethoxy carbonylhydrazones (**2**) (0.01 mol) and 1,8-diaminonaphthalene (0.01 mol) were heated in an oil bath at 120-125 °C for 1.5 h. The mixture was cooled to room temperature. The product was recrystallized from EtOH-H₂O /1:2 to give the pure product.

2-Methyl-1H-perimidine (**3**)

Yield: 1.33 g (%73), m.p. 215-216 °C (213-214 °C [12]). ¹H NMR (400 MHz, DMSO-*d*₆, δ , ppm): 10.54 (s, 1H, NH), 7.30 (d, $J = 7.6$ Hz, 2H, Ar-H), 7.20 (t, $J = 7.6$ Hz, 2H, Ar-H), 7.47 (dd, $J = 7.7$ Hz & $J = 2.0$ Hz, 2H, Ar-H), 2.29 (s, 3H, CH₃); LC-MS: 183.24 [M+H]⁺. Anal. Calcd. for C₁₂H₁₀N₂, C:79.10, H:5.53, N: 15.37; Found, C:79.04, H:5.47, N: 15.31.

2-Phenyl-1H-perimidine (**4**)

Yield: 1.73 g (%71), m.p. 189-190 °C (187-188 °C [18]). ¹H NMR (400 MHz, DMSO-*d*₆, δ , ppm): 10.63 (s, 1H, NH), 8.00 (s, 2H, Ar-H), 7.55-7.48 (m, 3H, Ar-H), 7.16-7.01 (m, 4H, Ar-H), 6.67 (d, $J = 8.0$ Hz, 1H, Ar-H), 6.52 (d, $J = 8.0$ Hz, 1H, Ar-H); LC-MS: 245.34 [M+H]⁺. Anal. Calcd. for C₁₇H₁₀N₂, C:83.58, H:4.95, N: 11.47; Found, C:83.50, H:4.86, N: 11.42.

Yield: 1.75 g (%68), m.p. 196-197 °C (196-197 °C [16]). ¹H NMR (400 MHz, DMSO-*d*₆, δ , ppm): 7.62 (d, $J = 7.0$ Hz, 2H, Ar-H), 7.47-7.27 (m, 7H, Ar-H), 6.84 (d, $J = 2.4$ Hz, 2H, Ar-H), 3.95 (s, 2H, CH₂); LC-MS: 259.09 [M+H]⁺. Anal. Calcd. for C₁₈H₁₄N₂, C:83.69, H:5.46, N: 10.84; Found, C: 83.60, H:5.38, N: 10.76.

2-Benzyl-1H-perimidine (**5**)

Yield: 1.28 g (%78), m.p. 184-185 °C (183-185 °C [16]). ¹H NMR (400 MHz, DMSO-*d*₆, δ , ppm): 10.65 (s, 1H, NH), 7.39 (t, $J = 7.0$ Hz, 2H, Ar-H), 7.10-6.97 (m, 6H, Ar-H), 6.88 (d, $J = 7.0$ Hz, 1H, Ar-H), 6.40 (d, $J = 7.0$ Hz, 1H, Ar-H), 3.57 (s, 2H, CH₂); LC-MS: 293.86 [M+H]⁺. Anal. Calcd. for C₁₈H₁₃ClN₂, C:73.85, H:4.48, N: 9.57; Found, C: 73.80, H:4.42, N: 9.51.

2-(4-Chlorobenzyl)-1H-perimidine (**6**)

Yield: 1.87 g (%69), m.p. 163-164 °C (159-160 °C [19]). ¹H NMR (400 MHz, DMSO-*d*₆, δ , ppm): 11.70 (s, 1H, NH), 7.36 (d, $J = 7.6$ Hz, 2H, Ar-H), 7.14-7.07 (m, 6H, Ar-H), 6.57 (d, $J = 7.6$ Hz, 2H, Ar-H), 3.66 (s, 2H, CH₂), 2.24 (s, 3H, CH₃); LC-MS: 273.36 [M+H]⁺. Anal. Calcd. for C₁₉H₁₆N₂, C:83.79, H:5.92, N: 10.29; Found, C: 83.71, H:5.85, N: 10.24.

2-(4-Methylbenzyl)-1H-perimidine (**7**)

Yield: 1.85 g (%67), m.p. 174-175 °C (173-175 °C [16]). ¹H NMR (400 MHz, DMSO-*d*₆, δ , ppm): 10.61 (s, 1H, NH), 7.42 (t, $J = 7.0$ Hz, 2H, Ar-H), 7.19-6.97 (m, 6H, Ar-H), 6.51 (d, $J = 7.0$ Hz, 1H, Ar-H), 6.28 (d, $J = 7.0$ Hz, 1H, Ar-H), 3.54 (s, 2H, CH₂); LC-MS: 277.26 [M+H]⁺. Anal. Calcd. for C₁₈H₁₃FN₂, C:78.24, H:4.74, N: 10.14; Found, C: 78.20, H:4.68, N: 10.08.

2-(4-Fluorobenzyl)-1H-perimidine (**8**)

Yield: 1.85 g (%67), m.p. 174-175 °C (173-175 °C [16]). ¹H NMR (400 MHz, DMSO-*d*₆, δ , ppm): 10.61 (s, 1H, NH), 7.42 (t, $J = 7.0$ Hz, 2H, Ar-H), 7.19-6.97 (m, 6H, Ar-H), 6.51 (d, $J = 7.0$ Hz, 1H, Ar-H), 6.28 (d, $J = 7.0$ Hz, 1H, Ar-H), 3.54 (s, 2H, CH₂); LC-MS: 277.26 [M+H]⁺. Anal. Calcd. for C₁₈H₁₃FN₂, C:78.24, H:4.74, N: 10.14; Found, C: 78.20, H:4.68, N: 10.08.

2-(4-Bromobenzyl-1H-perimidine) (9)

Yield: 2.56 g (%76), m.p. 172-173 °C (170-172 °C [16]). ¹H NMR (400 MHz, DMSO-*d*₆, δ, ppm): 10.62 (s, 1H, NH), 7.53 (t, *J* = 8.4 Hz, 2H, Ar-H), 7.36 (d, *J* = 8.0 Hz, 2H, Ar-H), 7.09 (t, *J* = 7.6 Hz, 2H, Ar-H), 6.98 (d, *J* = 8.4 Hz, 2H, Ar-H), 6.43 (brs, 2H, Ar-H), 3.56 (s, 2H, CH₂); LC-MS: 339.23, 337.19 [M+H]⁺. Anal. Calcd. for C₁₈H₁₃BrN₂, C:64.11, H:3.89, N: 8.31; Found, C: 64.06, H:3.84, N: 8.26.

2-(4-Methoxybenzyl-1H-perimidine) (10)

Yield: 2.04 g (%71), m.p. 205-206 °C (205 °C [19]) ¹H NMR (400 MHz, DMSO-*d*₆, δ, ppm): 10.30 (s, 1H, NH), 7.34 (d, *J* = 5.6 Hz, 2H, Ar-H), 7.08 (t, *J* = 5.2 Hz, 2H, Ar-H), 6.97 (t, *J* = 5.6 Hz, 2H, Ar-H), 6.89 (d, *J* = 5.2 Hz, 2H, Ar-H), 6.46 (d, *J* = 5.6 Hz, 2H, Ar-H), 3.69 (s, 3H, OCH₃), 3.53 (s, 2H, CH₂); LC-MS: 289.46 [M+H]⁺. Anal. Calcd. for C₁₉H₁₆N₂O, C:79.14, H:5.59, N: 9.72; Found, C: 79.10, H:5.52, N: 9.65.

2-(3-Chlorobenzyl-1H-perimidine) (11)

Yield: 1.92 g (%66), m.p. 175-176 °C (175-176 °C [16]). ¹H NMR (400 MHz, DMSO-*d*₆, δ, ppm): 10.65 (s, 1H, NH), 7.59 (s, 1H, Ar-H), 7.45-7.25 (m, 3H, Ar-H), 7.10-6.95 (m, 4H, Ar-H), 6.54 (d, *J* = 6.6 Hz, 1H, Ar-H), 6.27 (d, *J* = 7.0 Hz, 1H, Ar-H), 3.56 (s, 2H, CH₂); LC-MS: 293.79 [M+H]⁺. Anal. Calcd. for C₁₈H₁₃ClN₂, C:73.85, H:4.48, N: 9.57; Found, C: 73.81, H:4.40, N: 9.49.

2-(3-Methylbenzyl-1H-perimidine) (12)

Yield: 2.12 g (%78), m.p. 176-177 °C (175-176 °C [16]). ¹H NMR (400 MHz, DMSO-*d*₆, δ, ppm): 10.67 (s, 1H, NH), 7.59 (s, 1H, Ar-H), 7.48-7.27 (m, 3H, Ar-H), 7.13-6.92 (m, 4H, Ar-H), 6.52 (d, *J* = 7.0 Hz, 1H, Ar-H), 6.29 (d, *J* = 7.0 Hz, 1H, Ar-H), 3.61 (s, 2H, CH₂), 2.12 (s, 3H, CH₃); LC-MS: 273.36 [M+H]⁺. Anal. Calcd. for C₁₉H₁₆N₂, C:83.79, H:5.92, N: 10.29; Found, C: 83.71, H:5.85, N: 10.24.

2-(3-Fluorobenzyl-1H-perimidine) (13)

Yield: 2.18 g (%79), m.p. 164-165 °C (163-164 °C [16]). ¹H NMR (400 MHz, DMSO-*d*₆, δ, ppm): 10.76 (s, 1H, NH), 7.88 (s, 2H, Ar-H), 7.72-7.30 (m, 2H, Ar-H), 7.10-6.95 (m, 4H, Ar-H), 6.41 (d, *J* = 6.6 Hz, 1H, Ar-H), 6.25 (d, *J* = 6.6 Hz, 1H, Ar-H), 3.72 (s, 2H, CH₂); LC-MS: 277.61 [M+H]⁺. Anal. Calcd. for C₁₈H₁₃FN₂, C:78.24, H:4.74, N: 10.14; Found, C: 78.18, H:4.69, N: 10.06.

2-(3-Bromobenzyl-1H-perimidine) (14)

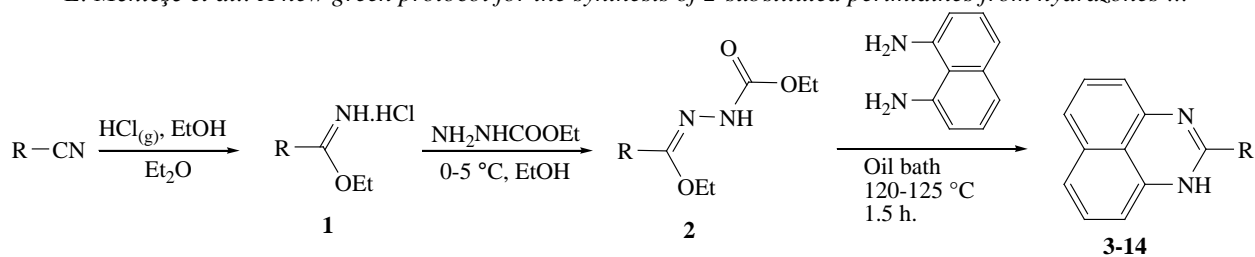
Yield: 2.76 g (%82), m.p. 162-163 °C (160-162 °C [16]). ¹H-NMR (400 MHz, DMSO-*d*₆, δ, ppm) δ 10.69 (s, 1H, NH), 7.63 (s, 1H, Ar-H), 7.54-7.20 (m, 3H, Ar-H), 7.10-6.79 (m, 4H, Ar-H), 6.55 (dd, *J*=6.6 Hz & *J*=1.2 Hz, 1H, Ar-H), 6.23 (dd, *J*=7.0 Hz & *J*=1.5 Hz, 1H, Ar-H), 3.56 (s, 2H, CH₂). LC-MS: 339.25, 337.29 [M+H]⁺. Anal. Calcd. for C₁₈H₁₃BrN₂, C:64.11, H:3.89, N: 8.31; Found, C: 64.03, H:3.81, N: 8.25.

RESULTS AND DISCUSSION

The syntheses of new perimidine derivatives were carried out by reacting 1,8-diaminonaphthalene with an equimolar amount of ethoxy carbonylhydrazone. The reaction was performed in an oil bath at 120-125 °C without using solvent and catalyst. In this reaction, ethoxy carbonylhydrazones were used instead of iminoesters because hydrazones are more stable than iminoesters. The approach provides an environmentally friendly pathway to obtain good yields. Moreover, ethoxy carbonylhydrazones were used for the first time to obtain perimidine derivatives, therefore, this technique is a good alternative to other synthetic methods of perimidine derivatives.

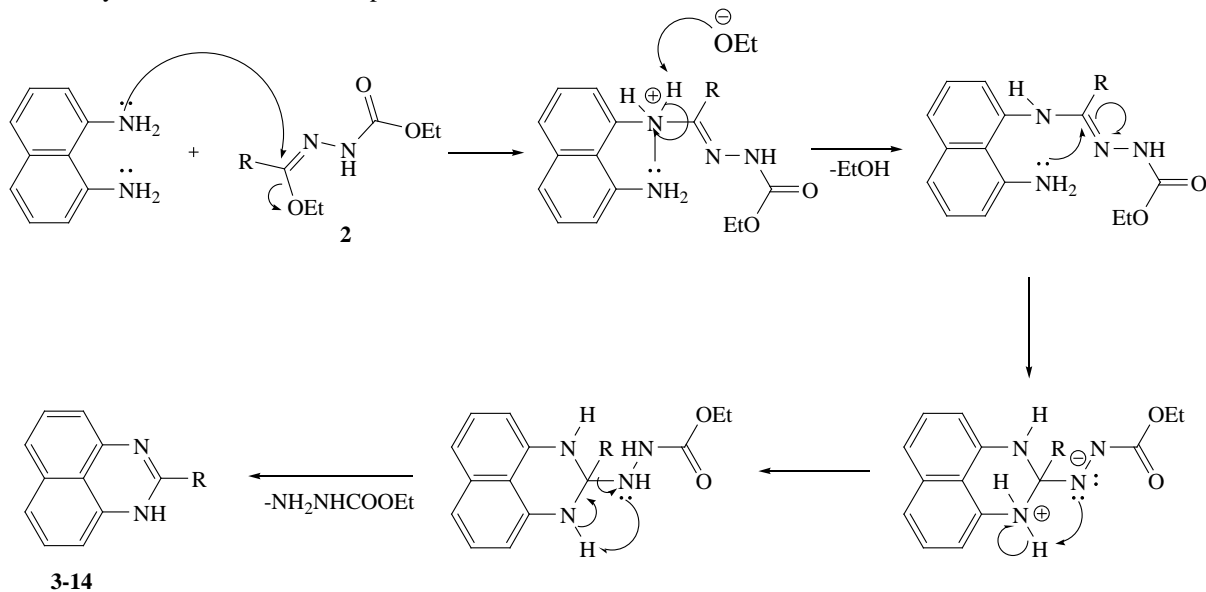
Firstly, iminoester hydrochlorides (**1**) were obtained by the Pinner method [20]. The reaction of ethyl carbazate with iminoester hydrochlorides (**1**) gave ethoxy carbonylhydrazones (**2**) which are useful intermediates for synthesis of potential bioactive heterocyclic compounds such as benzimidazole and triazole derivatives [21-27]. Then, 2-substituted perimidine derivatives (**3-14**) were synthesized by the reaction of ethoxy carbonylhydrazones with 1,8-diaminonaphthalene under solvent- and catalyst-free conditions (Scheme 2).

A mechanism of the type shown in Scheme 3 proposed for this reaction appears likely. In a former study, iminoester hydrochlorides were used by our group under solvent-free conditions to obtain perimidines, but the result was negative because of decomposition of iminoethers (**1**) at high temperatures. In this work, hydrazones (**2**) were used instead of iminoester hydrochlorides at high temperatures and the result was positive.



R: CH₃, C₆H₅, C₆H₅CH₂, 4-ClC₆H₄CH₂, 4-BrC₆H₄CH₂, 4-FC₆H₄CH₂, 4-CH₃C₆H₄CH₂, 4-CH₃OC₆H₄CH₂, 3-ClC₆H₄CH₂, 3-BrC₆H₄CH₂, 3-FC₆H₄CH₂, 3-CH₃C₆H₄CH₂

Scheme 2. Synthesis of 2-substituted perimidines



Scheme 3. Proposed mechanism for the cyclization reaction.

CONCLUSION

In conclusion, a green new method for the synthesis of 2-substituted perimidine derivatives was developed. In this method, 2-[(alkyl/aryl)(ethoxy)methylidene] hydrazine carboxylates were used for the first time to obtain perimidine derivatives. The present protocol was achieved under solvent- and catalyst-free conditions. Therefore, this method is more important than others in terms of green chemistry.

REFERENCES

- X. Bu, L. W. Deady, G. J. Finlay, B. C. Baguley, W. A. Denny, *J. Med. Chem.*, **44**, 200, (2001).
- N. M. Starshikov, F. T. Pozharskii, *Chem. Heterocycl. Com.*, **9**, 922 (1973).
- P. D. Woodgate, J. M. Herbert, W. A. Denny, *Heterocycles*, **26**, 102, (1987).
- I. A. S. Smellie, A. Fromm, R. M. Paton, *Tetrahedron Lett.*, **50**, 410, (2009).
- V. V. Patil, G. S. Shankarling, *Catal. Commun.*, **57**, 138 (2014).
- V. I. Minkin, V. N. Komissarov, *Mol. Cryst. Liq. Cryst. A*, **297**, 205 (1997).
- R. Davis, N. Tamaoki, *Org. Lett.*, **7**, 1461, (2005).
- A. F. Pozharskii, V. V. Dalnikovskaya, *Usp. Khim.*, **50**, 1559 (1981).
- K. A. Bello, S. N. Corns, J. Griffiths, *Journal of the Chemical Society, Chemical Communications*, 452 (1993).
- M. F. Brana, M. Garrido, M. L. L. Rodriguez, M. J. Morcillo, Y. Alvarez, Y. Valladares, G. Klebe, *Eur. J. Med. Chem.*, **25**, 209 (1990).
- A. Mobinikhaledi, M.A. Amrollahi, N. Foroughifar, H. F. Jirandehi, *Asian J. Chem.*, **17**, 2411 (2005).
- R.W. Alder, N.P. Hyland, J.C. Jeffery, T. Riis-Johannessen, D.J. Riley, *Org. Biomol. Chem.*, **7** 270, (2009).
- E. I. Hölljes, E. C. Wagner, *J. Org. Chem.*, **9**, 3 (1944).
- I. Yavari, M. Adib, F. Jahani-Moghaddam, H. R. Bijanzadeh, *Tetrahedron*, **58**, 6901, (2002).
- A. Mobinikhaledi, N. Foroughifar, R. Goli, *Phosphorus Sulfur*, **180**, 2549 (2005).
- B. Kahveci, N. Karaali, E. Menteşe, F. Yilmaz, *J. Chem. Res.*, **37**, 377 (2013).
- E. Menteşe, F. Yilmaz, N. Karaali, S. Ulker, B. Kahveci, *Russ. J. Bioorg. Chem.*, **40**, 336 (2014).
- M. A. Sierra, M. J. Mancheno, J. C. del Amo, I. Fernandez, M. Gomez-Gallego, *Chemistry*, **9**, 4943 (2003).

E. Mentese et al.: A new green protocol for the synthesis of 2-substituted perimidines from hydrazones ...

19. R. R. Reddy, C. V. C. Rao, *Indian J. Chem. B*, **32**, 367 (1993).
20. B. Kahveci, *Molecules*, **10**, 376 (2005).
21. B. Kahveci, F. Yilmaz, E. Mentese, F. S. Beris, *J. Chem. Res.*, 484 (2012).
22. N. Karaali, E. Mentese, F. Yilmaz, A. Usta, B. Kahveci, *S. Afr. J. Chem-S-Afr. T*, **66**, 72 (2013).
23. B. Kahveci, A. A. Ikizler, *Turk. J. Chem.*, **24**, 343 (2000).
24. O. Bekircan, B. Kahveci, O. B. Ozgumus, *Chinese J. Chem.*, **25**, 1871 (2007).
25. E. Mentese, S. Ulker, B. Kahveci, *Chem. Heterocycl. Com.*, **50**, 1671 (2015).
26. E. Mentese, H. Bektas, S. Ulker, O. Bekircan, B. Kahveci, *J. Enzym. Inhib. Med. Ch.*, **29**, 64 (2014).
27. E. Mentese, I. S. Dogan, B. Kahveci, *Chem. Heterocycl. Com.*, **49**, 1136 (2013).

НОВ "ЗЕЛЕН" ПРОТОКОЛ ЗА СИНТЕЗ НА 2-ЗАМЕСТЕНИ ПЕРИМИДИНИ ОТ ХИДРАЗОНИ В ОТСЪСТВИЕ НА КАТАЛИЗАТОР И РАЗТВОРИТЕЛ

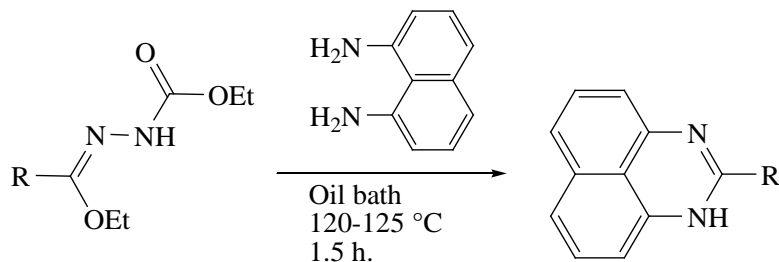
Е. Ментеше^{1*}, Ф. Йълмаз¹, Б. Кахведжи²

¹Департамент по химия, Факултет на наука и изкуство, Университет "Реджеп Таип Ердоган", 53100 Ризе, Турция

²Департамент по хранене и диететика, Факултет по здравни науки, Карадениз технически университет, 61080, Трабзон, Турция

Постъпила на 19 септември, 2016 г.; приета на 19 декември, 2017 г.

(Резюме)



Предложен е нов "зелен" протокол за синтез на 2-заместени перимидини. Протоколът включва реакция на етокси карбонилхидразон с 1,8-диаминонафталин в отсъствие на разтворител и катализатор. Процедурата е проста за изпълнение, икономична и щадяща околната среда.

Characterization by atomic force microscopy of gold nanoparticles functionalized with azocasein for protease colorimetric enzyme assay

Al. S. Chanachev¹, S. S. Simeonova¹, P. D. Georgiev¹, Tz. N. Ivanova¹, S. D. Petrova², K. T. Balashev^{1*}

¹Department of Physical Chemistry, Faculty of Chemistry and Pharmacy, St. K. Ohridski University of Sofia, 1 James Bourchier Blvd., 1164 Sofia, Bulgaria

²Department of Biochemistry, Faculty of Biology, St. K. Ohridski University of Sofia, 8 Dragan Tsankov Blvd., 1164 Sofia, Bulgaria

Submitted December 2, 2016; Accepted April 6, 2017

The colorimetric assay based on surface plasmon resonance of metal nanoparticles have proved to be applicable for sensors systems in the enzyme catalysis because of its simplicity, sensitivity and low cost. The preparation of stable suspensions of gold nanoparticles (GNPs) modified with proteins is a prerequisite for their use as an analytical tool for the colorimetric spectral analysis. In this report we propose a convenient experimental procedure for reproducible production of functionalized with azocasein GNPs. The GNPs were functionalized with azocasein in a stable suspension with optimized concentration of the azocasein. A concept for the test of protease activity using modified with azocasein GNP is also proposed. In order to studying the course of the enzyme reaction we applied UV-Vis spectroscopy and we analyzed the shift of the surface plasmon resonance maxima. For characterization of the morphology and the size of functionalized with azocasein GNPs we made series of Atomic Force Microscopy (AFM) images of samples taken at the beginning and at the end of the proteolytic enzyme reaction.

Key words: gold nanoparticles, azocasein, enzyme assay, Atomic Force Microscopy.

INTRODUCTION

In recent decades the development of biomedical sciences is strongly associated with a demand of new chemical approaches for diagnosis and treatment of many diseases. The embedding of protein molecules in various nanostructured materials and nano-sized objects (quantum dots, nanoparticles, etc.) is an effective way of improving their stability and targeting or some other functional properties. Thus, the functionalized with protein nanomaterials are widely used in contemporary pharmaceutical technology for the transport of dosage forms and in biocatalysis. The advantages of the nanoparticles which distinguish them from bulky materials are due to their specific chemical and physical properties. For example, the gold nanoparticles (GNPs) have unique characteristic absorption maximum at 520 nm because of their surface plasmon resonance, which in turn makes them after functionalization with proteins (e.g. antibodies, labeled proteins etc.) highly applicable in medicine as therapeutic agents in drug delivery system [1], for photothermal therapy [2], diagnosing and imaging agents [3, 4, 5]. The nanoscales' size, which meets the dimension of biological compounds, as well as their easy preparation, high surface area and easy functionalization makes them particularly interesting for accomplishing the related applications in tissue

engineering and regenerative medicine. There are various synthesis methods for producing gold nanoparticles (GNPs), but in practice are preferable those obtained from aqueous solutions of gold precursors (HAuCl₄) in the presence of stabilizing agents [6-10] and among them the most popular is the classical citrate method proposed by Turkevich [11]. Further biofunctionalization of the GNPs with amino acids, peptides, enzymes, DNA, is a challenging experimental step which paves the way for the development of various drug carriers, biomarkers, biosensors [12-14].

A potential candidate for such applications are GNPs modified with azocasein. Azocasein is a dye-marked protein which is primarily used as a substrate for colorimetric determination of enzyme activity. It is intriguing to explore the possibilities of improving the existing enzyme tests by functionalizing the GNPs with azocasein. Hence, the main aim of this article is to propose a simple and reproducible procedure for functionalization of such GNPs and to apply it in a protocol for determination of the enzyme activity. In such procedure, pre-synthesized by Turkevich method GNPs were further covered by layer or shell of azocasein. As a result, the functionalized with azocasein GNPs had plasmon absorption maxima at about 520 nm together with the absorption maxima of the azocasein at about 340 nm. The added enzyme Protease K, which digests

* To whom all correspondence should be sent:

E-mail: fhac@chem.uni-sofia.bg

proteins, is expected to hydrolase the protein shell of the GNPs and as a result one to observe an increasing of the intensity of both absorption maxima. The Atomic force microscopy (AFM) method was utilized for characterization of the modified with azocasein GNPs before and at the end of the enzyme reaction.

EXPERIMENTAL

Chemicals and reagents

Analytical grade tetrachloroauric acid ($\text{HAuCl}_4 \cdot 3\text{H}_2\text{O}$) was purchased from Panreac (PanreacQuímica S.A.U., Spain). Trisodium citrate ($\text{Na}_3\text{C}_3\text{H}_5\text{O}(\text{COO})_3 \cdot 2\text{H}_2\text{O}$) was also of analytical grade and were obtained from Merck (Germany). Azocasein and Protease K were obtained from Sigma-Aldrich. All the solutions were prepared with deionized water.

Experimental methods

The synthesis of gold nanoparticles was performed by the classical Turkevich method [11]. For the functionalization of the gold nanoparticles with azocasein we used following procedure: the solution of GNPs ($C = 50 \text{ mg/l}$), synthesized by Turkevich method was mixed with solution of azocasein (10^{-2} M) and water – 12,5 ml GNPs with 8,33 ml H_2O and 4,17 ml azocasein. This new solution is tempered at $35^\circ - 37^\circ \text{ C}$ (at this temperature interval Protease K has optimal enzyme activity). After the addition of Protease K ($C = 2 \text{ mg/ml}$) the samples for UV-Vis spectrophotometry and AFM were collected at every 5 minutes. In the same time the reaction solution was constantly homogenized with rotary magnetic stirrer. The samples were taken and the UV-Vis spectra were measured for a period of 40 minutes, which is considered as the end of the enzyme reaction.

The UV-Vis absorption spectra of the functionalized with azocasein GNPs were determined by spectrophotometer (Evolution 300 Thermo Scientific).

The size of GNPs functionalized with azocasein and Protease K was determined by means of AFM as described in [11, 15]. AFM imaging was performed on the NanoScopeV system (Bruker Ltd., Germany) operating in tapping mode in air at room temperature. We used silicon cantilevers which having tips with radius less than 10 nm (Tap300Al-G, Budget Sensors, Innovative solutions Ltd, Bulgaria), spring constant in the range of 1.5 to 15 N/m and the resonance frequency $150 \pm 75 \text{ kHz}$ were used. The scanning rate was set at 1 Hz and the images were captured in the height mode with 512×512 pixels resolution. Subsequently, all the images were

flattened by means of the Nanoscope software. The same software was used for section analysis and particle size determination.

RESULTS AND DISCUSSION

At Fig. 1A are presented UV-Vis absorption spectra of GNPs functionalized with azocasein. Before their functionalization the GNPs which were pre-synthesized by the Turkevich procedure. Their mean diameter was close to 20 nm and the corresponding absorption maxima was about 520 nm [15] while the absorption maxima of azocasein was about 340 nm.

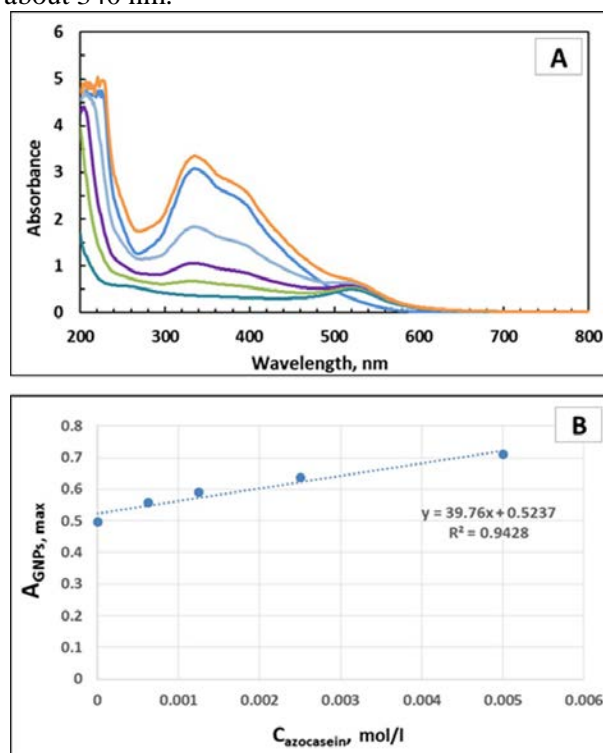


Fig 1. Comparison of UV-Vis absorption spectra with characteristic maxima: pure azocasein solution (340 nm), gold nanoparticles – pure (520 nm) and functionalized with different concentrations of azocasein (A). Absorption maxima intensity of functionalized gold nanoparticles as a function of azocasein concentration (B).

In the course of GNPs' functionalization the intensity of the UV-Vis plasmon maxima increases proportionally to the increasing of the concentration of azocasein as it is presented graphically at Fig. 1B. The linear dependence is based on the Beer law as follows:

$$A_{GNPs} = \epsilon C_{azocasein} + A_{GNPs}^0 = A_{azocasein} + A_{GNPs}^0 \quad (1)$$

Where A_{GNPs} is the total absorption maxima of the functionalized GNPs, containing shells of azocasein molecules with total concentration of the azocasein $C_{azocasein}$ varying in the range 0.8×10^{-3} to $5 \times 10^{-3} \frac{\text{mol}}{\text{l}}$. A_{GNPs}^0 – intercept of the linear dependence

which corresponds the absorption maxima of the bare pre-synthesized GNPs. The calculated value for the line slope is $\varepsilon = 39$ which is close to molar absorption coefficient for azocasein $\varepsilon = 38$.

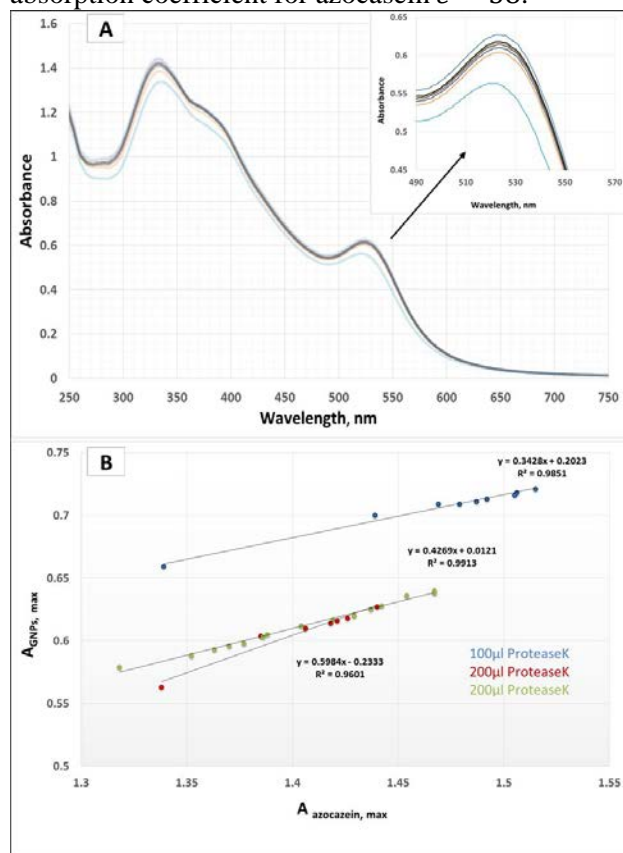


Fig. 2. The increasing of absorption maxima (340 nm and 520 nm) after addition of Protease K (200 ml 2 mg/ml) to the solution of functionalized with azocasein GNPs (A). *Inset:* Zoom of the increasing GNPs plasmon maxima (B) The linear correlation between the intensity of the plasmon maximum at 529 nm with the azocasein maximum at 340 nm.

At Fig. 2 are presented typical spectra obtained at certain time interval after the addition of enzyme Protease K to the solution of modified with azocasein GNPs. One can clearly observe (the inset in Fig. 2 A) the increasing intensity of the plasmon absorption maximum at 520 nm. It could be explain with the thinning of the GNPs' protein shells which have been digested upon the action of Protease K. At the same time the azocasein adsorption maximum at 340 nm also increases which is result of releasing of the azo-dye in the course of the enzyme reaction- a well-known fact from the classical tests for the protease activity. It is also interesting to point out the linear correlation between the intensity of both maxima as it is presented on the graphs at Fig. 2 B.

For studying the enzyme kinetics the maxima of the adsorption spectra of azocasein and the plasmon of the GNPs were taken at certain time intervals. The corresponding kinetic curves of enzyme reactions for

three separate experiments with different enzyme concentrations are presented on Fig. 3. For convenience the absorption maxima were normalized as follows:

$$\xi_i = \frac{A(t)_i - A(0)_i}{A(\infty)_i} \quad (3)$$

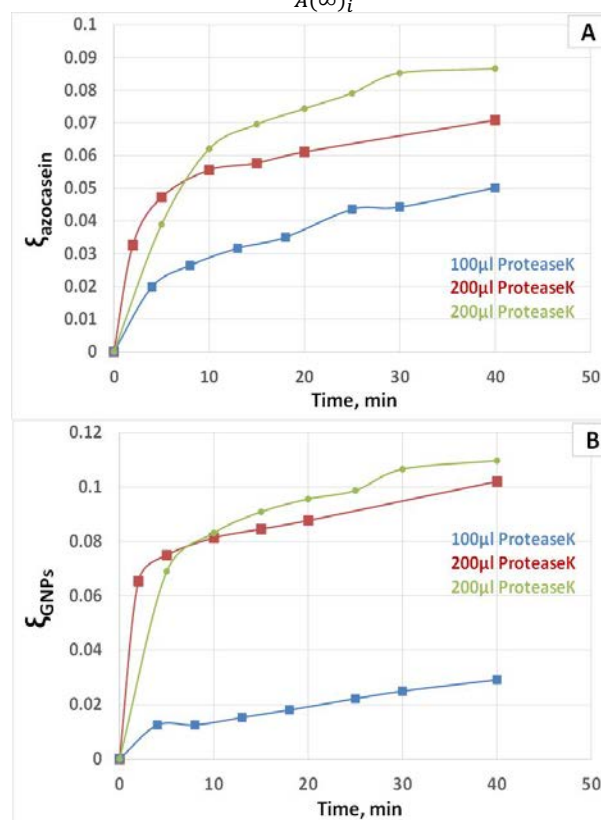


Fig. 3. Normalized kinetic curves of the Protease K action extracted from (A) azocasein adsorption maxima (340 nm) and (B) GNPs plasmon absorption maxima (520 nm). The volumes of Protease K (2 mg/ml) added to reaction mixture are presented on the legend.

Where $A(t)_i$ the adsorption maximum at certain t , $A(0)_i$ is the adoption at t_0 (before the addition of the Protease K) and $A(\infty)_i$ is the absorption maxima at the beginning at the end ($t = 40 \text{ min}$) of enzyme reaction. From the kinetics curves one can observe that the initial slopes increase with the increase of the enzyme concentrations, e.g. bigger enzyme concentration higher rate of the enzyme reaction.

To characterize the morphological changes of azocasein modified GNPs at the beginning of the enzyme reaction (before the addition of Protease K) and at the end of reaction, the AFM imaging was performed. At Fig. 4 are presented typical 2D topography images of GNPs deposited on mica supports. From the image at Fig. 4 A one can observe that after the deposition a small areas around the GNPs are formed. The height of these areas is around 5 nm which is comparable to the size of the protein molecules which implies that this areas are the azocasein shells of the modified GNPs. In the course

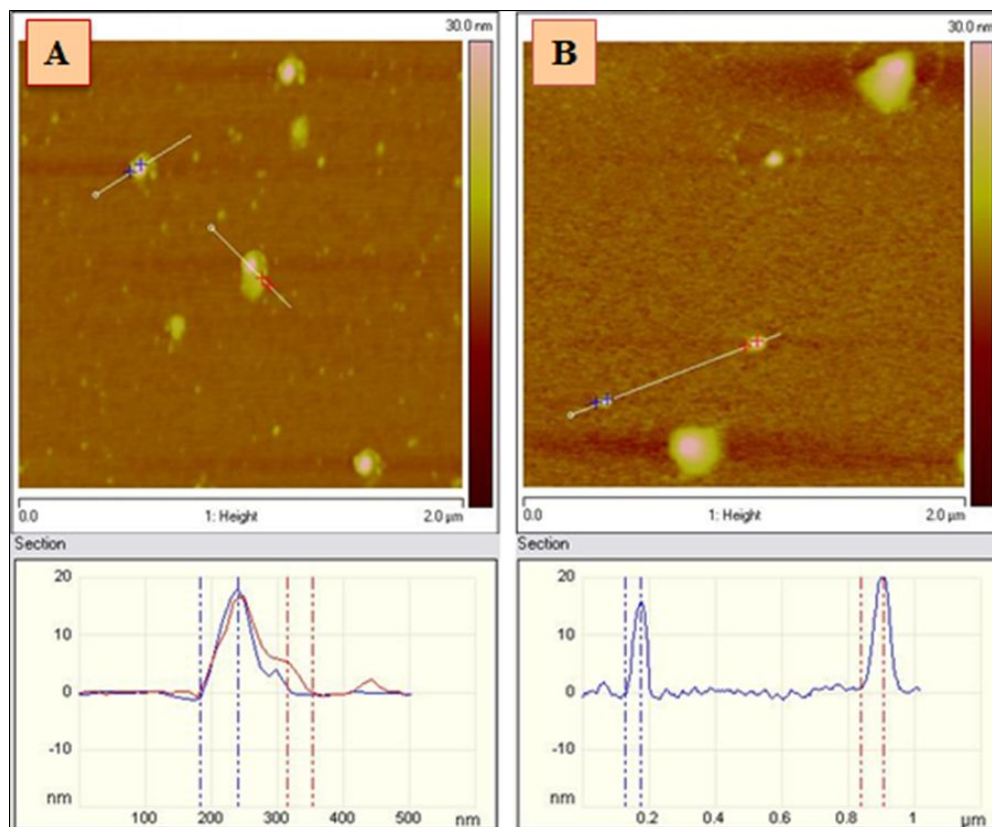


Fig. 4. AFM 2D images obtained after depositing of functionalized GNPs suspension on mica support, together with corresponding cross sections (A) before the addition of Protease K and (B) at the end of the enzyme reaction.

of the enzyme reaction since these shells were digested by the protease and as one can see in Fig.4B at the end of enzyme reaction those shells are missing. The sizes of the GNPs are about 20 nm at the beginning and a bit smaller, 18 nm at the end of reaction.

CONCLUSIONS

Simple and reproducible procedure for functionalization of the GNPs with azocasein was proposed. The prepared GNPs were characterized at first with UV-Vis spectroscopy. Azocasein GNPs were then used for substrate to the enzyme Protease K. The enzyme kinetics was studied by UV-Vis and AFM imaging was applied for characterization of GNPs morphological changes at the beginning of the enzyme reaction and at the very end. The data obtained from both experimental method - AFM and UV-Vis are in excellent agreement with each.

Acknowledgements. The authors are grateful to the H 2020 – TWINN-2015-Twinning.

REFERENCES

1. T.M. Sun, Y.C. Wang, F. Wang, J.Z. Du, C.Q. Mao, C.Y. Sun, *Biomaterials*, **35**, 836 (2014).
2. W. F. Zandberg, A. B. S. Bakhtiari, Z. Erno, D. Hsiao, B. D. Gates, T. Claydon, *Nanomedicine Nanotechnol., Biol. Med.*, **8**, 908 (2012).

3. T. L. Halo, K. M. McMahon, N. L. Angeloni, Y. Xu, W. Wang, A. B. Chinen, *Proc. Natl. Acad. Sci.*, **111**, 17104 (2014).
4. A. de la Zerda, S. Prabhulkar, V. L. Perez, M. Ruggeri, A. S. Paranjape, F. Habte, *Clin. Exp. Ophthalmol.* (2014).
5. K. Hayashi, M. Nakamura, K. Ishimura, *Adv. Health. Mater.*, **2**, 756 (2013).
6. J. A. Copland, M. Eghtedari, V. L. Popov, N. Kotov, M. Mamedova, M. Motamedi, A. A. Oraevsky, *Mol. Imag. & Biol.*, **6**, 341 (2004).
7. J. J. Storhoff, R. Elghanian, R. C. Mucic, C. A. Mirkin, R. L. Letsinger, *J. Am. Chem. Soc.*, **120**, 1959 (1998).
8. G. C. Bond, C. Louis, D. T. Thompson, *Catalysis by Gold* (vol. 6), Imperial College Press, London. 2006.
9. J. Polte, T. T. Ahner, F. Delissen, S. Sokolov, F. Emmerling, A.F. Thünemann, R. J. Kraehnert, *J. Am. Chem. Soc.*, **132**, 1296 (2010).
10. M. C. Daniel, D. Astruc, *Chem. Rev.*, **104**, 293 (2004).
11. J. Turkevich, P. Stevenson, J. Hillier, *Discuss. Faraday Soc.*, **11**, 55 (1951).
12. A. G. Tkachenko, H. Xie, D. Coleman, W. Glomm, J. Ryan, M. F. Anderson, S. Franzen, D. L. Feldheim, *J. Am. Chem. Soc.*, **125**, 4700 (2003).
13. S. H. Brewer, W. R. Glomm, M. C. Johnson, M. K. Knag, S. Franzen, *Langmuir*, **21**, 9303 (2005).
14. P. Khullar, V. Singh, A. Mahal, P. N. Dave, S. Thakur, G. Kaur, *J. Phys. Chem. C*, **116**, 8834 (2012).
15. P. Georgiev, A. Bojinova, B. Kostova, D. Momekova, T. Bjornholm, K. Balashev, *Colloid Surf. A*, **434**, 154(2013).

ОХАРАКТЕРИЗИРАНЕ НА ЗЛАТНИ НАНОЧАСТИЦИ, ФУНКЦИОНАЛИЗИРАНИ С АЗОКАЗЕИН С ПОМОЩТА НА АТОМНО-СИЛОВА МИКРОСКОПИЯ (AFM) И ПРИЛОЖЕНИЕТО ИМ ЗА КОЛОРИМЕТРИЧНИ ЕНЗИМНИ ТЕСТОВЕ НА ПРОТЕАЗА

Ал. Чаначев, С. Симеонова, П. Георгиев, Св. Петрова, Цв. Иванова, К. Балашев*

¹ *Софийски университет "Св.Климент Охридски", Факултет по химия и фармация, катедра „Физикохимия“, бул. "Джеймс Баучер" 1, 1164, fhas@chem.uni-sofia.bg*

² *Софийски университет "Св.Климент Охридски", Биологически факултет, катедра „Биохимия“, бул. "Драган Цанков" 8, 1164, София, България*

Постъпила на 2 декември, 2016 г.; приета на 6 април, 2017 г.

(Резюме)

Колориметричните тестове, разработени на основата на повърхностния плазмонен резонанс на златните наночастици са доказали своята приложимост за сензорни системи в ензимния катализ, като поради своята чувствителност и простота, така и поради ниската си цена. Подготовката на стабилни суспензии от златни наночастици, модифицирани с протеини, дава възможност за употребата им като подходящ аналитичен инструмент за колориметрични спектрални анализи. Настоящото изследване разглежда експериментална процедура за изготвянето на възпроизводим синтез на функционализирани с азоказеин златни наночастици в стабилна суспензия при различни концентрации на азоказеин. Предложена е концепция за тест за ензимна активност на протеаза, при използване на функционализирани с азоказеин златни наночастици. За по-доброто изучаване на тези системи, както и за да бъде изучена ензимната реакция в тях са направени изследвания чрез UV-Vis абсорбционна спектроскопия, като подробно е анализирано отместването на максимума в спектрите, съответстващ на повърхностния плазмонен резонанс. За да бъде изучена напълно системата е изследвана морфологията и размера на функционализираните с азоказеин частици, като е направена серия от AFM изображения на пробите, взети в началото и края на протеолитичната ензимна реакция.

Optimization scheme for a typical longitudinal three-level Rankine cycle cold energy power generation system for recycling liquid gas

Sh. Yao*, L. Xu, G. Feng, L. Tang

School of Energy and Power Engineering, Jiangsu University of Science and Technology, Zhenjiang 212000, Jiangsu, China

Received: October 15, 2017; Revised: January 2, 2018

This study investigates an intermediate fluid vaporizer in gasification systems for liquefied natural gas floating storage regasification units. A heated longitudinal three-level Rankine cycle system that uses the cold energy of liquefied natural gas to generate power was optimized. The system was then compared to the original longitudinal three-level Rankine cycle system established under the same conditions. Results showed that under a liquefied natural gas flow of 175 t/h, the net power output and exergy efficiency of the new system increase by 10.3% and 15.3%, respectively.

Keywords: Liquefied natural gas, Three-level Rankine cycle, Power generation, Heated

INTRODUCTION

Gasification of liquefied natural gas (LNG) before use releases a large amount of cold energy [1]. With the increase in the production and consumption of LNG for LNG cold energy utilization, research has focused on LNG and its application in power generation, air separation, liquefied carbon dioxide and carbon dioxide production, seawater desalination, refrigeration, and low-temperature culturing [2]. LNG cold energy generation is the most important measure to take full advantage of high-grade LNG cold energy [3]. Other methods of cold energy power generation include direct expansion, secondary media, joint, mixed media, and Brayton cycle and gas turbine utilization methods [4]. In the area of LNG cold energy power generation, the focus has shifted to low-temperature organic fluids composed of multi-stage Rankine cycles for the maximization of the application of LNG cold energy [5].

Li et al. [6] proposed cascade power utilization of solar energy and an LNG organic Rankine cycle system, which involves two types of working fluids: the working fluid in which hot water heated by solar energy is gasified first and the second working fluid in which the refrigerant is gasified after LNG becomes operable. The system combines low-temperature Rankine cycle power generation and the direct expansion method. Sun et al. [7] also established a Rankine cycle cold energy power generation system involving two methods, namely, the vaporization of Rankine cycle working fluid by solar heated water as the heat source and the direct expansion method. The system increases the temperature of the refrigerant entering the turbine

and improves the net output of the system. However, solar heating is affected by the weather, and many auxiliary equipments are required to provide sufficiently hot water when the system handles large amounts of LNG. Wenji Rao[8] used industrial waste heat as the heat source in a Rankine cycle and concluded that with the increase in evaporation pressure, thermal efficiency and power increase; however, industrial waste heat at high temperatures results in large differences in heat transfer temperature and consequently leads to a loss of a significant amount of energy. Given that these systems require volume or heat sources, they should be applied on land only.

Many scholars have studied systems that are applicable to water bodies. Hongchang Yang [9-11] proposed an LNG cold energy utilization segmentation model and established a horizontal and vertical three-level Rankine cycle according to the model. They also put forward an improved optimization scheme for existing problems on the basis of the concept of dual pumping. Chao Zhang [12] used a mixed refrigerant composed of methane, propane and ethane as circulating working fluids. The results showed that the ratio of the mixed working media provides an important contribution to the maximum net output. However, in the actual operation of the proposed system, the optimal mass fraction ratio of the refrigerants is difficult to determine, and the requirements for stable operation are relatively high. Guobiao Cui [13] used an LNG cold energy segmentation model and established five horizontal Rankine cycle power generation systems using LNG cold energy; all levels of the circulating heat originated from seawater, and the system efficiency reached 61%. In practice, systems

* To whom all correspondence should be sent:

based on a five-level Rankine cycle are complex and thus difficult to apply. Sangick Lee [14] used seawater as the heat source in the first-level Rankine cycle and exhaust gas as the heat source in the second-level Rankine cycle of a horizontal two-level Rankine cycle power generation system; the results indicated that this system is suitable for small-scale power fishing vessels, but the energy loss of the heat exchanger is considerable due to the high exhaust temperature. Junjiang Bao [15] proposed a two-stage condensed Rankine cycle system whose net power output and thermal efficiency are better than those of combined Rankine cycle systems. Li Boyang [16] adopted an LNG carrier and designed a set of systems that uses LNG cold energy and flue gas waste heat after natural gas combustion to generate electricity. This system involves only one level of Rankine cycle, and the working fluid is high-temperature flue gas. The system can save 2.77 million yuan per year. LNG carriers are transported year round; hence, their heat sources (i.e., high-temperature flue gas) can be stably supplied. In addition, the system involves only a quarter of a complete Rankine cycle and thus requires minimal power. These existing studies imply the need to improve turbines before working fluid temperature can benefit the net power output.

The liquefied natural gas floating storage regasification units (LNG-FSRU) system is usually placed offshore and thus requires long-distance land transport of natural gas; its delivery pressure should reach 7 MPa or higher [17], at which point LNG approaches a supercritical state. Power generation utilization using LNG gasification cold energy should be based on the heat source conditions of LNG gasification in land or on-board environments

to consider LNG high-grade cold energy generation. Given that the operating environment of LNG-FSRU lacks a stable high-temperature heat source, LNG-FSRU in the supercritical state of LNG gasification in a cold energy power generation program cannot be directly obtained from the existing LNG gasification of cold energy power generation program.

The LNG of an intermediate fluid vaporizer (IFV) system in LNG-FSRU is gasified in a supercritical state. The current work proposes two forms of the heated longitudinal three-level Rankine cycle power generation scheme according to the gasification parameters of LNG-FSRU and using seawater as the only heat source. The two proposed schemes are suitable for the cold energy utilization of LNG-FSRU regasification systems because they increase the temperature of the working fluid in the turbines and thus increase turbine efficiency. This work provides a solution for optimizing LNG-FSRU cold energy generation systems.

Composition of the heated longitudinal three-level Rankine cycle system

The molar composition of LNG is as follows: 95% methane, 3% ethane, and 2% propane. The gasification pressure is 8 MPa, which is supercritical pressure. Only one reference [9] previously proposed a three-level Rankine cycle power generation system that uses LNG cold energy during steaming. The two forms of the heated longitudinal three-level Rankine cycle power generation system proposed in the present study are shown in Figures 1 and 2. These proposed systems improve the inlet refrigerant of turbines 1 and 2 through the heat transfer between the working fluid and seawater temperature.

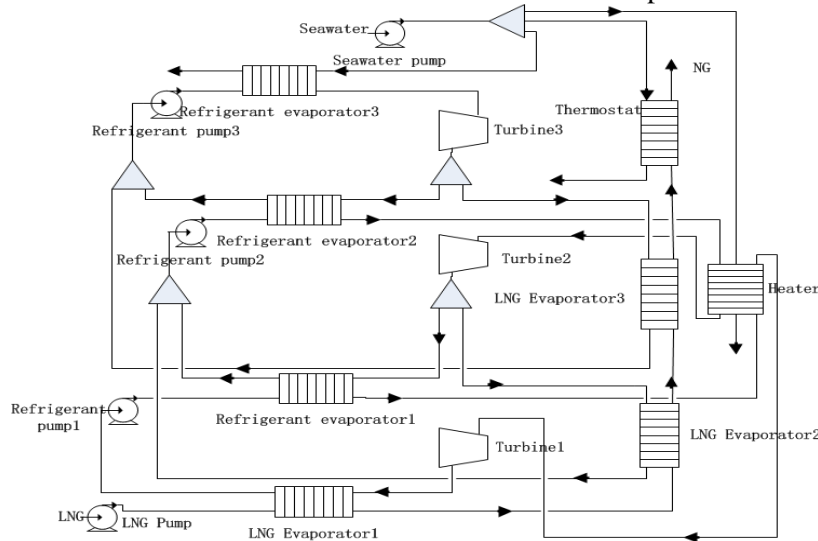


Fig.1. System diagram of the heated longitudinal three-level Rankine cycle (Form 1)

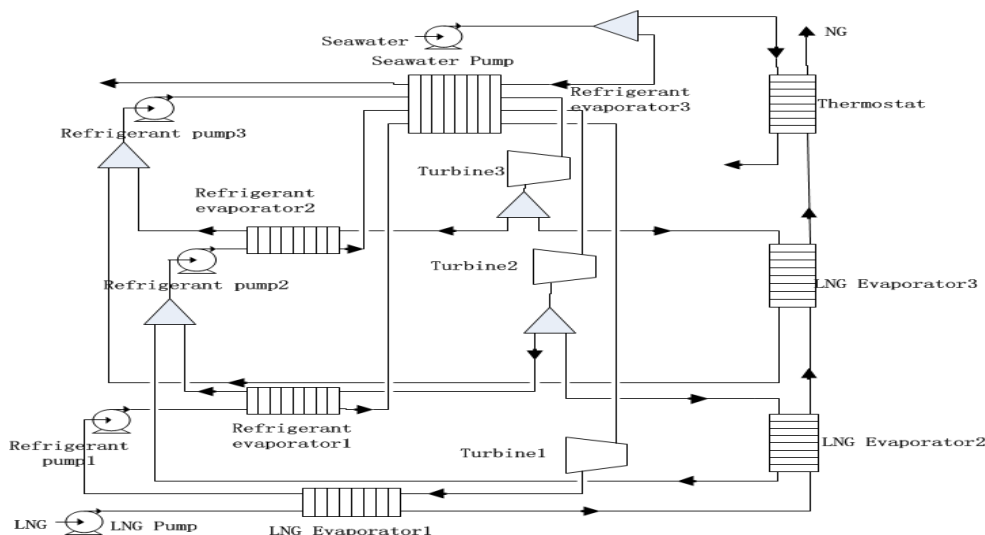


Fig. 2. System diagram of the heated longitudinal three-level Rankine cycle (Form 2)

The difference between Form 1 (Figure 1) and the original longitudinal three-level Rankine cycle is that in Form 1, the refrigerant entering turbines 1 and 2 is introduced into the heater for heat exchange with seawater to increase the temperature of the turbines and facilitate their operation.

The difference between Form 2 (Figure 2) and the original longitudinal three-Rankine cycle is that in Form 2, the refrigerant entering turbines 1 and 2 is introduced into the refrigerant evaporator 3 for heat exchange with seawater to increase the temperature of the turbines and facilitate their operation.

The calculation results showed that excluding that of refrigerant evaporator 3 and the heater, the equipment efficiency, optimum parameter matching, maximum net power output, and overall efficiency of the system are the same. Form 1 was used as an example to determine the optimal combination of refrigerant and parameters matching for heated longitudinal three-level Rankine cycle systems. Then, a thermodynamic comparison of the heated longitudinal three-level Rankine cycle system and the original longitudinal three-level Rankine cycle system was performed. The two forms of the heated longitudinal three-level Rankine cycle system were also compared in terms of energy loss, energy of equipment, and overall energy efficiency.

Determination of the optimal combination of refrigerant and parameter matching

Selection of system parameters. For the simulation calculations and analysis, the flow of LNG was assumed to be 175 t/h. The simulation calculation was conducted with the following settings:

- The condensed pressure of the circulating fluid was 110 kPa.
- The temperature of seawater serving as the heat source was 20 °C, and the output temperature of seawater was 15 °C. The ambient temperature was 25 °C.
- The minimum end difference of all heat exchangers was 5 °C.
- In all heat exchangers (except for heat exchangers whose hot fluids are seawater), the hot fluid outlet was subcooled at 2 °C.
- The efficiency of the turbine was 80% and that of the pump was 75%.
- The pressure and heat losses of all heat exchangers and pipes were ignored.
- The refrigerants at the outlet of the refrigerant evaporator were in a saturated gas state.

Optimization of refrigerant combination. In selecting the ideal working fluid, one should consider not only its effects on the net output and safety of the system but also whether its critical temperature matches the temperature of the heat source. The choice of refrigerant plays a key role in the recovery of the LNG cooling capacity of systems [18].

The condensing temperatures of common refrigerants under 110 kPa are shown in Table 1.

Table 1. Condensation temperatures of common refrigerants at 110 kPa

R1150	R170	R23	R116	R1270	R290	R717	R134a	R152a	R600a
-102.64°C	-87.22°C	-80.53°C	-77.20°C	-46.16°C	-40.55°C	-31.44°C	-24.24°C	-22.61°C	-9.93°C

LNG-FSRU systems also need to meet the requirements of daily life, such as fresh water resources and air conditioning. After recovery in three low-temperature Rankine cycles, LNG should have an adequate amount of cold energy to be used by other cold energy processes, such as desalination and cold storage. Therefore, LNG in three Rankine cycles is obtained after the recovery of the cold energy outlet temperature of about $-45\text{ }^{\circ}\text{C}$ [19,20]. Given that the minimum end of the heat exchanger in this work was set to $5\text{ }^{\circ}\text{C}$, the refrigerants R290 and R1270 shown in Table 1 were deemed as the most suitable for the third Rankine cycle. At the inlet of the system, the temperature of the LNG changed from $-162\text{ }^{\circ}\text{C}$ to $-158\text{ }^{\circ}\text{C}$ after it was pressurized by the pump. When R290 was selected as the refrigerant for the third Rankine cycle, the temperature of LNG cold energy utilization ranged from $-158\text{ }^{\circ}\text{C}$ to $-45.55\text{ }^{\circ}\text{C}$. When R1270 was selected as the refrigerant for the third Rankine cycle, the temperature of LNG cold energy utilization ranged from $-158\text{ }^{\circ}\text{C}$ to $-51.16\text{ }^{\circ}\text{C}$. The refrigerants R1150, R170, R23, R116, and R1270 meet the temperature range given in Table 1. The first and second Rankine cycles of the working fluid and the corresponding LNG inlet temperature should match as much as possible to reduce the exergy loss of the heat exchanger caused by large temperature differences. Therefore, R1150 and R170 were selected as possible refrigerants for the first Rankine cycle, and R23, R116, and R1270 were selected as possible refrigerants for the second Rankine cycle. When the refrigerant of the second Rankine cycle was R1270, the refrigerant of the third Rankine cycle could only be R290. Thus, 10 possible refrigerant combinations were identified.

In the HYSYS simulation, the net output of the system was calculated given the inlet temperatures of turbines 1 and turbine 2 (hereafter referred to as outlet temperature 1 and outlet temperature 2, respectively). The property package of the refrigerants was based on the Peng–Robinson equation. Under different working group combination schemes, the net power output of the system was hypothesized to reach the maximum point when the outlet temperature of the process was

set to the maximum value. When the refrigerant of the second Rankine cycle was R116, refrigerant evaporator 1 of the first Rankine cycle showed a temperature cross. R116 is a dry fluid; thus, the difference between the cold fluid outlet temperature of refrigerant evaporator 1 and the condensing temperature of refrigerant R116 was large. This condition led to temperature crossing in refrigerant evaporator 1. Table 2 shows the ranges of outlet temperature 1 and outlet temperature 2 corresponding to the maximum outlet temperature 1 under the combinations of different refrigerants (without temperature crossing). The temperature interval of outlet temperature 2 is also given.

Results of refrigerant filtering

In HYSYS, a system simulation with different ranges of outlet temperature 1 and outlet temperature 2 was performed under different combinations of refrigerants. The net work output was calculated accordingly. The net output of the system and the dryness of the corresponding refrigerant in the turbine 1 outlet are shown in Figure 3. When outlet temperature 1 was taken as the maximum value, the dryness of turbines 2 and 3 was constant. Thus, only the outlet refrigerant dryness of turbine 1 was considered. Figure 4 shows the outlet refrigerant dryness of turbine 3 when the net power output of the system reaches the maximum under the combination of different refrigerants.

Figures 3 and 4 show that when the refrigerant combinations were R1150, R23, and R290, outlet temperature 1 was $-16\text{ }^{\circ}\text{C}$, and outlet temperature 2 was $-41\text{ }^{\circ}\text{C}$. The system ultimately produced the highest net power output of 4394.090 kW . The dryness of turbine 3 was also high. In the combination of different refrigerants other than R170, R23, R1270 and R170, R23, R290, the system achieved the maximum net work output when the outlet refrigerant dryness of turbines 1 and 2 was equal to 1. When the combinations of refrigerants were R170, R23, R1270 and R170, R23, R290, the outlet refrigerant dryness of system turbines 1 and 2 was less than 1.

Table 2. Ranges of outlet temperature 1 and outlet temperature 2 corresponding to maximum outlet temperature 1

Combinations of refrigerants	Range of the outlet temperature 1	Range of the outlet temperature 2	Temperature interval of the outlet temperature 2
R1150,R23,R290	$-45.55\text{ }^{\circ}\text{C}\sim-16\text{ }^{\circ}\text{C}$	$-41\text{ }^{\circ}\text{C}\sim-80.59\text{ }^{\circ}\text{C}$	$4\text{ }^{\circ}\text{C}$
R1150,R23,R1270	$-51.16\text{ }^{\circ}\text{C}\sim-25\text{ }^{\circ}\text{C}$	$-41\text{ }^{\circ}\text{C}\sim-80.77\text{ }^{\circ}\text{C}$	$4\text{ }^{\circ}\text{C}$
R170,R23,R1270	$-51.16\text{ }^{\circ}\text{C}\sim-25\text{ }^{\circ}\text{C}$	$-67\text{ }^{\circ}\text{C}\sim-80.77\text{ }^{\circ}\text{C}$	$2\text{ }^{\circ}\text{C}$
R170,R23,R290	$-45.55\text{ }^{\circ}\text{C}\sim-16\text{ }^{\circ}\text{C}$	$-67\text{ }^{\circ}\text{C}\sim-80.59\text{ }^{\circ}\text{C}$	$2\text{ }^{\circ}\text{C}$
R1150,R1270,R290	$-45.55\text{ }^{\circ}\text{C}\sim-41\text{ }^{\circ}\text{C}$	$10.05\text{ }^{\circ}\text{C}\sim-46.8\text{ }^{\circ}\text{C}$	$8\text{ }^{\circ}\text{C}$
R170,R1270,R290	$-45.55\text{ }^{\circ}\text{C}\sim-41\text{ }^{\circ}\text{C}$	$-9\text{ }^{\circ}\text{C}\sim-46.8\text{ }^{\circ}\text{C}$	$4\text{ }^{\circ}\text{C}$

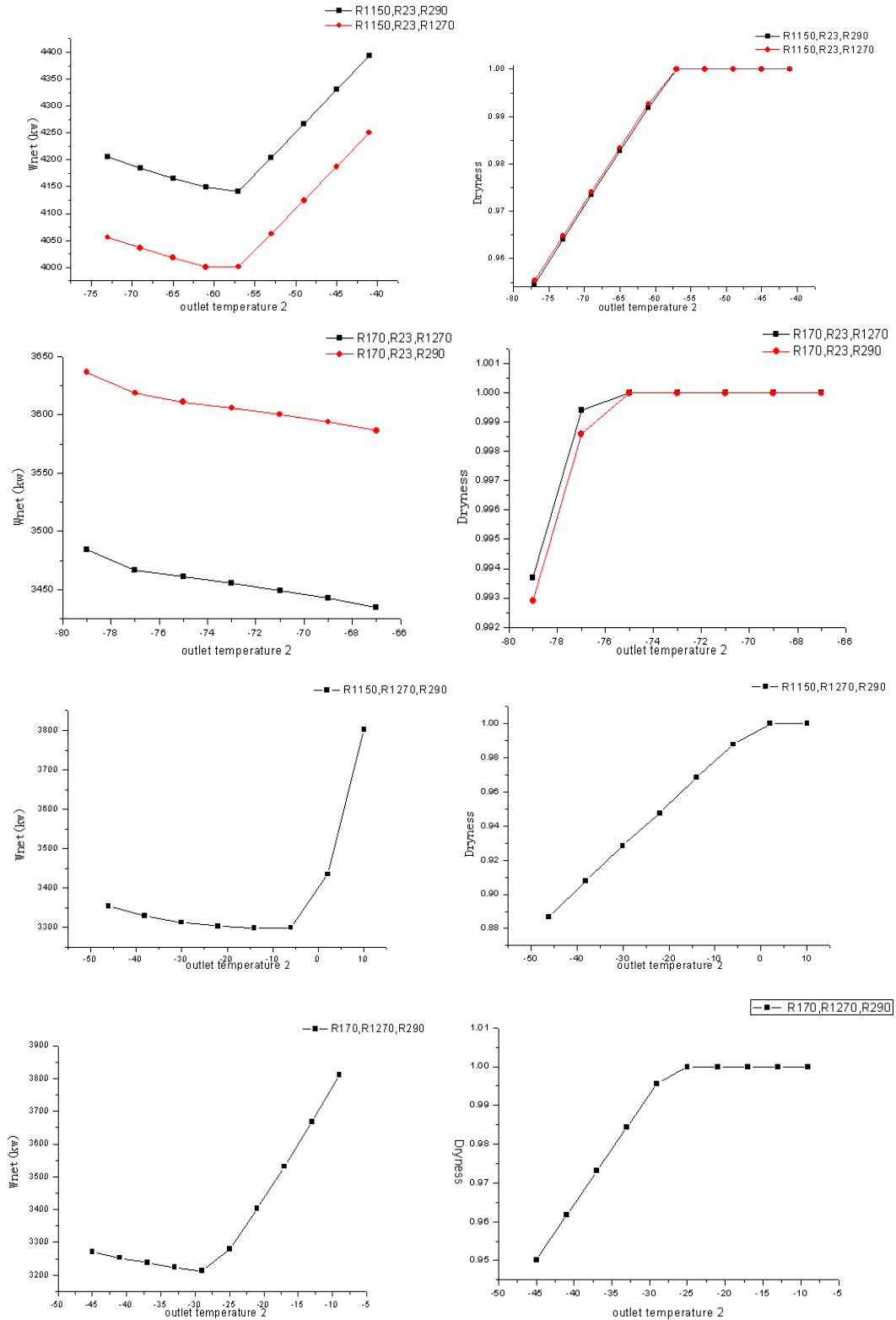


Fig. 3. Network output of the system (left) and dryness of turbine 1 (right) under different combinations of refrigerants

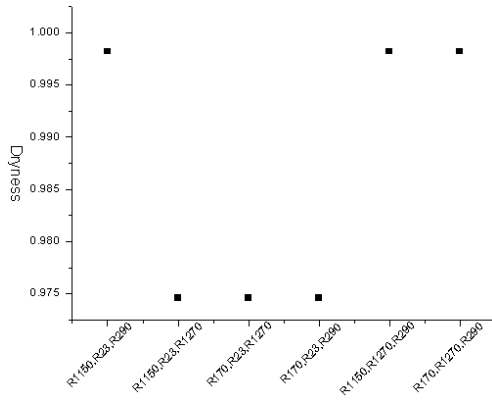


Fig. 4. Dryness of turbine 3 corresponding to the maximum output of the system under different combinations of refrigerants

However, in these two combinations, the system’s maximum network output was lower than that under the combination of R1150, R23, R290. Thus, using only the outlet refrigerant dryness of turbine 3 in the comparison does not affect the results.

Figures 3 and 4 show that the optimal working combination was between R1150, R23, R290 and R1150, R23, R1270. The maximum net power output under the two combinations and the combinations of other refrigerants revealed obvious differences. The NG outlet temperature of LNG evaporator 3 was $-45.55\text{ }^{\circ}\text{C}$ when the working fluid of the third Rankine cycle was R290. The NG outlet temperature of LNG evaporator 3 was $-51.16\text{ }^{\circ}\text{C}$ when the working fluid of the third Rankine cycle was R1270. Therefore, the temperature span of the working combination R1150, R23, R290 was larger than the temperature span of the working combination R1150, R23, R1270. When the two working combinations were used under optimal conditions, the output of the working combination R1150, R23, R290 was large. Therefore, R1150, R23, and R290 were determined to be the best combination of refrigerants for the system.

DETERMINING THE OPTIMUM PARAMETER MATCHING

Table 3. Maximum outlet temperature 2 at different outlet temperatures 1 under the combination of refrigerants R1150, R23 and R290

Outlet temperature 1	$-43\text{ }^{\circ}\text{C}$	$-40\text{ }^{\circ}\text{C}$	$-37\text{ }^{\circ}\text{C}$	$-34\text{ }^{\circ}\text{C}$	$-31\text{ }^{\circ}\text{C}$	$-28\text{ }^{\circ}\text{C}$	$-25\text{ }^{\circ}\text{C}$	$-22\text{ }^{\circ}\text{C}$	$-19\text{ }^{\circ}\text{C}$	$-16\text{ }^{\circ}\text{C}$
Maximum outlet temperature 2	$-50\text{ }^{\circ}\text{C}$	$-50\text{ }^{\circ}\text{C}$	$-50\text{ }^{\circ}\text{C}$	$-50\text{ }^{\circ}\text{C}$	$-50\text{ }^{\circ}\text{C}$	$-50\text{ }^{\circ}\text{C}$	$-50\text{ }^{\circ}\text{C}$	$-50\text{ }^{\circ}\text{C}$	$-46\text{ }^{\circ}\text{C}$	$-41\text{ }^{\circ}\text{C}$

Figure 3 also shows that when outlet temperature 1 was given and outlet temperature 2 was taken as the maximum value, the net output of the system was maximum under the working combinations of R1150, R23, and R290. The influence of outlet temperature 1 on the net output of the system was also determined. In the calculation, the maximum value of outlet temperature 2 was calculated with a given outlet temperature 1. When the process was established and the working combinations were set to R1150, R23, and R290, the maximum outlet temperature 1 at different outlet temperatures 2 was determined. The results are shown in Table 3. Outlet temperature 1 was divided by the temperature interval of $3\text{ }^{\circ}\text{C}$. When the combination of refrigerants was R1150, R23, and R290 and the system reached the maximum outlet temperature 2 at different outlet temperature 1, the outlet refrigerant dryness of turbines 1 and 3 remained constant. Thus, only the outlet refrigerant dryness of turbine 2 needed to be considered. The net output of the system and the outlet refrigerant dryness of turbine 2 when the system reached the maximum outlet temperature 2 at different outlet temperatures 1 are shown in Figure 5. Figure 5 shows that when outlet temperature 1 reached the maximum value of $-16\text{ }^{\circ}\text{C}$, outlet temperature 2 also reached the corresponding temperature range with the maximum value of $-41\text{ }^{\circ}\text{C}$. At the same time, the system achieved the maximum net output of 4394.090 kW . This result indicates the correctness of the assumptions. When the outlet refrigerant dryness of turbine 2 was less than 1, the net power output of the system increased with the decrease in outlet temperature 1. When the outlet refrigerant dryness of turbine 2 was equal to 1, the net output of the system increased with the increase in outlet temperature 1. This phenomenon is consistent with that shown in Figure 3.

Therefore, when the system refrigerant combination was R1150, R23, and R290, outlet temperature 1 was $-16\text{ }^{\circ}\text{C}$, and outlet temperature 2 was $-41\text{ }^{\circ}\text{C}$. The net work output of the system reached the maximum of 4394.090 kW .

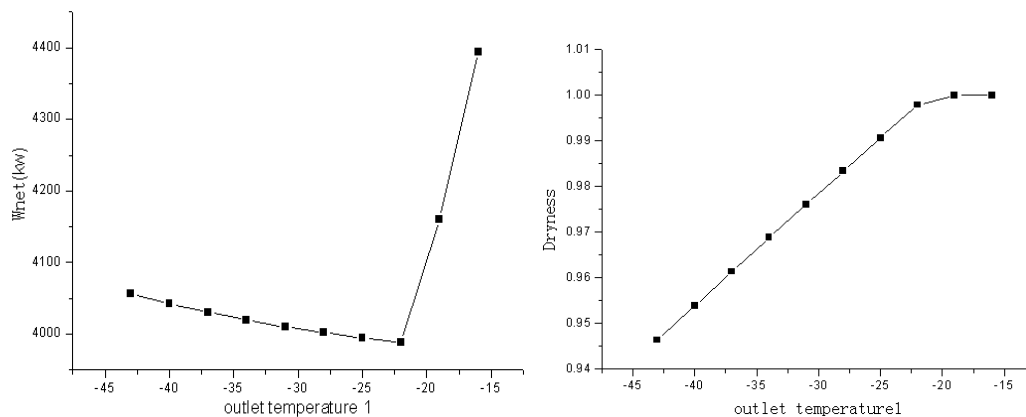


Fig. 5. Net output of the system and outlet refrigerant dryness of turbine 2

Table 4. Comparison of exergy loss and net power output of the heated longitudinal three-level Rankine cycle and the original longitudinal three-level Rankine cycle

Program	Original longitudinal three-level Rankine cycle		Heated longitudinal three-level Rankine cycle	
Equipment	Exergy loss (kW)	Exergy efficiency	Exergy loss (kW)	Exergy efficiency
LNG evaporator 1	3266.63	65.9%	3203.43	72.9%
LNG evaporator 2	624.70	79.7%	116.19	92.2%
LNG evaporator 3	1845.55	65.6%	1513.29	67.9%
LNG thermolator	1649.63	13.1%	1649.63	13.1%
Refrigerant evaporator 1	435.94	91.9%	130.91	97.9%
Refrigerant evaporator 2	750.75	85.1%	724.29	85.1%
Refrigerant evaporator 3	1296.09	38.9%	1216.76	38.9%
Refrigerant pump 1	3.69	45.0%	6.67	45.0%
Refrigerant pump 2	9.95	61.5%	9.60	61.5%
Refrigerant pump 3	36.17	61.4%	33.96	61.4%
LNG pump	967.69	11.6%	967.69	11.6%
Seawater pump	168.86	88.8%	170.59	88.8%
Turbine 1	277.64	69.6%	492.30	70.8%
Turbine 2	666.82	72.1%	715.27	72.2%
Turbine 3	1396.99	75.7%	1311.48	75.7%
Heater			699.30	82.6%
Exergy loss of the system (kW)		13397.1		12262.06
Net output power of system (kW)		3982.92		4394.090
Exergy efficiency of the system		22.9%		26.4%
Refrigerants	R1150, R23, R290		R1150, R23, R290	

Thermodynamic analysis and comparison of heated longitudinal three-level Rankine cycle power generation systems

The definitions of exergy loss and exergy efficiency of the equipment and system are similar to those in ref. [15].

The results are shown in Table 4. As shown in Table 4, the heated longitudinal three-level Rankine cycle scheme reduced the exergy loss of the three LNG evaporators and the three refrigerant

evaporators in comparison with the original longitudinal three-level Rankine cycle. The increase in the exergy efficiency of LNG evaporator 2 was most obvious. The exergy loss of the three turbines of the heated longitudinal three-level Rankine cycle increased, but the exergy efficiency was not reduced and even slightly increased. In terms of the performance of the entire system, the heated longitudinal three-level Rankine cycle improved by 10.32% relative to the original three-level Rankine cycle.

Table 5. Comparison of exergy loss and exergy efficiency of related equipment in the two forms of the heated longitudinal three-level Rankine cycle system and exergy efficiency of the systems

Equipment	Heated longitudinal three-level Rankine cycle system (Form 1)		Heated longitudinal three-level Rankine cycle system (Form 2)	
	Exergy loss (kW)	Exergy efficiency	Exergy loss (kW)	Exergy efficiency
Refrigerant evaporator 3	1216.76	38.9%	1916.07	30.3%
Heater	699.30	82.6%		

Moreover, the exergy efficiency of the former increased by 15.3%, and the total exergy loss decreased by 8.5%.

Contrast of the two forms of the heated longitudinal three-level Rankine cycle system

A comparison of the exergy loss and exergy efficiency of related equipment in the two forms of the heated longitudinal three-level Rankine cycle system and the exergy efficiency of each form are shown in Table 5.

The number of heat exchangers in Form 2 was less than that in Form 1. Thus, refrigerant evaporator 3 was a four-stream, complicated heat exchanger. As shown in Table 5, the exergy efficiency of the new heat exchanger was relatively large, and the exergy efficiency of refrigerant evaporator 3 improved even with a large number of heat exchangers in Form 2. In actual processes, the appropriate form is selected according to specific circumstances, such as funds and area.

CONCLUSIONS

To improve the inlet refrigerant temperature of turbines and ultimately enhance turbine performance, this work proposed two forms of the heated longitudinal three-level Rankine cycle power generation system. A thermodynamic exergy analysis of the existing longitudinal three-level Rankine cycle was performed. The optimal refrigerant combination and parameter matching for the heated longitudinal three-level Rankine cycle power generation system were determined. In both forms, the parameter matching, exergy efficiency, exergy loss, and net output of the system were the same. The specific conclusions are as follows:

(1) For the heated longitudinal three-level Rankine cycle, the ideal combination of refrigerants was R1150, R23, and R290. The turbine inlet temperature of the second-level Rankine cycle was $-16\text{ }^{\circ}\text{C}$, whereas that of the first-level Rankine cycle was $-41\text{ }^{\circ}\text{C}$. The net power output reached the maximum of 4394.09 kW, and the efficiency was 26.4%.

(2) Compared with those of the original three-level Rankine cycle, the net output and exergy efficiency of the heated longitudinal three-level Rankine cycle increased by 10.3% and 15.3%, respectively, and the total exergy loss decreased by

8.5%.

REFERENCES

1. L.J. Wang, G.G. Ma, Y. Yu, Y. Yang, H.F. Guo, *Petrochemical Applications*, **9**, 22 (2012).
2. Y. Chen, Y.L. Ju, *Chinese Journal of Chemical Engineering*, **66** (S2), 387 (2015).
3. H.M. He, W.S. Lin, *Cryogenics and Superconductivity*, **6**, 432 (2006).
4. K. Wang, X.S. Lu, A.Z. Gu, *Cryogenic Engineering*, **1**, 53 (2005).
5. Y.N. Liu, K.H. Guo, *Cryogenics and Superconductivity*, **2**(38), 13 (2010).
6. P.C. Li, J. Li, G. Pei, A. Munir, J. Ji, *Solar Energy*, **127**, 136 (2016).
7. X.H. Sun, B.D. Chen, L. Wang, S.X. Song, Y. Ma, G. J. Zhang, *Natural Gas Industry* **32**(10), 103 (2012).
8. W.J. Rao, L.J. Zhao, C. Liu, J.L. Xu, M.G. Zhang, *Journal of Engineering Thermophysics*, **35**(2), 214 (2014).
9. H.C. Yang, Optimization of Cold Energy Power Generation System for Liquefied Natural Gas (LNG). Master's thesis, Beijing University of Technology, 2010.
10. H.C. Yang, Y.W. Lu, G.L. Liu, P.F. Lv, C.F. Ma, Y.T. Wu, *Natural Gas Industry*, **7**, 98 (2010).
11. H.C. Yang, Y.W. Lu, C.F. Ma, Y.T. Wu, *Renewable Resources*, **1**, 72 (2011).
12. C. Zhang, H.G. Jin, G.F. Shao, X.L. Bu, Q.L. Zhang, H.Y. Fan, *Oil and Gas Chemical Industry*, **4**, 54 (2015).
13. G.B. Cui, Study on Improvement of Rankine Circulation System Using LNG Cold Energy, Dissertation, Southwest Petroleum University, 2014.
14. S. Lee, B.C. Choi, *Journal of Mechanical Science and Technology* **30**(3), 1389 (2016).
15. J.J. Bao, Y. Lin, R.X. Zhang, N. Zhang, G.H. He, *Energy Conversion and Management*, **143**, 312 (2017).
16. B.Y. Li, Y.Q. Zhang, X.R. Zhang, D.F. Tian, *Navigation of China*, **1**, 914 (2016).
17. H.M. He, W. S. Lin, A. Z. Gu, *Cryogenic Engineering*, **6**, 58 (2006).
18. L. Zhang, W. Gao, L.M. Yu, X.R. Zhang, Y. Liu, *Cryogenics and Superconductivity*, **2**, 51 (2015).
19. H.Y. You, G.G. Ma, M. Huang, Q.L. Xu, W. Zhou, *Natural Gas Technology*, **1**(04), 65 (2007).
20. L. He, W. Gao, L. Zhang, L.M. Yu, X.R. Zhang, Y. Liu, S.R. Wang, *Chemical Industry*, **33**(07), 11 (2015).

**ОПТИМИЗАЦИОННА СХЕМА НА ТИПИЧНА НАДЛЪЖНА СИСТЕМА С РАНКИНОВ
ЦИКЪЛ НА ТРИ НИВА, ИЗПОЛЗВАЩА СТУДЕНА ЕНЕРГИЯ, ЗА ГЕНЕРИРАНЕ НА
ЕНЕРГИЯ ЗА РЕЦИКЛИРАНЕ НА ТЕЧЕН ГАЗ**

Ш. Яо*, Л. Сю, Г. Фън, Л. Тан

*Училище по енергийно инженерство, Университет на Дзиенсу за наука и технология, Джъндзян 212000,
Дзиенсу, Китай*

Постъпила на 15 октомври, 2017 г.; коригирана на 2 януари, 2018 г.

(Резюме)

В настоящата статия се изследва междинен течен изпарител за газификационни системи за подвижни регазификационни устройства за съхраняване на втечен природен газ. Оптимизирана е нагреваема система, базирана на надлъжен Ранкинов цикъл на три нива, използваща студената енергия на втечен природен газ за производство на енергия. Системата е сравнена с оригиналната надлъжна система с Ранкинов цикъл на три нива при същите условия. Установено е, че при поток на втечения газ от 175 t/h, нетната изходна мощност и ефективността на ексергията на новата система нарастват съответно с 10.3% и 15.3%.

Lactic acid and M(II) d-metals (Cu, Co, Mn, Cd) milli- and micro- quantities interaction: FTIR and ESI-MS analysis

N. S. Krstić^{1*}, R. S. Nikolić¹, V. D. Dimitrijević¹, D. M. Đorđević¹, M. N. Stanković¹, I. M. Krstić², M. G. Nikolić¹

¹Department of Chemistry, Faculty of Sciences and Mathematics, University of Niš, Višegradska 33, 18000 Niš, Serbia

²Faculty of Occupational Safety, University of Niš, Čarnojevića 10, 18000 Niš, Serbia

Received: November 6, 2017; Revised: December 30, 2017

This study investigated the interaction of M(II) d-biometal ions (Cu, Co, Mn) and toxic Cd(II) ion with lactic acid, which is present in human body as a result of intake or as a product of biological processes, at milli- and micro-molar level, under approximately physiological conditions by FTIR and ESI-MS spectroscopy. Spectroscopic investigations showed that the lactic acid in the tested system behaves as a monodentate ligand, it comes to interact at all concentration levels, and the most pronounced interaction is in the model system with Co(II) ion.

Keywords: M(II) d-metals, Milli- and Micro-interactions, Spectroscopy

INTRODUCTION

In biological systems d-biometal cations easily interact with molecules of water and various parts of different organic and inorganic biomolecules, as natural constituents or substances introduced into the human body. These complex associates, built *via* O-, N- and S- donor atoms, have an important role in biological processes [1-3].

Copper is a biogenic element found in numerous enzymes' systems. The Cu(II) ion (d^9 configuration) can give coordination compounds of various coordination and geometry through O-, N-, and S-donor atoms of different biomolecules and small molecules [1, 4].

Cobalt as a micro-element has a role in the metabolism of proteins and amino acids as the constituent parts of metalloenzymes. The Co(II) ion (d^7 configuration) easily interacts with parts of other molecules and builds complex particles with a coordination number 4, as well as a coordination number 6 *via* the O-, but also *via* the N-donor atom [1].

Manganese is an element weakly present in biological systems, but it also has an irreplaceable role in detoxification from oxygen free radicals as a cofactor of numerous enzymes. The Mn(II) ion (d^5 configuration) easily builds complexes with a coordination number 6 which are only slightly stable and easily interact with other molecules, which leads to changes in the ligands and the building of new products [1, 5].

Cadmium is a toxic metal, and it is not a biometal. In the human body this metal can enter

through the food chain. Toxicity of cadmium is partly a consequence of its ability to bind instead of biometals with similar physicochemical characteristics over -SH of the active sites of some enzymes and block their activity, because of higher affinity for thiol groups. This metal induces oxidative damage to red blood cells in different tissues [6,7].

The carboxyl group as a part of many compounds (pharmaceuticals, supplements) is a "universal" O-donor ligand which can form complexes of different coordination, and can act as a monodentate or a bidentate ligand [8, 9].

α -Hydroxycarboxylic acids are constitutive components of many biochemical processes in the living world. They are often used in pharmaceutical preparations [10,11]. Lactic acid, 2-hydroxypropanoic acid, (LA) is formed by fermentation of sugars and other carbohydrates under the action of anaerobic bacteria and it can be ingested with food into the body. In medicine it is used as a component of the Ringer's and Hartman's solutions [12]. Lactic acid is a suitable molecule for model systems for the study of interaction of biometals with O-donor ligands in biosystems. With M(II) metal ions from solutions of molar concentrations, depending on the conditions of complexation, properties and synergistic effect of the metal ions, LA can form different types of complex associates [10, 11, 13, 14] With M(II) d-metal ions LA can form complexes of the type $[M(LA)_2R]$, where it behaves as a bidentate ligand, and R is molecule of solvent [15]. Cu(II) ion can form mononuclear and binuclear complexes with aliphatic α -hydroxycarboxylic acids at different pH values [10, 11, 16].

* To whom all correspondence should be sent.

E-mail: nenad.krstic84@yahoo.com

Our previous studies have shown that there is a mobility of metal ions from biological hard mineral tissue of teeth that had been exposed to the impact of various media (lactic acid, acetic acid, etc.) as a result of the interaction of metal ions with the test media [13, 17]. In the literature there are not enough data about interactions of d-metals and LA under approximately physiological conditions, and at the level of micro-molar concentration at which they are present in human body.

Products of interaction of M(II) d-biometal ions (Cu, Co, Mn) and toxic Cd(II) ion with LA were investigated at milli-molar and micro-molar level, under approximately physiological conditions by FTIR and ESI-MS spectroscopy.

EXPERIMENTAL

Experimental procedure for FTIR characterization of M(II)–LA interactions.

The solid products of the M(II)-LA interaction were obtained by mixing a solution of M(II) ions, and a ligand in a molar ratio of 1:2 in favor of the ligand, at room temperature, under conditions in which the hydroxide is not precipitated (pH~5.5 for Cu, and approximately physiological pH for others M(II) ions), and separated by centrifugation after 7 days. FTIR spectra were recorded on a FTIR instrument Bomem MB-100 (Hartmann & Braun, Canada), with a DTGS/KBr (deuterated triglycine sulfate/KBr) detector in the wave number range of 4000-400 cm⁻¹, and were processed with ACD/Labs 10.08 software.

Experimental procedure for ESI-MS characterization of M(II)–LA interactions.

Binary solutions M(II)–LA were prepared by mixing stock solutions of M(II) ion (100 μmol/L) and ligand (100 μmol/L) in various proportions in order to obtain different metal/ligand ratios. ESI-MS analysis was performed 30 min after mixing without pH adjustment.

ESI-MS analysis of the model solutions was performed in negative ionization mode by using LCQ DECA Ion Trap mass spectrometer (Thermo Finnigan, USA). ESI-MS spectra and LOOP chromatograms (total ion current chromatograms of loop injected samples) were processed with Xcalibur LCQ Advantage 1.4 software. M(II) ion-ligand interaction strength was estimated by comparing the areas of ESI-MS ion current chromatograms for pure ligand solution (P₁) and M(II)–ligand solution (P₂), their relative difference being expressed as:

$$\Delta P = \frac{P_1 - P_2}{P_1} \times 100\% \quad (1)$$

The value of ΔP is actually the fraction of the ligand involved in ion-ligand interaction so that the larger ΔP value indicates stronger interaction and increased binding of M(II) ions to ligand on micromolar level [18, 19].

RESULTS AND DISCUSSION

FTIR

FTIR spectrum of LA is characterized by the presence of absorption bands of carbonyl group (Figure 1). The band at 2633 cm⁻¹ originates from the intra-molecular hydrogen bonds. The band appearing at 2500-3300 cm⁻¹ can be attributed to vibrations of –O–H from –COOH group, while the band of free –O–H group appears at 3230-3550 cm⁻¹. Together, these bands cover the region 2500-3550 cm⁻¹, and thus cover bands that originate from the C–H vibration. FTIR spectrum of LA is characterized by a strong band at 1730 cm⁻¹ ν(C=O) and bands at 1430 cm⁻¹ ν(C–O–H in plane), 1240 cm⁻¹ ν(C–O), i 930 cm⁻¹ ν(C–O–H out of plane) [20, 21].

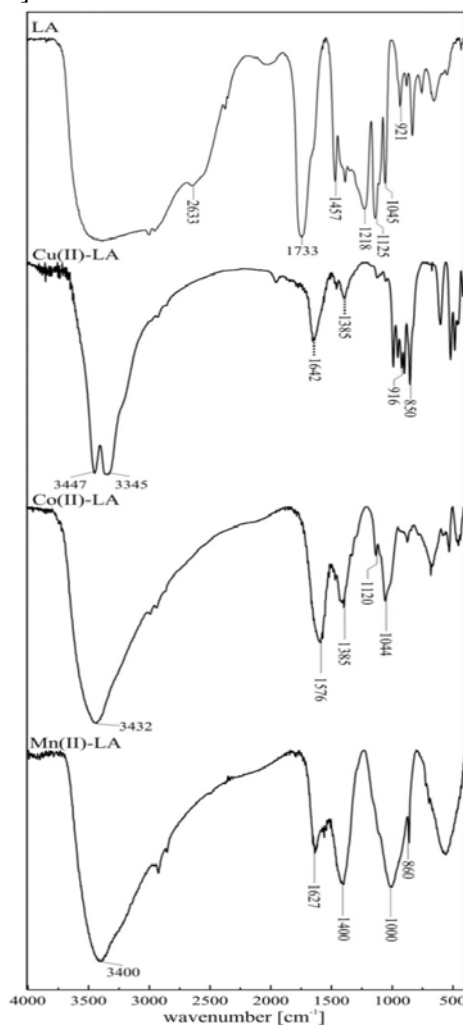


Fig. 1. FTIR spectra of LA, and solid products of interactions of M(II) d-biometal ions with LA.

The FTIR spectra of the obtained solid products of the interaction of the investigated M(II) d-biometal ions with lactic acid are shown in Fig. 1. The disappearance of the intra-molecular hydrogen bond band indicates potential interaction between M(II) ions and O-donor atoms of the ligand. The shifts of $\nu(\text{C}=\text{O})$ band ($\nu_{\text{asym}}(\text{C}=\text{O})$) and $\nu(\text{C}-\text{O}-\text{H})$ band ($\nu_{\text{sym}}(\text{C}-\text{O})$) are very indicative since frequencies of $\nu_{\text{asym}}(\text{C}=\text{O})$ and $\nu_{\text{sym}}(\text{C}-\text{O})$ are the main features of transition metal complexes with carboxylate ligands. The difference $\Delta\nu = \nu_{\text{asym}}(\text{COO}) - \nu_{\text{sym}}(\text{COO})$ may be used to determine the coordination of M(II) ion with O-donor atoms of LA carboxylic group [1, 8, 22-24]. In the investigated model systems *Cu(II)-LA*, *Co(II)-LA* and *Mn(II)-LA* the shifts of $\nu_{\text{asym}}(\text{C}=\text{O})$ bands were to 1642 cm^{-1} , 1576 cm^{-1} and 1627 cm^{-1} respectively; and the shifts of $\nu_{\text{sym}}(\text{C}-\text{O})$ bands were to 1385 cm^{-1} , 1385 cm^{-1} and 1400 cm^{-1} , respectively. The $\Delta\nu$ values of 257 cm^{-1} (*Cu(II)-LA*), 191 cm^{-1} (*Co(II)-LA*) and 221 cm^{-1} (*Mn(II)-LA*) indicate that lactic acid behaves as a monodentate ligand [10, 11, 15, 20, 22].

The investigated system with the toxic Cd(II) ion behaved spectroscopically in a similar way to the system with Mn(II) ion, probably because these two ions are spectroscopically similar (full/semi-full d-level) [18, 23, 24].

The strength of metal-ligand interactions according to the position of R-C-O---M vibrations,

based on values of $\Delta\nu$, decreases in the series $\text{Co(II)} > \text{Cu(II)} \sim \text{Mn(II)/Cd(II)}$ probably due to the physico-chemical properties of the investigated M(II) ions [25, 26].

ESI-MS

Figure 2 shows the ESI-MS ion current chromatogram in the m/z range from 88 to 90 and the mass spectrum recorded in negative ionization mode for the loop injection of lactic acid at a flow rate of $100\text{ }\mu\text{L}/\text{min}$. One of the most prominent peaks in the mass spectrum of LA was that of lactate anion $[\text{LA}-\text{H}]^-$ at $m/z = 89$ with relative intensity of 100% and it served for adjusting optimal working conditions of the instrument. Ions $[\text{LA}-\text{MeOH}]^-$ at $m/z = 121$ and $[\text{2LA}-\text{H}]^-$ dimer at $m/z = 178$ could also be identified.

Figure 3 shows the ESI-MS ion current chromatogram in the m/z range from 88 to 90 and the mass spectrum recorded in negative ionization mode for the loop injection of LA with Cu(II) ion at a flow rate of $100\text{ }\mu\text{L}/\text{min}$. In comparison to the mass spectrum in Figure 1, the peak intensities for $[\text{LA}-\text{H}]^-$ and $[\text{2LA}-\text{H}]^-$ decrease by about 20% and 10%, respectively. However, new ionic species appeared and we could identify $[\text{LA}+\text{Cu}]^-$ at $m/z = 152$. These spectral changes indicate that interactions between Cu(II) ion and LA occurred even at the micromolar level.

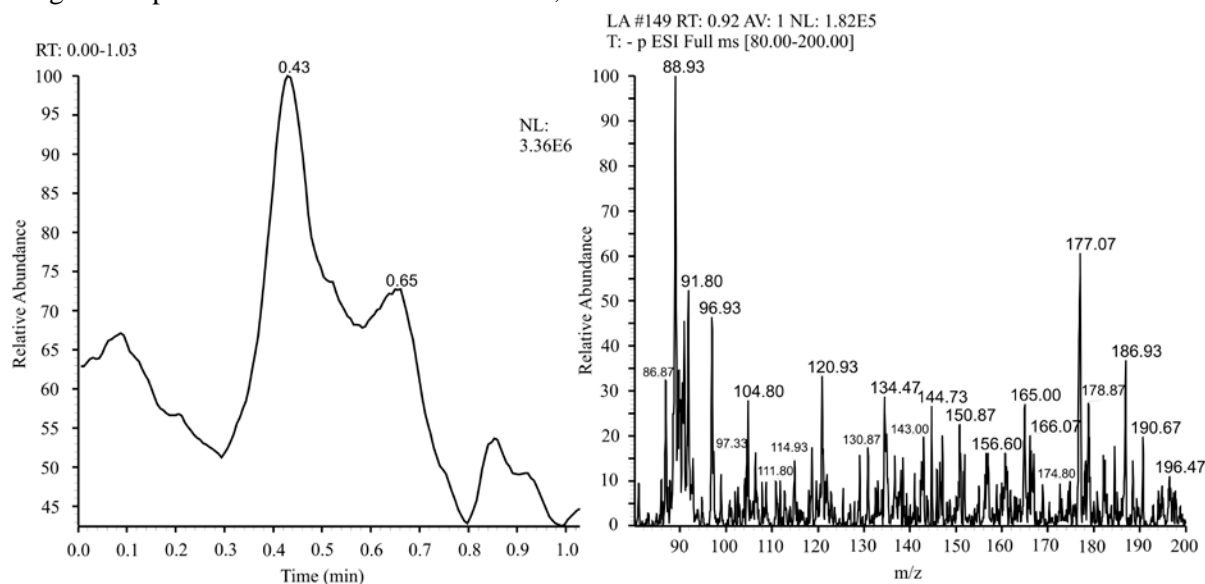


Fig. 2. ESI-MS ion current chromatogram in the m/z range from 88 to 90 and mass spectrum recorded in negative ionization mode for the loop injection of LA at a flow rate of $100\text{ }\mu\text{L}/\text{min}$ ($c_{\text{LA}} = 5.00\text{ }\mu\text{mol}/\text{L}$, solvent: $\text{MeOH}/\text{H}_2\text{O} = 50/50$).

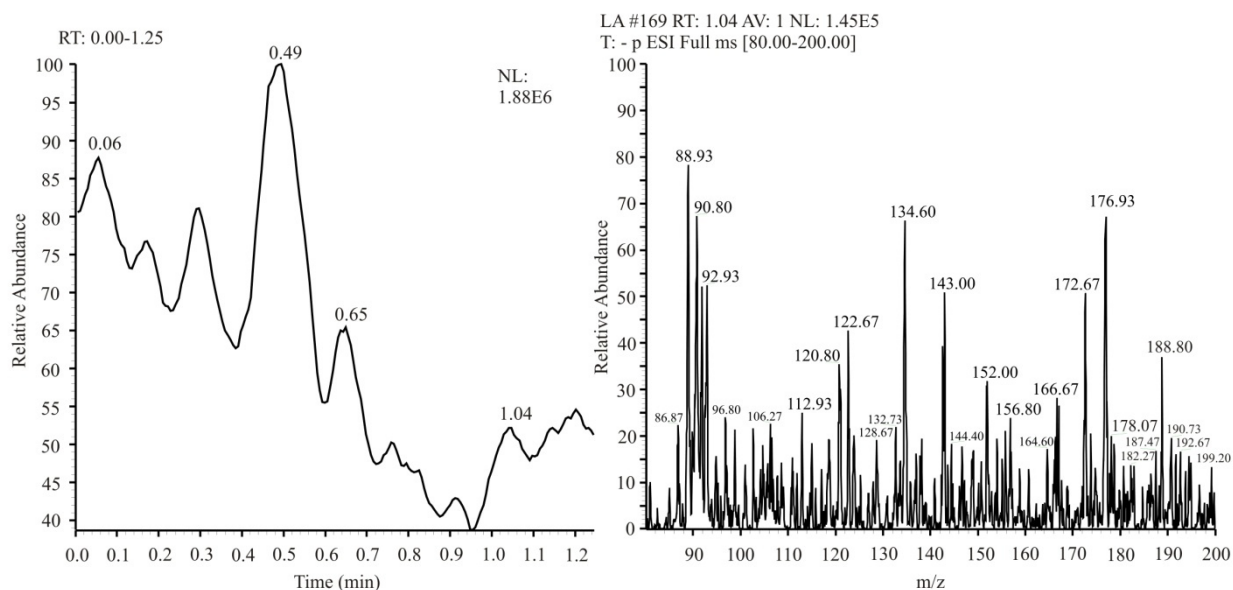


Fig. 3. ESI-MS ion current chromatogram in the m/z range from 88 to 90 and mass spectrum recorded in negative ionization mode for the loop injection of LA with Cu(II) ion at a flow rate of $100 \mu\text{L}/\text{min}$ ($c_{\text{LA}} = 1.00 \mu\text{mol}/\text{L}$, $c_{\text{Cu(II)}} = 9.00 \mu\text{mol}/\text{L}$, solvent: MeOH/H₂O = 50/50).

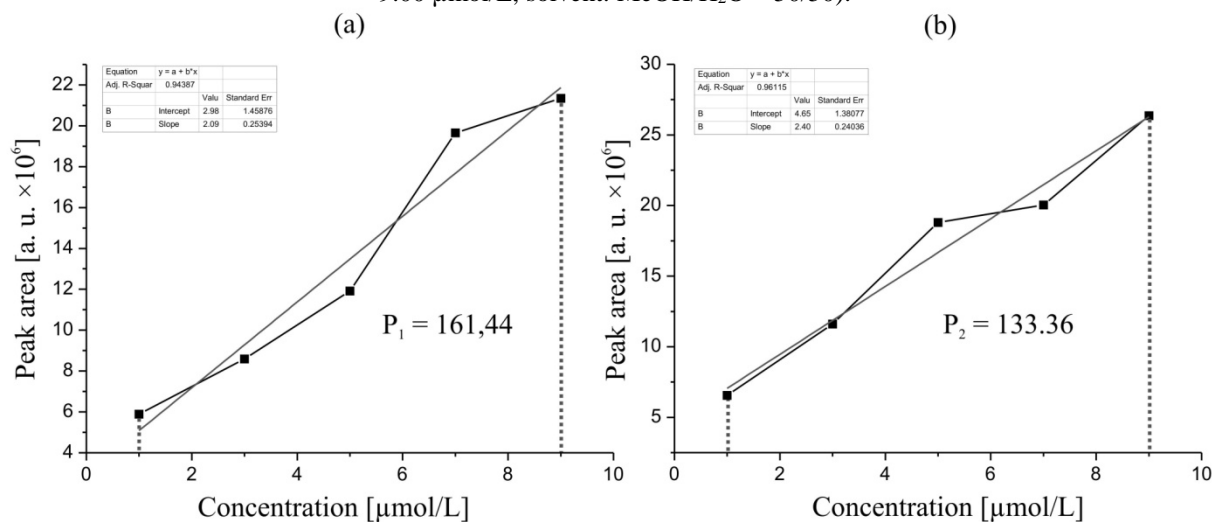


Fig. 4. Plot of the peak areas of the ESI-MS chromatograms of the loop injection vs. LA concentration for pure LA (a) and Cu(II)–LA system (b).

The quantitative analysis of the lactate anion, [LA–H]⁻, was performed by injecting exact volumes of LA solution of known concentration by using LOOP apparatus. Areas below LOOP chromatograms (Fig. 4a and b) were determined with Xcalibur software. Calibration curve for LA was obtained by linear fitting of areas in LOOP chromatographic peaks for the m/z range 88-90 as a function of LA concentration. Integral area value for the LA system was $P_1 = 164.44$ ($R^2 = 0.9439$, Fig. 4a), and for the Cu(II)–LA system the value was $P_2 = 133.36$ ($R^2 = 0.9612$, Fig. 4b).

The obtained results for investigated model systems were analysed as mentioned before for the the Cu(II)-LA model system [18]. The values of the sub-integral areas of the investigated binary

systems and their ΔP (Eq. 1) values are shown in Table 1.

Table 1. Values of sub-integral areas and their ΔP values

	LA	Cu-LA	Co-LA	Mn-LA	Cd-LA
P [a.u.]	161.44	133.36	107.55	146.17	147.84
R ²	0.9439	0.9612	0.9439	0.9468	0.9457
ΔP [%]	/	17.39	33,38	9.46	8.42

The area under the peaks in the LOOP chromatograms in the presence of the investigated metal ions is lower than the analog area of the lactic acid without metal ions, which is in accordance with results of other similar studies [18, 19]. These results indicate that there is considerable interaction of M(II)-LA at the micromolar level, which decreases in the order: Co(II)-LA > Cu(II)-LA > Mn(II)-LA ~ Cd(II)-LA.

According to the results of spectroscopic examinations it can be noticed that the interaction is most pronounced between Co(II) ion and lactic acid and less pronounced between the toxic Cd(II) ion and lactic acid, because Cd(II) ion has a lower affinity for O-donor atoms, considering that it is a softer acid in regard to d-metals (HSAB theory) [6, 25, 26].

According to results, substitution of metals with similar physico-chemical properties of the active centers of some biological systems (e.g. enzymes, hard mineral and different media) on micro-molar level could be expected [13, 17].

CONCLUSION

The spectroscopic investigations showed that lactic acid interacts with the investigated M(II) d-biometal ions and the toxic Cd(II) ion at both investigated levels of concentration. FTIR characterization of the isolated products of interaction of M(II)-LA showed that LA acts as a monodentate ligand. Lower values of surface of ESI-MS LOOP chromatograms of the examined system of M(II)-LA compared to the pure ligand (LA) indicated that the interaction between M(II) d-biometal ions or the toxic Cd(II) ion, and lactic acid occurs at the micro-molar level. According to the spectroscopic results Co(II)-LA interaction was the most pronounced compared to the other investigated metals..

Acknowledgement: This work was supported by the Ministry of Education, Science and Technological Development of the Republic of Serbia (Grants no. TR31060 and TR34008).

REFERENCES

1. N. S. Krstić, R. S. Nikolić, M. N. Stanković, N. G. Nikolić, D. M. Đorđević, *Trop. J. Pharm. Res.*, **14(2)**, 337 (2014).
2. N. A. El-Ragehy, M. Abdelkawy, A. El-Bayoumy, *Anal. Lett.*, **27(11)**, 2127 (1994).
3. S. S. Mitić, G. Z. Miletić, A. N. Pavlović, B. B. Arsić, V. V. Živanović, *J. Serb. Chem. Soc.*, **73(8-9)**, 879 (2008).
4. R. R. Crichton, *Biological Inorganic Chemistry An Introduction*, Elsevier, 2008.
5. N. Krstić, R. Nikolić, M. Krstić, *Hem. preg.*, **55(6)**, 154 (2014) (in Serbian).
6. B. Kaličanin, R. Nikolić, in: *Wide spectra of quality control*, Akyr, Isin (eds), Croatia: InTech, Rijeka, 2011, p. 211.
7. J. M. Jovanović, R. S. Nikolić, G. M. Kocić, N. S. Krstić, M. M. Krsmanović, *J. Serb. Chem. Soc.*, **78(2)**, 197 (2013).
8. C. Dendrinou-Samara, G. Tsotsou, L. V. Ekateriniadou, A. H. Kortsaris, C. P. Raptopoulou, A. Terzis, D. A. Kyriakidis, D. P. Kessissoglou, *J. Inorg. Biochem.*, **71**, 171 (1998).
9. R. P. Sharma, S. Singh, A. Singh, V. Ferreti, *J. Mol. Struct.*, **918**, 188 (2009).
10. R. Carballo, B. Covelo, S. Balboa, A. Castiñeiras, J. Niclós, *Z. Anorg. Allg. Chem.*, **627**, 948 (2001).
11. R. Carballo, A. Castiñeiras, S. Balboa, B. Covelo, J. Niclós, *Polyhedron*, **21**, 2811 (2002).
12. S. Spasić, Z. Jelić-Ivanović, V. Spasojević-Kalimanovska, *Fundamentals of biochemistry*, Belgrade, 2000. (in Serbian)
13. R. Nikolić, B. Kaličanin, N. Krstić, *Connect. Tissue Res.*, **53(3)**, 229 (2012).
14. M. Obradović, D. Veselinović, P. Đurđević, *Physicochemical methods of testing the balance of the complexing environments*, Faculty of Philosophy, Niš, Faculty of Physical Chemistry, Belgrade, 1996. (in Serbian)
15. A. A. El-Asmy, E. M. Saad, M. S. El-Shahawi, *Transit. Metal Chem.*, **19**, 406 (1994).
16. J. Piispanen, L. H. J. Lajunen, *Acta Chem. Scand.*, **49**, 241 (1995).
17. R. S. Nikolić, N. V. Radosavljević-Stevanović, T. D. Anđelković, M. N. Stanković, N. S. Krstić, *J. Serb. Chem. Soc.*, **79**, 1395 (2014).
18. R. S. Nikolić, N. S. Krstić, G. M. Nikolić, G. M. Kocić, M. D. Cakić, D. H. Anđelković, *Polyhedron*, **80**, 223 (2014).
19. D. H. Anđelković, R. S. Nikolić, D. Z. Marković, T. D. Anđelković, G. M. Kocić, Z. B. Todorović, A. Lj. Bojić, *J. Serb. Chem. Soc.*, **78(1)**, 137 (2012).
20. A. P. B. Lever, *Inorganic electronic spectroscopy 1, 2*, Mir, Moskva, 1987.
21. R. Drago, *Physical methods in chemistry 1, 2*, Mir, Moskva, 1981.
22. K. Nakamoto, *Infrared and Raman spectra of inorganic and coordination compounds, Part A and B*, 6th ed., John Wiley and Sons Inc., New Jersey, 2009.
23. F. Dimiza, F. Perdih, V. Tangoulis, I. Turel, D. Kessissoglou, G. Psomas, *J. Inorg. Biochem.*, **105**, 476 (2011).
24. M. A. Agotegaray, M. Dennehy, M. A. Boeris, M. A. Grela, R. A. Burrow, O. V. Quinzani, *Polyhedron*, **34**, 74 (2012).
25. A. Cotton, G. Wilkinson, *Advanced inorganic chemistry*, 3rd ed., John Wiley and Sons, New York-London-Sydney, 1976.
26. C. E. Mortimer, *Chemistry*, 5th ed. Litton Educational Publishing Inc., Belmont, California 94002, 1983.

ИЗСЛЕДВАНЕ НА ВЗАИМОДЕЙСТВИЕТО МЕЖДУ МЛЕЧНА КИСЕЛИНА И M(II) d-МЕТАЛИ (Cu, Co, Mn, Cd) НА МИЛИГРАМОВО И МИКРОГРАМОВО НИВО ЧРЕЗ FTIR И ESI-MS АНАЛИЗ

Н.С. Кръстич^{1*}, Р.С. Николич¹, В.Д. Димитриевич¹, Д.М. Джорджевич¹, М.Н.Станкович¹, И.М. Кръстич², М.Г. Николич¹

¹Департамент по химия, Факултет по науки и математика, Нишки университет, Вишеградска 33, 18000 Ниш, Сърбия

²Факултет по безопасност на труда, Нишки университет, Чарноевича 10, 18000 Ниш, Сърбия

Постъпила на 6 ноември, 2016 г.; коригирана на 30 декември, 2017 г.

(Резюме)

Взаимодействието на M(II) d-биометални йони (Cu, Co, Mn) и токсичния Cd(II) йон с млечна киселина, която се намира в човешкото тяло в резултат на поглъщане или като продукт от биологични процеси на мили- или микромолярно ниво, е изследвано при приблизително физиологични условия с помощта на FTIR и ESI-MS спектроскопия. Установено е, че млечната киселина в изследваната моделна система се отнася като монодентатен лиганд; тя взаимодейства на всички концентрационни нива и най-силно изразеното взаимодействие е с Co(II) йон.

Correlation analysis of physicochemical parameters of the ecological status: a case study of Ibar River (Serbia)

L. M. Takić¹, B. Ž. Todorović^{1*}, A. S. Zdravković¹, N. M. Elezović², N. V. Živković³

¹Faculty of Technology, University of Niš, Serbia

²Faculty of Technical Sciences, University of Priština, Serbia

³Faculty of Occupational Safety, University of Niš, Serbia

Received: February 2, 2017; Accepted: December 15, 2017

The aim of this work is to determine the mutual dependence of selected physicochemical and geochemical parameters using correlation analysis and to assess the ecological status of water quality. The goal of this method is the faster and more precise interpretation of monitoring data, identification of pollution sources, and assessment of river water quality. In this regard, we used the water quality parameters of river Ibar from the monitoring station "Raška". This station is the most representative one for determining water quality, because it is located in the middle course of the Ibar River and is under the heaviest pollutant loads. Comparative analysis showed a deviation of the measured values of biochemical oxygen demand (BOD₅), total organic carbon (TOC), NH₄⁺ and PO₄³⁻ from the prescribed reference values, which indicates the presence of organic matters in the river Ibar. This water body was attributed moderate ecological status (class III), while the comparison with the limit values of priority and priority hazardous substances indicated the lack of good chemical status. Based on correlation analysis, it can be concluded that there is pluvial erosion and that oxygen regime is influenced by changes in atmospheric temperature rather than by organic pollutants.

Keywords: Correlation analysis, Ibar River, Ecological status, Chemical status

INTRODUCTION

Current problems of pollution of watercourses in the Republic of Serbia require an ecological status assessment, stressing on the significance of achieving sustainable water management principles set by the Directive 2000/60EC and preserving the environment [1]. Surface water quality is determined by natural processes (atmospheric conditions, level of precipitation and soil erosion), human activities (urbanization, industrial and agricultural activities) and increased exploitation of water resources [2, 3]. Discharges of industrial and municipal wastewater, as well as agricultural effluents are considered persistent sources of pollution [4]. The quality of surface waters faithfully reflects the impact of human activities, particularly in terms of impaired quality of watercourses and characteristics of aquatic ecosystems. According to the ranking of eighteen major river flows, the Ibar River has been classified as one of the most polluted surface waters in Serbia [5]. The Ibar River springs under Hajla Mountain in eastern Montenegro. Being 280 km long and with basin surface of 8060 km², it is the longest and the most important tributary of the Western Morava River [6]. In its middle course, the Ibar River becomes the recipient of unpurified industrial wastewater from the power plant "Obilic", the fertilizer factory in Kosovska Mitrovica and

Mining, Metallurgical and Chemical conglomerate (MMCC) "Trepca". In this area, water quality of the Ibar River is also influenced by the factory "Leposavic" (processing of zinc and lead) and large number of flotation tailing dumps [7]. Ibar gorge is naturally predisposed to develop erosion and torrent processes that are conditioned by geomorphological conditions of the terrain (steep reliefs, steep slopes), geological conditions of the terrain (high erodibility rocks, intensive sediment yield) and poor protection of hillside cliff vegetation (poorly afforested area, bare land).

The Republic Hydrometeorological Service of Serbia (RHSS) monitors the water quality of the Ibar River at the measuring stations "Batrage", "Raška" and "Kraljevo". Monitoring station "Raška" is the most representative one in terms of determining water quality due to the fact that it is located in the middle course of the Ibar River, with the highest pollutant loads.

The aim of this paper is to assess water quality of the Ibar River at the monitoring station "Raška" by determining ecological and chemical status and to identify pollution on the basis of correlations between water quality parameters with the aid of multivariate statistical analysis.

EXPERIMENTAL

The enactment of the Regulation on establishment of surface and groundwater bodies

* To whom all correspondence should be sent.

E-mail: vinarce2001@yahoo.com

and the Regulation on the parameters of ecological and chemical status of surface waters and parameters of chemical status and quantitative status of groundwaters enabled the conditions for RHSS monitoring in accordance with the requirements of the EU Water Framework Directive [8-10].

Ecological status indicates the quality of the structure and functioning of an aquatic ecosystem joined to surface waters and classification in line with the special Regulation [8]. Ecological status of the river is classified as Excellent (Class I), Very good (Class II), Good (Class III), Poor (Class IV) and Very poor (Class V) according to chemical and physicochemical quality elements which are significant for biological elements of a given surface water and surface water body [9]. According to the Regulation on establishment of surface and groundwater bodies, the Ibar River is classified as aquatic water body of the Type-2 (large rivers, dominance of middle layers). Current regulation defines target allowable concentrations of certain parameters for given classes of ecological status of surface waters (Table 1).

For the purpose of assessment of the current water quality of the Ibar River at the monitoring station "Raška", the ecological and chemical status was determined in accordance with the Regulation on the parameters of ecological and chemical status of surface waters and parameters of chemical status and quantitative status of groundwaters and regulation on limit values for priority hazardous substances which pollute surface water and the deadlines for achieving them [10, 11]. The paper analyzes the latest available data by RHSS for 13 water quality parameters, those being: the flow rate (Q), water temperature (T), pH, suspended matter (SM), dissolved oxygen (DO), BOD₅, TOC, chemical oxygen demand (COD), NH₄⁺, PO₄³⁻, Cl⁻ and P [12].

The reference condition indirectly defines the goal that aquatic body must achieve. Therefore, the values of these parameters are compared with reference values which define the condition of a water body in which changes of physicochemical and biological parameters are considered negligible, i. e., there is a low level of changes in the natural water quality of the Ibar River [13].

Multivariate statistical methods were used to characterize and evaluate water quality and they are a useful tool for determination of weather and seasonal variations due to natural and

anthropogenic impacts. Correlation analysis explains the connection of parameters by monitoring the basic factors that are not directly visible. High correlation of data in the analysis (positive or negative) represents a high possibility that the data are influenced by the same factors, while relatively non-correlated data are influenced by different factors, which is the axiom of the analysis. The software package *Statistica7.0* is applied.

The indicators of the water quality are mutually correlated, and Pearson's correlation coefficient was used for measurement of the intensity of their stochastic connection. Pearson's correlation coefficient is the measurement of the intensity and direction of linear connection of the two parameters [14]. The obtained matrix of Pearson's correlation coefficient enables identification of dependence, that is, strength and direction of connections between variables [15].

Table 1. Chemical limits of the classes of ecological status for aquatic bodies of Type 2.

Parameter	Units	I-II	II-III	III-IV	IV-V
pH	-	6.5-8.5	6.5-8.5	6.5-8.5	<6.5/>8.5
DO	[mg L ⁻¹]	8.5	7.0	5.0	4.0
BOD ₅	[mg L ⁻¹]	1.8	4.5	6.0	20.0
TOC	[mg L ⁻¹]	2.0	5.0	7.0	23.0
NH ₄ ⁺	[mg L ⁻¹]	0.05	0.1	0.8	1.0
NO ₃ ⁻	[mg L ⁻¹]	1.5	3.0	6.0	15.0
PO ₄ ³⁻	[mg L ⁻¹]	0.02	0.1	0.2	0.5
P	[mg L ⁻¹]	0.05	0.2	0.4	1.0
Cl ⁻	[mg L ⁻¹]	50.0	100	-	-

Basic characteristics of Pearson's correlation coefficient (r) are as follows:

- The value of the coefficient is within the interval from -1 to 1. If r is negative, the connection between variables is also negative (high values of one variable correspond to low values of the second variable); if r is positive, the connection between variables is positive (high values of one variable correspond to high values of the second variable; low values of one variable correspond to low values of the second variable).
- If $r = \pm 1$, there is a complete linear connection between two variables.
- If the variable is in correlation with itself, then $r = 1$.
- If $r = 0$, two variables are uncorrelated, which does not mean that they are independent.
- If two variables are independent, then $r = 0$ [14].



Figure 1. Location of the monitoring station „Raška“.

In this paper, we have monitored the value of Pearson's correlation coefficient that is higher or equal to 0.8, which corresponds to strong and significant mutual dependence between the parameters. Monitoring station "Raška", 93 km away from the mouth of the West Morava River, is the most exemplary one for the assessment of the Ibar River water quality taking into account its undeniable pollutant loads and its status of the major hydrological station (Figure 1).

RESULTS AND DISCUSSION

The values of hydrological, chemical and physicochemical parameters of Ibar River water quality at the monitoring station "Raška", as well as their mean values are presented in Table 2. Measured pH values show the basic character of the Ibar River water, whereas parameters with the highest variability are Q, SM, BOD₅ and COD. High volume discharge of the Ibar River from January to April ($Q > 50 \text{ m}^3 \text{ s}^{-1}$) was conditioned by precipitation or snow melting (Table 2).

Table 2. Values of hydrological, physicochemical, and chemical [mg L^{-1}] parameters for monitoring station "Raška"

Parameter	Sampling date											Average
	16.01.	14.02.	09.03.	08.05	18.06.	08.07.	19.08.	02.09.	08.10.	07.11.	16.12.	
Q [$\text{m}^3 \text{ s}^{-1}$]	42.4	32	40.1	35.3	53.9	15.9	11.4	14.7	17.6	14.7	19.4	27.0
T [$^{\circ}\text{C}$]	4.2	5.2	8.0	14.0	14.0	17.6	18.0	15.2	10.4	10.8	3.0	10.9
pH	8.4	8.4	8.4	8.5	8.4	8.4	8.4	8.4	8.4	8.4	8.4	8.4
SM	1.9	14.0	47.0	55.0	11.0	7.0	24.0	11.0	23.0	4.0	3.0	19.8
DO	11.0	10.7	10.9	8.8	9.9	8.3	7.7	9.5	8.8	9.0	12.6	9.7
BOD ₅	nd	2.8	2.6	3.4	2.9	1.4	3.1	1.7	3.1	2.0	2.4	2.5
TOC	7.3	5.2	4.7	4.3	3.7	3	3.7	3.2	4.1	4.2	3.1	4.2
HPK	nd		12.4	11.0	nd	11.2	nd	3.5	10.0	6.0	8.0	8.9
NH ₄ ⁺	0.8	0.4	0.4	0.1	0.2	0.3	0.2	0.5	0.1	0.1	1.0	0.3
NO ₃ ⁻	1.5	1.8	1.6	0.6	1.1	1.4	2.0	0.2	1.0	0.4	0.7	1.1
PO ₄ ³⁻	0.4	0.1	0.2	0.1	0.1	0.1	0.2	0.2	0.1	0.1	0.1	0.1
TP	0.4	0.2	0.2	0.5	0.1	0.1	0.2	0.2	0.2	0.2	0.2	0.2
Cl ⁻	10.0	9.0	8.0	9.0	7.0	15.0	20.0	16.0	10.0	16.0	12.0	12.0

Nd: not detected

Table 3. The comparison between the measured values of physicochemical parameters and their reference values.

Physicochemical parameters	Comparison
pH	within the limits
DO	within the limits
BOD ₅	deviates
TOC	deviates
NH ₄ ⁺	deviates
NO ₃ ⁻	within the limits
PO ₄ ³⁻	deviates

By comparing the values of the physicochemical parameters with their reference values, the deviation of BOD₅, TOC, NH₄⁺ and PO₄³⁻ from the allowed limits was determined (Table 3). Organic matter and nutrients loading in the middle course of the Ibar River is attributed to the inflow of a large number of untreated municipal and industrial wastewater as well as to coastal erosion. Ecological status, according to the European Water Framework Directive, is an expression of the quality of the structure and functioning of aquatic systems associated with a surface water body [9]. The results of ecological status assessment in terms of physicochemical parameters of the water quality at the monitoring station "Raska" are presented in Table 4.

Table 4. Ecological status of the Ibar River at the monitoring station "Raška".

Physicochemical parameters	Ecological status
pH	I
DO	I
BOD ₅	II
TOC	II
NH ₄ ⁺	III
NO ₃ ⁻	I
PO ₄ ³⁻	III

The ecological status of the Ibar River water quality at the monitoring station "Raška" is classified as Moderate (class III), due to exceeding values of parameters that define good status NH₄⁺, PO₄³⁻ and TP.

The values of the indicators of surface water pollution by organic matter (BOD₅ and TOC) exceed the reference values for an excellent ecological status and, therefore, correspond to a good ecological status. NH₄⁺ occurs due to bacterial decomposition of dissolved organic matter that comes into the recipient by municipal water discharge or rinsing of agricultural land [4, 16]. If the pH is greater than 9, ammonia in the molecular form is toxic to the living world [16, 17]. The largest part of the phosphorus pollution of surface

water appears as a consequence of municipal and industrial wastewater treatment [4].

The assessment of the chemical status based on the comparison between the concentration of priority and priority hazardous substances and their allowed average year concentrations (PGK) and maximum allowable concentration (MDK), in accordance to the Resolution, is presented in Table 5.

When assessing chemical status, the first and the second group of environmental quality standards (EQS) were taken into account; therefore, EQS implies the concentration of individual priority substance or group of priority substances in surface waters that should not be exceeded with the aim to protect the environment and human health. The concentrations of priority substances such as Cd, Pb and Hg and their compounds exceed the limits prescribed by EQS, which makes us conclude that a good chemical status of the Ibar River was not achieved. Increased concentrations of heavy metals in this part of the Ibar River are the result of the confluence of mining and industrial wastewater, as well as wastewater from flotation and metallurgical dumps.

Heavy metals dissolved in surface waters are less stable and extremely toxic due to their ability to accumulate in the aquatic organisms, thus reaching the food chain [18-20]. The matrix of Pearson's coefficients of water quality parameters of the Ibar River at the monitoring station "Raška" is presented in Table 6. A strong negative correlation between DO and T ($r = -0.86$) confirms the theory which claims that oxygen becomes more soluble in water at low temperatures, while a strong positive correlation between DO and NH₄-N ($r = 0.9$) is explained by ammonification of nitrogen circulation cycle which indicates the organic origin of nitrogen compounds in the aquatic ecosystem [21]. Low correlation of DO with BOD₅ and COD indicates that the oxygen regime is under a greater influence of atmospheric conditions rather than the presence of organic pollutants in water. The matrix shows a strong positive correlation between Q, pH and SM ($r = 0.97$, $r = 0.91$, respectively), as expected, because the content of suspended matter increases in case of higher flows due to erosion and sediment resuspension [14]. Great number of phosphorus transformations occur in the fresh waters, and for this reason organic and inorganic forms dissolved in water make the total phosphorus. It is important that both high and low pH values can influence the complexation of

Table 5. Assessment of chemical status according to the concentration of priority and priority hazardous substances

Substances	PGK [$\mu\text{g L}^{-1}$]	MDK [$\mu\text{g L}^{-1}$]	Chemical status
<i>Organic</i>			
Alachlor	$<2 \times 10^{-3}$	$<2 \times 10^{-3}$	good
Anthracen	$<5 \times 10^{-4}$	$<5 \times 10^{-4}$	good
Atrazine	$<1 \times 10^{-3}$	$<1 \times 10^{-3}$	good
Chlorfenvinphos	$<1 \times 10^{-2}$	$<1 \times 10^{-2}$	good
Chlorpyrifos	$<5 \times 10^{-3}$	$<5 \times 10^{-3}$	good
Cyclodiene pesticides	$<1 \times 10^{-2}$	-	good
Total DDT	$<1 \times 10^{-3}$	-	good
p, p'-DDT	$<1 \times 10^{-3}$	-	good
Diuron	$<2 \times 10^{-3}$	$<2 \times 10^{-3}$	good
Endosulfan	$<5 \times 10^{-3}$	$<5 \times 10^{-3}$	good
Fluoranthene	$<5 \times 10^{-4}$	$<5 \times 10^{-4}$	good
Hexachlorbenzene	nd	$<1 \times 10^{-3}$	good
Hexachlorobutadiene	nd	$<1 \times 10^{-3}$	good
Hexachlorocyclohexane	$<1 \times 10^{-3}$	$<1 \times 10^{-3}$	good
Isoproturon	$<1 \times 10^{-3}$	$<1 \times 10^{-3}$	good
Octylphenol	$<1 \times 10^{-3}$	-	good
4 - (1,1, 3,3 - Tetramethylbutyl)	nd	6.1×10^1	good
Phenol	$<5 \times 10^{-4}$	$<5 \times 10^{-4}$	good
Naphthalene	$<1 \times 10^{-3}$	$<1 \times 10^{-3}$	good
(4- (para) Nonylphenol)	$<1 \times 10^{-3}$	$<1 \times 10^{-3}$	good
Pentachlorobenzene	$<1 \times 10^{-3}$	-	good
Pentachlorophenol	3×10^{-2}	3×10^{-2}	good
Terbutryne	nd	3×10^{-1}	good
<i>Inorganic</i>			
Ni	2×10^1	3.4×10^1	good
Pb	7×10^0	2.4×10^1	good
Cd	4×10^{-1}	1.4×10^0	good is not achieved
Hg	5×10^{-2}	1.0×10^{-1}	good

nd-not detected

Table 6. Correlation matrix of water quality parameters at the monitoring station "Raška"

	Q	T	pH	SM	DO	BOD ₅	HPK	NH ₄ ⁺	NO ₃ ⁻	PO ₄ ³⁻	TP
Q	1.00	0.03	0.97	0.91	0.05	0.75	0.52	0.21	0.05	0.34	0.93
T		1.00	0.21	0.26	0.86	0.32	0.11	0.57	0.18	0.05	0.16
pH			1.00	0.93	0.22	0.66	0.43	0.34	0.13	0.32	0.96
SM				1.00	0.36	0.79	0.48	0.47	0.05	0.01	0.97
DO					1.00	0.03	0.26	0.90	0.25	0.16	0.20
BOD ₅						1.00	0.44	0.28	0.07	0.14	0.77
HPK							1.00	0.32	0.81	0.44	0.31
NH ₄ ⁺								1.00	0.13	0.13	0.34
NO ₃ ⁻									1.00	0.31	0.26
PO ₄ ³⁻										1.00	0.04
TP											1.00

phosphorus with the tendency to accumulate by binding to organic matter. At increased flow, there is positive correlation between pH and TP ($r = 0.97$), that is, pH and SM ($r = 0.93$), which indicates that the natural balance of circulating phosphorus significantly depends on the value of these indicators of water quality. Also, the interdependency of matrix parameters DO, T and NH₄⁺, as well as PO₄³⁻ and COD is the consequence of water pollution due to agricultural practices,

appearance of leachates from farms as well as scattered illegal dumps and industrial wastewater discharges into the Ibar River.

The result of parameter correlation analysis results shows the overall synergistic effect of complex biochemical processes occurring in aquatic ecosystems of the Ibar River due to the above mentioned atmospheric and anthropogenic impacts.

CONCLUSION

The ecological status of water quality of the Ibar River at the monitoring station "Raška" is classified as moderate (class III) which is a sign of deviation from the required water quality. Comparative analysis showed that certain parameters, BOD₅, TOC, NH₄⁺ and PO₄³⁻ exceeded their reference values. It was concluded that good chemical status was not achieved, due to the increased concentrations of heavy metals, cadmium, lead and mercury and their compounds which exceed the limits prescribed by EQS.

Multivariate statistical analysis, expressed by the Pearson's coefficients matrix, demonstrates the synergy of correlation between water quality parameters and identifies the pollution sources which have an impact on the ecological status of the Ibar River. The most significant correlations between parameters, i.e. the values of Pearson's coefficient above 0.8, clearly show the cause of impaired water quality and indicate the need to improve the existing monitoring implementation. The importance of preserving and improving the water quality of the Ibar River implies considering the actual quality of water at the monitoring station "Raška", which is affected by the combination of loads due to: weather conditions, catchment pluvial erosion and sediment resuspension, the inflow of mining and industrial wastewater, leachate wastewater from flotation and metallurgical waste dumps. The conducted two-stage methodology, the assessment of water quality and correlation analysis suggest the need for operational monitoring with the aim to monitor the improvement of the water quality of the Ibar River after the implementation of anti-pollution programmes.

Acknowledgements. *The investigations presented in this paper are the part of the research done within the projects No. III 43014 and No. TR 33034, funded by the Ministry of Science and Technological Development of the Republic of Serbia.*

REFERENCES

1. Agency for Environmental Protection of the Republic of Serbia. Status of surface waters, 2015.
2. S. R. Carpenter, N. F. Caraco, D. L. Correll, R. W. Howarth, A. N. Sharpley, V. H. Smith, *Ecol. Appl.*, **8**, 559 (1998).
3. H. P. Jarvie, B. A. Whitton, C. Neal, *Sci. Total. Environ.*, **210**, 79 (1998).
4. M. Vega, R. Pardo, E. Barrado, L. Deban, *Water Res.*, **32**, 3581 (1998).
5. B. Tubić, K. Zorić, B. Vasiljević, J. Tomović, A. Atanacković, V. Marković, M. Paunović (Proc. BALWOIS, Ohrid, Macedonia), 2012.
6. Regulation on determining the spatial plan for special purpose areas of hydropower plants on the river Ibar, *Official Gazette of RS*, 58/2012.
7. M. Barać, N. Vitas, S. Janičijević, Heavy metals and landfills of Trepca in the middle course of the river Ibar, *Ecologica*, **16**, 401 (2009).
8. Regulation on establishment of surface and groundwater bodies, *Official Gazette of Republic of Serbia*, 96/2010.
9. Regulation on the parameters of ecological and chemical status of surface waters and parameters of chemical status and quantitative status of groundwaters, *Official Gazette of Republic of Serbia*, 74/2011.
10. http://ec.europa.eu/environment/water/waterframework/index_en.htm.
11. Regulation on limit values for priority hazardous substances which pollute surface water and the deadlines for achieving them, *Official Gazette of Republic of Serbia*, 24/2014.
12. Results of testing the quality of surface and groundwater for 2013 in: Hydrological Yearbook. Republic Hydrometeorological Service of Serbia, 2014.
13. Regulation on the determination of reference conditions for surface water body types, *Official Gazette of Republic of Serbia*, 67/2011.
14. N. Jaćimović, D. Kostić, S. Grašić, N. Nenadić, *Vodoprivreda*, **46**, 163 (2014).
15. Regulation on the national list of environmental indicators, *Official Gazette of Republic of Serbia*, 37/2011.
16. M. Varol, B. Gökot, A. Bekleyen, B. Sen, *River Res. Appl.*, **28**, 1428 (2012).
17. M. Saeedi, S. Daneshvar, A. R. Karbassi, *Int. J. Env. Sci. Tech.*, **1**, 135 (2004).
18. M. Gallo, A. Trento, A. Alvarez, H. Beldoménico, D. Campagnoli, *Water, Air, Soil Pollut.*, **174**, 367 (2006).
19. G. M. Morrison, D. M. Revitt, J. B. Ellis, *Water Sci. Technol.*, **22**, 53 (1990).
20. M. Varol, B. Sen, *Environ. Monit. Assess.*, **159**, 543 (2009).
21. K. P. Singh, A. Malik, D. Mohan, S. Sinha, *Water Res.*, **38**, 3980 (2004).

КОРЕЛАЦИОНЕН АНАЛИЗ НА ФИЗИКОХИМИЧНИТЕ ПАРАМЕТРИ НА ЕКОЛОГИЧНИЯ СТАТУС: ПРИМЕР С РЕКА ИБАР (СЪРБИЯ)

Л.М. Такич¹, Б.Ж. Годорович^{1*}, А. С. Здравкович¹, Н. М. Елезович², Н.В. Живкович³

¹Технологичен факултет, Нишки университет, Сърбия

²Факултет по технически науки, Университет на Прищина, Сърбия

³Факултет по професионална безопасност, Нишки университет, Сърбия

Постъпила на 2 февруари, 2017 г.; приета на 15 декември, 2017 г.

(Резюме)

Предмет на настоящата работа е определянето на взаимозависимостта между избрани физикохимични и геохимични параметри с помощта на корелационен анализ и оценката на екологичния статус на качеството на водата. Разработката цели по-бързо и по-точно интерпретиране на мониторинговите данни, идентифициране на източниците на замърсяване и оценка на качеството на речната вода. За целта са използвани данните за качеството на водата от мониторинговата станция „Рашка“. Тази станция е най-представителна за оценка на качеството на водата, тъй като се намира в средното течение на река Ибар и е подложена на най-тежко замърсяване. Сравнителният анализ показва отклонение на измерените стойности за биохимично необходим кислород, тотален органичен въглерод, NH_4^+ и PO_4^{3-} от предписаните референтни стойности, което сочи за наличие на органична материя в реката Ибар. Водата в тази река е оценена със среден екологичен статус (клас III), а сравнението с граничните стойности за приоритетни и приоритетни вредни вещества свидетелства за отсъствие на добър химичен статус. На основата на корелационния анализ може да се заключи, че е налице плувиална ерозия и режимът на кислорода се влияе повече от промени в атмосферната температура, отколкото от наличие на органични замърсители.

Determination of fluoride in toothpaste and in mouthwash products by GC/FID/HS

T.N. Rizov, S.S. Paneva*

Medical College "Y. Filaretova", Medical University, Sofia 1606, Bulgaria

Received: December 9, 2017; Accepted: January 14, 2018

Fluorine is imported into the human organism mainly by products for oral hygiene, toothpastes and various liquids for freshening and cleansing the oral cavity. The necessity to control its content is imposed by the requirements for safety and standardized cosmetic products production. The determination was performed by gas chromatography, flame ionization detector and automatic vapor-phase sampler "headspace" (HS). The method was based on derivatization of fluoride anions with triethylchlorosilane (TETCS) in acidic environment. The reaction was realized in the HS vials and after that triethylfluorsilane was determined by gas phase injection. The calibration of the method lies within a concentration interval of 100 – 2000 ppm for toothpaste and 50 - 1000 ppm for mouthwash products. The repeatability, expressed as relative standard deviation at optimized reaction conditions and GC determination was $\pm 5\%$ for toothpaste and $\pm 3.5\%$ for mouthwash products. The presented gas-chromatographic method with flame ionization detector and HS appliance enables the quick and precise detection of fluorine in cosmetic products. The method is applicable to various other environments (matrices) – foods, food supplements, drugs.

Keywords: Fluoride; Gas chromatography; Headspace (HS); Toothpaste; Mouthwash products; Triethylfluorsilane (TEFS)

INTRODUCTION

Fluorine is a microelement essential for the organism. It stimulates bone cell formation (osteoblasts), strengthens the skeleton; it is engaged in tooth enamel formation; it has bactericide effect, improves gum blood circulation, prevents caries formation and parodontal diseases in children. On the other hand, excessive fluorine amounts stimulate fluorosis development – it damages the enamel with appearance of red to dark brown stains on it with following defects in the bone tissue; it delays the development of the nervous system that particularly affects growing up organisms and disturbs the processes of ossification and mineralization of the bone tissue.

Various approaches to supply fluorine to various population groups have been implemented in the time over the world. Experiments were conducted (USA) to fluorinate the water for drinking and everyday necessities. Food supplements have been designed, as well as fluorine supplementation of various food products, especially of those, designed for children. Many countries implement fluorine prevention among children through adequate pills. Currently, fluorine delivery to the human organism is mainly realized by products for oral hygiene, toothpastes and various liquids for freshening and cleansing the oral cavity. The implementation of fluorine in toothpastes started in the 60s of the past century substantiated by active scientific research

on its effect on human health. The main focus of the studies was oral health with an emphasis on dental caries. The evidence supported fluorine benefits revealing significant reduction of caries incidence rate at application of fluorine-containing toothpastes and liquids for dental hygiene [1, 2].

Practically, the fluorine amount that is necessary and beneficial for the organism varies in very narrow margins and its increase over the upper limit is hazardous.

This fact requires the implementation of a method for control during the production and of the end products that is sensitive, reliable as much as possible, easily applicable and relatively cheap.

Several techniques have been implemented to analyze water soluble fluorides in toothpaste and similar products: fluoride ion selective electrode [3]; ion selective electrode and ion chromatography [4]; capillary electrophoresis [5]. Currently, the most frequently used analytical technique is gas chromatography with flame ionization detector. The gas chromatographic conditions, as well as the chemical reaction when chlorine in triethylchlorosilane is substituted by fluorine in acidic environment are almost equivalent. The new resulting compound triethylfluorsilane can be determined by gas chromatographic method with good analytical parameters. The various developed and published methods contain significant

* To whom all correspondence should be sent.
E-mail shmesti@yahoo.com

differences in the sample preparation before the gas chromatographic determination itself. The standard method set by Directive 83/514 [6] envisages triethylenefluorsilane extraction with a non-polar solvent from the reaction mixture and injection of an aliquot portion into the GC. Wejnerowska *et al.* [7] developed a principally different approach to sample preparation. After the chemical reaction they used an adsorbent instead of a solvent to extract the fluorine compound. The adsorbent was placed in a HS vial and underwent solid-phase headspace micro-extraction and gas chromatography–flame ionization detection.

The aim of the current study was to develop a new efficient, fast and relatively inexpensive method for determination of fluoride in toothpaste and in mouthwash products based on the very rich experience and the high technological levels achieved by the gas chromatography systems.

Reagents and Materials

⇒ *Reagents*: sodium fluoride; triethylchlorosilane – TETCS; sulfuric acid; deionized water (all reagents of quality grade “pure for gas chromatography” or higher).

⇒ *Materials*: various toothpaste brands with/without added fluorine; various mouthwash brands with/without added fluorine.

Gas chromatograph *Clarus 580*, *Perkin Elmer* with flame ionization detector and automatic vapor phase sampler “headspace” *Turbomatrix HS16*, analytical column *Elite CLP 30 m*, 25 mm, 0.25 μ m, vials for HS - 20 mL.

Gas-chromatographic conditions: detector temperature (250°C), injector (220°C), column (60°C for 5 min, followed by a raise with 10°C/min up to 150°C and 2-min detention); carrier gas helium 20 mL/min.

HS conditions: oven 70°C; transfer 110°C; needle 75°C; carrier gas 28 psi, thermostat 10 min; pressurize time 1.5 min; injection time 0.04 min.

EXPERIMENTAL

Toothpaste

Preparation of basic standards of fluoride: B 1 - 0.11 g of NaF (0.05g F) in 50 ml of water in a glass flask (0.5 mg/ml) and *B 2* – 1 ml of *B 1* in 10 ml of water (0.05 mg/ml).

Preparation of laboratory standards: toothpaste without added fluorine, basic composition similar as much as possible to the analyzed one.

The following laboratory standards were prepared: 1 ml *B 2* plus 0.5 g paste plus 48.5 ml water; 5 ml *B 2* plus 0.5 g paste plus 47.5 ml water; 1 ml *B 1* plus 0.5 g paste plus 48.5 ml water; 2 ml *B 1* plus 0.5 g paste plus 47.5 ml water. The produced mixtures were homogenized for 30 min in an ultrasound tub.

Preparation of laboratory samples: 0.5 g of the analyzed toothpaste was added to 50 ml of water (glass flask). The mixture was homogenized for 30 min in an ultrasound tub. Three laboratory samples were prepared for each sample.

Of each of the prepared laboratory standards and samples, 1 ml was added into a HS vial plus 1 ml of 50% sulfuric acid and 0.1 ml of triethylchlorosilane (TECS). After adding TECS, the vial must be closed as quickly as possible. The vials were agitated in a shaker at 30°C for 60 min and after that were mounted in the sockets of the HS appliance. Each vial can be injected once.

Mouthwash products

Preparation of basic standard of fluoride: B 3: 1 ml of *B 1* to 50 ml with mouthwash products without fluorine in a glass flask.

Preparation of laboratory standards in HS vials: 0.1 ml of base 3 plus 0.9 ml of water plus 1 ml of 50% sulfuric acid plus 100 μ l of TECS; 0.3 ml of base 3 plus 0.7 ml of water plus 1 ml of 50% sulfuric acid plus 100 μ l of TECS; 0.5 ml of base 3 plus 0.5 ml of water plus 1 ml of 50% sulfuric acid plus 100 μ l of TECS; 1 ml of base 3 plus 1 ml of 50% sulfuric acid plus 100 μ l of TECS.

Preparation of laboratory samples: for each analyzed lot two samples were taken. 1 ml of each sample was diluted with 50 ml of mouthwash product without fluorine in a glass flask. Of each of the produced solutions two samples were prepared in headspace vials, respectively: 0.3 ml of sample plus 0.7 ml of water plus 1 ml of 50% sulfuric acid plus 100 μ l of TECS and a similar one, with 0.5 ml of sample. After adding TECS, the vial must be closed as quickly as possible. The vials were agitated for 15 min in a shaker at 30°C and after that they were mounted in the sockets of the HS appliance.

The concentration interval of calibration of the toothpaste was 100 – 2000 ppm, and for mouthwash products - 50 – 1000 ppm. The repeatability, expressed as relative standard deviation at optimized reaction conditions and GC determination, was \pm 5% for toothpaste and \pm 3.5% for mouthwash products.

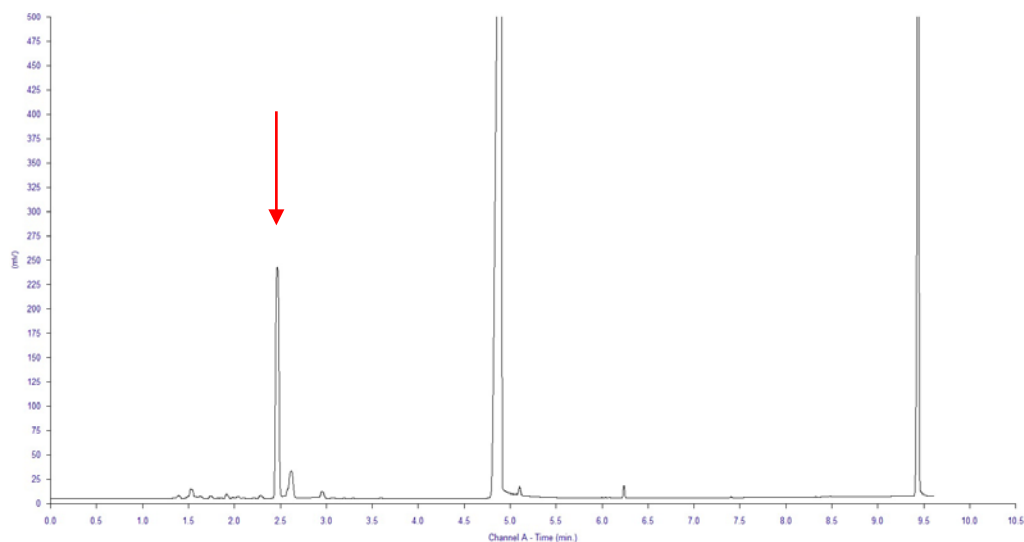


Fig. 1. Chromatogram of a toothpaste with added fluorine (rt = 2.45 min)

The figure 1 presents a chromatogram of a toothpaste sample with added fluorine. The graph clearly outlines the good resolution guaranteeing the achievement of good analytical parameters of the present method.

The method can be applied for various product types, including foods, food supplements, drugs, etc. The optimization of the conditions of the course of the reaction for production of TECS and of the gas chromatographic determination can lead to very high sensitivity at adequate repeatability and absence of systematic error.

CONCLUSION

The proposed gas-chromatographic method with flame ionization detector enables a quick and precise detection of fluorine in cosmetic products. The optimization of the conditions of the course of the reaction for production of TECS and of the gas chromatographic determination can lead to very high sensitivity at adequate repeatability and absence of systematic error. The method can be

also applied to other environments (matrices) – foods, food supplements, drugs.

REFERENCES

1. J.D. Featherstone, *J. Amer. Dental Assoc.*, **131**, 887 (2000).
2. V.C.C. Marinho, J.P.T. Higgins, S. Logan, A. Shaiham, Fluoride toothpastes for preventing dental caries in children and adolescents (Cochrane Review). The Cochrane Library, Chichester, UK, John Wiley & Sons Ltd, 2004.
3. Ş. Tokalioğlu, Ş. Kartal, U. Şahin, *J. Chromatogr. A*, **1150**, 173 (2007).
4. T. Itota, T.E. Carrick, S. Rusby, O.T. Al-Naimi, M. Yoshiyama, J.F. McCabe, *J. Dent.* **32**, 117 (2004).
5. P. Wang, S.F.Y. Li, H.K. Lee, *J. Chromatogr. A*, **765**, 353 (1997).
6. Directive 83/514/EEC of 27 September 1983 on the approximation of the laws of the Member States relating to methods of analysis necessary for checking the composition of cosmetic products. *Official Journal of the European Communities*, L 291.9, 24.10.1983
7. G. Wejnerowska, A. Karczmarek, J. Gaca, *J. Chromatogr. A*, **1150**, 173 (2007).

**ОПРЕДЕЛЯНЕ НА ФЛУОРИД В ПАСТА ЗА ЗЪБИ И ПРОДУКТИ ЗА ОРАЛНА ХИГИЕНА
С ИЗПОЛЗВАНЕ НА ГАЗОВА ХРОМАТОГРАФИЯ С ПЛАМЪКОВ ЙОНИЗАЦИОНЕН
ДЕТЕКТОР И АВТОМАТИЧНО УСТРОЙСТВО ЗА ВНАСЯНЕ НА ПРОБИ (GC/FID/HS)**

Т.Н. Ризов, С.С. Панева*

Медицински колеж „Й. Филаретова”, Медицински университет-София, София 1606, България

Постъпила на 9 декември, 2017 г.; приета на 14 януари, 2017 г.

(Резюме)

Флуорът се внася в човешкия организъм главно чрез продукти за орална хигиена, пасти за зъби и различни течности за почистване и освежаване на устата. Необходимостта от контрол на съдържанието му се определя от изискванията за безопасност при производството на козметични продукти. Определянето на флуора е извършено чрез газова хроматография с пламъков йонизационен детектор и автоматично устройство за внасяне на газови проби. Методът се основава на дериватизацията на флуоридните аниони с триетилхлорсилан в кисела среда. Реакцията се провежда в съчетата на устройството за внасяне на газови проби, след което триетилфлуорсиланът се определя чрез инжектиране на газовата фаза. Калибрирането се извършва в концентрационния интервал 100 – 2000 ppm за пастите за зъби и 50 - 1000 ppm за продуктите за орална хигиена. Повторяемостта, изразена като относително стандартно отклонение, е $\pm 5\%$ за пастите за зъби и $\pm 3.5\%$ за продуктите за орална хигиена. Предложеният газ-хроматографски метод с пламъков йонизационен детектор и автоматично устройство за внасяне на газови проби дава възможност за бързо и прецизно определяне на флуор в козметични продукти. Методът е приложим и към различни други матрици – храни, хранителни добавки, лекарства.

Modeling of organic Rankine cycle for suitable working fluid in HYSYS for power generation in Pakistan

M. Ur-Rehman¹, M. Sh. Khurram^{1*}, S. Rafiq^{1*}, Sh. A. Memon², M. Ghauri^{1*}, F. Jamil¹, M. H. Jaffery³, M. Gh. Doggar⁴

¹Department of Chemical Engineering, COMSATS University Islamabad, Lahore Campus, Pakistan

²Department of Environmental Engineering and Management, Mehran University of Engineering and Technology, Jamshoro, Pakistan

³Department of Electrical Engineering, COMSATS University Islamabad, Lahore Campus Pakistan

⁴Energy Research Center, COMSATS University Islamabad, Lahore Campus
Pakistan

Received: November, 24, 2017; Revised: 21 December, 2017

In this study organic Rankine cycle was modeled using Aspen HYSYS 8.8 to find suitable working fluids in 9 different locations which enlightened the scope of organic Rankine cycle in Pakistan. Different working fluids, namely R141b, R21, R142b and R245fa under different solar radiation-based temperature conditions at boiler inlet are reported in this study. R21 was found as the most promising working fluid due to its relatively better work output from a 0.59 MW turbine exploiting low quality heat, as compared to above mentioned working fluids investigated in this study.

Keywords: Organic Rankine cycle (ORC); Waste heat; Solar-thermal energy; Aspen HYSYS 8.8.

INTRODUCTION

Pakistan relies on different sources for power generation to meet its electricity demand. These sources are mainly comprised of natural gas, hydel, coal, nuclear, LPG and fuel oil [1-4]. There is a continuous increase in demand of electricity in the country. However, the conventional sources for power production are limited and affect the environment by producing large amount of greenhouse gases as byproducts [5].—Organic Rankine cycle (ORC) has a wide scope in Pakistan due to its potential utilization with waste heat recovery and solar energy. The ORC technology operates below 200°C and is innocuous to the environment. In Pakistan industrial waste heat and solar energy are the main energy resources for organic Rankine cycle. Almost 200 plants of ORC are working in different regions of the world [6]. Energy demand increases with increase in population growth. ORC modeling and its technology development may eliminate and secure energy future of Pakistan and would help in mitigating the current energy crisis of the country.

In contrast to steam Rankine cycle, organic Rankine cycle deploys organic fluid instead of water and consists of the same four processes named: compression (pump used for compression), vaporization (boiler for vaporization), expansion (turbine used for expansion work) and condensation (condenser for condensation) [6, 7]

Waste heat recovery from combined cooling, heating and power (CCHP) systems offers a way of utilizing the energy of fuel efficiently, economically and reliably. In addition to this, the overall efficiency of the plants also improves along with less degradation to the environment [7-10].

Velez et al. studied different working fluids for Rankine cycle operating at low temperature. Working fluids like water, some hydrocarbons and coolants were studied by modifying the inlet conditions (pressure and temperature) of the turbine. The influence of pressure ratio and inlet temperature of the turbine were also studied [11]. Ekwonu et al. investigated modeling of gas engines waste heat integrated with Rankine cycle and organic Rankine cycle in Aspen HYSYS 7.3 for potential waste heat recovery and consumption. The influence of exhaust gas temperature at different operating conditions on the efficiency and power of the system was investigated and compared [12]. Some researchers discussed the combination of ORC with waste heat and solar energy for power generation. However, these studies were conducted in different domestic weather conditions [13,14].

In this study, organic Rankine cycle was modeled to identify a working fluid appropriate for different climates in Pakistan for power generation from solar and waste heat energy. In this way an inexpensive alternate source for power generation could be employed.

* To whom all correspondence should be sent.

E-mail srafiq@ciitlahore.edu.pk;

mshkhurram@ciitlahore.edu.pk; drghauri@ciitlahore.edu.pk

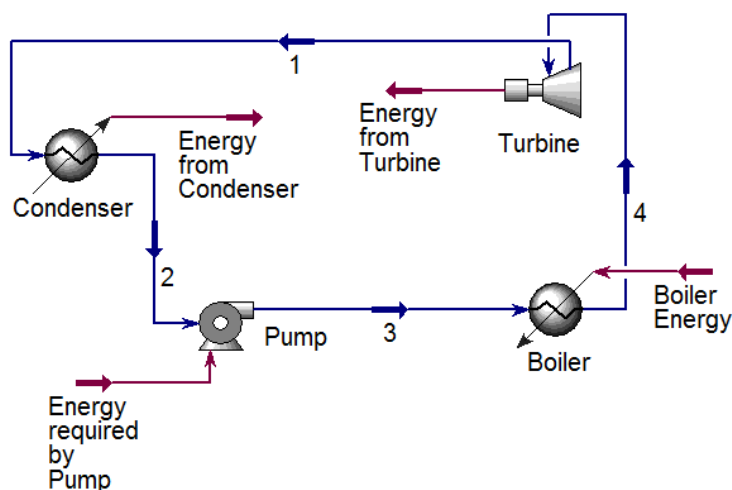


Fig. 1. Rankine cycle

WORKING OF ORGANIC RANKINE CYCLE (ORC)

The working fluid in liquid state is pumped into the boiler where it is heated at constant pressure by an external heat source like solar-thermal energy and/or waste heat, etc. This heat energy changes its phase into superheated vapors. Superheated vapors turn the turbine, expand and generate power. The expansion causes cooling at the outlet of turbine. The vapors are later condensed by removing latent heat at constant pressure to become a saturated liquid. This saturated liquid is introduced to the pump inlet all the time and the cycle goes on. Boiler and condenser are assumed to be isobaric whereas pump and turbine are assumed to be isentropic in nature. The process flow diagram of modeled organic Rankine cycle is shown in Figure 1.

SOLAR ENERGY AND ORC

Sun is the only sustainable energy resource and radiates in a unit second more energy than consumed by the earth inhabitants [14]. Depletion trends of fossil fuels have made it inevitable focusing renewable and sustainable energy resource development. Earth receives 174 PW from solar radiation at the upper atmosphere, 30% of this energy is reflected back whereas the rest of it is utilized by different sources such as water evaporation, etc. Total energy absorbed by the earth

is 3850000 EJ per year [15]. If only 0.22% of earth area is covered with solar collectors having just 8 % efficiency, then this would be enough in meeting the present global energy requirements [16]. Pakistan is situated in the sunny belt and has long sunny days throughout the year. This exposure varies to some extent from place to place due to the geographical location of Pakistan. The minimum intensity of solar energy in Pakistan is 4.45KWh/m² and the highest one is of 6.65KWh/m² per day with a reported maximum of 7 KWh/m² per day. The annual mean value of solar radiation in Pakistan is 5.5 KWh/m² per day during the course of its sunshine hours[14, 17, 3].

INVESTIGATED LOCATIONS OF PAKISTAN

The highest temperature recorded in Pakistan was 53.5°C on May 26th, 2010. It was the highest temperature measured in Asia [17]. The daily mean temperatures of 9 different locations of Pakistan that were investigated in the current study are shown in Table 1 [18].

MODELING OF ORGANIC RANKINE CYCLE USING ASPEN HYSYS 8.8

Organic Rankine cycle simulations were carried out using Aspen HYSYS 8.8 process simulator. HYSYS is useful for thermodynamic analysis at steady state conditions.

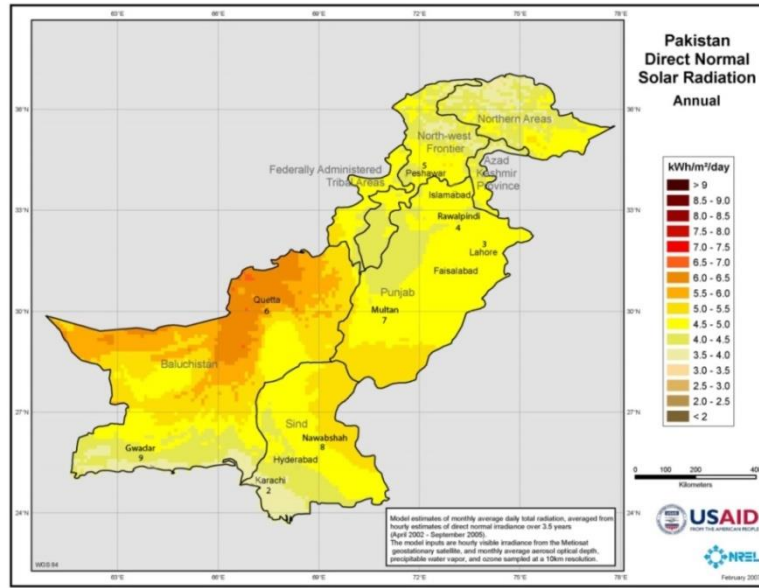


Fig. 2. Solar energy potential in Pakistan and the identified locations [14]

Table 1. Daily mean temperature of locations investigated [18]

Cities of Pakistan (9locations)	Daily Mean Temperature (°C)												
	Jan	Feb	Mar	Apr	May	Jun	July	Aug	Sep	Oct	Nov	Dec	Year
Islamabad (1)	10.1	12.1	16.9	22.6	27.5	31.2	29.7	28.5	27	22.4	16.5	11.6	21.34
Karachi (2)	18.1	20.2	24.5	28.3	30.5	31.4	30.3	28.9	28.9	27.9	23.9	19.5	26.03
Lahore (3)	12.8	15.4	20.5	26.8	31.2	33.9	31.5	30.7	29.7	25.6	19.5	14.2	24.32
Rawalpindi (4)	10.35	12.3	16.9	22.8	27.85	34.3	30	28.5	27.1	22.45	16.5	12	21.75
Peshawar (5)	11.2	12.9	17.4	23.2	28.6	33.1	32.2	30.7	28.9	23.7	17.6	12.5	22.67
Quetta (6)	3.7	6	11.1	16.6	21	25.6	27.9	26.4	21.1	14.6	9.2	5.1	15.69
Multan (7)	13	15.5	21.5	28	32	35.5	34	33	31	26.5	20	14.5	25.38
Nawabshah (8)	15.2	18.2	23.95	29.65	34	35.6	33.9	32.45	31	27.9	22.1	16.8	26.72
Gwadar (9)	18.95	20.1	23.2	26.8	29.55	30.5	29.7	28.65	28	26.85	23.5	20.1	25.48

It has the advantage of including fluid properties and ready to use optimization tools. Peng Robinson equation of state was used as the thermodynamic model.

The evaporator's heat duty was evaluated as a function of evaporator inlet temperature and pressure conditions. The process was assumed at steady state conditions, no drop in pressure or heat loss in the condenser, the evaporator or the pipes and constant isentropic efficiencies of 75% were considered for the turbine and pump.

The organic Rankine cycle process flow diagram in simulation is the same as shown in Figure 1. The inlet and outlet pressures of pump are 4.7 bar (0.47MPa) and 17.5 bar (1.75MPa), respectively. The flow rate is 25.51 kg/s. The refrigerants R142b,

R21, R141b and R245fa were used in the simulations. R142b evaporates at 91°C, R21 evaporates at 114°C, R141b evaporates at 148°C and R245fa evaporates at 115°C. The inlet temperatures used were the temperatures of all the investigated locations as listed in Table 1.

The total cycle energy efficiency was determined using the following equations:

$$\eta = \frac{\dot{W}_{\text{turbine}} - \dot{W}_{\text{pump}}}{\dot{Q}_{\text{evaporator}}} \quad (1)$$

where,

$$\dot{W}_{\text{turbine}} = \dot{m} \times (h_1 - h_2) \quad (2)$$

$$\dot{W}_{\text{pump}} = \dot{m} \times (h_3 - h_4) \quad (3)$$

$$\dot{Q}_{\text{evaporator}} = \dot{m} \times (h_4 - h_1) \quad (4)$$

Pump, turbine, heater (boiler) and cooler (condenser) were the unit operations used in ORC simulations. HYSYS uses the following assumptions and equations in calculating unknown variables of the mentioned unit operations:

- *For pump:*

The pump unknown variables were calculated using equations (5-7):

$$\dot{W}_{\text{pump},i} = \text{power required ideal} = \frac{(P_{\text{out}} - P_{\text{in}}) \times \dot{m}}{\rho_{\text{Liquid}}} \quad (5)$$

Equation (5) shows the ideal power required by the pump to increase the pressure of the liquid. The actual power required by the pump can be estimated by using the following co-relation:

$$\text{Efficiency (\%)} = \eta_{\text{Pump}} = \frac{\dot{W}_{\text{Pump},i}}{\dot{W}_{\text{Pump}}} \times 100\% \quad (6)$$

When the pump efficiency is less than 100%, it means that the excessive amount of energy goes into raising the temperature of the outlet stream.

Combining equations (5) and (6) gives the correlation equation (7) for the estimation of the actual power required for the pump:

$$\dot{W}_{\text{Pump}} = \frac{(P_{\text{out}} - P_{\text{in}}) \times \dot{m} \times 100\%}{(\rho_{\text{Liquid}} \times \eta_{\text{Pump}})} \quad (7)$$

- *For turbine:*

Efficiency of turbine is the ratio of actual power (\dot{W}_{Turbine}) obtained from the turbine in the expansion process to the power obtained for isentropic expansion ($\dot{W}_{\text{Turbine},i}$). It can be given by the following relation equation (8):

$$\text{Efficiency (\%)} = \eta_{\text{Turbine}} = \frac{\dot{W}_{\text{Turbine}}}{\dot{W}_{\text{Turbine},i}} \times 100\% \quad (8)$$

- *Evaporator and condenser:*

For the calculation of the performance to cycle it is only necessary to determine the amount of heat required for the process to run the turbine, our objective was not to study the conditions of the utility itself, the condenser and evaporator available in software was used.

RESULTS AND DISCUSSIONS

It was found that the energy obtained from the turbine using different working fluids remains the same (Table 2). Following table shows the energy obtained from the turbine at work.

Table 2. Energy from turbine (MW)

Energy from Turbine(MW)	R245fa	R142b	R21	R141b
	0.43	0.56	0.59	0.57

The results obtained were plotted as the relationships of inlet temperature and the boiler duty for different working fluids. These graphs are shown in figures 3 to 20.

The boiler duty decreases with increase in inlet feed temperature to the boiler. As a result, less amount of heat is required to evaporate the working fluid. The graphs were plotted for monthly temperatures and the boiler duty for different locations of Pakistan. It was found that at given conditions working fluids as investigated follow the order: R141b > R245a > R21 > R142 heat to produce vapors. Working fluid R245fa required less amount of heat to produce vapors. The working fluid R21 required a larger amount of heat than the working fluid R142, but a smaller amount of heat than R141b.

FOR ISLAMABAD (LOCATION 1)

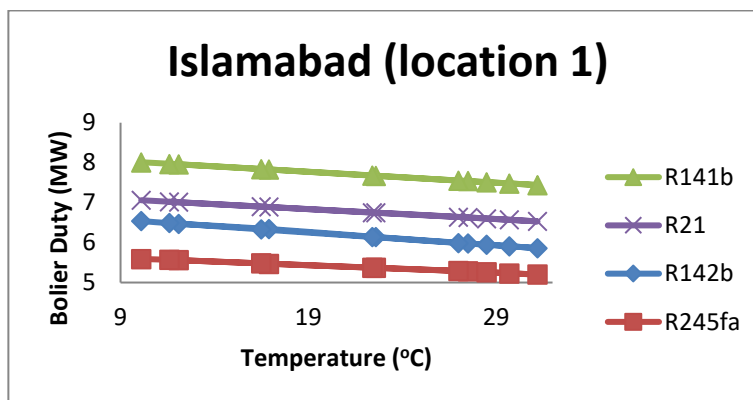


Fig. 3. For Islamabad (location 1): Temperature (°C) vs boiler duty (MW)

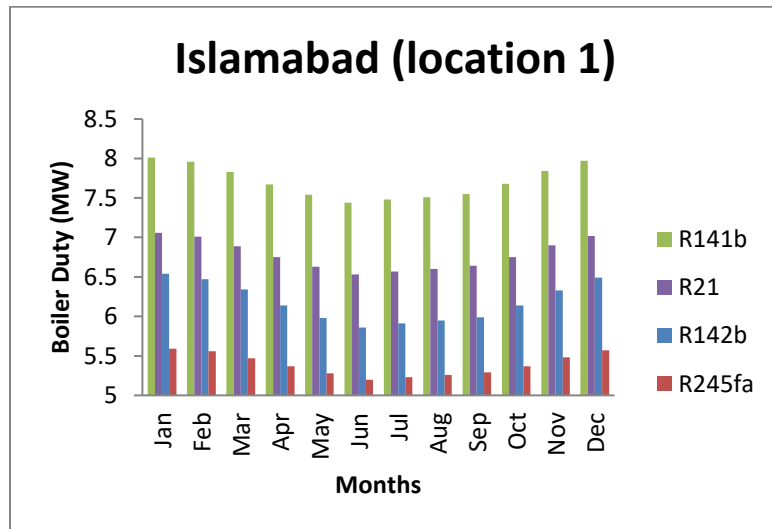


Fig. 4. For Islamabad (location 1): Boiler duty (MW) vs months

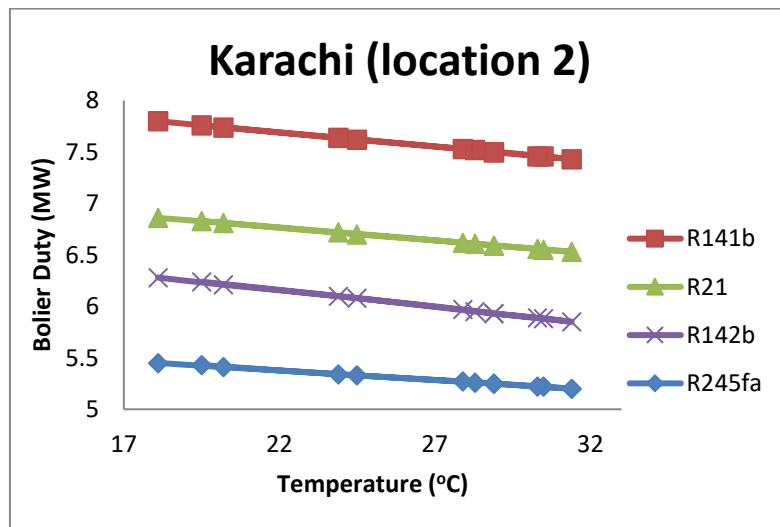


Fig. 5. For Karachi (location 2): Temperature (°C) vs boiler duty (MW)

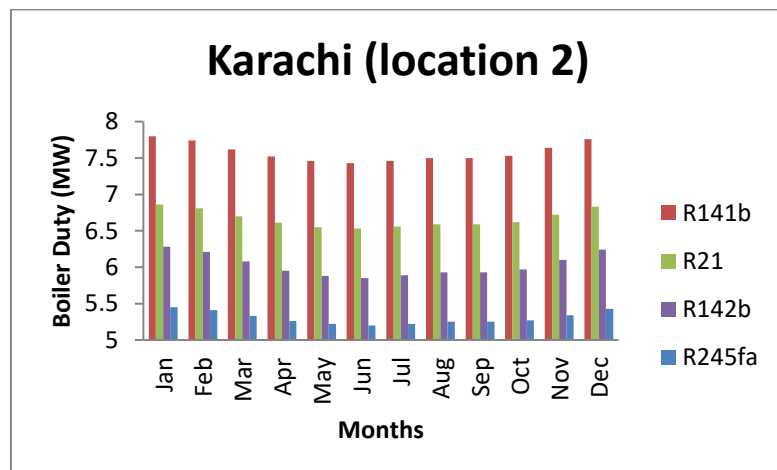


Fig. 6. For Karachi (location 2): Boiler duty (MW) vs months

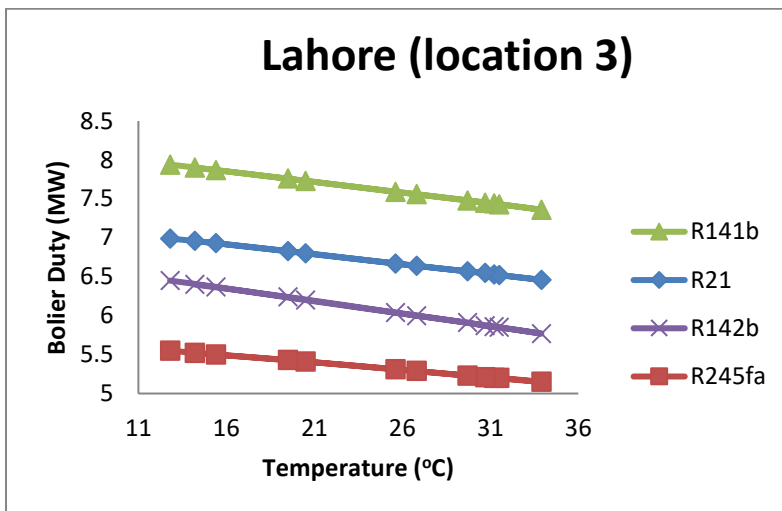


Fig. 7. For Lahore (location 3): Temperature (°C) vs boiler duty (MW)

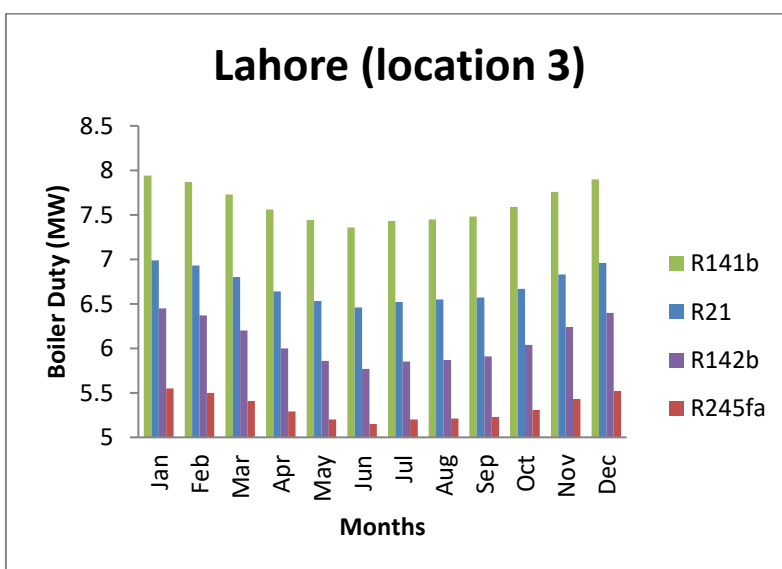


Fig. 8. For Lahore (location 3): Boiler duty (MW) vs months

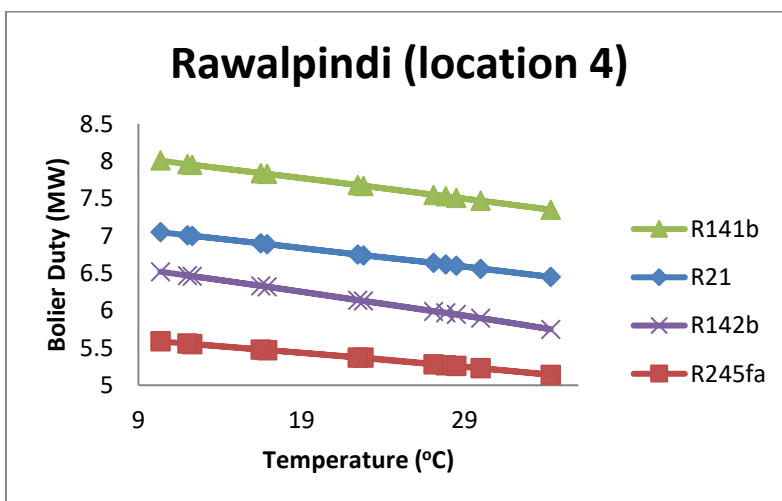


Fig. 9. For Rawalpindi (location 4): Temperature (°C) vs boiler duty (MW)

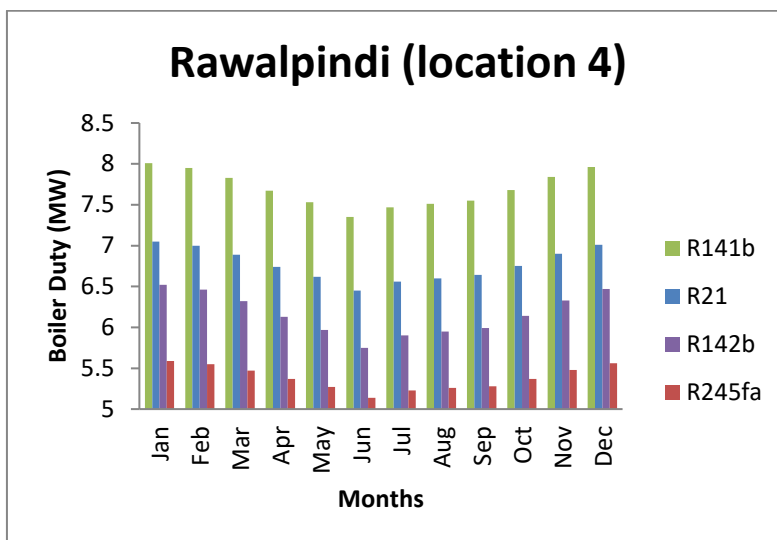


Fig. 10. For Rawalpindi (location 4): Boiler duty (MW) vs months

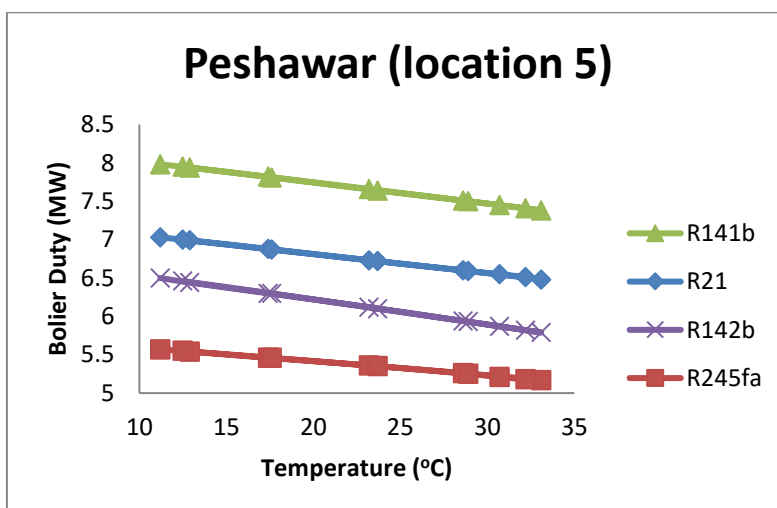


Fig. 11. For Peshawar (location 5) Temperature (°C) vs boiler duty (MW)

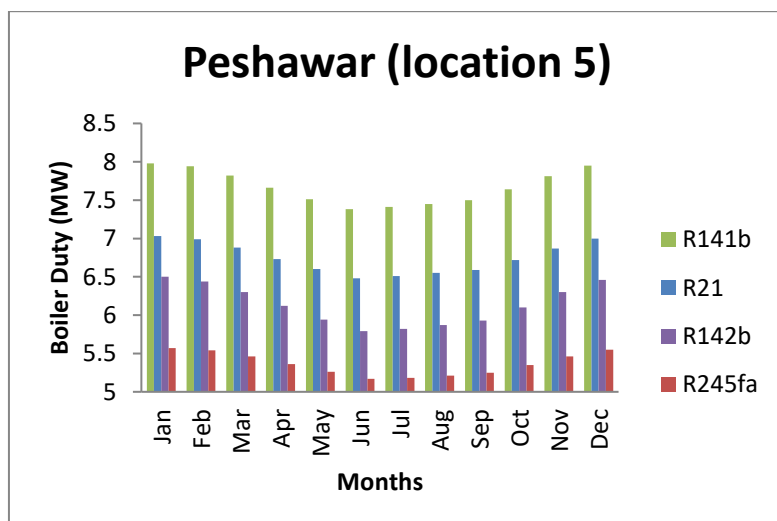


Fig. 12. For Peshawar (location 5): Boiler duty (MW) vs months

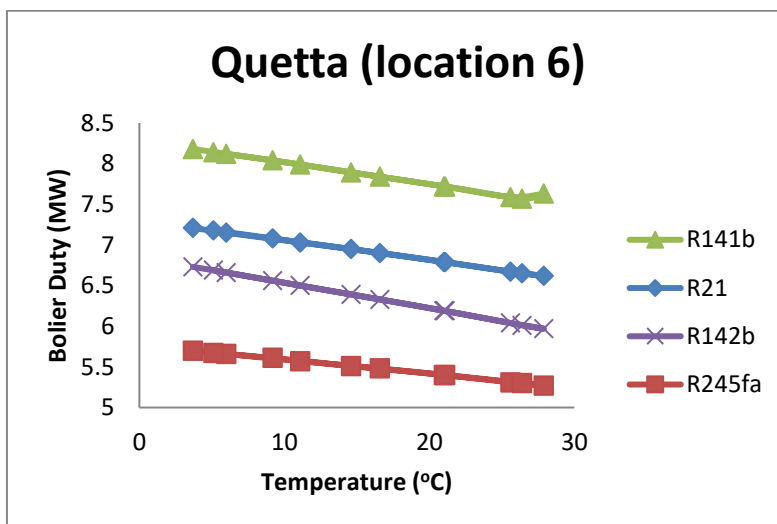


Fig. 13. For Quetta (location 6): Temperature (°C) vs boiler duty (MW)

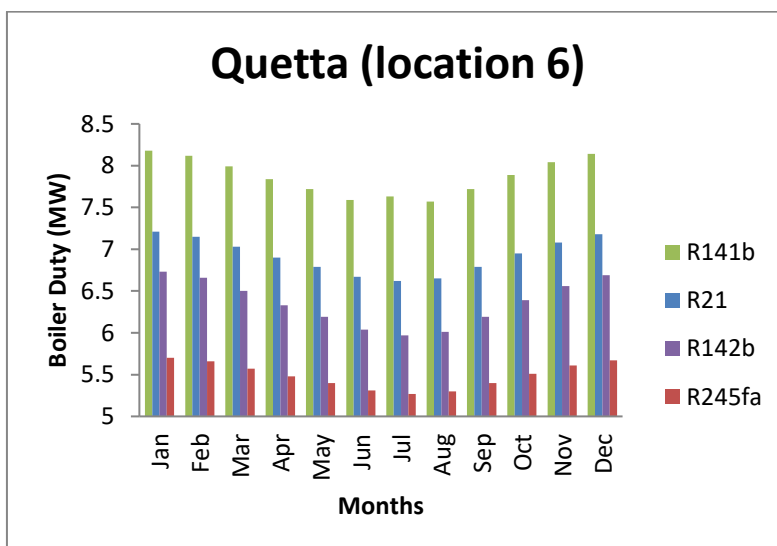


Fig. 14. For Quetta (location 6): Boiler duty (MW) vs months

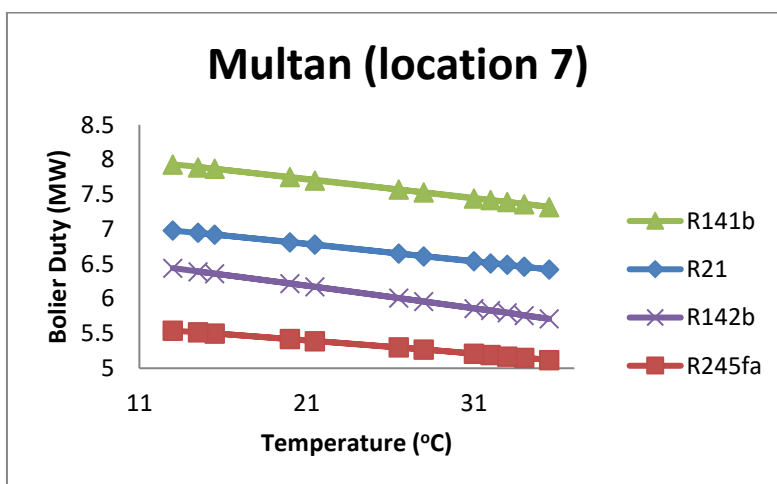


Fig. 15. For Multan (location 7): Temperature (°C) vs boiler duty (MW)

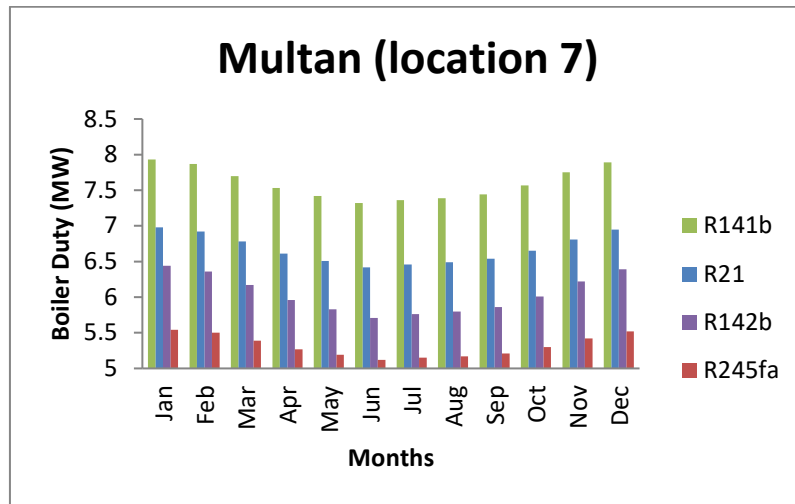


Fig. 16. For Multan (location 7): Boiler duty (MW) vs months

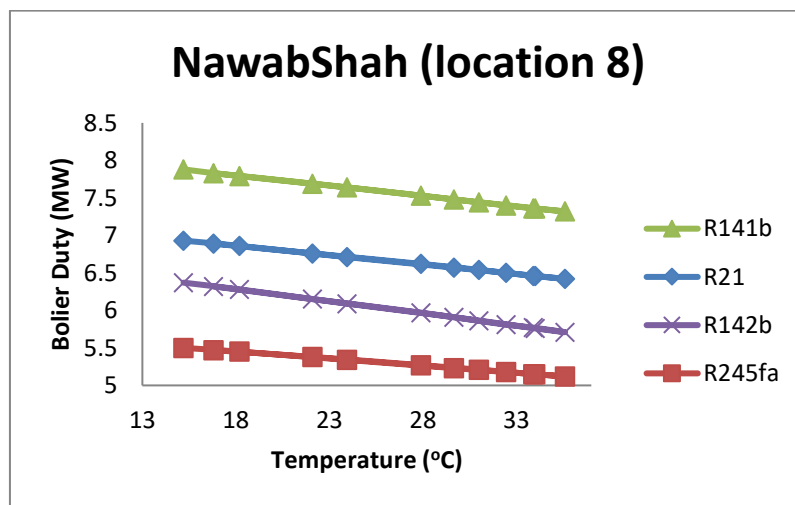


Fig. 17. For Nawabshah (location 8): Temperature (°C) vs boiler duty (MW)

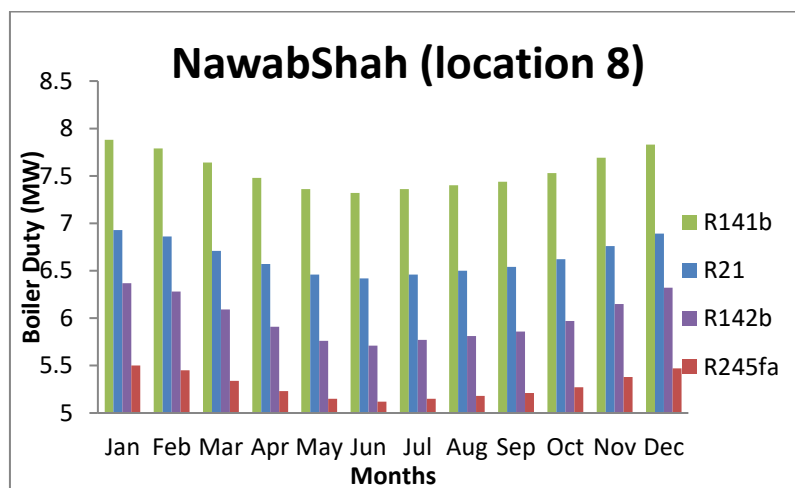


Fig. 18. For Nawabshah (location 8): Boiler duty (MW) vs months

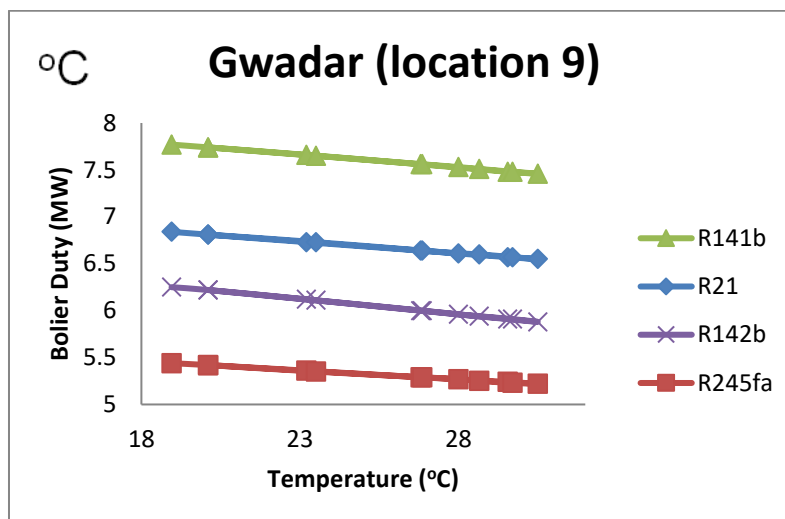


Fig. 19. For Gwadar (location 9): Temperature (°C) vs boiler duty (MW)

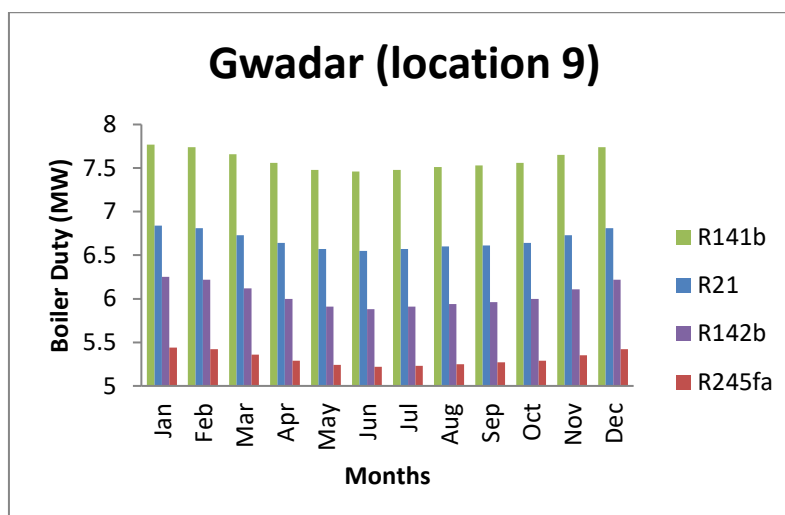


Fig. 20. For Gwadar (location 9): Boiler duty (MW) vs months

CONCLUSIONS

Based on simulations results, it can be concluded that:

- R21 was identified as propitious working fluid based upon the relatively better work output from the turbine which is 0.59 MW by exploiting low-quality heat.
- The organic working fluid R141b gives work output of 0.57 MW, but it requires more energy as compared to R21.
- The working fluid R142b gives work output of 0.56 MW by using low-quality heat as compared to R21 and R141b but it is not recommended because it is extremely flammable and dangerous for the ozone layer.

FUTURE WORK RECOMMENDATION

Selection of working fluid is very critical as it requires certain factors to be considered that include:

- Cost effectiveness and availability;
- Non-toxicity and non-flammability;
- Low global warming potential and zero ozone depletion factor;
- Low viscosity, thermal and chemical stability;
- Low freezing point.

Acknowledgement: Authors acknowledge the financial support provided by COMSATS University Islamabad, Lahore Campus.

REFERENCES

1. G. Abdullah, A. Shair, W. S. Ali, *EJBM*, **7**, 442 (2015).
2. A.W. Bhutto, A. A. Bazmi, G. Zahedi., *Renew. Sust. Energ. Rev.*, **15**, 3207 (2011).
3. M.A. Chaudhry, R. Raza, S.A. Hayat, *Renew. Sust. Energ. Rev.*, **13**, 1657 (2009).
4. B. Fatima, F. Ali, History of Private Power in Pakistan. Sustainable Development Policy Institute, Islamabad, 2007.

5. M. Abid, M.S. Khurram, S. Rafiq, S.A. Memon, M. Ghauri, K. Shahzad, M. Jaffery, M.G. Doggar, N. Muhammad, *JoET*, **6**, 352 (2017).
6. K. Arun, S.K Shukla, *Proc. Technol.*, **23**, 454 (2016).
7. K. C. Kavvadias, A. P. Tosios, Z. B. Maroulis, *Energy Convers. Manage.*, **51**, 833 (2010).
8. S. M. Lai, C.W. Hui, *Energy*, **34**, 1693 (2009).
9. F.A. Al- Sulaiman, I. Dincer, F. Hamdullahpur, *Appl. Therm. Eng.*, **31**, 2829 (2010).
10. G. Angrisani, A. Rosato, C. Roselli, M. Sasso, S. Sibilio, *Appl. Therm. Eng.*, **38**, 78 (2012).
11. F. Velez, J.S. Jose, M. C. Martin, G. Antolin, F. Chejne, A. Quijano, *Fuel Process. Technol.*, **103**, 71 (2012).
12. M. C. Ekwonu, S. Perry, E. A. Oyedoh, *ACER*, **3**, 42 (2014).
13. J. Freeman, K. Hellgardt, C.N. Markides, *Appl. energy.*, **138**, 605 (2015).
14. S. Adnan, A.H. Khan, S. Haider, R. Mahmood, *J. Renew. Sustain. Energy*, **4**, 1 (2012).
15. GOP Pakistan Economic Survey, Islamabad. Economic Advisers Wing: Ministry of Finance, (2014).
16. GSRR - REN 21, Renewables, 2013. http://www.ren21.net/Portals/0/Documents/Resources/GSR2013/GSR_2013_lowres.pdf.
17. H. B. Khalil, S. J. H. Zaidi, *Renew. Sust. Energ. Rev.*, **31**, 194 (2014).
18. GOP Pakistan Meteorological Department. 2013. <http://www.pmd.gov.pk/>

МОДЕЛИРАНЕ НА ОРГАНИЧЕН RANKINE ЦИКЪЛ ЗА ПОДХОДЯЩ РАБОТЕН ФЛУИД ЧРЕЗ HYSYS ЗА ПРОИЗВОДСТВО НА ЕНЕРГИЯ В ПАКИСТАН

М. Ур-Рехман¹, М. Ш. Хурам^{1*}, С. Рафик^{1*}, Ш. А. Мемон², М. Гаури^{1*}, Ф. Джамил¹, М. Х. Джафери³, М. Г. Догар⁴

¹ Департамент по инженерна химия, COMSATS Институт по информационна технология, Лахор, Пакистан

² Департамент по инженерство и мениджмънт на околната среда, Мехран Университет по инженерство и технология, Джамишоро, Пакистан

³ Департамент по електроинженерство, COMSATS Институт по информационна технология, Лахор, Пакистан

⁴ Център по енергийни изследвания, COMSATS Институт по информационна технология, Дефенс роуд, Лахор, Пакистан

Постъпила на 24 ноември, 2017 г.; коригирана на 21 декември, 2017 г.

(Резюме)

В настоящата статия е моделиран органичен Rankine цикъл с използване на Aspen HYSYS 8.8 за намиране на подходящия работен флуид в 9 различни области, представителни за обхвата на органичния Rankine цикъл в Пакистан. Изследвани са различни работни флуиди, именно R141b, R21, R142b и R245fa, при различни температурни условия на входа на нагревателя, базирани на слънчевото греене. Установено е, че R21 е най-перспективният работен флуид, даващ относително по-добър ефект за 0.59 MW турбина с използване на нискокачествено гориво, в сравнение с другите изследвани флуиди.

Net analyte signal-based methods for the simultaneous determination of paracetamol, propyphenazone and caffeine by UV spectrophotometry

G. Gergov^{1*}, A. Alin², P. Katsarov³, V. Simeonov⁴, D. Yankov⁵, Y. Al-Degs⁶

¹Department of Chemistry, Faculty of Pharmacy, Medical University Sofia 1000, 2 Dunav st., Bulgaria

²Department of Statistics, Dokuz Eylul University, Izmir, Turkey

³Department of Pharmaceutical Sciences, Faculty of Pharmacy, Medical University-Plovdiv, 4002, Bul. Vasil Aprilov 15-A, Bulgaria

⁴Laboratory of Chemometrics and Environmetrics, Faculty of Chemistry and Pharmacy, Sofia University "St. Kliment Ohridski", 1164 Sofia, J. Bourchier Blvd. 1, Bulgaria

⁵Institute of Chemical Engineering, Bulgarian Academy of Sciences, 1113 Sofia, Acad. G.Bonchev str., bl.103, Bulgaria

⁶Chemistry Department, The Hashemite University, Zarqa, Jordan

Received: July 18, 2017; Revised: September 8, 2017

Three different net analyte signal-based (NAS) methods - NAP CLS, HLA/GO and HLA XS were successfully applied for the determination of ternary mixtures of paracetamol (PAR), propyphenazone (PRO) and caffeine (CAF). The methods used absorbance UV-spectral data for resolving this complex system with overlapping drug spectra. A reduced five-level orthogonal design was used for the formation of a calibration set including the three compounds. The chemometric models were tested on an external validation dataset with concentrations within the calibration range. All proposed chemometric algorithms could be successfully applied for the determination of the above compounds in the pharmaceutical tablet formulation *Saridon*®. The obtained results showed that the NAS performance was similar compared to partial least-squares method (PLS-1). In addition, the use of the net analyte signal concept allowed the calculations of the analytical figures of merit. A moving window wavelength selection strategy was used, which significantly reduced the number of factors and improved the analytical recoveries.

Keywords: Drugs, Spectral overlap, NAS, NAP CLS, HLA/GO, HLA/XS, Wavelength selection

INTRODUCTION

The area of spectroscopy is one of the most promising fields in pharmaceutical analysis. Processing of the measured spectra is therefore needed to extract information about the components of interest. Chemometrics contribute to the processing of the spectra by delivering algorithms to find differences between spectra (classification) [1-8] or to link spectra to concentrations of compounds (calibration) [9,10]. In recent years the resolution of highly overlapped spectra has advanced dramatically due to the development of robust numerical methods.

The application of multivariate calibration techniques on spectral data offers the great advantage of speeding up complex systems resolution. Among the various chemometric approaches applied for multicomponent analysis, classical least squares (CLS), principal component regression (PCR), partial least squares regression (PLS) have been successfully adopted in many quantitative assays of pharmaceutical formulations [11, 12]. Hybrid linear analysis (HLA) is a relatively new linear algorithm, which combines the advantages of knowing pure component spectra (like CLS) with the modeling advantage of ignoring all other species (e.g., PLS) [13]. Two variants of HLA

algorithms were introduced which did not require the pure spectrum to be known. Finally hybrid linear analysis developed by Xu & Schechter called HLA/XS [14], hybrid linear analysis called HLA/GO and net analyte pre-processing combined with classical least squares (NAP/CLS) developed by Goicoechea & Olivieri [15] were applied for resolving multicomponent pharmaceutical mixtures [16].

In the case of pharmaceutical analysis, either full-factorial or central composite designs are often employed for calibration. The preparations studied require designs other than full-factorial ones, which would imply too many calibration mixtures. Brereton's experimental plans are a suitable strategy to reduce calibration samples [17].

Multicomponent drug formulations are a great challenge for analytical chemists to develop reliable and easy methods for simultaneous estimation which do not require individual calculations for every single component [18]. The pharmaceutical multidrug formulations, in which one dominant drug is combined with other related drugs, are designated to enhance the pharmacological effects of each substance and to cover a wider medical treatment. One such popular combination, containing paracetamol as a dominant drug and

* To whom all correspondence should be sent.

E-mail: ggergov@abv.bg

propyphenazone and caffeine in smaller quantities is named *Saridon*®. *Saridon*® is manufactured by Bayer and it is a widely prescribed combination for pain relief in Eastern Europe.

Paracetamol (PAR) (4-hydroxyacetanilide) is a synthetic drug, derived from p-aminophenol. It is a widely used over-the-counter analgesic and antipyretic agent, which has no antiinflammatory properties. Therefore, it helps to prevent headache and other pain and is a major ingredient in numerous cold and flu remedies [19].

Propyphenazone (PRO) (3-dimethyl-1-phenyl-3-pyrazolin-5-one) is derived from pyrazolone. It is an analgesic, antipyretic and anti-inflammatory agent [20]. It is a non-steroidal antiinflammatory drug (NSAID) incorporated together with paracetamol into many over-the-counter analgesic combinations.

Caffeine (CAF) (3,7-dihydro-1,3,7-trimethyl-1H-purine-2,6-dione) is a xanthine substance used as a psychotropic stimulant drug [21]. Caffeine is also known to synergistically increase the analgesic effect of paracetamol and propyphenazone [22, 23], providing relief for symptoms like headache, muscular aches, neuralgia, backache, joint pain, rheumatic pain, migraine, toothache and menstrual pain.

It is found that the combination of the above mentioned drugs is also very effective in controlling fever originating from bacterial or viral infection. It is usually available in a tablet dosage form as a single unit dose with drug concentrations in varying proportions, but in *Saridon*® the content is: 250 mg of paracetamol, 150 mg of propyphenazone and 50 mg of caffeine.

Literature survey revealed several analytical methods reported for the determination of ternary combinations of PAR, PRO and CAF. Separation techniques such as HPLC and HPTLC have been reported for the analysis of this drug mixture in pharmaceutical dosage forms [24-26]. Vidal *et al.* carried out spectrophotometric determination by means of a single flow-through UV multiparameter sensor [27]. Derivative ratio zero-crossing spectrophotometric method of the three analytes was also demonstrated by Dink *et al.* [24]. The same authors proposed UV chemometric determination of this ternary mixture in pharmaceutical preparations [28]. De Luca *et al.* applied chemometric methods not only for absorbance but in derivative spectra for better resolving of the above drugs with a novel mathematical procedure including wavelength selection [29].

In the work of Gergov *et al.* [30] on the same drug mixture and *Saridon*® formulation the predictability

of different PLS algorithms was investigated. This motivated us to further extend our work and to investigate the quantitative power of NAS-based methods and to compare them with PLS. NAS multivariate models may benefit from suitable wavelength selection which avoids heavily overlapped spectral regions. A sensor selection approach based on moving spectral windows strategy was applied in this work.

The goal of the present study was to compare different NAS calibration approaches (NAP CLS, HLA/XS, HLA/GO) and PLS1. Thus, an optimal chemometric methodology could be offered to solve the significant problems of modeling and analysis of multicomponent pharmaceutical systems.

EXPERIMENTAL

Reagents and solutions

Paracetamol, propyphenazone and caffeine were purchased from Sigma-Aldrich. All stock solutions were prepared by dissolving 100 mg of the corresponding compounds in 1 L of water. 22 mixtures, containing 0 – 24 mg L⁻¹ of PAR, 0 – 20 mg L⁻¹ of PRO and 0 – 20 mg L⁻¹ of CAF in possible compositions were prepared from the stock solutions.

Apparatus and software

Absorption spectra were recorded over the λ range of 190 – 820 nm using a quartz cuvette of 1.0 cm optical path, by a HP8452A diode-array UV-VIS spectrophotometer.

Data were handled using MATLAB® software (ver. 7.0.1). Multivariate calculations by PLS1 and HLA were performed using MVC1 program which is available on the Internet and performed under MATLAB environment (MATLAB, ver. 7.0.1) or by our MATLAB codes which are available by request [31]. Before running MVC1, the spectral data for calibration, validation and real samples were saved in special format that is compatible with MVC1. MVC1 has the ability to display graphical presentations related to calibration tools.

Sample solutions

Pharmaceutical formulations were assayed by weighing the content of five tablets and crushing them into fine powder. An amount exactly corresponding to the average tablet weight was suspended in water and made up to a volume of 1000 mL. The suspension was sonicated for 10 min and then filtered through a PTFE 0.45 μ m membrane filter. Samples for analysis were obtained after serial dilution 1:25 of this filtrate with water and analyzed.

Design of the experiment - calibration and validation sets

A calibration design set of 22 samples was used based on five levels, which was coded between -2 and +2 for each compound in the mixture. The levels were related to the concentrations of the compounds [17]. The same calibration design was used in our previous study [30]. The concentrations of the calibration set solutions were prepared within the linear range of the calibration graph. The design had a value of $r_{12} = 0.0$, so the two concentration vectors were orthogonal to one another. The difference vector [1 3 2 0] and cyclical generator -2, -1, 2, 1 were used in the calibration design matrix. The construction of multilevel calibration designs has been described in the literature [17]. A validation set was prepared in order to test the performance of the models. The chosen concentration levels of the three solutes were within the ranges selected for the calibration set.

Theoretical background

HLA method. Hybrid linear analysis (HLA) is a relatively new linear algorithm, which can be used when data for the considered pure analyte are available [13]. The main idea of HLA is to obtain a limited number of factors of a data matrix in which the contribution of the analyte of interest has been removed, and is therefore based on net analyte signal (NAS) calculation. The net analyte signal (NAS) for analyte k (r^*k) is given by the following equation:

$$r^*k = [I - R_{-k}(R_{-k})^+]r = P_{NAS,kr} \quad (1)$$

where R is $J \times J$ orthogonal projection matrix which projects a given vector onto the NAS space, r is the spectrum of a given sample, I is $J \times J$ unitary matrix, R_{-k} is $J \times I$ a column space spanned by the spectra of all other analytes except k , $(R_{-k})^+$ is the pseudo-inverse of R_{-k} usually computed by singular value decomposition using A factors.

HLA HS method. There are different alternative approaches, which can be used in order to estimate the R_k matrix. One of them is proposed by Xu and Schechter [14]. Each spectrum from the calibration matrix is divided by its concentration, except for the zero concentrations, and the sum of the resulting spectra is calculated using the following equation (2):

$$s_{cal} = \frac{1}{I'} \sum_{i=1}^{I'} \frac{r_{i,cal}}{c_{ik}} \quad (2)$$

where I' is the number of the calibration samples for which c_{ik} is different from 0.

The resulting mean spectrum is obtained from the spectral matrix using the following equation (3):

$$(R_{-k})_{i',j} = R_{i',j} / c_{ik} - s_{cal,j}^T \quad (3)$$

The calibration spectra with $c_{ik} = 0$ are then added to the matrix from equation (3) and thus the desired matrix R_k is obtained. The net sensitivity vector s_k^* is calculated through projection of $s_{k,LS}$ on the NAS area, using least squares method approximation according to the following equation:

$$s_k^* = P_{NAS,k} \begin{bmatrix} R^T c_k \\ c_k^T c_k \end{bmatrix} \quad (4)$$

The concentration of κ for the unknown sample is calculated from the r spectrum using the equation (5), which is a basic step in the prediction for the methods, based on net analyte signal (NAS) [6].

$$c_{un,k} = \frac{s_k^T P_{NAS,k} r}{s_k^T P_{NAS,k} s_k} = \frac{s_k^T P_{NAS,k} P_{NAS,k} r}{s_k^T P_{NAS,k} s_k} = \frac{(s_k^*)^T r_k^*}{\|s_k^*\|^2} \quad (5)$$

HLA GO method. The applied HLA GO [11] method in this research involves the use of mean (uncentred) calibration profile. At first it is obtained as:

$$\bar{r}_{cal} = \frac{1}{I} \sum_{i=1}^I r_{i,cal} \quad (6)$$

where $r_{i,cal}$ is the profile for the i -th calibration sample. Then the contribution of analyte k is subtracted from the data matrix R in the following way:

$$R_{-k} = R - \frac{c_k \bar{r}_{cal}^T}{\bar{c}_{k,cal}} \quad (7)$$

where $\bar{c}_{k,cal}$ is the mean (uncentred) calibration concentration of analyte k . The calculation of net sensitivity (s_k^*) is then carried out according to the following equation:

$$s_k^* = P_{NAS,k} \begin{bmatrix} \bar{r}_{cal}^T \\ \bar{c}_{k,cal} \end{bmatrix} \quad (8)$$

NAP CLS method. The last possible approach to estimate the net sensitivity vector s_k^* and R_{-k} matrix includes approximation of $s_{k,LS}$ using least squares method for obtaining the R_{-k} matrix (equation 9) and s_k^* (equation 4).

$$R_{-k} = R - c_k s_{k,LS} \quad (9)$$

This method is called NAP CLS [11] and includes the following steps: (1) preprocessing of the raw initial spectral matrix R through projection on the space, orthogonal to the space of all mixture components, except for the k analyte, which results in obtaining the net analyte signal matrix R_k^* and regression of the obtained matrix with the concentrations using classical CLS procedure.

Figures of merits for the analytical method. Selectivity, sensitivity, signal to noise ratio, LOD

and LOQ are among the valuable analytical information that can be obtained from NAS [32]. MVC1 contains a special sub-routine, based on net analyte signal concept for estimation of figures of merit for the analytical method [31].

Determination of number of factors(A). The optimal number of principal factors is essential in building multivariate models [33]. The prediction error decreases with the number of factors used until an optimal value is reached. Most of the information is usually in the first factors but it is not guaranteed that the useful information is exclusively reserved to these factors. Full crossvalidation is the most used validation method, in which one reference at a time is removed from the calibration set, after that the same sample is predicted by using the calibration built with the other references. Several tests have been proposed to select the number of PCs.

The root mean square error of prediction (RMSEP) was chosen to express the prediction error when PLS1 and HLA/GO procedures were applied. This parameter represents an estimate of the error when other samples are predicted with that model. The best prediction ability of the models is reached when the prediction error is at its lowest value.

$$SEP = \frac{1}{C} \left[\frac{\sum_{i=1}^m (C_{pred} - C_{act})^2}{m} \right]^{\frac{1}{2}} \quad (10)$$

where C_{act} indicates the actual concentration in the sample, C_{pred} is predicted concentration, C is the mean of real concentrations in the validation set and m is the number of samples in the prediction set.

Another important statistical parameter in evaluating the model quality is R^2 . It represents an index of quality in fitting all data to a straight line and represents the fraction of total variance explained by the model. It is computed as:

$$R^2 = 1 - \frac{\sum_1^m (C_{act} - C_{pred})^2}{\sum_1^m (C_{act} - C)^2} \quad (11)$$

where C represents the mean of the true concentrations in the prediction set.

The last statistical parameter for evaluating the quality of validation is relative error of prediction:

$$REP(\%) = \frac{100}{C} \left[\frac{1}{I} \sum_1^m (C_{act} - C_{pred})^2 \right]^{\frac{1}{2}} \quad (12)$$

Softwares. The NAP/CLS, HLA/HS, HLA/GO and PLS1 algorithm was applied using the Toolbox MVC1 written for MATLAB [31],

because these routines allow one to evaluate the figures of merit based of the NAS theory.

RESULTS AND DISCUSSION

Spectral overlapping and data preprocessing

The zero-order UV spectra of PAR, PRO and CAF in a concentration ratio equivalent to the content of the commercial pharmaceutical formulation in water are shown in Fig.1. The wavelength range from 190–300 (56 wav) was selected because of the absence of absorbance after 300 nm for all of the drugs. It is obvious that the studied analytes in combination could not be determined directly in this spectral region because of strong overlapping.

Regression model building and wavelength optimization

With the aim to extract the most significant analytical information from the spectral region of 56 wavelengths the NAP/CLS, HLA/HS, HLA/GO and PLS1 calibration models were firstly developed on data. Selection of the optimum number of factors to be used within the all proposed algorithms allows one to model the system with the optimum amount of information. In the present work, cross-validation has been used to select the optimum number of factors. The statistical parameters of model prediction for both chemometric methods are presented in Table 1. A comparative study of the statistical parameters of all chemometric approaches was undertaken.

The models were validated by an external validation set. The results from the calibration methods with net analyte signal were much better when the calibration was carried out in a selected spectral region instead of the whole spectrum. The results from applying the NAP CLS, HLA GO, HLA XS and PLS1 methods for calibration with and without spectral selection are presented in table 1. The spectral selection was carried out using moving window strategy on the absorption spectra in order to define the most informative spectral regions [34]. As shown, without the wavelength selection the factors number was much smaller for the NAS methods compared to PLS. The RMSEP and REP values for PAR and PRO were lower with the NAS methods in comparison with PLS, whereas CAF showed similar RMSEP and REP values with NAS and PLS methods. The slope and intercept values for PRO were unsatisfactory.

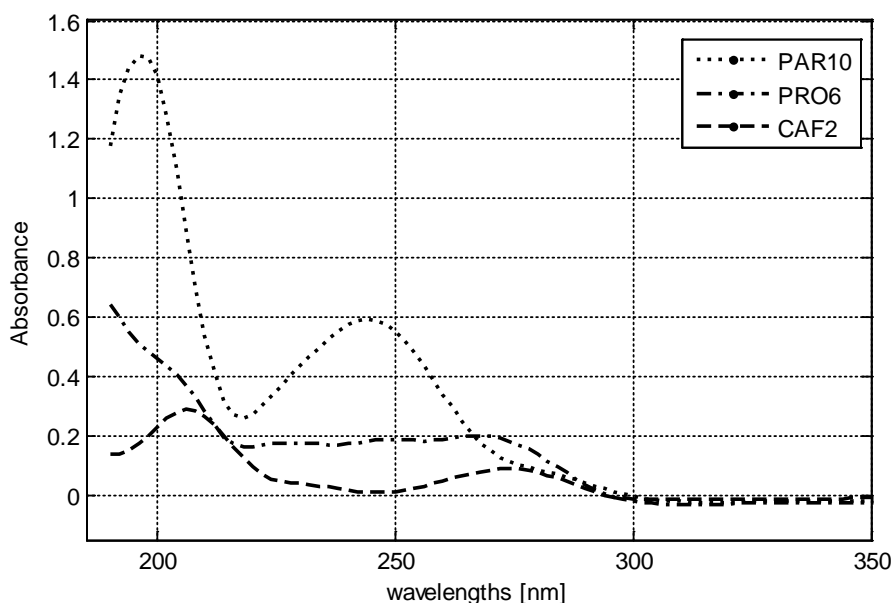


Fig.1. Absorbance spectra in water of paracetamol ($10 \mu\text{g mL}^{-1}$), propyphenazone ($6 \mu\text{g mL}^{-1}$) and caffeine ($2 \mu\text{g mL}^{-1}$).

After wavelength selection the number of the factors was significantly reduced. The obtained RMSEP values were much lower, especially for PRO and CAF. The estimated RMSEP and REP values were approximately the same and in some cases even better for the NAS calibration methods compared to PLS. For PRO and CAF the RMSEP and REP values were highly reduced after the spectral selection and were even lower for NAS than the PLS method. PRO showed the lowest values with HLA XS and CAF – with NAP CLS. Compared to the other two components, CAF had the lowest values for RMSEP and REP. After the wavelength selection PRO gave better values for the slope and the intercept.

Analytical figures of merit

Net-analyte signal (NAS) is a suitable method to characterize the analytical figures of merit related to the multivariate calibration during drugs quantification [35]. NAS calculations, in fact, could be applied for univariate, classical and inverse multivariate calibration [36]. For classical multivariate calibration, the basic equation that is needed to estimate figures of merit is:

$$s_k^* = [I - S_k S_k^+] s_k, \quad (13)$$

where S is the matrix of sensitivities collected for the other solutes (other than the solute of interest), s_k is the sensitivity vector of the analyte, and s_k^* is the estimated net part of the k -th component that is orthogonal to the other constituents [37].

The best candidate for s_k is the pure spectrum of the analyte of interest. NAS is necessary to find

meaningful parameters to assess the analytical performance of multivariate calibration like sensitivity (SEN), selectivity (SEL), limit of detection (LOD), limit of quantification (LOQ).

SEN was estimated from the net signal of analyte k (s_k^*) as $\|s_k^*\|$ [37]. SEL which measures the extent of spectral overlapping was estimated as $\|s_k^*\|/\|s_k\|$ [37]. LOD which gives the minimum detectable amount of the solute k was given as $3\|\varepsilon\|/\|s_k^*\|$ [35]. The minimum quantifiable amount of the solute was estimated as $10\|\varepsilon\|/\|s_k^*\|$ [35]. In the former two equations, $\|\varepsilon\|$ represents the instrumental noise which was estimated by recording five spectra of the blank over the range 190-300 nm (2 nm resolution). Then the norms of blank readings ($\|NAS_{blank}\|$) were estimated, and $\|\varepsilon\|$ was taken as the standard deviation of estimated norms [35]. Analytical sensitivity (γ) was given as:

$$\gamma = \frac{SEN}{\|\varepsilon\|}$$

The estimated figures of merit of the three drugs are presented in Table 2.

Sensitivity (SEN), selectivity (SEL), analytical sensitivity (γ), and limit of detection (LOD) were estimated using MVC1 toolbox, containing a special sub-routine based on net analyte signal concept for estimation of figures of merit for the analytical method. Estimated FOM for PAR, PRO and CAF were determined with all algorithms and used to compare analytical methods. The obtained results are given in Table 3.

Table 1. Comparison of validation parameters of NAP CLS, HLA GO, HLA XS and PLS1 methods before and after wavelength selection for the three components

Component	Statistical parameters	Multivariate methods				
		NAP CLS		HLA GO		
PAR	Sensor range(nm)	190-300	250-268	190-300	250-268	
	Factors	4	2	4	2	
	RMSEP($\mu\text{g mL}^{-1}$)	0.1921	0.1636	0.2271	0.1550	
	REP(%)	2.52	2.14	2.97	2.03	
	R ²	0.9968	0.9977	0.9956	0.9979	
	Slope	1.0504	0.9786	1.0603	0.9753	
	Intercept	-0.2476	0.1850	-0.3007	0.1507	
	Recovery(%) (RSD)	101.82(1.04)	100.28 (2.25)	102.2(0.88)	100.08(2.02)	
			HLA XS		PLS	
	Sensor range(nm)	190-300	250-268	190-300	250-268	
	Factors	4	2	8	3	
	RMSEP($\mu\text{g mL}^{-1}$)	0.1625	0.1952	0.3160	0.1512	
	REP(%)	2.13	2.56	4.14	1.98	
	R ²	0.9977	0.9968	0.9916	0.9981	
Slope	1.0113	0.9827	0.9597	0.9701		
Intercept	-0.0651	0.2143	-0.0056	0.2172		
Recovery(%) (RSD)	100.93 (2.14)	101.14(2.51)	95.77(1.75)	99.80 (1.78)		
PRO		NAP CLS		HLA GO		
	Sensor range(nm)	190-300	230-248	190-300	210-278	
	Factors	6	2	7	5	
	RMSEP($\mu\text{g mL}^{-1}$)	0.4822	0.2084	0.5203	0.4236	
	REP(%)	8.84	3.82	9.54	7.77	
	R ²	0.9453	0.9898	0.9363	0.9578	
	Slope	0.9211	0.9381	0.8667	0.9162	
	Intercept	-0.1249	0.0561	0.1110	0.6046	
	Recovery(%) (RSD)	90.02(3.19)	95.60(1.28)	89.0(4.78)	104.4(7.69)	
			HLA XS		PLS1	
	Sensor range(nm)	190-300	240-268	190-300	210-278	
	Factors	9	2	10	6	
	RMSEP($\mu\text{g mL}^{-1}$)	0.5150	0.1729	0.7082	0.2609	
	REP(%)	9.44	3.17	12.98	4.78	
R ²	0.9376	0.9930	0.8819	0.9839		
Slope	0.8827	0.9737	0.7004	0.9110		
Intercept	0.1173	0.1076	0.9740	0.1497		
Recovery(%) (RSD)	89.75(9.34)	102.13(1.95)	90.08(8.60)	95.73(3.79)		
CAF		NAP CLS		HLA GO		
	Sensor range(nm)	190-300	220-278	190-300	210-258	
	Factors	6	5	6	5	
	RMSEP($\mu\text{g mL}^{-1}$)	0.1467	0.0353	0.1471	0.0954	
	REP(%)	4.42	1.01	4.43	2.87	
	R ²	0.8597	0.9927	0.8592	0.9407	
	Slope	0.9309	0.9288	0.9282	1.0277	
	Intercept	0.0117	0.0346	0.0272	0.1054	
	Recovery(%) (RSD)	93.93(8.20)	99.96(3.32)	94.69(8.5)	93.86(4.21)	
			HLA XS		PLS1	
	Sensor range(nm)	190-300	210-258	190-300	210-258	
	Factors	6	5	7	5	
	RMSEP($\mu\text{g mL}^{-1}$)	0.1674	0.0608	0.1289	0.0441	
	REP(%)	5.04	1.83	3.89	1.33	
R ²	0.8176	0.9759	0.8917	0.9873		
Slope	1.0823	0.9542	0.9205	0.9288		
Intercept	-0.2713	0.1312	0.0385	0.0346		
Recovery(%) (RSD)	88.93(8.41)	99.57(4.36)	94.91(7.13)	102.02(3.94)		

Table 2. Figures of merits of PAR, PRO, CAF for NAP CLS and HLA GO methods.

Figure of merit	NAP CLS		HLA GO		HLA XS		PLS1	
	PAR							
Range(nm)	190-300	250-268	190-300	250-268	190-300	250-268	190-300	250-268
A	4	2	4	2	4	2	8	3
SEL	0.13	0.012	0.14	0.012	0.13	0.012	0.074	0.013
SEN ^a	0.064	0.0022	0.066	0.0022	0.065	0.0022	0.036	0.0023
γ	8.6	6.6	8.6	7.8	8.4	6.1	12	6.8
LOD ^b	0.35		0.35		0.36		0.33	0.41
PRO								
Range(nm)	190-300	230-248	190-300	210-278	190-300	240-268	190-300	210-278
A	6	2	7	2	9	5	10	6
SEL	0.05	0.02	0.041	0.017	0.033	0.012	0.03	0.016
SEN ^a	0.024	0.0043	0.019	0.0042	0.016	0.0044	0.014	0.0063
γ	8	20	6.9	6.4	6.8	3.4	5.8	4.7
LOD ^b	0.39		0.46		0.46		0.30	0.36
CAF								
Range(nm)	190-300	220-278	190-300	210-258	190-300	210-258	190-300	210-258
A	6	5	6	5	6	5	7	5
SEL	0.15	0.03	0.15	0.04	0.17	0.035	0.16	0.06
SEN ^a	0.063	0.0079	0.064	0.012	0.069	0.01	0.066	0.018
γ	21	17	20	9.1	22	7.7	22	11
LOD ^b	0.14		0.15		0.14		0.13	0.099

^a SEN and analytical sensitivity (γ) measure the changes in response as a function of the concentration (mL μg^{-1}).

^b Limit of detection (LOD) is the lowest concentration of an analyte that can be detected, but not necessarily quantified ($\mu\text{g mL}^{-1}$).

Table 3. Assay results from application of NAP CLS, HLA XS, HLA GO and PLS on the pharmaceutical tablet Saridon®.

Method	Drug	A	Sensor range(nm)	Recovery(%) (RSD)
NAP CLS	PAR	4	190-300	98.41 (2.49)
		2	250-268	98.98 (3.13)
	PRO	6	190-300	88.49 (1.29)
		2	230-248	103.94 (0.99)
	CAF	6	190-300	89.44 (2.32)
		4	250-298	94.70 (2.73)
HLA XS	PAR	4	190-300	95.53 (2.15)
		2	250-268	99.54 (3.09)
	PRO	4	190-300	95.53 (2.15)
		2	250-268	99.54 (3.09)
	CAF	6	190-300	75.89 (1.37)
		4	220-298	99.14 (3.59)
HLA GO	PAR	4	190-300	98.90 (2.41)
		2	250-268	99.14 (3.12)
	PRO	7	190-300	84.96 (2.35)
		7	210-288	87.16 (0.74)
	CAF	6	190-300	88.51 (2.03)
		4	270-298	93.61 (2.85)
PLS	PAR	8	190-300	92.52 (2.36)
		3	250-268	98.71 (3.12)
	PRO	10	190-300	88.57 (1.19)
		6	210-278	104.92 (0.72)
	CAF	7	190-300	96.43 (2.43)
		6	260-288	96.43 (2.43)

Analysis of commercial formulations

Again, as shown, the number of factors was smaller for the NAS methods, compared to PLS. After the wavelength selection the estimated recoveries for all three components of the Saridon® tablet were much higher.

CONCLUSIONS

A comparative study on the application of multivariate calibration methods NAP/CLS, HLA/HS, HLA/GO and PLS1 for simultaneous determination of paracetamol (PAR), propyphenzone (PRO) and caffeine (CAF) has been

performed using data extracted from UV spectra. In general, comparable results were obtained after applying net-analyte signal methods compared with PLS-1 model using less factors for paracetamol and propyphenazone. Only for caffeine determination PLS1 model give slightly better results. As a conclusion after applying the studied methods for calibration – the most suitable model for the determination of PAR is HLA GO, whereas for the analysis of PRO and CAF it is better to use respectively HLA XS and NAP CLS.

REFERENCES

- 1.S. Lekova, D. Tsankova, *Journal of Chemical Technology and Metallurgy (JCTM)*, **52**, 52 (2017).
- 2.D. Tsankova, S. Lekova, *Journal of Chemical Technology and Metallurgy (JCTM)*, **50**, 638 (2015).
- 3.D. Tsankova, S. Lekova, K. Nikolova, G. Terziiski, *Annals of Faculty Engineering Hunedoara – International Journal of Engineering, Romania*, **XIII**, 275 (2015).
4. I. Vlaeva, Kr. Nikolova, I. Bodurov, M. Marudova, D. Tsankova, S. Lekova, A. Viraneva, T. Yovcheva, *IOP Conf. Series: Journal of Physics, Conf. Series*, **794**, 012034, (2017).
- 5.M.Tobiszewski, M.Nedyalkova, S. Madurga, F. Pena-Pereira, J. Namieśnik, V. Simeonov, *Ecotoxicology and environmental safety*, **147**, 292 (2018).
- 6.M.A., Nedyalkova, B.V. Donkova, V. D. Simeonov, *Journal of AOAC International*, **100**, 359 (2017).
- 7.M. Nedyalkova, H. Hristov, V. Simeonov, *Open Chemistry*, **15**, 61 (2017)
- 8.M. Wiczerzak, B. Kudlak, G. Yotova, M. Nedyalkova, S.Tsakovski, V.Simeonov, J. Namieśnik *Science of the Total Environment*, **571**, 259 (2016).
- 9.J. Gabrielsson, N. Lindberg, T. Lundstedt, *Journal of Chemometrics* **16** (3), 141 (2002).
- 10.I. Singh, P. Juneja, B. Kaur, P. Kumar, *Analytical Chemistry*, Article ID 795178, **13** (2013).
11. R. Ergon, *Chemom. Intell. Lab. Syst.*, **81**, 68 (2006).
12. B. Hemmateenejad, R. Ghavami, R. Miri, M. Shamsipur, *Talanta*, **68**, 1222 (2006).
13. A.J. Berger, T. Koo, I. Itzkan, M.S. Feld, *Anal. Chem.*, **70**, 623 (1998).
14. L. Xu, I. Schetcher, *Anal. Chem.* **69**, 3722 (1997).
15. H. C. Goicoechea, A.C. Olivieri, *Anal. Chem.* **71** 4361 (1999).
16. A. Espinosa-Mansilla, I.D. Merás, M.J.R Gómez, A.M. de la Peña, F. Salinas, *Talanta*, **58**(2), 255 (2002).
17. R.G. Brereton, *Analyst*, **122** (12), 1521 (1997).
18. V. Rodenas, M.S. Garcia, C. Sanchez-Pedreno, M. I. Albero, *Talanta*, **52**, 517 (2000).
19. B. Ward, J.M. Alexander-William, *Acute Pain*, **2**, 140 (1999).
20. J.K. Aronson, *Meyler's Side Effects of Drugs: The International Encyclopedia of Adverse Drug Reactions and Interactions* (15th ed.), Elsevier Science, Amsterdam, 2006.
21. A. Smith, *Food Chem. Toxicol.*, **40**, 1243 (2002).
22. N. Iqbal, B. Ahmad, K.H. Janbaz, *Biopharm. Drug Dispos.*, **16**, 481 (1995).
23. H.G. Kraetsch, T. Hummel, J. Lötsch, R. Kussat, G. Kobal, *Eur. J. Clin. Pharmacol.*, **49**, 377 (1996).
24. E. Dinç, G. Kökdil, F. Onur, *Journal of Pharmaceutical and Biomedical Analysis*, **26**, 769 (2001).
25. A. Hałka-Grysińska, P. Ślęzak, G. Zaręba, W. Markowski, A. Klimek-Turek, T.H. Dzido, *Anal. Methods*, **4**, 973 (2012).
26. D. Emre, N. Özaltın, *J. Chromatogr. B*, **847**, 126 (2007).
27. A. Domínguez-Vidal, A. Molina Díaz, *Microchimica Acta*, **141**, 157 (2003).
28. E. Dinc, C. Serin, F. Tugcu-Demiroz, T. Doganay, *International Journal of Pharmaceutics*, **250**, 339 (2003).
29. M. De Luca, F. Oliverio, G. Ioele, G. Ragno, *Chemometrics and Intelligent Laboratory Systems*, **96**, 14 (2009).
30. G. Gergov, A. Alin, M. Doychinova, M. De Luca, V. Simeonov, Y. Al-Degs, *Bulgarian Chemical Communications*, **49** (2), 410 (2017).
31. A.C. Olivieri, H.C. Goicoechea, F.A. Inon, *Chemometrics and Intelligent Laboratory Systems*, **73**, 189 (2004).
32. H.C. Goicoechea, A.C. Olivieri, *Trends Anal. Chem.*, **10**, 599 (2000)
33. D.M. Haaland, E.V. Thomas, *Anal. Chem.*, **60**, 1193 (1988)
34. L. Xu, I. Schechter, *Anal. Chem.* **68**, 2392 (1996)
35. S. Yousefinejad, B. Hemmateenejad, *Drug Test. Anal.*, **4**, 507 (2012).
36. V. Lorber, K. Faber, B. Kowalski, *Anal. Chem.*, **69** 1620 (1997).
37. Y. S. Al-Degs, *Food Chemistry*, **117**, 485 (2009).

МЕТОДИ, ОСНОВАВАЩИ СЕ НА НЕТНИЯ СИГНАЛ НА АНАЛИТА ЗА ЕДНОВРЕМЕННО ОПРЕДЕЛЯНЕ НА ПАРАЦЕТАМОЛ, ПРОПИФЕНАЗОН И КАФЕИН ЧРЕЗ УВ СПЕКТРОФОТОМЕТРИЯ

Г. Гергов^{1*}, А. Алин², П. Кацаров³, В. Симеонов⁴, Д. Янков⁵, И. Ал-Дегс⁶

¹ Департамент по химия, Факултет по фармация, Медицински университет, София 1000, ул. Дунав 2, България

² Департамент по статистика, Университет Докуз Ейлул, Измир, Турция

³ Департамент по фармацевтични науки, Фармацевтичен факултет, Медицински университет-Пловдив, 4002, бул. Васил Априлов 15а, България

⁴ Лаборатория по хеометрия и енвиронметрия, Факултет по химия и фармация, Софийски университет „Св. Кл. Охридски“, София 1164, бул. Дж. Баучер 1, България

⁵ Институт по инженерна химия, Българска академия на науките, 1113 София, ул. Акад. Г. Бончев, бл. 103, България

⁶ Департамент по химия, Университет Хашемит, Зарка, Йордания

Постъпила на 18 юли, 2017 г.; приета на 8 септември 2017 г.

(Резюме)

Три различни метода, основаващи се на нетния сигнал на анализа - NAP CLS, HLA/GO и HLA XS, са приложени успешно за определяне на тройни смеси от парацетамол, пропифеназон и кофеин. Абсорбционни УВ спектрални данни са използвани за разделяне на тази сложна система с припокриващи се спектри на лекарствата. Редуциран ортогонален дизайн на пет нива е използван за формиране на калибрационна система, включваща трите съединения. Хеометричните модели са проверени с помощта на външна валидационна система от данни с концентрации в обсега на калибриране. Всички предложени хеометрични алгоритми са приложени успешно за определяне на горните съединения във фармацевтичната таблетна форма *Saridon*®. Получените резултати показват, че методът, основаващ се на нетния сигнал на анализа дава подобни резултати на тези с метода на частичните най-малки квадрати. В допълнение, използването на концепцията за нетния сигнал на анализа позволява да се изчислят аналитичните параметри. Използвана е стратегия на подвижен прозорец на дължината на вълната, която значително намалява броя на факторите и подобрява аналитичните добиви.

Study on copper ions adsorption from aqueous solution by Emeraldine

S. I. Lavrova-Popova^{1*}, Z. L. Yaneva², G. I. Hlebarov¹, B. K. Koumanova¹

¹University of Chemical Technology and Metallurgy, 8 Kliment Ohridski Blvd., Sofia 1756, Bulgaria.

²Trakia University, Students Campus, 6000 Stara Zagora, Bulgaria.

Received December 7, 2017; Revised February 5, 2018

The influence of *in situ* synthesized emeraldine (salt and base) on the removal of copper ions from aqueous media is discussed. Physicochemical parameters such as initial copper ion concentration, emeraldine dosage and contact time between adsorbent and Cu(II) ions in aqueous solution were studied. An assessment of the equilibrium and the kinetics of sorption of copper ions was made. The experimental results were fitted to the isotherms of Langmuir, Freundlich, Toth and Baudu. It was established that the Toth and Baudu isotherms are suitable for the case of emeraldine salt. The Langmuir model gave satisfactory correlation with the experimental results only in the low concentration range of copper ion sorption using emeraldine base. The maximum sorption capacity of emeraldine base at 50 mg.dm⁻³ initial copper ions concentration (q_e^{\max} 7.5 mg.g⁻¹) was higher than that of the emeraldine salt. Probably, the mechanism of copper ions sorption includes physisorption, chemisorptions, as well as intraparticle diffusion during the later stages of the process.

Keywords: *In situ* polymerization, Emeraldine, Copper ions removal, Aqueous medium.

INTRODUCTION

The wastewaters generated from printed board manufacturing, metal finishing and plating, semiconductor manufacturing, textile dyes production, and others, as well as the landfill leachates, contain toxic heavy metals such as arsenic, lead, mercury, cadmium, chromium, copper, nickel, and zinc. Many heavy metals are essential trace elements for humans, animals and plants in small amounts, but in larger amounts cause acute and chronic toxicity. Despite the treatment processes used, some quantities of the heavy metals remain in the treated industrial wastewater [1]. The widely used processes for industrial wastewater treatment are chemical precipitation, ion exchange, adsorption, membrane filtration, photocatalysis, flotation and electrochemical processes [2]. Among them adsorption and complexation are the most convenient and simple methods. It is well known that the adsorption efficiency depends on the type and properties of the sorbent. Different polymeric compounds such as polyaniline, polypyrrole, chitosan, etc., are used [3-6]. The aniline polymerization leads to production of polyaniline in three idealized oxidation states – leucoemeraldine, emeraldine and (per)nigraniline [7, 8]. Emeraldine exists as emeraldine salt and emeraldine base. The deprotonated emeraldine base has more free electron pairs in its structure in comparison with the protonated emeraldine salt, which contributes to the better complexation ability of this polyaniline form [9, 10].

The aim of this study was to synthesize both emeraldine salt and base, and to study their application for copper ions removal from aqueous media.

EXPERIMENTAL

The experiments were carried out with pure for analysis aniline (C₆H₅NH₂), hydrochloric acid (HCl), ammonium persulfate ((NH₄)₂S₂O₈), sodium hydroxide (NaOH), CuSO₄·5H₂O, sodium acetate (C₂H₃NaO₂) and acetic acid (CH₃COOH). Distilled water was used throughout.

Emeraldine salt synthesis

Emeraldine was synthesized through oxidative polymerization using aniline monomer (C₆H₅NH₂) and ammonium persulfate ((NH₄)₂S₂O₈) as an oxidant. Distilled aniline was diluted with 1 M HCl to 2 l in a volumetric flask. Ammonium persulfate was diluted with distilled water to 800 ml and both solutions were cooled in a refrigerator at 5 °C. After that the oxidant solution was added dropwise to the 0.5 M aniline solution. The mixture was stirred at room temperature for 1 h and then was left to polymerize. The greenish-black suspension of emeraldine salt was filtered and the precipitate was washed several times with distilled water. After dewatering it was dried in an oven at 40 °C to constant mass. The dried polymer was ground to a fine homogeneous powder.

Emeraldine base synthesis

Protonated emeraldine salt was converted to emeraldine base through washing with 1 M NaOH to pH 10.0 – 11.0. The polymer was dried at 40 °C to

* To whom all correspondence should be sent
E-mail: engeco2001@uctm.edu

constant mass and after that was ground to a fine homogeneous powder.

Preparation of standard solutions of copper ions

Initial stock solution with concentration of 1 g.dm⁻³ of Cu²⁺ was prepared using CuSO₄.5H₂O, diluted with freshly distilled water to 1 l. Then standard solutions with concentrations of 1.0, 2.0, 4.0, 6.0, 8.0, 10.0, 30.0, and 50.0 mg.dm⁻³ were prepared.

Equilibrium study

The adsorption equilibrium for the removal of copper ions was studied using 50 cm³ of aqueous solutions containing Cu²⁺ from 1 to 50 mg.dm⁻³ contacting with 0.1 g of the two forms of emeraldine (salt and base). Shaking was carried out until equilibrium was achieved.

The amount of adsorption at equilibrium [11] in mg.g⁻¹ was computed as follows:

$$q_e = \frac{(C_o - C_e)V}{m} \quad (1)$$

where C_o and C_e are the initial and equilibrium copper ion concentrations (mg.dm⁻³), respectively, V is the volume of solution (dm³) and m (g) is the mass of the polymer.

Kinetic study

The adsorption kinetics was studied using 50 cm³ of aqueous solutions containing 50 mg.dm⁻³ Cu²⁺ contacting with 0.1, 0.5, 1.0 and 1.5 g of two forms of emeraldine (salt and base). The samples were taken for analysis at 1, 3, 5, 7, 10, 15, 30, 60 and 360 min, respectively.

The efficiency of Cu²⁺ removal by polyaniline was calculated according to the formula:

$$RE, \% = 100 - \left(\frac{C_t}{C_o}\right) 100 \quad (2)$$

where C_o is the initial Cu²⁺ concentration and C_t is the concentration at time t in mg.dm⁻³.

Instrument and measurements

Inductively coupled plasma – optical emission spectroscopy ("Prodigy" High dispersion ICP-OES, Tellelyne Leeman Labs) was used for determination of the copper ions concentration. In order to avoid Cu²⁺ precipitation, the pH of the aqueous solutions was adjusted to 5 with acetate buffer [12].

Modelling

In this study the obtained results were fitted into the isotherms of Langmuir, Freundlich, Toth and Baudu, and the kinetic experimental data were analysed by comparative estimation of the applicability of the pseudo-first order (PFO), pseudo-second order (PSO), the mixed pseudo-

first/pseudo-second order (MFSO) kinetics models, as well as by the intraparticle diffusion (ID) model [13-18] by non-linear regression analyses.

RESULTS AND DISCUSSION

Equilibrium study

Figures 1 and 2 present the experimental equilibrium data of the copper ions sorption on emeraldine salt and base, respectively, and the applied four isotherm models: Langmuir, Freundlich, Toth and Baudu. The calculated isotherm model parameters for both investigated systems, as well as the values of the error functions are presented in Table 1.

The shape of the experimental isotherm of Cu²⁺ sorption on emeraldine salt outlines two sections: an initial gradual increase of the ions concentration in the solid phase followed by a tendency for equilibrium establishment in the low concentration range (C_o 5-15 mg.dm⁻³), and a subsequent sharp, almost linear sorption capacity increase in the middle and high concentration range C_o 15-36 mg.dm⁻³.

The error analyses proved commensurable applicability of the four equilibrium models due to the approximately equal values of R², SSE, MSE and RMSE.

Baudu has remarked that the calculation of the Langmuir coefficients, b and q_{mL}, by the measurement of tangents at different equilibrium concentrations shows that they are not constants in a broad concentration range. He has transformed the Langmuir equation to the following expression:

$$q_e = \frac{q_{m0}b_0C_e^{(1+x+y)}}{1 + b_0C_e^{(1+x)}} \text{ with } (1+x+y) \text{ and } (1+x) < 1 \quad (3)$$

where q_e is the adsorbed amount at equilibrium (mg.g⁻¹), C_e is the equilibrium concentration of the adsorbate (mg.dm⁻³), q_m is the Baudu maximum adsorption capacity (mg.g⁻¹), b₀ is the equilibrium constant, and x and y are the Baudu parameters. For lower surface coverage, this equation reduces to the Freundlich model, i.e.:

$$q_e = \frac{q_{m0}b_0C_e^{(1+x+y)}}{1 + b_0} \quad (4)$$

The predicted monolayer sorption capacity of the emeraldine salt by the Baudu model was q_m = 2.117 mg.g⁻¹ (Table 1), while by the Langmuir equation the determined value of the parameter was q_m = 81.924 mg.g⁻¹. Considering the fact that the experimentally obtained maximum equilibrium capacity of the sorbent was q_e 6.6 mg.g⁻¹, the Langmuir q_m value is unacceptable. The latter observation questions the accuracy of the two-parameter model, although, according to the plots in Figure 1 and the very close

Table 1. Values of the equilibrium model parameters and error functions.

System	Copper ions-Emeraldine salt				Copper ions-Emeraldine base			
	Equilibrium model	Model parameters		Error function	Equilibrium model	Model parameters		Error function
Langmuir	q _m	8.251	R ²	0.976	q _m	81.924	R ²	0.987
	b	0.179	SSE	1.555	b	0.003	SSE	1.699
			MSE	0.222			MSE	0.340
			RMSE	0.471			RMSE	0.583
Freundlich	K _f	0.267	R ²	0.986				
	n _f	0.903	SSE	1.729				
			MSE	0.346				
			RMSE	0.588				
Toth	q _{mT}	249.289	R ²	0.995	q _{mt}	390.063	R ²	0.987
	K _T	1.082	SSE	0.232	K _t	85.706	SSE	1.724
	m _T	0.596	MSE	0.039	mt	0.596	MSE	0.431
			RMSE	0.197			RMSE	0.657
Baudu	q _m	4.952	R ²	0.995	q _m	2.117	R ²	0.986
	b _o	0.50	SSE	0.235	b _o	0.135	SSE	1.732
	x	-0.638	MSE	0.047	x	-0.770	MSE	0.577
	y	0.240	RMSE	0.217	y	0.728	RMSE	0.760

values of the calculated by non-linear regression analyses error functions R², SSE, MSE and RMSE, the four model isotherms almost overlapped and equally fitted to the experimental equilibrium data of copper sorption on the emeraldine salt.

Besides, the adsorption capacity predicted by the four mathematical models - approximately 6.9 mg.g⁻¹, was approximately equal to the experimentally obtained value.

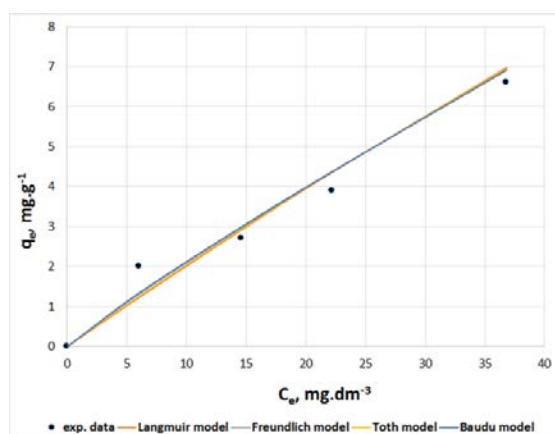


Fig. 1. Experimental and model isotherms of the copper ions sorption on emeraldine salt.

From a statistical point of view, due to the higher number of isotherm parameters in Toth and Baudu empirical models, it could be accepted that they simulate the model variations more accurately. In the absence of a theoretical model that could account for the chemical heterogeneity of the surface, and simultaneous prevalence of different sorption mechanisms, isotherm models having a greater number of model constants are able to better predict the system behavior.

Toth has modified the Langmuir equation to reduce the error between experimental data and predicted values of equilibrium adsorption data. The application of his equation is best suited to multilayer adsorption similar to BET isotherms which is a special type of Langmuir isotherm and has very restrictive validity. The Toth correlation is given as:

$$q_e = \frac{q_{mT} C_e}{(1/K_T + C_e^{m_T})^{1/m_T}} \quad (5)$$

where q_e is the adsorbed amount at equilibrium (mg.g⁻¹), C_e is the equilibrium concentration of the adsorbate (mg.dm⁻³), q_{mT} is the Toth maximum adsorption capacity (mg.g⁻¹), K_T is the Toth equilibrium constant, and m_T is the Toth model exponent. Besides, the model is useful in describing heterogeneous adsorption systems, which satisfy both low- and high-end boundaries of the concentration.

The experimental isotherm for the system copper ions/emeraldine base (Figure 2) is characterized with well-balanced tendency towards equilibrium establishment. The Langmuir adsorption isotherm is based on the assumption that maximum adsorption occurs when a saturated monolayer of adsorbate molecules is present on the adsorbent surface, the energy of adsorption is constant, and there is no migration or interaction between the adsorbate molecules in the surface plane. However, according to the shapes of the experimental and model isotherms presented in Figure 2, obviously, the Langmuir model gave satisfactory correlation with the experimental results only in the low concentration range. A tendency similar to the one observed for the system copper ions/emeraldine salt

with regard to the values of the monolayer capacity predicted by the Langmuir and Baudu models was outlined. The comparative analyses of the experimentally determined maximum equilibrium capacity ($q_e^{exp} = 7.5 \text{ mg.g}^{-1}$) and the q_m values of 8.251 mg.g^{-1} (Langmuir model) and 4.952 mg.g^{-1} (Baudu model) (Table 1) proved the predominant accuracy of the four-parameter model. The isotherms in Figure 2 display unsatisfactory correlation between the experimental equilibrium data and the Freundlich model in the high concentration region due to the observed significant deviation between the modes of both isotherms. The latter conclusion was proved by the power value of the regression coefficient and the higher values of the SSE, MSE and RMSE functions (Table 1) as compared to these of the Toth and Baudu models.

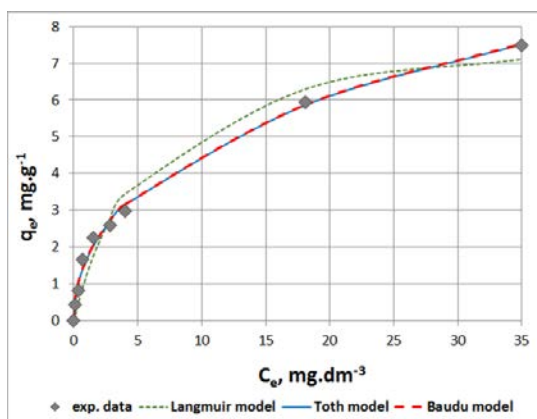


Fig. 2. Experimental and model isotherms of the copper ions sorption on emeraldine base.

Thus, according to the modes of the four model isotherms and the values of the error functions calculated by non-linear regression analyses (Table 1), it could be concluded that the sorption behavior of the copper ions on emeraldine base at equilibrium conditions was best represented by the three- and four-parameter models of Toth and Baudu, respectively, as they are characterized with the highest correlation coefficients (R^2 0.995) and the lowest SSE, MSE and RMSE values.

Kinetic study

The kinetics behaviour of copper ions during their adsorption on emeraldine salt and base was described by four kinetics models: the pseudo-first, pseudo-second, mixed pseudo-first/pseudo-second order models, and the intraparticle diffusion model (Table 2).

The experimental kinetic curve of the copper ions sorption on emeraldine salt, plotted as $C_t = f(t)$ (Figure 3), revealed the highest sorption rate in the initial stages of the process. The system reached equilibrium within the first 10 min after the beginning of the process. The highest adsorption capacity attained was $q_t = 7.1 \text{ mg.g}^{-1}$ and the highest removal efficiency of the copper ions was 29.6 %. The experimental data were modelled by the pseudo-first order, pseudo-second order, the mixed pseudo-first/pseudo-second order kinetics models, as well as by the intraparticle diffusion model. The values of the calculated kinetic parameters and error functions are presented in Table 2.

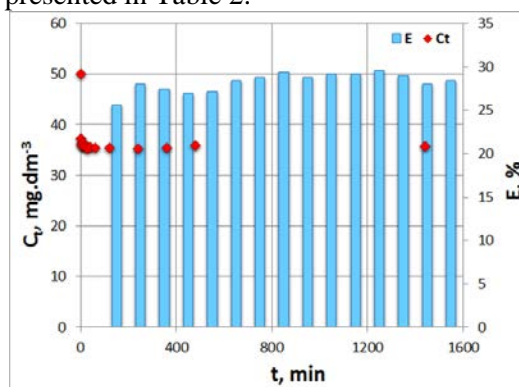


Fig. 3. Experimental kinetic curve and efficiency of the copper ions sorption on emeraldine salt.

The analyses of the experimental data, model parameters and error functions proved that the mixed order model satisfactorily correlated the kinetic experimental data of the copper ions sorption on emeraldine salt (Table 2, Figure 4).

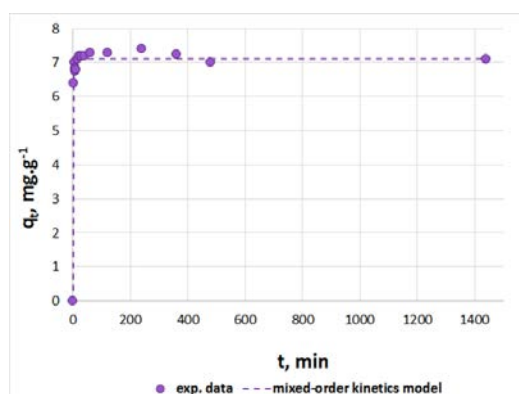


Fig. 4. Mixed order kinetics model for the system copper ions-emeraldine salt; a) initial kinetics curve section.

Table 2. Values of the kinetic model parameters and error functions for the systems copper ions-emeraldine base and copper ions-emeraldine salt.

Polymer	Mass, g	PFO model				PSO model				Intraparticle diffusion model				Mixed order model						
		k_1	Model parameter q_e	R_1^2	Error function MSE	k_2	Model parameter q_e	R_2^2	Error function MSE	k_1	Model parameter k_2	R_{11}^2	Error function R_{12}^2	k_1	Model parameter f	R^2	Error function MSE	RMSE		
Polyaniline salt	0.1	0.01	0.871	0.458	2.198	1.512	0.0240	7.0323	0.9113	0.064	0.325	0.1972	0.0182	0.6223	0.8905	1.471	0.991	0.990	0.048	0.219
	0.1	4.483×10^{-4}	0.595	0.488	0.098	0.312	1.416×10^{-2}	0.591	0.504	84.929	9.216	0.0232	0.0109	0.7726	0.6507	0.2904	0.3712	0.998	0.016	0.128
Polyaniline base	0.5	1.552×10^{-3}	0.593	0.594	0.763	0.873	8.915×10^{-2}	1.913	0.961	104.751	10.235	0.0521	0.0004	0.9914	0.9716	0.1920	0.2297	0.918	0.094	0.307
	1.0	1.309×10^{-3}	0.942	0.991	0.007	0.083	4.822×10^{-2}	0.218	0.911	62.788	7.924	0.0469	0.0095	0.9466	0.9640	0.039	1.2×10^4	0.923	0.053	0.230
1.5	1.315×10^{-3}	0.555	0.912	0.077	0.278	0.234	0.0407	0.759	7.492×10^{-2}	86.557	0.0388	0.0018	0.9832	0.9122	0.081	422.39	0.959	0.015	0.122	

Model	Equation
Non-linear form	$\frac{dq_t}{dt} = k_1(q_e - q_t)$ (6)
Linear expression	$\log(q_e - q_t) = \log q_e - \frac{k_1}{2.303} t$ (7)
Non-linear form	$\frac{dq_t}{dt} = k_2(q_e - q_t)^2$ (8)
Linear expression	$\frac{1}{q_e - q_t} = \frac{1}{q_e} + k_2 t$ (9)
Non-linear form	$q_t = k_1 t^{0.5} + I$ (11)
Linear expression	$\ln\left(\frac{1-F}{1-f_2 F} = -k_1 t\right)$ (13)
	$F = \frac{q_t}{q_e}$ (14)
	$f_2 = \frac{k_2 q_e}{k_1 + k_2 q_e}$ (15)

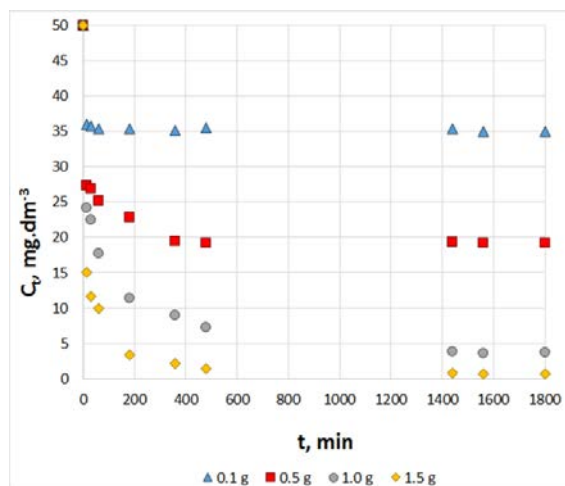


Fig. 5. Experimental kinetic curves of copper ions sorption on emeraldine base – effect of adsorbent mass.

The experimental kinetic curves of the copper ions sorption on polyaniline base, plotted as $C_t = f(t)$ (Figure 5), displayed that the sorption rate in the initial stages of the process was the highest.

The removal efficiency at the fifteenth min was 28, 45.4, 51.6 and 70 %, using 0.1, 0.5, 1.0 and 1.5 g of emeraldine base, respectively. The system reached equilibrium approximately 400 min after the beginning of the process. The highest adsorption capacity attained was $q_t = 7.5 \text{ mg.g}^{-1}$ with 0.1 g emeraldine base. An increase in removal efficiency with increasing adsorbent mass was observed. The increase in the sorbent mass contributes to the increase in surface area and number of active sites. The optimal removal efficiency of 97.14 %, using 1.5 g of emeraldine base was achieved after approximately 400 min. Simultaneously, with emeraldine mass increasing, its adsorption capacity decreased. The lowest adsorption capacity attained was $q_t = 1.6 \text{ mg.g}^{-1}$ with 1.5 g emeraldine base after 1800 min. After that, no significant removal was observed, probably due to the saturation of the active sites. The experimental data were modelled by the pseudo-first order, pseudo-second order, the mixed pseudo-first/pseudo-second order kinetics models, as well as by the intraparticle diffusion (ID) model. The values of the calculated kinetic parameters and error functions are presented in Table 2. According to the experimental results and model data, the kinetics behavior of the studied system with 0.1 g of emeraldine base was best described by the mixed order model (Table 2, Figure 6). The experimental series with 0.5 g and 1.5 g emeraldine base were best represented by the intraparticle diffusion model. The highest values of the correlation coefficient (R_1^2 0.991) and the lowest values of the error functions SSE, MSE and RMSE characterized the pseudo-first order model applied to the system copper ions-emeraldine base (1.0 g) (Table 2, Figure 7).

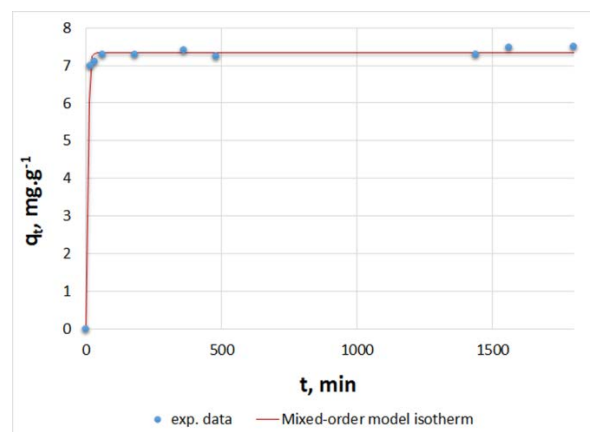


Fig. 6. Mixed order kinetic model for the system copper ions-emeraldine base (0.1 g emeraldine base); a) initial kinetics curve section.

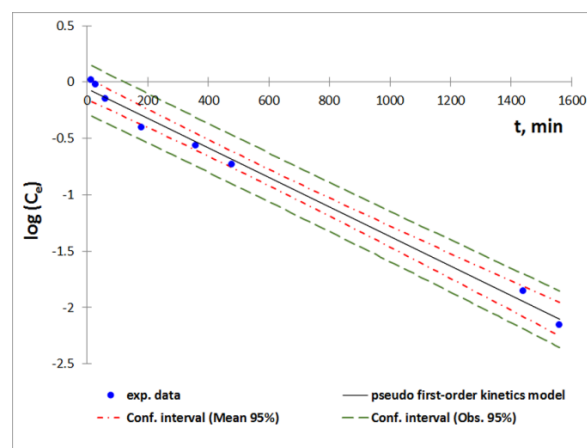


Fig. 7. Linear regression of the pseudo first-order kinetics model for the system copper ions-emeraldine base (1.0 g emeraldine base).

CONCLUSIONS

The comparative analyses of the equilibrium experimental data for the sorption behavior of the copper ions on emeraldine salt and base outlined that the base displayed higher affinity, as the attained maximum sorption capacity at 50 mg.dm^{-3} initial copper ions concentration ($q_e^{\text{max}} 7.5 \text{ mg.g}^{-1}$) was approximately 1.14 times higher than that for the salt compound.

Based on the above stated observations for the sorption behaviour of both investigated systems, an explicit conclusion whether chemisorption or intraparticle diffusion was the general rate controlling mechanism during the copper ions sorption on emeraldine base and salt could not be withdrawn due to the close values of the statistical errors. Probably, the mechanism of sorption included physisorption, chemisorption and intraparticle diffusion during the later stages of the process.

REFERENCES

1. J. Garbarino, H. Hayes, D. Roth, R. Antweiler, T. Brinton, H. Taylor, in: U.S. Geological survey circular 1133, R. Meade (ed.), Reston, Virginia, 1995.
2. M. Barakat, *Arabian J. Chem.*, **4**, 361 (2011).
3. N. Mahato, N. Parveen, M. H. Cho, *Mater. Lett.*, **161**, 372 (2015).
4. A. Speltini, M. Sturini, F. Maraschi, A. Profumo, *Trends Environ. Anal. Chem.*, **10**, 11 (2016).
5. B. Wang, Y. Zhu, Z. Bai, R. Luque, J. Xuan, *Chem. Eng. J.*, **325**, 350 (2017).
6. P. Kanmani, A. Jeyaseelan, M. Kamaraj, P. Sureshbabu, K. Sivashanmugam, *Bioresour. Technol.*, **242**, 295 (2017).
7. J. Stejskal, P. Kratochvil, A. D. Jenkins, *Collect. Czech. Chem. Commun.*, **60**, 1747 (1995).
8. G. Ćirić-Marjanović, *Synth. Met.*, **177**, 1 (2013).
9. J. Stejskal, R. Gilbert, *Pure Appl. Chem.*, **74**, 5, 857 (2002).
10. R. Borah, S. Baerjee, A. Kumar, *Synth. Met.*, **197**, 225 (2014).
11. M. Vanderborght, E. Van Grieken, *Anal. Chem.*, **49**, 311 (1977).
12. Md. Awual, I. Rahman, T. Yaita, Md. Khaleque, M. Ferdows, *Chem. Eng. J.*, **236**, 100 (2014).
13. N. Ayawei, A. N. Ebelegi, D. Wankasi, *J. Chem.*, (Hindawi), **2017**, 11 (2017).
14. K. Foo, B. Hameed, *Chem. Eng. J.*, **156**, 1, (2010).
15. O. Amrhar, H. Nassali, M. S. Elyoubi, *J. Chem. Pharm. Res.*, **7**, 892 (2015).
16. H. Boparai, M. Joseph, D. O'Carroll, *J. Hazard. Mater.*, **186**, 458 (2011).
17. A. Günay, I. Tosun, *J. Hazard. Mater.*, **146**, 362 (2007).
18. Y. Ho, *Water Res.*, **40**, 119 (2006).

ИЗСЛЕДВАНЕ НА АДСОРБЦИЯТА НА МЕДНИ ЙОНИ ОТ ВОДЕН РАЗТВОР С ИЗПОЛЗВАНЕ НА ЕМЕРАЛДИН

С. И. Лаврова-Попова^{1*}, З. Л. Янева², Г. И. Хлеббаров¹, Б. К. Куманова¹

¹Химикотехнологичен и металургичен университет, бул. Климент Охридски 8, София 1756, България

²Тракийски университет, Студентски кампус, 6000 Стара Загора, България

Постъпила на 7 декември, 2017 г.; коригирана на 5 февруари, 2018 г.

(Резюме)

Обсъдено е влиянието на *in situ* синтезиран емералдин (сол и база) върху отстраняването на медни йони от водни разтвори. Определени са физикохимични параметри като начална концентрация на медни йони, количество емералдин и време на контакт между адсорбента и Cu(II) йони във воден разтвор. Оценени са равновесието и кинетиката на сорбция на медните йони. Експерименталните резултати са приложени към изотермите на Langmuir, Freundlich, Toth и Vaudu. Установено е, че изотермите на Toth и Vaudu са подходящи за описване на сорбцията с емералдинова сол. Моделът на Langmuir дава задоволителна корелация с експерименталните резултати само при ниски концентрации на медни йони с използване на емералдинова база. Максималният сорбционен капацитет на емералдиновата база при начална концентрация на медните йони $50 \text{ mg} \cdot \text{dm}^{-3}$ ($q_e^{\max} 7.5 \text{ mg} \cdot \text{g}^{-1}$) е по-висок от този на емералдиновата сол. Най-вероятно, сорбционният механизъм на медните йони включва физисорбция, хемисорбция и дифузия в частиците при последните етапи на процеса.

Insight into polymer-borate hybrid films - structural approach

H. Hristov, M. Nedyalkova*, V. Simeonov

*Faculty of Chemistry and Pharmacy, University of Sofia „St. Kl. Ohridski“,
J. Bourchier Blvd. 1, Sofia 1164, Bulgaria*

Received: July 1, 2017; Revised: January 18, 2018

Transparent organic-inorganic hybrid films (mass ratio PVA/PEG/B₂O₃=10/7/1) are obtained by polymer-assisted sol-gel synthesis and solution-casting method at ambient temperature. An aqueous solution of boric acid (H₃BO₃) and ethanol solution of trimethyl borate ((CH₃O)₃B) with pH adjustment are used as sources of cross-linking borate units. Surface morphology and structure of the obtained hybrid films are studied by scanning electron microscopy (SEM), Fourier transform infrared (FTIR) spectroscopy and X-ray diffraction (XRD). XRD indicated that amorphous structure with poor crystallinity is formed. SEM showed a homogeneous and microporous surface free of crystallites. The results of FTIR spectroscopy revealed that the borate unit types and chemical bonds in the hybrid network are functionally dependent on the type of boron-containing solution and pH. The most crosslinked hybrid structure including a large number of polyborate ions is obtained from an aqueous solution of H₃BO₃ at pH 10. Based on spectral data a probable crosslinking mechanism in the hybrid network consisting of B-O-C bonds of ester complexes and hydrogen bonds is proposed.

Keywords: Organic-inorganic hydrogels; Polymer-borate hybrid films; Poly(ethylene glycol); Poly(vinyl alcohol); Boric acid.

INTRODUCTION

Hydrogels are subject to considerable attention in the past 50 years, due to their excellent promise in a wide range of applications. They also have a degree of flexibility very comparable to natural tissue due to their significant water content. The biocompatibility properties and swelling effects in biological conditions make them an ideal class of materials for biomedical applications, such as drug delivery and tissue engineering. It is essential to develop biodegradable materials by modification of traditional natural or non-degradable polymers about specific environmental problems. Commercially available biodegradable polymers are mainly limited to the natural polysaccharides, aliphatic polyesters, and polyethers, for example, polyethylene glycol (PEG), polyvinyl alcohol (PVA) [1-6].

PVA is a water-soluble polymer, employed in practical applications due to its excellent chemical resistance, biocompatibility, good film-forming capability, non-toxicity, and biodegradability in the presence of suitable microorganisms. The properties of PVA make it particularly interesting for the industrial elaboration of new environmentally friendly biomaterials. PVA-hydrogels obtained in the presence of crosslinking agents (a second polymer, an inorganic species or organically modified nanostructures) produce materials with a significant change in structure and

properties [3-13].

PEG possesses properties such as high hydrophilicity, solubility in water and organic solvents, biocompatibility and absence of immunogenicity, antigenicity, toxicity. (PEG)-based hydrogels are applied as optically transparent photoactive substrates, solid polymer electrolytes, biomedical and cosmetic materials with tunable properties. Polymer blends and organic-inorganic hydrogels based on PVA/PEG are extensively studied for material packaging, anti-microbial films, contact lenses, real-time immunoassays, tissue engineering matrices, acid-resistant biomembranes and drug delivery systems [1-5, 10-14].

H₃BO₃ is a weak Lewis acid possessing antibacterial properties, and in dilute aqueous solutions, B(OH)₄⁻ and B(OH)₃ species are existing simultaneously. At a concentration higher than 0.025M and pH between 7 and ten a shifting of acid-base equilibrium occurs, and various stable polyborate anions are formed [15]. The crosslinking efficiency of borate ions is well known, as well as the formation of diol complexes so that H₃BO₃ relatively well dissolves in polyvalent alcohols and polysaccharides to obtain organic-inorganic hydrogels with biomedical applications [16-21].

The purpose of this study is the preparation of PVA/PEG/Borate hybrid films by different boron-containing solutions and respective pH adjustment, as well as their structural-morphological characterization by XRD, FTIR and SEM. A

* To whom all correspondence should be sent
E-mail: mici345@yahoo.com

probable crosslinking mechanism of the polymer-borate hybrid network based on infrared spectral data is proposed.

EXPERIMENTAL

Transparent self-standing hybrid films with mass ratio PVA/PEG/B₂O₃= 10/7/1 are obtained by the sol-gel process and solution casting method at an ambient temperature as referred in our previous studies [22-24]. The following analytical grade reagents are used: polyvinyl alcohol 72000 (PVA)-98% hydrolyzed, polyethylene glycol 400 (PEG), trimethyl borate (CH₃O)₃B, boric acid (H₃BO₃), ammonia solution 25% (NH₃.H₂O). Stock solutions of 4wt. % PVA and 4wt. % H₃BO₃ are prepared in double distilled water, while 4wt. % (CH₃O)₃B in ethanol. The pH value is adjusted of 5 to 10 by ammonia solution (absent of alkali ions). The hydrogels are made by initially mixing and homogenization of relevant amounts of PEG and boron containing solutions, after that PEG-borate mixture is added to the PVA by constant stirring. PVA-PEG-borates viscous solutions are cast onto glass plates, dried at ambient temperature for one week, after that the dried films are peeled off. The surface morphology is observed by SEM (JEOL JSM 5510). XRD is carried out on Siemens D500 diffractometer. FTIR spectra of starting materials and obtained hydrogel films are recorded a Bruker Tensor 27 instrument.

RESULTS AND DISCUSSION

The SEM micrographs of hybrid films prepared of the boric acid solution are presented in Figure 1.

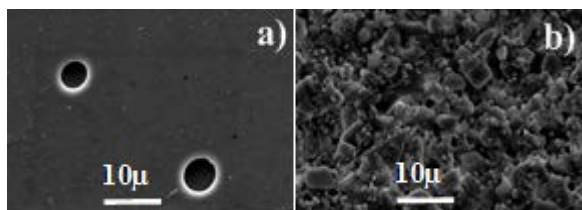


Fig. 1. SEM images of PVA/PEG/Borate hybrid films prepared from an aqueous solution of H₃BO₃ at (a) pH 5 and (b) pH 10.

The surface morphology of the hybrid film, obtained from boric acid solution without adjustment of pH (pH=5) is shown as a relatively homogeneous microporous surface structure with large single surface pores and free of crystallites (Fig.1a). The absence of microstructure in the SEM picture also indicates the amorphous as well as homogeneous nature of the samples. The surface of the film obtained by a boric acid solution with pH correction (pH=10) is different. The micrograph

shows the presence of roughness and randomly distributed structural aggregates (Fig.1b).

The structure of PVA/PEG/borate hybrid film is studied by XRD. The X-ray diffraction pattern of the sample obtained by boric acid solution without adjustment of pH (pH=5) is represented in Figure 2.

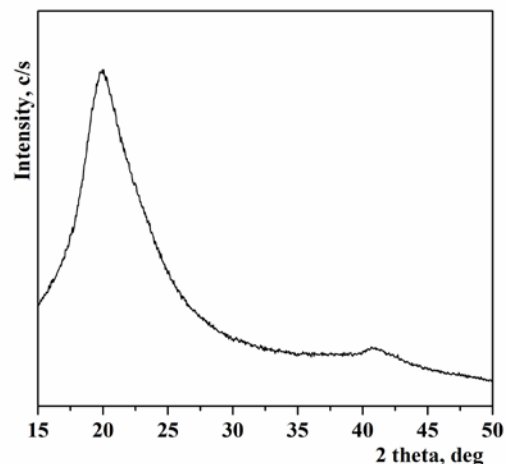


Fig. 2. XRD pattern of PVA/PEG/Borate hybrid film prepared from an aqueous solution of H₃BO₃.

The diffractogram contains an amorphous halo at 19.7 deg2θ (relatively broad peak) and a diffused peak at 40.9 deg2θ, originating from the semi-crystalline nature of PVA. There are no reflections indicating crystallization of boric acid. XRD confirmed the homogeneous and amorphous structure of the hybrid film-observed by SEM.

The structural changes caused by cross-linking of polymers and hydrated borate species derived from different solutions at different pH values are studied by FTIR spectroscopy. IR spectra of the starting polymer compounds and aqueous solutions of boric acid (pH 10 and pH 5) are presented in Figures 3 and 4, respectively.

The following vibrational modes are assigned to the chemical bonds in polymer compounds (Fig. 3): 3700-3100 cm⁻¹ (ν_sH-OH, ν_sC-OH, hydrogen bonds), 2850-2960 cm⁻¹ (ν_sCH₂), 2300-1900 cm⁻¹ (δ hydrogen bonds), 1650 cm⁻¹ (bending of H₂O), 1460 cm⁻¹ (O-H and δCH₂), 1380 cm⁻¹ (δ_{as}CH₃), 950 cm⁻¹ (γC-OH), 780-850 cm⁻¹ (bending vibrations of CH₂). Absorption bands in the regions 1330-1220 cm⁻¹ (δC-OH) and 1065-1020 cm⁻¹ (νC-OH) can be attributed to the primary alcohol (PEG), while these the in intervals 1370-1260 cm⁻¹ (δC-OH) and 1120-1080 cm⁻¹ to (νC-OH) from the secondary alcohol (PVA). Absorption bands in the region 1200-970 cm⁻¹ are related to C-O bonds, while these in the area of 1100-1000 cm⁻¹ are related to C-O-C stretching vibrations of esters [1, 2, 10-24].

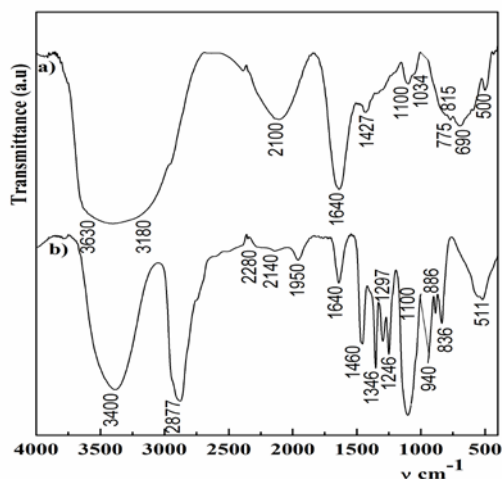


Fig. 3. FTIR spectra of (a) 4% aqueous solutions of PVA, (b) PEG₄₀₀.

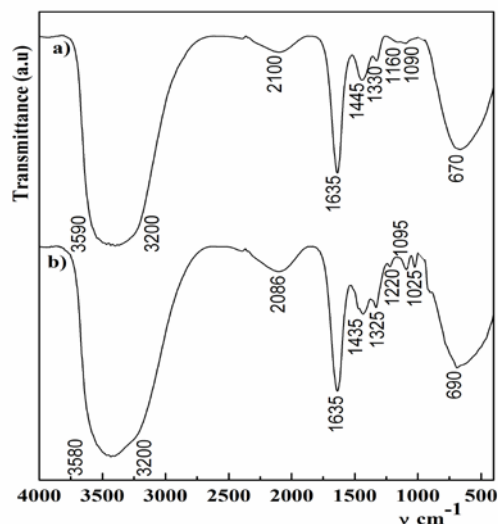


Fig. 4. FTIR spectra of 4 % aqueous solution of H₃BO₃ at (a) pH 10, (b) pH 5.

The main structural units under which boron exists in crystals, glasses and aqueous solutions are BO₃ and BO₄ groups and their rearrangement leads to superstructural species such as pentaborate, triborate, diborate, a.g. The B-O bonds frequency regions are 1500-1200 cm⁻¹ (νB-O of BO₃), 1200-850 cm⁻¹ (νB-O of BO₄) and 800-600 cm⁻¹ (bending vibrations for various borate segments). The bands in the intervals 1440-1430 cm⁻¹, 1330-1220 cm⁻¹, 690-660 cm⁻¹ are related only to BO₃ units of orthoborates (BO₃³⁻), metaborates (BO₂⁻), pyroborates (B₂O₅⁴⁻) (Fig. 4). The vibrational frequencies at 1430 cm⁻¹, 1320 cm⁻¹, 1220 cm⁻¹, 1090 cm⁻¹, 690 cm⁻¹ are assigned to pentaborates (B₅O₈⁻) and these at 1430 cm⁻¹, 1320 cm⁻¹, 1020 cm⁻¹, 915 cm⁻¹, 690 cm⁻¹ - to triborates (B₃O₅⁻) [22-28]. The spectrum changes when pH of an aqueous solution of boric acid is adjusted to pH 10 (Fig 4a). The main differences affect the band at 1220 cm⁻¹,

which is shifted to higher wavenumber-frequency of 1500-1200 cm⁻¹. At the same time, new bands appear in the region 1160-1080 cm⁻¹ related to BO₄ groups, probably tetraborates and diborates (B₄O₇²⁻: 1445 cm⁻¹, 1330 cm⁻¹, 1160-1080 cm⁻¹, 670 cm⁻¹). These effects are explained by partial transformation of BO₃ to BO₄ and are reported in [25-28].

FTIR spectra of hybrid films prepared from aqueous solutions of H₃BO₃ and ethanol solutions of (CH₃O)₃B (pH 10 and pH 5) are presented in Figures 5 and 6, respectively.

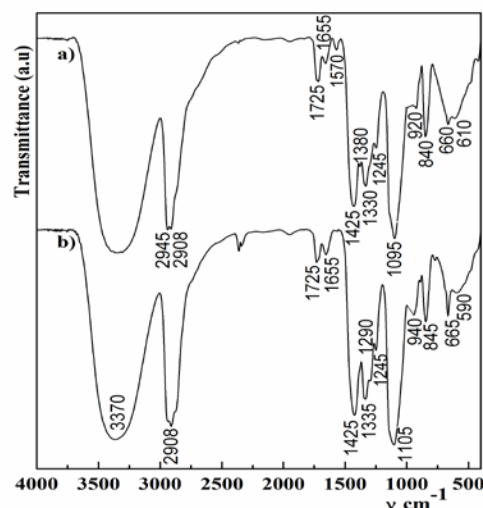


Fig. 5. FTIR spectra of hybrid films prepared with an aqueous solution of H₃BO₃ at (a) pH 10, (b) pH 5.

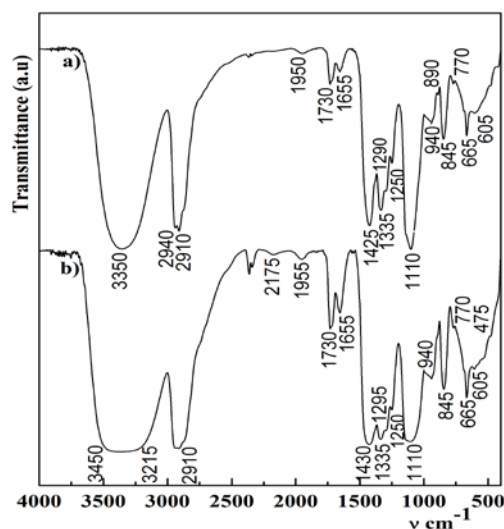


Fig. 6. FTIR spectra of hybrid films prepared with an ethanol solution of (CH₃O)₃B at (a) pH 10, (b) pH 5.

The comparison of FTIR spectra of the polymer-borate films and these of initial compounds indicates that the main changes are associated with characteristic frequencies concerning OH groups of PEG and H₃BO₃. The characteristic bands of the hybrid film obtained from an aqueous solution of

H_3BO_3 are shifted compared with the original vibrations of PEG.

Two types of crosslinking interactions between inorganic and organic components are observed - hydrogen bonding and ester type. It can be seen that absorption modes 2908 cm^{-1} (vsCH_2), 1655 cm^{-1} (bending vibration of H_2O), and 590 cm^{-1} (bending vibration of OH^-) are displaced to higher wavenumbers compared to PEG and PVA (Fig. 5). The same tendency is observed with absorption bands at 1105 cm^{-1} (C-O-C or C-O-B of esters) and 845 cm^{-1} (rocking mode of CH_2), overlapping with the region of BO_4 groups ($1200\text{--}850\text{ cm}^{-1}$). Furthermore, the absence of absorption bands in the region $2280\text{--}1950\text{ cm}^{-1}$ and frequency was shifting from 3400 cm^{-1} to 3370 cm^{-1} is due to the appearance of intermolecular hydrogen bonds. Hydrogen bonding interaction between the polymers and different boron species in solutions as well as water molecules is taking place. Replacement of intramolecular hydrogen bonds (present in all precursors) with intermolecular (involved in all hybrid films) is reported in [23, 24]. The opposite tendency is observed for absorption bands at 1425 cm^{-1} , 1335 cm^{-1} , 1290 cm^{-1} (C-OH of PEG), being shifted to lower wave number frequencies. In this interval are also included the specific modes concerning BO_3 groups ($1500\text{--}1200\text{ cm}^{-1}$). Based on these effects the formation of PEG-borate ester complexes including BO_3 and BO_4 groups is assumed. Polymer-borate ester bonds (B-O-C) are expected to be in the absorption interval $1400\text{--}1000\text{ cm}^{-1}$ concerning C-OH, C-O-C, and B-O (from BO_3 and BO_4 units) chemical bonds. The characteristic frequency of B-O-C bonds is noted at 1030 cm^{-1} and is reported in [16-18]. The FTIR spectrum of a hybrid film prepared from aqueous solutions of H_3BO_3 at pH 10 shows differences expressed by the higher BO_4/BO_3 ratio (Fig. 5a). The absorption bands assigned to B-O bonds in BO_4 groups are shifted to lower wave number frequencies (1095 cm^{-1} , 920 cm^{-1} , 840 cm^{-1}), and their intensities are increased. Moreover, the intensity of bands near to 1100 cm^{-1} (BO_4 groups) increases simultaneously with the decrease in those in the region $1425\text{--}1250\text{ cm}^{-1}$ (BO_3 groups). This is indirect evidence that the organic-inorganic borate films obtained from aqueous solutions of H_3BO_3 at pH 10 contain more PEG- BO_4 crosslinked structures.

FTIR spectra of films obtained from an ethanol solution of $(\text{CH}_3\text{O})_3\text{B}$ at pH 10 are similar to those of films prepared with aqueous solutions of H_3BO_3 without pH correction (Fig. 6a). This fact is explained with the low degree of hydrolysis of

$(\text{CH}_3\text{O})_3\text{B}$ in ethanol, i.e. negligible amounts of hydrated borate ions, respectively crosslinked PEG- BO_4 containing structures exist. When the synthesis is carried with an ethanol solution of trimethyl borate without pH adjustment, there is almost no hydrolysis (in a solution lacking hydrated borate ions) and the network is represented mainly by hydrogen bonding. The films are completely soluble in contrast to these obtained by aqueous solutions of H_3BO_3 that swell [23].

Taking into account the spectral data, the following crosslinked PEG-borate structures involved in the construction of the hybrid network are proposed (Fig. 7). It is suggested that PVA-PEG-Borate network is based on initially crosslinked PEG-borate ester complexes entanglement through hydrogen bonds to long PVA chains.

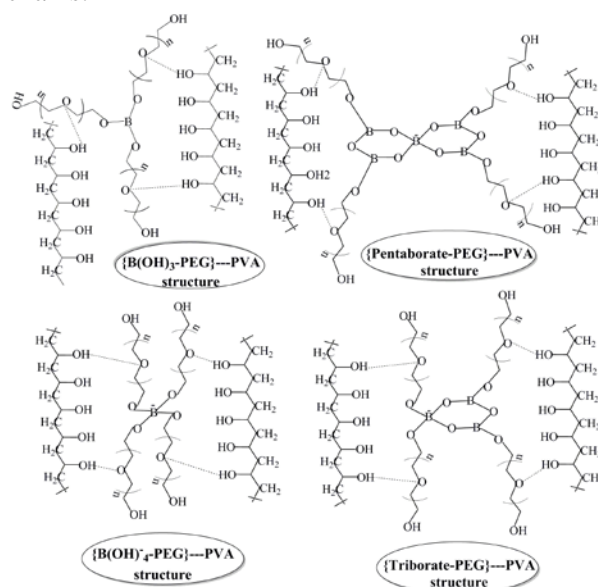


Fig. 7. A possible mechanism for the formation of PVA/PEG/Borate hybrid network based on cross-linked PEG-borate structures.

CONCLUSIONS

Transparent PVA/PEG/Borate hybrid films are prepared under different conditions by polymer-assisted sol-gel process and solution casting method.

The amorphous, homogeneous and microporous nature of the hybrid materials was confirmed by SEM and XRD analyses.

By FTIR spectroscopy it was found that the types of borate units and chemical bonds in the hybrid network are functionally dependent on the type of boron-containing solution and pH. The BO_4/BO_3 ratios, type of crosslinking, final structure and morphology of hybrid network are depending on experimental conditions. The best crosslinking hybrid structures with a predominant amount of

polyborate ions are obtained from an aqueous solution of H_3BO_3 at pH 10.

Based on FTIR data a probable mechanism of the formation of a hybrid network involving PEG-borate ester complexes linked through the hydrogen bonds of PVA chains is supposed.

Acknowledgments: Authors are grateful to Operational programme "Science and Education for Smart Growth", project BG05M2OP001-2.009-0028 and to National Science Fund (NSF), project DCOST 01/6 - 2017

REFERENCES

1. H. S. Mansur, R. L. Orefice, A. A. P. Mansur, *Polymer*, **45**, 7193 (2004).
2. K. A. Tawab, M. M. Magida, S. M. Ibrahim, *J. Polym. Environ.*, **19**, 440 (2011).
3. E. Carretti, S. Grassi, M. Cossalter, I. Natali, G. Caminati, R. G. Weiss, P. Baglioni, L. Dei, *Langmuir*, **25**, 8656 (2009).
4. A. S. Hoffman, *Adv. Drug Deliv. Rev.*, **54**, 3 (2002).
5. D. Myung, P. E. Duhamel, J. R. Cochran, J. Noolandi, C. N. Ta, C. W. Frank, *Biotechnol. Prog.*, **24**, 735 (2008).
6. J. Maitra, V. K. Shukla, *Am. J. Polym. Sci.*, **4**, 25 (2014).
7. E. Chiellini, A. Corti, S. D'Antone, R. Solaro, *Prog. Polym. Sci.*, **28**, 963 (2008).
8. N. Rescignano, E. Fortunati, S. Montesano, C. Emiliani, J. M. Kenny, S. Martino, I. Armentano, *Carbohydr. Polym.*, **99**, 47 (2014).
9. H. Awada, C. Daneault, *Appl. Sci.*, **5**, 840 (2015).
10. M. Türk, M. Zakir, O. Rzayev, G. Kurucu, *Health*, **2**, 51 (2010).
11. M. S. Hahn, *Mater. Matters*, **5.3**, 62 (2010).
12. V. Saez-Martinez, G. Atorrasagasti, B. Olalde, I. Madarieta, F. Morin, N. Garagorri, *Int. J. Polym. Mater. Polym. Biomater.*, **62**, 502 (2013).
13. Z. W. Abdullah, Y. Dong, I. J. Davies, S. Barbhuiya, *Polym.-Plast. Technol. Eng.*, **56**, 1 (2017).
14. Y. Zhang, L. Ye, *Polym.-Plast. Technol. Eng.*, **50**, 776 (2011).
15. R. E. Mesmer, C. F. Baes, F. H. Sweeton, *Inorg. Chem.*, **11**, 537 (1972).
16. I. Uslu, H. Daştan, A. Altaş, *e-Polym.*, **133**, 1 (2007).
17. S. Mondal, A. K. Banthia, *J. Eur. Ceram. Soc.*, **25**, 287 (2005).
18. M. Das, S. Ghatak, *Bull. Mater. Sci.*, **35**, 99 (2012).
19. N. Roy, N. Saha, T. Kitano, P. Saha, *Soft Mater.*, **8**, 130 (2010).
20. I. Colinet, L. Picton, G. Muller, D. Le Cerf, *Carbohydr. Polym.*, **69**, 65 (2007).
21. Y. Kato, K. Suwa, S. Yokoyama, T. Yabe, H. Ikuta, Y. Uchimoto, M. Wakihara, *Solid State Ionics*, **152-153**, 155 (2002).
22. H. Hristov, P. Vasileva, N. Riskov, C. Dushkin, *J. Optoelectron. Adv. Mater.*, **11**, 1343 (2009).
23. P. Vasileva, H. Hristov, N. Riskov, C. Dushkin, *Nanoscience and Nanotechnology*, E. Balabanova and I. Dragieva (eds.), Sofia, **10**, 201 (2010).
24. H. Hristov, P. Vasileva, M. Nedialkova, *Nanoscience and Nanotechnology*, E. Balabanova and E. Mileva (eds.), Sofia, **12**, 47 (2012).
25. E. Kamitsos, A. Patsis, M. Karakassides, G. Chyrssikos, *J. Non-Cryst. Solids*, **126**, 52 (1990).
26. Krogh-Moe, *Phys. Chem. Glasses*, **6**, 46 (1965).
27. E. Kamitsos, M. Karakassides, G. Chyrssikos, *J. Phys. Chem.*, **91**, 1073 (1987).
28. G. Ramadevudu, S. R. L. Srinivasa, M. S. A. Hameed, M. C. Narasimha, *Int. J. Eng. Sci. Technol.*, **3**, 6998 (2011).

ПОГЛЕД КЪМ ХИБРИДНИ ПОЛИМЕР-БОРАТНИ ФИЛМИ – СТРУКТУРЕН ПОДХОД

Хр. Христов, М. Недялкова*, В. Симеонов

Факултет по химия и фармация, Софийски университет „Св. Кл. Охридски“, бул. Дж. Баучер 1, София 1164, България

Постъпила на 1 юли, 2017 г.; коригирана на 11 януари, 2018 г.

(Резюме)

Прозрачни органично-неорганични филми (масово съотношение PVA/PEG/ $B_2O_3=10/7/1$) са получени чрез полимерно асистиран зол-гелен синтез и формоване из разтвор при стайна температура. Воден разтвор на борна киселина (H_3BO_3) и етанолов разтвор на триметилборат ($(CH_3O)_3B$) с определено рН са използвани като източници на омрежващи боратни единици. Повърхностната морфология и структурата на получените хибридни филми са изучени с помощта на сканираща електронна микроскопия (SEM), Fourier трансформираща инфрачервена спектроскопия (FTIR) и рентгенова дифракция (XRD). XRD сочи че се образува аморфна структура със слаба кристалинност. SEM показва хомогенна микропореста повърхност, свободна от кристалини. Резултатите от FTIR спектроскопията показват, че видовете боратни единици и химичните връзки в хибридната мрежа са функционално зависими от вида на бор-съдържащия разтвор и рН. Най-силно омрежената хибридна структура, включваща голям брой полиборатни йони, се получава от воден разтвор на борна киселина при рН 10. Въз основа на спектралните данни е предложен вероятен механизъм на омрежването в хибридната мрежа, състояща се от В-О-С връзки на естерни комплекси и водородни връзки.

Nonlinear predictive control based on artificial neural network model for pilot reformer plant: Approach for ratio control

B. Parvizi*, A. Khanlarkhani, Y. Palizdar

Institute of Material and Energy (MERC), Karaj, Iran

Received: November 23, 2017; Revised: January 9, 2018

The reformer box is an important operation unit in many refineries such as petrochemical, oil refineries and DRI (direct reduction of iron) production plants for producing syngas from different hydrocarbons. As the heart of a DRI production plant in MIDREX technology, it is very crucial to control the syngas composition in desired condition, especially hydrogen to carbon monoxide ratio which should be kept in a limited range of 1.6-2 to achieve the most proper reducing gas for converting the iron pellets to sponge iron with best percentage of carbon. In operation, this process package is difficult to handle from control stand point due to its nonlinear behavior, multivariable interaction and existence of constraints on its different reaction conditions. Neural network techniques have been increasingly used for a wide variety of applications where statistical methods have been traditionally employed. In this work we proposed a multi input multi output (MIMO) feed forward neural network based multivariable control strategy to simultaneously control the inlet gas composition and reaction temperature, to control the outflow gas composition in desired condition. Modeling and controlling were investigated by use of data collected from a methane reforming pilot plant using CO₂ and steam, in process conditions near to those in a MIDREX reforming plant in sponge iron production. Different reaction temperatures from 700 to 1100 °C with different values of gases were randomly selected and used to generate around 5000 data sets of input- output data structure. Gas conversions and H₂/CO ratio were considered as the set points and tracking results of each showed the effective performance of the neural network- model predictive control (NN-MPC) strategy in this application.

Key words: Neural network, model predictive control, reformer, DRI plant

INTRODUCTION

Model predictive control (MPC) is now the most widely implemented advanced process for the control of technology. Control algorithms use an explicit process model to predict the future performance of a plant and the term “model predictive control” came from this definition. The most important section of MPC is choosing the model as it can simplify and accelerate the controller if selected properly. Although plants normally operate in a nonlinear manner, most of the MPC techniques implemented are based on linear models, which is mainly for their easier implementation, stability and general robustness in comparison to nonlinear ones which are relatively more complex. Generally, nonlinear modeling methods can be divided in two main groups: fundamental and empirical. The first group includes theoretical and mathematical relations focused on mass, energy, momentum balance and kinetics of reactions. Such methods are very useful in case of availability of mechanistic information. These methods have been widely used in MPC for some processes that exhibit highly nonlinear behavior, as well as large operating regions, such as different reactors for oil and gas production [3-5]. The second one includes data from driven models which can relate the input- output data

in a dynamic mode *via* black box estimators. One of these methods is the neural network, which has become an attractive tool in developing models for various types of complex non-linear systems [6,7]. A neural network-based predictive controller usually will be designed for non-linear systems with an iterative multilayer network prediction model in a predictive strategy. Moreover, addition of different constraints in MPC is a feature that makes this method prominent to other control strategies.

One of the process systems, which is full of nonlinearities, is the reformer package which converts hydrocarbons, mainly methane, to syngas using steam and carbon dioxide. The reaction takes place in a tubular reactor filled of mostly nickel alloy catalyst at around 900-1100 °C *via* an extremely endothermic reaction. Besides desired reactions, probability for occurrence of some undesirable reactions like production of coke will be high if the process parameters are not fixed at optimum, which can lead to formation of hot spot and rupture of reforming tubes [8]. One of the main controlling set points in reforming tubes is H₂/CO ratio in outflow gases which desired value varies with its application. For example, in DRI plant using MIDREX technology which is reviewed in this study, the ratio should be 1.5-2 in order to be most efficient in its usage.

* To whom all correspondence should be sent
E-mail: behzadparvizi@gmail.com

As some examples of NN-MPC applied in the literature, in the following some of recent studies are presented: Ruano *et al.* applied neural network based MPC for controlling HVAC system in order to maintain thermal comfort and simultaneously minimize the energy spent in both winter and summer time. Their report showed that their feasible and robust approach is able to achieve energy savings greater than 50%, under normal building occupation [9]. In another work done by Shi Li a NMPC was applied for an intensified continuous reactor working in high pressure and temperature conditions and designed to replace the traditional batch reactor for a hydrogenation process. The performances of nonlinear and linear MPC were compared with satisfactory performance for NMPC and failure of LMPC due to high nonlinearities of the process [10] was found. A parallel-structured model using NN (GNN) for incorporation into a general NMPC structure to an experimental distillation column control was proposed by Jing Ou. The experimental results demonstrated the effectiveness of the approach for a nonlinear process subject to a variety of constraints and environmental effects [11]. Paisan *et al.* used a multi-layer feed forward neural network model based predictive control scheme for a multivariable nonlinear steel pickling process. The results of this study were reported as better performance in the control of the system over the conventional PI controller in all cases [12]. In another paper, a nonlinear predictive control strategy was developed and applied to an industrial crystallization process simulator by Damour *et al.* The control scheme comprised an artificial neural network predictive controller and a more suitable manipulated variable. Simulation results showed the efficiency of the proposed control strategy to improve the process control [13].

The motivation behind this paper was also training an NN-predictive control network for setting the conversions and the outflow gas ratios specially hydrogen and carbon monoxide. The neural network was trained by use of around 5000 input-output samples extracted from a reformer pilot plant in randomly sufficient numbers to cover the whole operating range. 6 inputs were CH₄, CO, CO₂, H₂O and H₂ volumetric flowrate and reaction temperature and 5 output parameter were for gas compositions. All the implementations for ANN and MPC were done in MATLAB/SIMULINK environment. After the network was designed and trained the controller performance was investigated in terms of set point tracking and system forward movement and its arrangement to provide the

required changes.

METHODOLOGY

Data generation

A pilot plant was built specifically to evaluate experimental data gathering of methane reforming with steam and carbon dioxide. The basic design of this pilot plant was scaled down from an industrial unit of DRI production using MIDREX technology. It essentially consists of a tubular reactor with 2" diameter and 2 m height, filled with three levels of catalysts (inert, semi-active and active) with different percentage of nickel oxide. The reactor was fixed in a cubic electrical heater designed to reach to 1400 °C with three heating zones. Five temperature sensors (TT) were implemented on inlet, outlet and three sections of heater to accurately control the reaction temperature. Five mass flow controllers (Alicat-MCR) for gas cylinder lines and one vortex flow meter (Yokogawa-DY015) on the steam line were used to accurately control the reactant flow rates. The plant is schematically shown in Figure 1.

Methane, steam, carbon dioxide, carbon monoxide, hydrogen and nitrogen were mixed and preheated up to around 500 °C through electrical heaters, and then the mixture flowed to the reactor on three levels of catalysts. The reaction occurred at 900-1100 °C and produced syngas was then cooled *via* a water condenser and was subjected to composition analysis through online gas chromatography. The typical reaction conditions, and catalyst properties used in MIDREX plant used in operation of the pilot are listed in table 1.

Application of artificial neural network

One of the main features of the neural network is parallel processing of databank for capturing the dynamics of a complex and multivariable system. In case of enough and informative dataset in hand, a good network of neurons, layers and connections in its various types, like multilayer perceptron, radial basis function, recurrent neural network, etc., can predict the behavior of an unknown system and consequently can keep the system optimized and in desired position when used in a predictive control strategy. In this study, a multilayer perceptron feed forward neural network with back-propagation algorithms was used to predict the reformer behavior and syngas produced.

The model had 6 inputs, 4 hidden layers with 5 neurons in each one and 5 neurons in the output layer. The considered learning rule and training function are Levenberg Marquardt (LM) and trainlm, respectively.

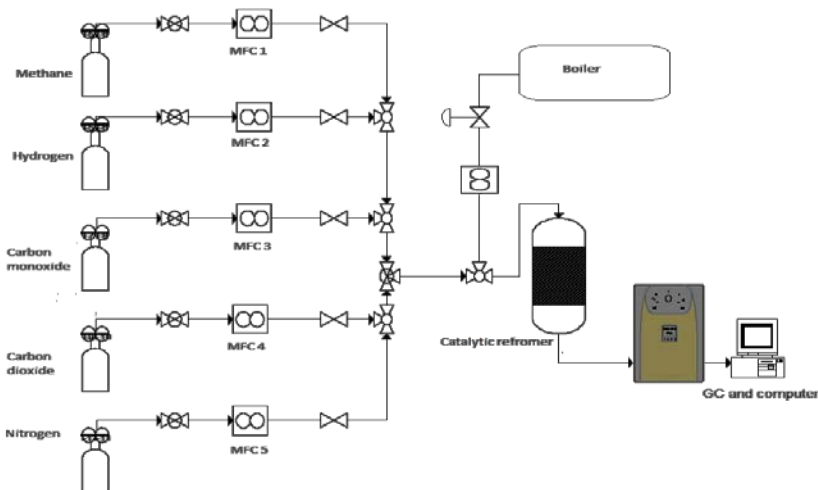


Fig. 1. Schematic diagram of the experimental system

Table 1. Reaction conditions in a MIDREX reformer

Catalyst parameters			
Type	Particle size (mm)	Porosity	Sphericity
Raschig ring	16×6×1	0.52	0.656
Tortuosity	Loose density(kg/m ³)	Bed density (kg/m ³)	
2.74	2390	1362	
Reaction conditions			
Pressure (bar)	Temperature (°C)	CO ₂ %	CO%
2	900-1100	15.21	17.4
H ₂ %	H ₂ O %	N ₂ %	CH ₄ %
31.09	13.94	1.5-2	19.73

The algorithm is an iterative technique that locates the minimum of a function that is expressed as the sum of squares of non-linear functions [8]. A number of 3461 data were utilized during training session and 742 data were used for testing the structure. Among structures and configurations tested, four hidden layers predicted the best and nearest results to the actual ones. The log sigmoid function was employed as an activation function and 872 numbers of epochs considered to overcome over and under fitting of data. The prediction error between the plant and network outputs was used as the training signal. So NN plant model which uses plant inputs and outputs in its history to predict future values of the plant output will be used in the NN-based model predictive controller and will calculate the predicted control input that will optimize plant performance over a specified future time horizon. The NN-MPC structure is shown in Fig. 2. As depicted, the structure is composed of two neural networks, one which mimics the plant behavior (yellow block) and the other the model in MPC controller. For a desired time horizon, the controller will optimize the plant output using the neural network plant model for calculating controller moves and predicting plant output. Neural network controller was trained in order to produce the correct controller moves generated by the optimization

algorithm [14].

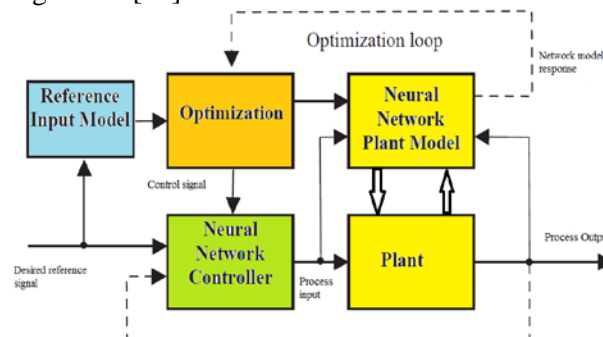


Fig 2. NN-MPC basic structure

RESULTS AND DISCUSSION

ANN model with the above description was developed with the aim of estimation of the output parameters for the catalytic reformer, from input parameters. Around 70 % of the datasets were used for training of the neural network. The performance indicators related to the train, test and validation of the ANN model including the R² and MSE are listed in Table 2.

Table 2. Performance of the developed ANN network

	No. of data	MSE	R ²
Train	3461	7.19e ⁻⁵	9.99e ⁻¹
Validation	742	1.83e ⁻⁴	9.97e ⁻¹
Test	742	5.43e ⁻⁵	9.99e ⁻¹

A comparison between the real experimental and predicted data separately is presented in Figures 3, 4, 5, 6, and 7 for CH₄, CO, CO₂, H₂ and H₂O, respectively.

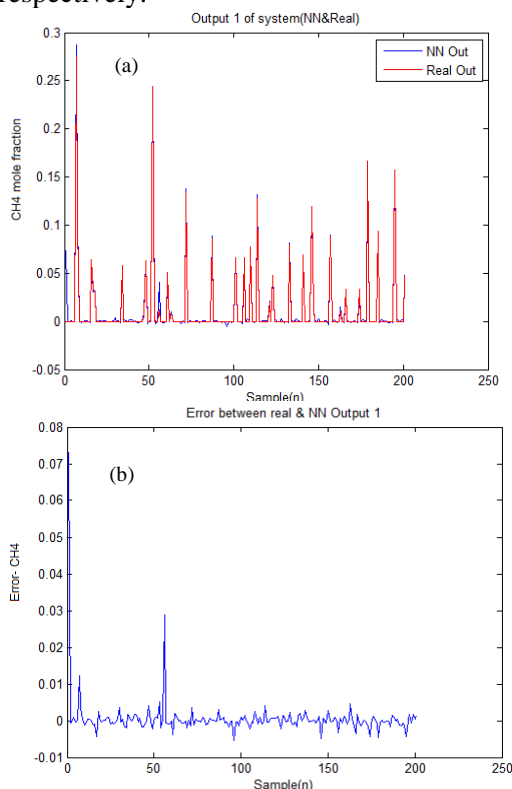


Fig. 3: (a) Comparison of model output and real data (b) and related Error for outlet CH₄ composition

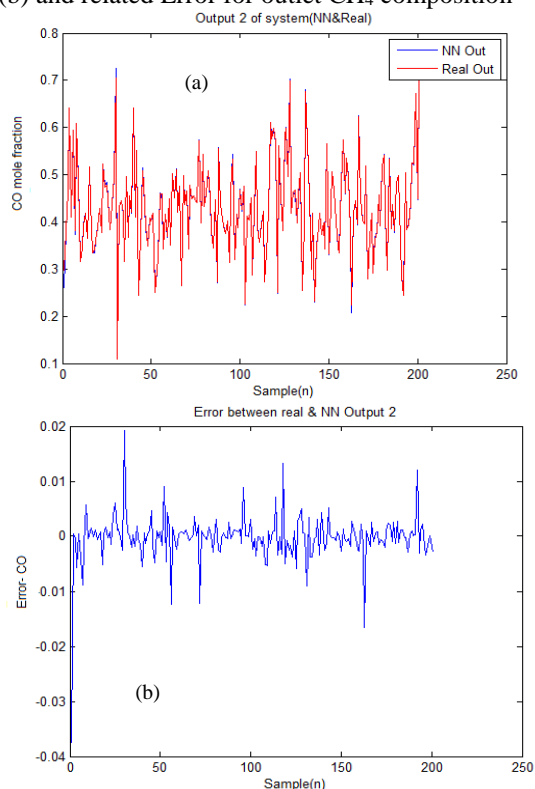


Fig. 4. (a) Comparison of model output and real data (b) and related error for outlet CO composition

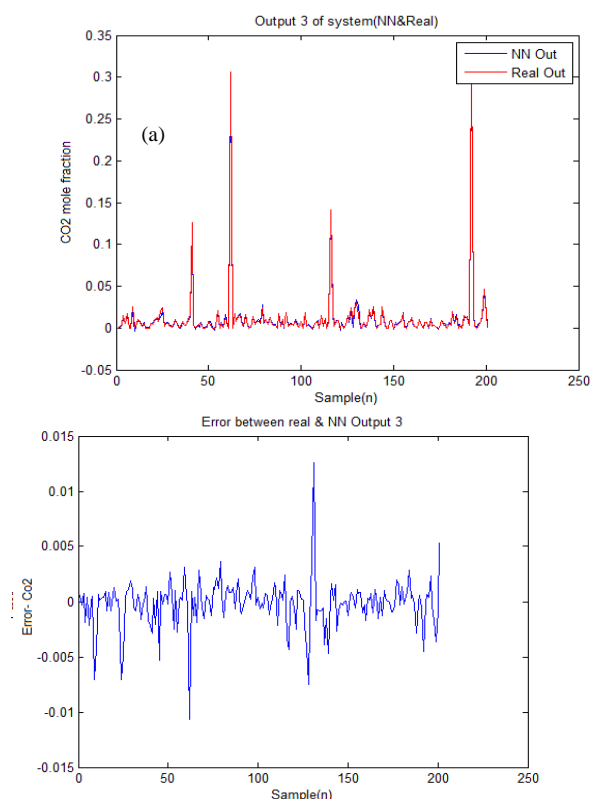


Fig. 5. (a) Comparison of model output and real data (b) and related error for outlet CO₂ composition

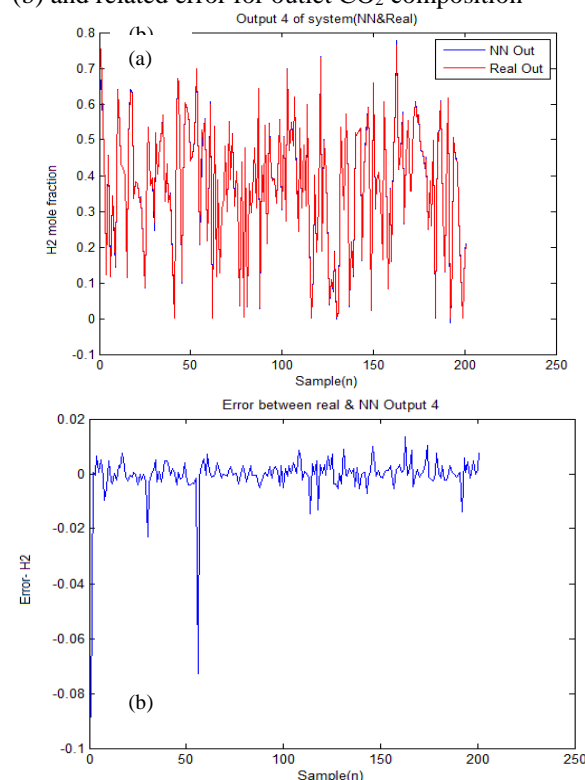


Fig. 6: (a) Comparison of model output and real data (b) and related error for outlet H₂ composition

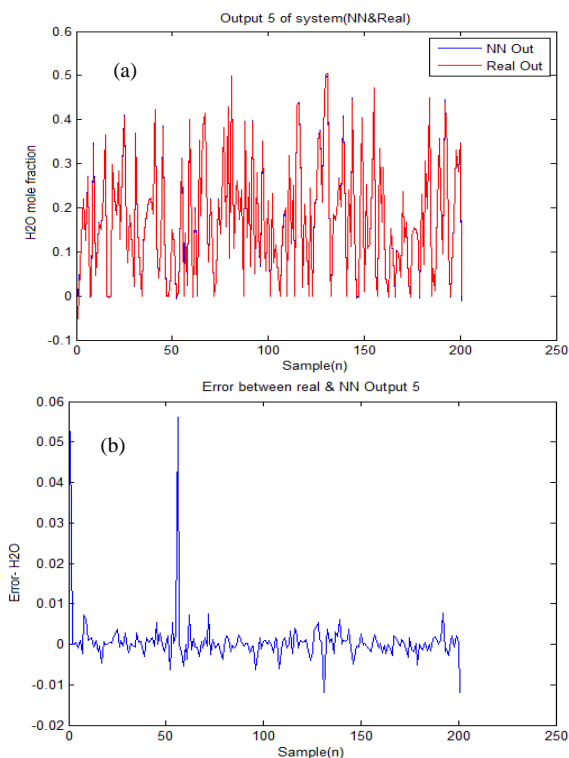


Fig. 7: (a) Comparison of model output and real data (b) and related error for outlet H₂O composition

As can be seen, there is excellent agreement between the predicted results by ANN and the real datasets from experimental setup, it is so obvious

that the neural network fits and follows the real data diagram in a consistent way.

Also the error plot, as can be defined the difference between the modeled and real experimental data shows the deviation more clearly, however there are some step differences in some data which can be due to some outlying experimental data, all of them are in an acceptable range. It should be noted that in order to have a clearer plot, 200 sets of data are used in each graph which can be generalized to all datasets.

General mechanistic model mentioned in section 2, was coded in MATLAB/SIMULINK environment. The system was composed of 6 input variables (CH₄, CO, CO₂, H₂O, H₂ volumetric flow rate, and reaction temperature) and 5 output variables (outflow composition of each above gases). The schematic views of structured neural network MPC in Simulink is shown in Fig. 8.

There are two main blocks, as system NN model, which is the plant model and MPC control which includes NN controller and optimizer. One of the MPC strategies in this study was to use the gas conversions as the measured variable while the flowrate of the inlet gas and temperature was the manipulated variable. The predictive controller was implemented using prediction horizon of 4 and control horizon of 3.

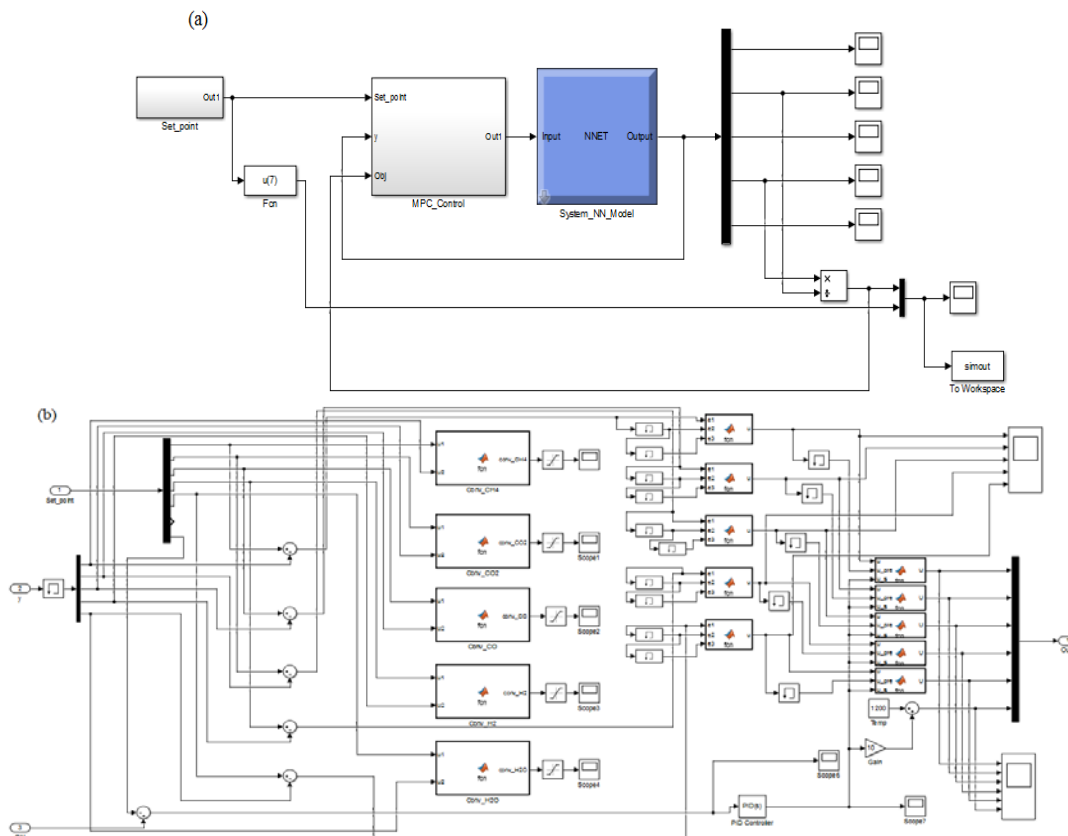


Fig. 8 (a) General view of the NN MPC structure; (b) Detailed structure of the MPC controller

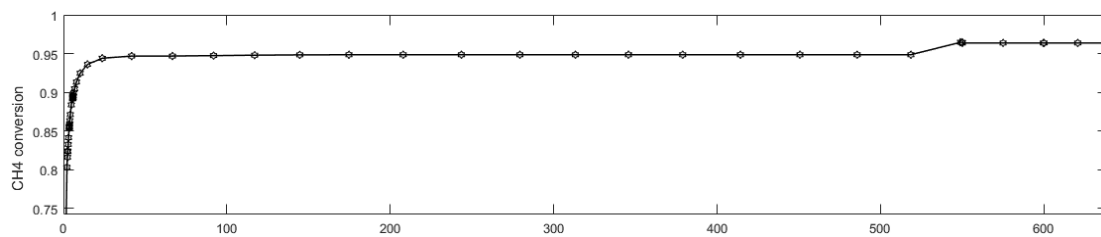


Fig. 9. Control output-CH₄ conversion

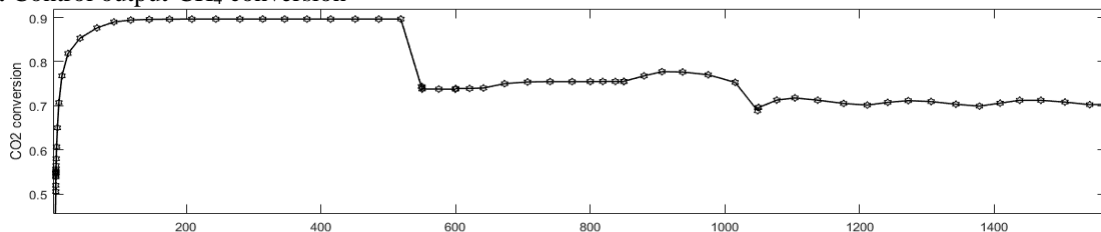


Fig. 10. Control output-CO₂ conversion

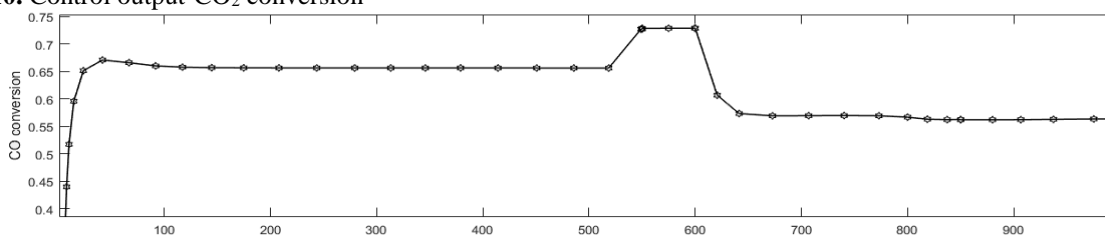


Fig. 11. Control output-CO conversion

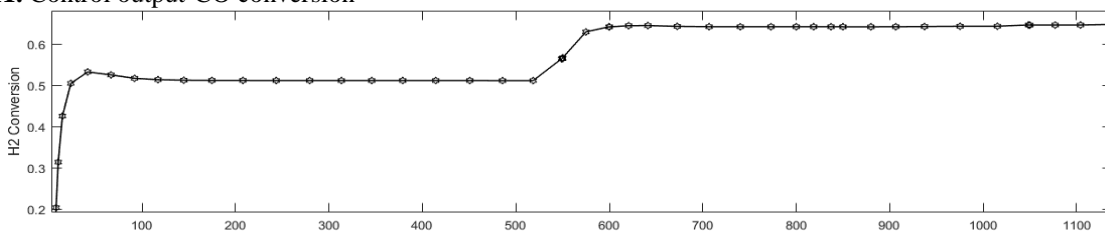


Fig. 12. Control output-H₂ conversion

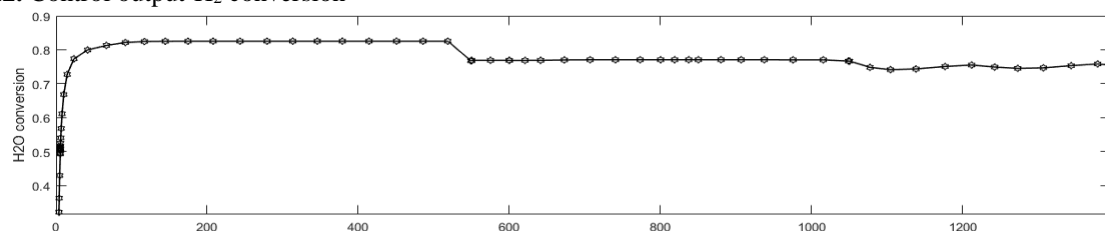


Fig. 13. Control output-H₂O conversion

Figure 9 shows the methane conversion obtained when the reference set point was 0.94. The process was observed to overshoot before attaining steady state after about 20 sec.

Figures 10, 11, 12 and 13 depict the conversion of CO, CO₂, H₂ and H₂O, respectively. As it can be seen in each of the graphs, the system has got its stability after around 20 sec at the optimum desired conversion.

As the other MPC strategy used in this study, was the H₂/CO ratio which as mentioned above should be between 1.5- 2.

By considering this range as our set point and also by manipulating this value, the inputs arrangement were change to produce required control signal.

Figure 14 shows the control object change bychanging in desired ratio from 1.6 to 1.8 and 2. It can be seen in figures 15 (a-e) that in order to track the reference signal how each input variable would change. The performance obtained with the neural network plant model in the predictive control scheme was indeed

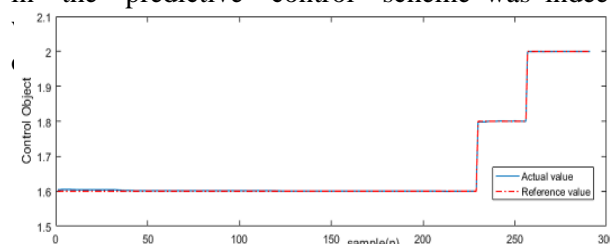


Fig. 14 Set point tracking diagram

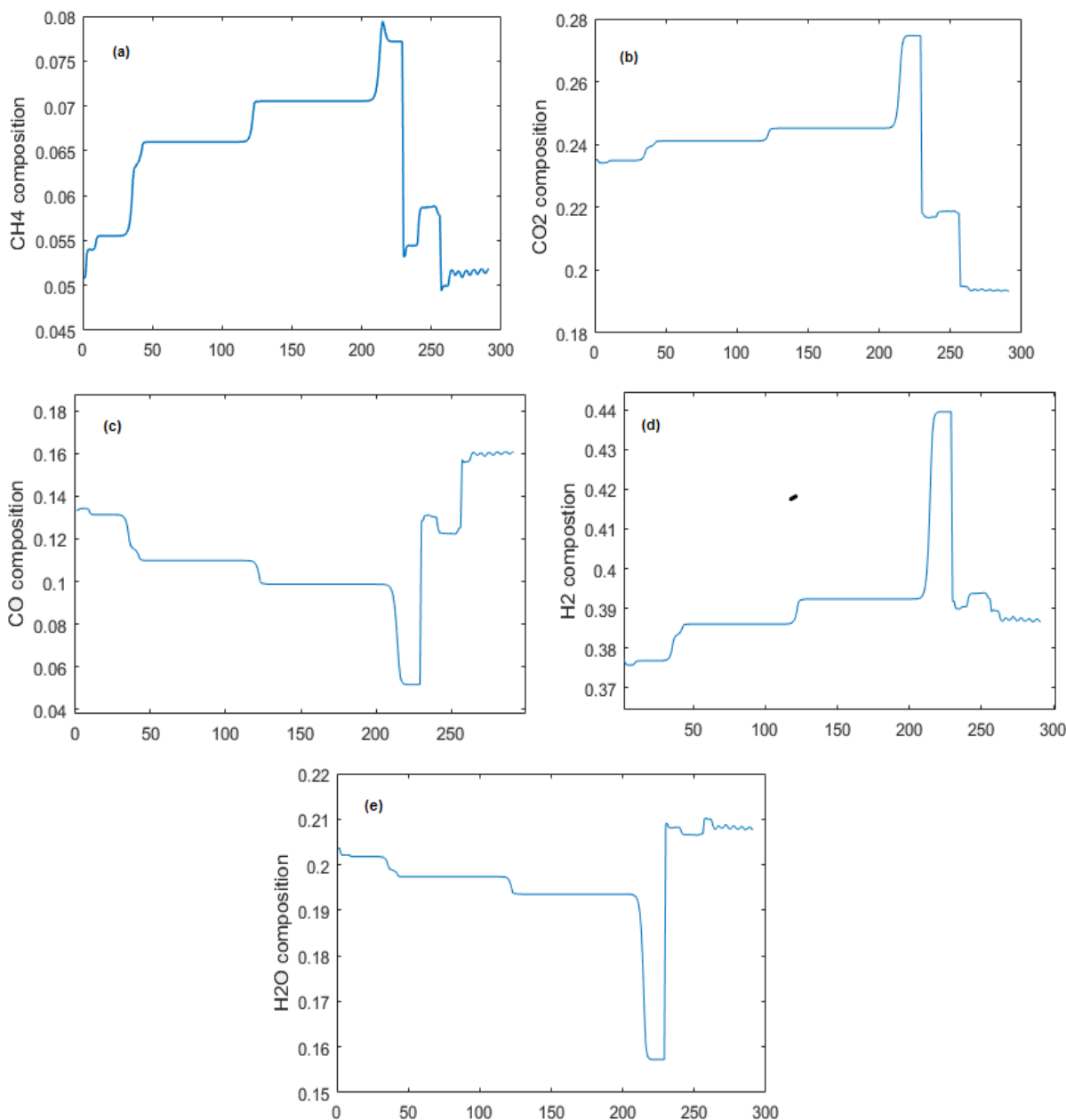


Fig.15. Gas composition arrangement with changing the set point (a) CH₄ (b) CO₂ (c) CO (d) H₂ (e) H₂O

CONCLUSION

An optimal neural network based on predictive control of constrained nonlinear systems was studied. The neural network controller was designed by minimizing an MPC type cost function off-line for a set of training data got from a reformer pilot plant. The neural network designed as plant model predicted the plant behavior with a very good accuracy. Implementation of the NN-MPC controller for the set point tracking case revealed that this controller was able to force process output variables follow their target values smoothly and with a good and logical margin.

REFERENCES:

- 1.S.J. Qin, T.A. Badgwell, *Cont. Eng. Prac.* **11** (7) 733 (2003).
- 2.M.L. Darby, M Harmse, M Nikolaou, MPC: current practice and challenges, in: Symposium Preprints of IFAC Symposium on Advanced Control of Chemical Processes, ADCHEM 2009, Part 1, Istanbul, Turkey p. 88, 2009.
- 3.S. Craven, J. Whelan, B. Glennon, *J. Process Control*, **24**, 344 (2014).
- 4.T.F. Finkler, M. Kawohl, U. Piechotka, S. Engell, *J. Process Control*, **24**, 399 (2014).
- 5.A.S.R. Brasio, A. Romanenko, J. Leal, L. O.Santos, N.C.P. Fernandes, *J. Process Control*, **23**, 1471 (2013).
- 6.B. Zare Nezhad, A. Aminian, *Appl Thermal Eng.* **30** (6,

B. Parvizi et al.: Nonlinear predictive control based on artificial neural network model for pilot reformer plant...

- 7), 692 (2010).
- 7.S. Rani Patra, R. Jehadeesan, S. Rajeswari, S.A.V Satyamurthy, *Int. J. Comp. Appl.*, **1**(26) 63 (2010).
8. Direct Reduction Plant, *MIDREX Company Operations Manual*, **1**, 8 (1981).
- 9.E. Ruano, P.M. Ferreira, Neural Network based HVAC Predictive Control, Proceedings of the 19th World Congress of the International Federation of Automatic Control, Cape Town, South Africa. August 24-29, 2014.
10. S. Li, Y. Li, *Neurocomputing*, **185**, 93 (2016).
11. J. Ou, R.R. Rhinehart, *Control Engineering Practice*, **11** 723 (2003).
12. P. Kittisupakorn, P. Thitayasook, M.A. Hussain, W. Daosud, *Journal of Process Control*, **19**, 579 (2009).
13. C. Damour, M. Benne, B. Grondin-Perez, J.-P. Chabriat, *Journal of Food Engineering*, **99**, 225 (2010).
14. F. S. Mjalli, *Chemical Engineering Science*, **60**, 239 (2005).

НЕЛИНЕЕН ПРЕДСКАЗВАЩ КОНТРОЛ НА ОСНОВАТА НА ИЗКУСТВЕН МОДЕЛ НА НЕВРОННА МРЕЖА ЗА ПИЛОТНА УСТАНОВКА: ПОДХОД ЗА КОНТРОЛ НА СЪОТНОШЕНИЯТА

Б. Парвизи*, А. Ханлархани, И. Пализдар

Институт по материали и енергия, Карадж, Иран

Постъпила на 23ноември, 2017 г.; коригирана на 9 януари, 2018 г.

(Резюме)

Реформерът е важна операционна единица в много рафинерии, например, за нефт и масло, както и в заводи за директна редуция на желязо, за производство на синтетичен газ от различни въглеводороди. Като централна част от завод за директна редуция на желязо чрез MIDREX технология, е много важно да се контролира съставът на синтетичния газ в желани съотношения, особено съотношението водород:въглерод, което трябва да е в интервала от 1.6-2 за да се получи най-подходящият редуциращ газ за конвертиране на желязните пелети в гъбесто желязо с най-добро процентно съдържание на въглерод. Този процес се управлява трудно поради нелинейното отнасяне, многостранното взаимодействие и наличието на ограничения върху реакционните условия. Техниките на невралните мрежи се използват все повече за голям брой приложения, където традиционно се използват статистически методи. В настоящата статия се предлага неврална мрежа с много входове и изходи за многостранен едновременен контрол на състава на входящия газ, реакционната температура и състава на изходящия газ. Моделирането и контролът са изследвани върху база данни, събрани от пилотна установка за реформинг на метан с използване на CO₂ и пара при условия близки до тези в MIDREX реформинг завод за производство на гъбесто желязо. Реакционни температури от 700 до 1100 °C с различни произволно избрани стойности на газовете са използвани за генериране на структура от около 5000 набора от входящи-изходящи данни. Конверсията на газа и съотношението H₂/CO са зададени параметри и резултатите от проследяването им показват ефективността на модела за предсказващ контрол с използване на неврални мрежи.

Co, Ni, Cu phthalocyanines with tetra substituted bisbenzimidazole

M. Canlıca

Yildiz Technical University, Chemistry Department, Inorganic Chemistry Division, Davutpaşa Campus, 34220, Esenler, Istanbul, Turkey

Received: October 7, 2016, Accepted: January 17, 2018,

Cyclotetramerization of bulky substituted phthalonitrile derivative **3** to the Co(II)Pc, Ni(II)Pc and Cu(II)Pc derivatives [4,5,6] was accomplished in quinoline with DBU at reflux temperature. The complexes were characterized by UV-Vis, FT-IR, mass spectra and elemental analysis.

Keywords: Metal phthalocyanines, Bulky substituent, bisbenzimidazole

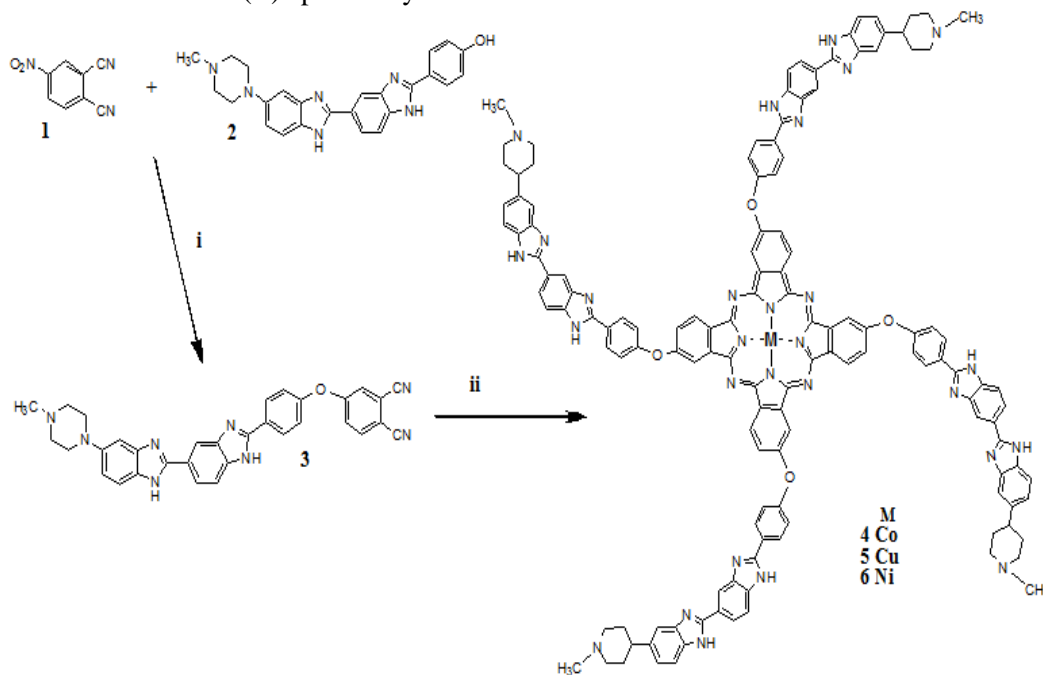
INTRODUCTION

Phthalocyanines (Pcs) were first discovered by accident in 1928 at Messrs Scottish Dyes Ltd and their geometric structure was elucidated [1,2]. They are an interesting class of compounds with increasingly diverse industrial and biomedical applications, such as photosensitization [3], non-linear optics [4], catalysis [5], etc. due to their properties and use in different fields [6,7]. Pcs can coordinate with most metals and can be substituted at the periphery and non-periphery with a variety of substituents. Axial ligands can also be bound to the central metal ion depending on the ability of the ion to coordinate. Bisbenzimidazole is an organic compound used as a fluorescent stain for DNA in molecular biology applications [8,9]. The electrochemical properties of various metal (II) phthalocyanine

(MPc) complexes have been investigated thoroughly [10-13]. These properties are important for advance applications [14-16]. In this paper, we synthesized and characterized mononuclear Co(II)Pc, Ni(II)Pc and Cu(II)Pc. The complexes were substituted with four bisbenzimidazole substituents at the peripheral (β) position, Scheme 1.

EXPERIMENTAL

Materials: Cobalt(II) acetate, nickel(II) acetate and copper(II) acetate as anhydrous metal(II) acetate salts were purchased from Merck. Quinoline was freshly used, all solvents, for example, dimethylsulfoxide (DMSO), dimethylformamide (DMF), dichloromethane(DCM) and chloroform (CHCl_3) were purchased from Merck.



Scheme 1. Synthetic route and reaction conditions for **4,5,6**. **i:** DMSO, 7 days, room temperature, **ii:** Quinoline, overnight, reflux temperature

* To whom all correspondence should be sent:

E-mail: mcanlıca@yahoo.com

1,8-diazabicyclo[5.4.0]undec-7-ene (DBU) and all other reagents were obtained from suppliers and used as received. Bisbenzimidide as Hoechst 33258 was obtained from Aldrich and used without further purification. The chemical name is 2-[2-(4-hydroxyphenyl)-6-benzimidazolyl]-6-(1-methyl-4-piperazyl)benzimidazoletrihydro chloride.

Equipment: The UV-Vis absorption spectra were obtained using a Varian Cary 500 UV-Vis/NIR spectrophotometer. FT-IR data (ATR) were recorded using a Perkin-Elmer spectrum 100 FTIR spectrometer. Elemental analysis was done on a Finnigan Flash EA 1112 Series elemental analysis instrument. Mass spectral data were collected with a Bruker AutoFLEX III Smartbeam MALDI-TOF/TOF mass spectrometer. The instrument was operated in positive ion mode using an m/z range of 400 – 3000. The voltage of the ion sources was set at 19 and 16.7 kV for ion sources 1 and 2, respectively, while the lens was set at 8.50 kV. The reflector 1 and 2 voltages were set at 21 and 9.7 kV, respectively. The spectra were acquired using dithranol as the MALDI matrix, using a 354 nm Nd:YAG laser.

Synthesis: The target precursors were prepared by a nucleophilic aromatic substitution reaction between 4-nitrophthalonitrile **1** and bisbenzimidide **2**. Bisbenzimidide derivatives of metal phthalocyanines **4-6** were obtained in quinoline in the presence of DBU at the reflux temperature.

4-(4-(5-(4-Methylpiperazin-1-yl)-1H,1'H-2,5'-bibenzimidazol-2'-yl)phenoxy) phthalonitrile (3): Compound **2** (500 mg) was dissolved in dry DMSO (15 mL) and **1** (162 mg) was added in argon atmosphere. To this reaction mixture finely ground anhydrous potassium carbonate (0.650 g) was added and the same amount was added again after 24 h of stirring. After a total of 7 days of stirring, the reaction mixture was poured into water (550 mL) resulting in the formation of a dark yellow precipitate of **3**. The crude product was centrifuged several times and was further recrystallized from ethanol; finally, the pure product was dried over P₂O₅ for two weeks. Yield: 0.390 g. IR(ATR) ($\nu_{\max}/\text{cm}^{-1}$): 3078 (Ar-CH), 2232 (C \equiv N), 1591 (C=C), 1247 (C-O-C). ¹H NMR (DMSO-*d*₆): δ , ppm 13.19 (2H, br, s N-H), 8.52 (1H, s, Ar-H), 8.3 (2H, m, Ar-H), 8.1 (2H, d, J = 8.8 Hz, Ar-H), 7.9 (2H, br, s, Ar-H), 7.5 (2H, m, Ar-H), 7.4 (2H, m, Ar-H), 6.6 (2H, m, Ar-H), 3.02 (4H, m, cyclohexane-H), 2.65 (4H, m, cyclohexane-H), 1.10 (3H, br, s, CH₃). Anal. calcd. for C₃₃H₂₆N₈O: C, 71.98; H, 4.76; N, 20.35 %. Found: C, 77.18; H, 4.70; N, 15.42 %. LC-MS: m/z . calcd. 550.06, found [M]⁺: 550.61.

General procedure for 4-6: A mixture of compound **3** (0.100 g) and Co(OAc)₂(0.008 g) for **4**, Ni(OAc)₂(0.008 g) for **5** and Cu(OAc)₂(0.008 g) for **6** in 0.6 mL of quinoline with 6 drops of DBU was refluxed in a sealed tube in argon gas at 185°C for 24 h. After cooling to room temperature, the reaction mixture was treated with ethanol to precipitate the product. The residue was filtered off and then washed several times with methanol, water and finally washed with methanol, ethanol, acetonitrile and acetone for 24 h, consecutively in a Soxhlet apparatus. Finally, the dark green cobalt, nickel and copper phthalocyanines were dried over P₂O₅ for 10 days. All of these compounds are soluble in DMSO and have mp > 350°C.

Cobalt phthalocyanine (4): Yield 0.030 g. UV-vis (DMSO): λ_{\max}/nm 680, 343. IR (ATR): ($\mu_{\max}/\text{cm}^{-1}$) 3050 (Ar-CH), 1564 (C=C), 1259 (C-O-C). Anal. calcd. for C₁₃₂H₁₀₄N₃₂O₄Co: C, 70.11; H, 4.64; N, 19.82. Found: C, 70.49; H, 4.65; N, 20.05%. MALDI-TOF-MS: m/z calcd. 2261.38, found 2273.4 [M+Li+5H]⁺.

Nickel phthalocyanine (5): Yield 0.035 g. UV-vis (DMSO): λ_{\max}/nm 682, 341. IR (ATR): ($\mu_{\max}/\text{cm}^{-1}$) 3050 (Ar-CH), 1564 (C=C), 1256 (C-O-C). Anal. calcd. for C₁₃₂H₁₀₄N₃₂O₄Ni: C, 70.12; H, 4.64; N, 19.82. Found: C, 69.49; H, 3.50; N, 19.81%. MALDI-TOF-MS: m/z calcd. 2261.14, found 2272.4 [M+Li+4H]⁺.

Copper phthalocyanine (6): Yield 0.025 g. UV-vis (DMSO): λ_{\max}/nm 684, 334. IR (ATR): ($\mu_{\max}/\text{cm}^{-1}$) 3050 (Ar-CH), 1564 (C=C), 1255 (C-O-C). Anal. calcd. for C₁₃₂H₁₀₄N₃₂O₄Cu: C, 69.97; H, 4.63; N, 19.78. Found: C, 70.49; H, 4.50; N, 18.85%. MALDI-TOF-MS: m/z calcd. 2266.0, found 2269.9 [M+4H]⁺.

RESULTS AND DISCUSSION

4-Nitrophthalonitrile **1** was synthesized as reported in [17]. Bisbenzimidide **2** was obtained from commercial suppliers. The synthesis of phthalodinitrile **3** was based on the reaction of compound **3** with an excess of compound **2**. The reactions were carried out in dry DMSO in the presence of K₂CO₃ as a base, at room temperature, and good yields were obtained. The 4-nitrophthalonitrile **1** reacted with commercial bisbenzimidide **2** to obtain compound **3** in a reasonable good yield. MPcs **4**, **5** and **6** were prepared by cyclotetramerization of phthalonitrile **3** in the presence of anhydrous Co(OAc)₂, Ni(OAc)₂, and Cu(OAc)₂, respectively, by using quinoline with DBU at the reflux temperature, Scheme 1. Column chromatography on silica gel using CHCl₃ as mobile

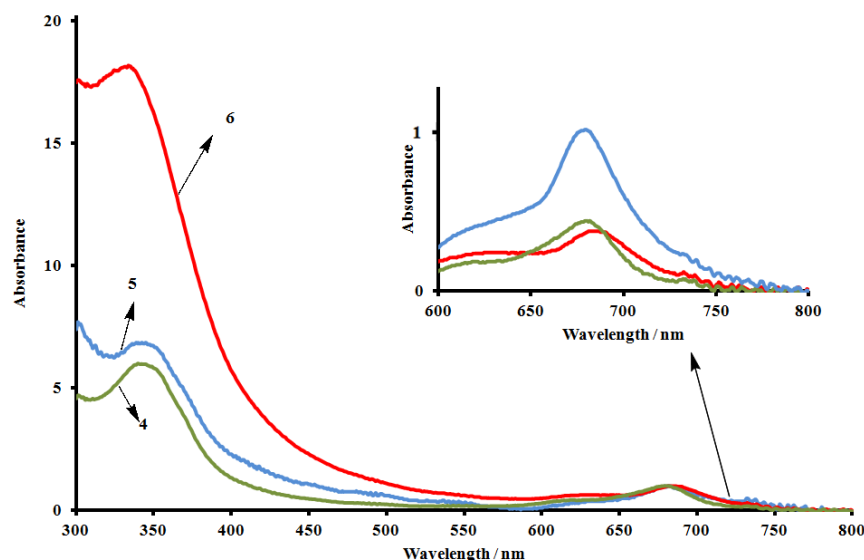


Fig. 1. Absorption spectra of **4-6** in DMSO

phase was used to purify complexes **4-6**. The structure and purity of the CoPc, NiPc and CuPc derivatives were confirmed by UV-Vis, IR, mass spectral data and elemental analyses.

The IR spectra of **4-6** clearly indicated the absence of OH groups of **2**. CN vibrational peaks were observed at 2232 cm^{-1} for compound **3**. A diagnostic feature of the formation of **4-6** from the phthalodinitrile derivative **3** was the disappearance of the sharp CN vibration of the latter. The IR spectra were very similar for compounds **3-6** and showed Ar-O-Ar peaks at 1247 , 1259 , 1256 , 1255 cm^{-1} , respectively.

Elemental analysis results were also consistent with the theoretical values of the proposed structures for **3-6**.

The purified Pcs were further characterized by mass spectra. The expected mass values corresponded to the found values for all complexes. Both protonated ion peaks for complexes **4-6** and a Li adducted ion peak were found, except for complex **6** which has a molecular ion peak. The ion peaks of complexes **4-6** were observed at 2273.4 , 2272.4 and 2269.9 amu , respectively. These results confirm that the complexes have been synthesized successfully.

The UV-Vis spectra of **4-6** in DMSO are shown in Fig. 1. The Pcs show typical electronic spectra with two strong absorption regions, one of them in the UV region at about 300-400 nm (B-band) and the other in the visible region at 600-750 nm (Q-band) and are characteristic of Q-band transition of M(II)Pcs with D_{4h} [18] Aggregation behavior of Pc is depicted as a coplanar association of rings progressing from monomer to dimer and higher order complexes and it is dependent on concentration, nature of solvent and substituents,

metal ions and temperature [19]. Aggregation in M(II)Pcs is typified by the broadened or split Q-band, the high energy band being due to the aggregate and the low energy band due to the monomer [18]. The UV-Vis spectra of the metal phthalocyanines resemble those of other Pcs. The broad Q-band with the vibration band at almost 620 nm for **4-6** has been reported to indicate aggregation of phthalocyanine complexes in general [18]. In Fig. 1, complexes **4-6** show Q-band absorptions of the monomers at 681, 679, 683 nm, respectively, in DMSO. Red shifting of the spectra observed in Q-bands of **4, 5** and **6** is due to the electron density enhancement caused by the central metal [20]. The complexes **4-6** show B-bands at 343, 341 and 334 nm in DMSO, respectively. Typical of Pcs, the intensity of the B-bands is high relative to the Q-band; this may be due to aggregation. The bulky substituents of the Pc molecules considerably affect the degree of conjugation between the rings and substituent. It can be seen from the electronic absorption spectra of complexes **4-6** that the Q-band is broad. CONCLUSION

We described the synthesis and characterization of novel Co(II), Ni(II) and Cu(II) phthalocyanine derivatives which contain a bisbenzimidate unit on each benzo group substituent at peripheral position. The effect of bisbenzimidate as a bulky substituent to the Pc molecule was observed.

Acknowledgments: This work was supported by the Research Fund of the Yildiz Technical University (Project No: 27-01-02-07).

REFERENCES

- 1.L.R. Milgram, in: Colours of life, Oxford University Press, Oxford, 1st ed., 1977.
- 2.J. M. Roberts, *J. Chem. Soc.*, 1195, 1936.
- 3.N. Kobayashi, R. Kondo, S.I. Nakajima, T. Osa, *J. Am. Chem. Soc.*, **112**, 9640 (1990).
- 4.N.B. McKeow, *Chemistry and Industry*, 513 (1999).
5. Y.H. Tse, P. Janda, H. Lam, J. Zang, W.J. Pietro, A.B.P. Lever, *Anal. Chem.*, **67**, 981, 1995.
- 6.S. Chatterjee, T. S. Srivastava, *J. Porphyrins Phthalocyanines*, **3**, 424, 1999.
- 7.M.G. Waltera, A.B. Rudineb, C. C. Wamser, Porphyrins and Phthalocyanines in solar photovoltaic cells, *J. Porphyrins Phthalocyanines*, **14**, 759, 2010.
- 8.J. Renzhe, J. B. Kenneth, *Biochemistry*, **85**, 8939, 1988
- 9.G. Cosa, K.S. Focsaneanu, J.R.N. McLean, J.P. McNamee, J.C. Scaiano, *Photochemistry and Photobiology*, **73**(6), 585, 2001.
10. S. Khene, S. Moeno, T. Nyokong *Polyhedron*, **30**(12), 2162, 2011.
11. J.H. Zagal, *Coord. Chem. Rev.*, **119**, 89, 1992.
12. I. A. Akinbulu, S. Khene, T. Nyokong *Electrochimica Acta*, **55**(23), 7085 (2010).
13. T.T. Tasso, T. Furuyama, N. Kobayashi, *Inorg. Chem.*, 52(16), 9206, 2013.
14. Racheal O. Ogbodu, Tebello Nyokong *Spectrochimica Acta Part A: Molecular and Biomolecular Spectroscopy*, **121**(5), 81, 2014.
15. A. Maringa, T. Mugadza, E. Antunes, T. Nyokong, *Journal of Electroanalytical Chemistry*, **700**(1), 86, 2013
16. C.C. Leznoff, A.B.P. Lever (eds.), *Phthalocyanines: Properties and Applications*, 1-4, VCH, New York, 1989, 1993, 1996.
17. B.N. Acher, G. M. Fohlen, J. A. Parker, J. Keshavayya, *Polyhedron*, **6**, 1463, 1987
18. M.J. Stillman, T. Nyokong In: Leznoff CC, Lever ABP, (eds.) *Phthalocyanines: Properties and Applications*, VCH, New York, **1**, 139, 1989.
19. H. Enkelkamp, R.J.M. Nolte, *J. Porphyrins Phthalocyanines*, **4**, 454, 2000.
20. T. Nyokong, in: J. Jiang (ed.) *Functional Phthalocyanine Molecular Materials*, **135**, 94, 2010.

ФТАЛОЦИАНИНИ НА Co, Ni И Cu С ТЕТРАЗАМЕСТЕН БИСБЕНЗИМИД

М. Джанлъджа

Технически университет на Илдиз, Департамент по химия, Отдел по неорганична химия, Давутпаша кампус, 34220, Есенлер, Истамбул, Турция

Постъпила на 7 октомври, 2016 г.; приета на 17 януари, 2018 г.

(Резюме)

Проведена е циклотетрамеризация на обемистия заместен фталонитрил 3 с производните Co(II)Pc, Ni(II)Pc and Cu(II)Pc [4,5,6] в хиолин с 1,8-диазабицикло[5.4.0]ундек-7-ен при температура на кипене. Комплексите са охарактеризирани чрез елементен анализ, UV-Vis, FT-IR и масови спектри.

Application of direct simulation Monte Carlo for development of micro gas sensor

M. B. Gerdroodbary*¹, D. D. Ganji¹, M. Taeibi-Rahni², Sh. Vakilipour³, R. Moradi⁴

¹Department of Mechanical Engineering, Babol University of Technology, Babol, Iran

²Department of Aerospace Engineering, Sharif University of Technology, Tehran, Iran

³Faculty of New Sciences and Technologies, University of Tehran, Tehran, Iran

⁴Department of Chemical Engineering, School of Engineering & Applied Science, Khazar University, Baku, Azerbaijan

Received: November 26, 2017; Revised: January 1, 2018

Development of a new micro gas sensor is essential for the analysis of the outcome of gas separation devices. In this paper, direct simulation Monte Carlo (DSMC) modeling of low-pressure gas sensor was performed to investigate the effect of physical parameters on the performance and main characteristics of this type of actuator in various operating conditions. Extensive parametric studies were done and the effect of ambient pressure, temperature and gap of arms were comprehensively investigated. Our findings showed that gap size significantly influences the flow features and force generation inside the sensor.

Keywords: Knudsen force; DSMC; Rarefied gas; Gas sensor; MEMS.

INTRODUCTION

In recent years, the application of sensors for the detection of gas has become significant due to their importance in industrial devices. Since the first step for the separation of a mixture is detection, the development of this sensor could highly enhance the performance of separation techniques such as membranes, cryogenic column and gas centrifuges [1-3]. In addition, several researchers have tried to develop new simple devices for the detection of dangerous gases such as NH₃, CO and H₂S. There are various techniques to sense the gas component or measure the pressure of the gases. One of the primary goals of the scientists is to develop micro electronic devices for this purpose [4-6].

Since the current sensor for analyzing and sensing of the gas is spacious and expensive, scholars have focused on new methods and devices which are small and simple. The development of the micro-electromechanical system (MEMS) has enabled researchers to decrease the size of the device in micro-scale. Consequently, micro sensors are highly developed due to their applications in different devices such as medical instruments. One of the new methods for gas detection is the application of the Knudsen force which is highly sensitive to the properties of the gas. Indeed, the non-homogeneity of the temperature in low-pressure conditions produces a force known as Knudsen force. Previous studies [7-9] have shown that this type of force is highly sensitive to the pressure of the domain, temperature difference and the type of gas

of the domain. These special characteristics motivated the researchers [8] to use this approach for measurement of pressure.

A lot of studies have been devoted to recognize the characteristics of the Knudsen force in rarefied conditions. Ketsdever *et al.* [7] reviewed more than hundred papers and documents to present a comprehensive literature review on the origin of the Knudsen force and its history. Since Crookes radiometer [8] was the first device which applied Knudsen force, various researchers performed extensive studies on this device. Passian *et al.* [9,10] investigated thermal transpiration at the microscale by a Crookes cantilever.

Several works have been performed to apply a direct simulation Monte Carlo (DSMC) for the simulation of a rarefied gas. Poozesh and Mirzaei [11] simulated a fluid flow in a body-fitted grid system using the lattice Boltzmann method. Several similar works also applied this method for solving engineering problems [12-16]. In 2016, Strongrich *et al.* [17, 18] introduced a new device for sensing the pressure by Knudsen force. In this sensor, the hot arm is fixed while the cold arm known as shuttle arm could move and the capacitor is attached to the shuttle arm. Since the gap of these two arms is too small, the Knudsen force acts on the cold side and this could be measured by the capacitor. Fig 1 schematically presents the main mechanisms inside the MIKRA. In our previous work [19], the effect of Knudsen thermal force on the performance of a low-pressure micro gas sensor was completely investigated.

* To whom all correspondence should be sent:

E-mail: mbarzegarg@yahoo.com

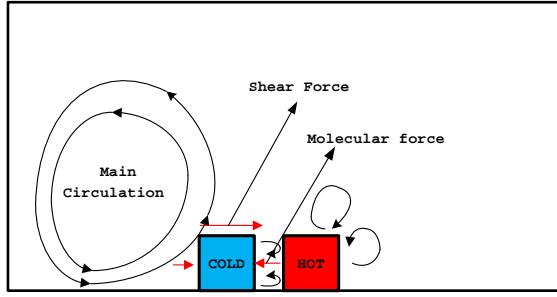


Fig. 1. Scheme of flow inside the MEMS sensor

In the present work, DSMC approach was applied to study the main mechanism of the Knudsen force in rarefied gas condition on the performance of the micro gas sensor (MIKRA). In the first step, the model of the problem is presented and the particle approach is explained. In order to investigate the main technique of this sensor, the flow feature of gas inside the device was thoroughly studied. In addition, the effects of significant parameters such as different ambient pressures, temperature difference of the arms and gap space on the main characteristics of this sensor are presented. Lastly, effective terms on the mechanism of force generation in the low-pressure condition were determined.

NUMERICAL APPROACH

Geometry and assumptions

The generated grid and the boundary condition applied on the model are displayed in Figure 2. According to the size and dimensions of problem, the size of the domain in our work was $600 \times 300 \mu\text{m}$ in x and y direction and 150 by 75 collision cells were generated in the x and y directions, respectively. It was also supposed that the whole surfaces are fully diffuse.

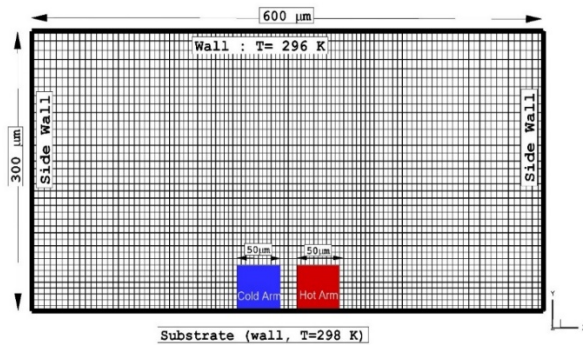


Fig. 2. The boundary conditions and grid of the present model

Governing equations and solver

In order to simulate the low-pressure flow, a conventional numerical method such as CFD was not applied due to assumption of the continuum in the whole domain. In fact, Navier–Stokes equations could not predict the main features of the flow. Thus,

Boltzmann equation as a high-order equation should be used and molecular approach is the best approach for such rarefied gas regime. Eq. 1 presents the general formula of the Boltzmann equation:

$$\frac{\partial}{\partial t}(nf) + \mathbf{c} \cdot \frac{\partial}{\partial \mathbf{r}}(nf) + \mathbf{F} \cdot \frac{\partial}{\partial \mathbf{c}}(nf) = Q \quad (1)$$

where n, \mathbf{c} and f are number density, molecular velocity and velocity distribution function, respectively.

Furthermore,

$$Q = \int_{-\infty}^{+\infty} \int_0^{4\pi} n^2 (f^* f_1^* - f f_1) g \sigma d\Omega d^3 c_1$$

is the collision integral which defines the variation in the velocity distribution function as a result of intermolecular collisions.

Scientists present various methods for solving the Boltzmann equation. Among various techniques, the DSMC method of Bird [20] is a vigorous and reliable approach for a low-pressure gas flow. In fact, this approach is a particle method based on the kinetic theory for simulation of rarefied gases. Among numerous available DSMC codes, open-source *dsmcfoam* code seems a reliable and professional open code for the simulation of our problem [21]. *dsmcFoam* has been established and presented as toolbox of OpenFOAM version 1.7.

Boundary conditions

In our problem, the whole boundaries of the model were walls with constant temperature. The pressure of the domain varied from 62 pascals to 1500 pascals which induces a Knudsen number from 4.64 to 0.3, respectively. The details of boundary conditions are depicted in fig. 2. The main gas of the domain is nitrogen. As mentioned in the main reference [17], the temperature of the cold and hot arm varied with the pressure of the domain and it is presented in Table 1.

Table 1. Temperature of the cold and hot arm

Pressure	Kn	Hot Arm	Cold Arm
(pa)	-	(K)	(K)
62	4.48	348	304.5
155	1.8	346	304.5
387	0.72	342	304
966	0.29	323	302

Numerical procedure

In order to simulate the collision model in all simulations, the variable hard sphere (VHS) collision model was applied. Since the computational time is related to the number of simulator particles [20], collision pairs were

determined based on the no time counter (NTC) method.

In this study, the gap (distance between the heater and shuttle arms) is known as the length characteristic (L) and it is about 20 microns. The total number of simulated particles was approximately $2.48 \times 10^{+5}$. The space domain was discretized by using squared cells ($\Delta x = \Delta y$), with $\Delta x = 4 \mu m$, i.e., 150 cells were taken in the x -direction, while the number of cells in the y -direction depends on the aspect ratio H/W where H and W are the width and height of the domain, respectively. It is equal to $n_c = 150 \times (H/W)$. The number of particles per cell on the NTC scheme is fixed to 20 and the time step is chosen to be sufficiently smaller (about 1/3) than the cell traversal time, defined as $W / (n_c v_0)$ in order to obtain v_0 , the $v_0 = \sqrt{2k_B T_0 / m}$, with k_B and m denote the Boltzmann constant and the gas molecular mass, respectively. According to our calculations, the time step should be less than $3.5 \times 10^{-7} s$. We set the time step equal to $1 \times 10^{-8} s$, smaller than the mean collision time and close to the time step of the previous works of Strongrich *et al.* [17]. The physical time of these simulations was 0.03 s to reach steady state condition. For a typical simulation, twenty particles were initially set in each cell to minimize the statistical scatter.

RESULTS AND DISCUSSION

Verification

Validation of obtained results is the first step for the simulation studies. In this study, the values of the Knudsen forces on the shuttle arm were compared with experimental data of Strongrich *et al.* [17] at different pressures (fig. 3). The figure also presents the results of SPARTA-DSMC code obtained by Strongrich *et al.* [17]. The comparison confirms that

the deviation of obtained data (dsmcfoam) from experimental data is not noticeable and the obtained results are reasonable and reliable for the further studies.

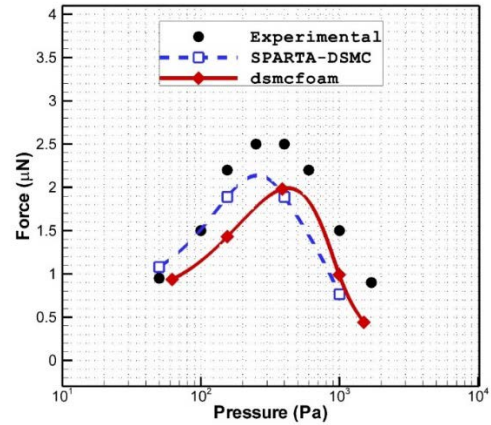


Fig. 3. Comparison of the of obtained results (dsmcfoam) with experimental and numerical data of Strongrich *et al.* [17]

The difference between the numerical and experimental data is due to diverse reasons. The gap distance is the primary reason for this difference.

Flow feature

Figure 4 illustrates the temperature distribution along the streamline patterns for various operating pressures. The figure clearly shows that the circulation is significant at high Knudsen force ($P=387$ pa). Since the pressure of the domain determines the main characteristics (such as Knudsen number), it is expected that the variation of this term considerably influences the main feature and this is clearly observed in the figure of low-pressure condition ($P=62$ pa) wherein noticeable kinks in the contour lines are detected.

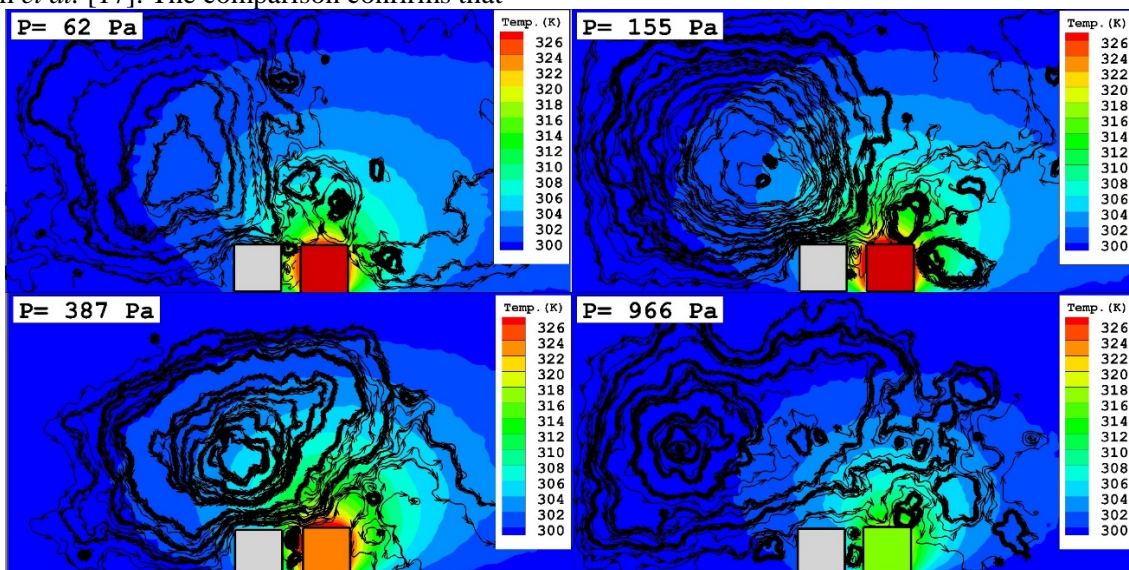


Fig. 4. Flow pattern and temperature distribution inside the MIKRA

As shown in the figure, these kinks originate at the sharp corners on the top of the arms. On the other side, intermolecular collisions rapidly flatten those kinks in the gap of the arms in the high-pressure cases, and the absence of intermolecular collisions allows these kinks to diffuse much further away from the hot arms in the low-pressure conditions as demonstrated in Fig. 4.

In order to reveal the main origin of net force on the shuttle arm, the difference in the pressure on both sides of the cold arm should be investigated. Figure 5 demonstrates the pressure ratio (I) inside the domain for defined pressure conditions. The pressure ratio was calculated as follows:

$$I = \frac{P}{P_{ave}} \quad (1)$$

where P and P_{ave} denote the local and average pressure of the domain, respectively. According to the contour of the pressure ratio, it is found that the pressure is non-uniformly distributed inside the domain. Indeed, this non-homogeneity of the pressure field is the main reason for an exceptional feature of rarefied gases in our problem. It should be mentioned that non-uniform distribution of temperature does not produce macroscopic streams in the continuum regime, and we do not notice pressure gradients in the absence of external forces. Nevertheless, bulk flows are simply created in a low-pressure condition when there is temperature difference inside the domain. In fact, these streams direct particles in the vicinity of the arms and hereafter make a non-uniform pressure distribution.

Since this is the main driving mechanism for force generation inside Knudsen pumps [22-24], previous studies named this phenomenon as thermal transpiration.

In order to clearly explain the main difference between the various models, the effective terms and mechanism of force generation should be initially explained. As shown in figure 1, thermal gradient in the very low-pressure domain induces a distinctive flow pattern according to pressure and boundary conditions. Thermal stress slip flow (TSS) is the first driven flow in the rarefied domain. This force induces flows from the hot side to the cold side inside the gap of arms. Thermal creep flow is known as the second main force in the low-pressure domain. This type of force, conversely, is produced by the tangential temperature gradient near the wall. The third main force in low-pressure condition is the thermal edge flow and it occurs in sharp corners. According to these explanations, the large circulation of the domain is due to thermal stress slip flow and the thermal edge flow occurs on the right side of the hot arm in the vicinity of the edge. Since thermal stress slip flow which induces a hot to cold flow produces the measurable Knudsen force on the shuttle arm, this study greatly focuses on this type of force.

Thermally driven flow is the main cause for the generation of the Knudsen force. Hence, the analysis of temperature distribution inside the domain is significant. Figure 4 clearly depicts that the temperature gradient is dominant at the high Knudsen number. Indeed, rarefied gas allows molecules to transmit the temperature of hot arm to the domain. As the pressure of the domain is increased, the intermolecular reaction reduces the temperature gradient inside the domain. One of the main significant aspects of the high temperature gradient inside the domain is the pressure difference. Figure 5 clearly confirms that the pressure difference is significant in rarefied

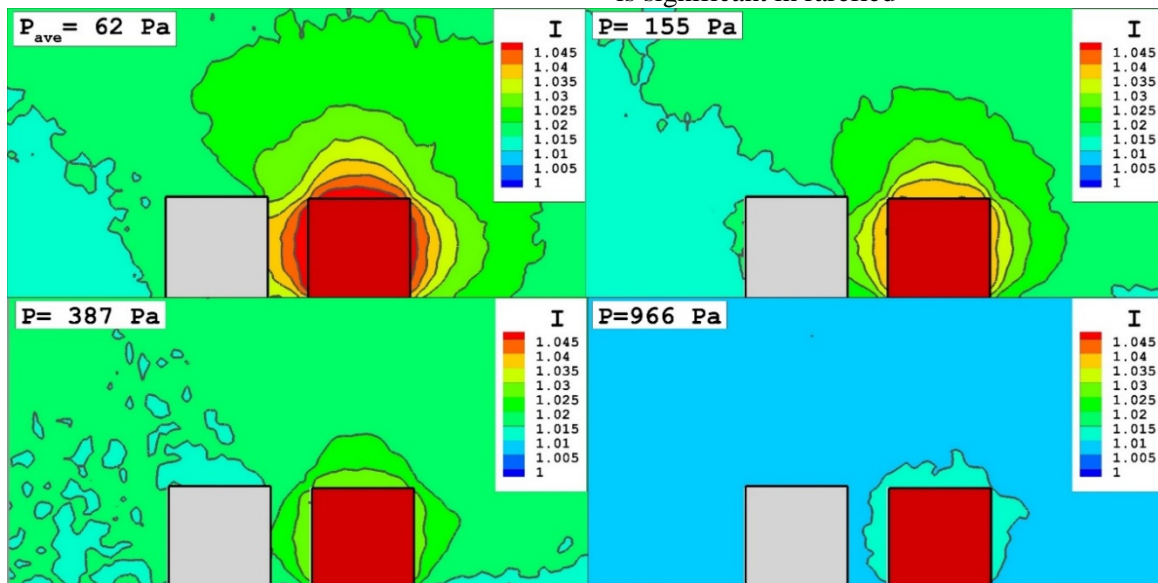


Fig. 5. The distribution of the pressure ratio inside the MIKRA

conditions. Indeed, the temperature gradient induces the pressure difference on the two sides of the cold arm. Our simulation shows that the value of the shear stress on the top of the cold arm is small and is about 1% of the molecular force on the two sides of the cold arm.

In order to investigate the influence of the pressure and temperature distribution on the force production inside the MIKRA, the force distribution of the two sides of the cold arm is plotted in figure 6. The plot clearly shows that the variation of the force on the left side of the cold arm is constant while the force distribution on the right side of the cold arm varies along the height of the arm. The variation of the force confirms that the force production inside the MIKRA is due to the pressure gradient induced by temperature distribution.

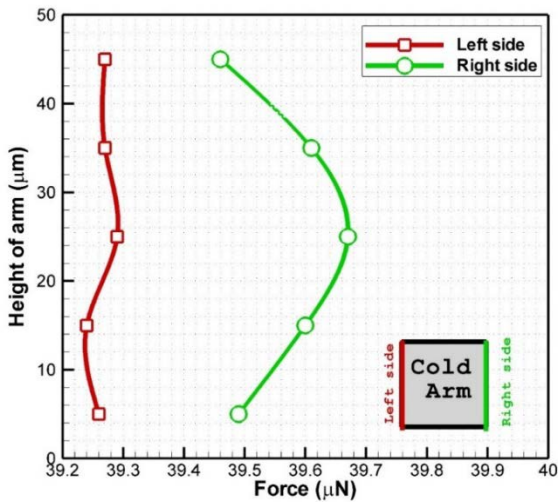


Fig. 6. Comparison of the force distribution on two sides of the cold arm at P=387 pa

Effect of gap distance

Figure 7a compares the temperature distribution and streamline patterns inside the domain for different gap sizes at a specific pressure (P=387 pa) with a similar temperature difference. The contour clearly shows that the flow pattern becomes uniform and the main circulation is strengthened in the low gap size. Since the temperature inside the gap is not significantly varied and the vortex is limited by the gap size, no vortex is formed inside the gap. On the top of the arm, the relatively large space along the thermal creeping flow (cold to hot) permits a big vortex to be formed and the pressure driven flow effectively takes away some molecules from the top wall of the arms and thus releases some pressure therein. In fact, the non-uniform pressure along with large space intensifies the formation of Poiseuille flows and hence a large vortex is formed on the top of the arms.

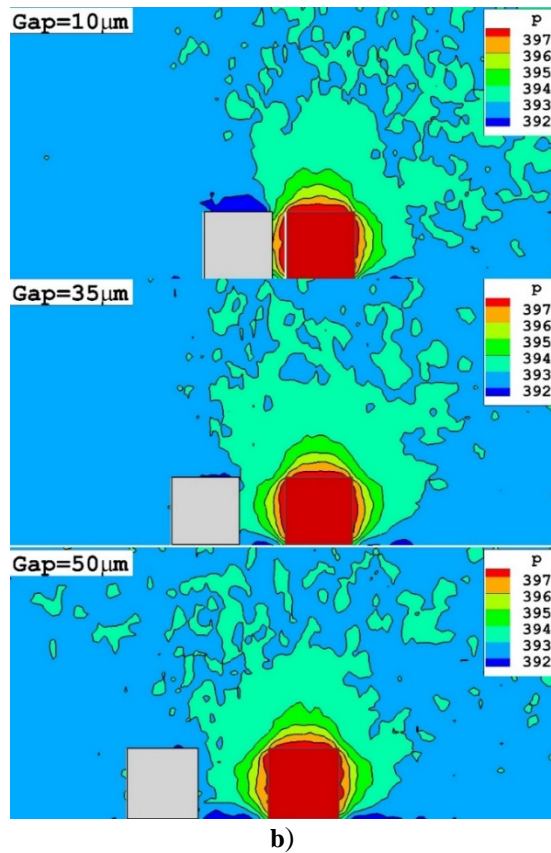
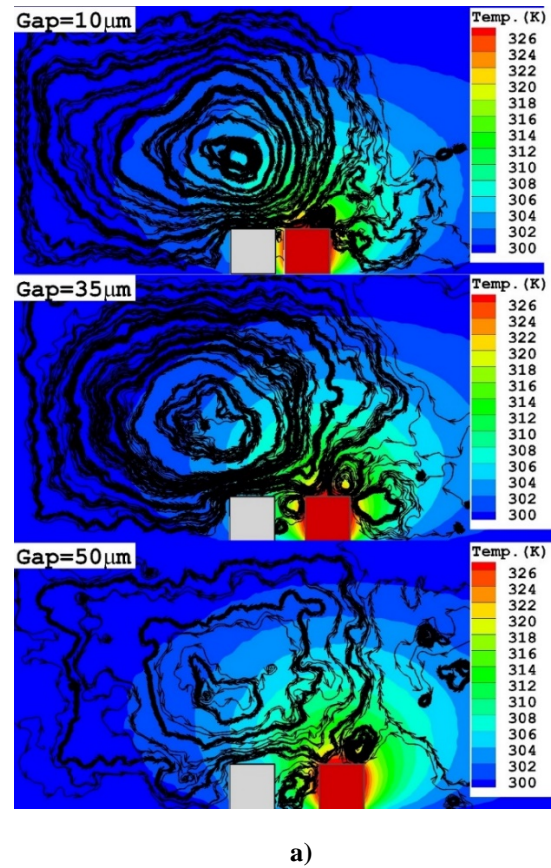


Fig. 7. Effects of gap on a) temperature and streamline b) pressure distribution inside the domain at P=387 pa

As the gap size is increased (Gap=35 μm), the Knudsen number decreases. Hence, the non-uniform distribution of temperature inside the gap only induces a non-uniform density gradient in the whole domain and pressure gradient diminishes on the top of arm [23]. This distance also declines the strength of thermal creeping flow. Figure 7b compares the pressure distribution for different gap sizes. Hence, the formation of the main vortex deteriorates when the gap size is increased. In addition, a small vortex is generated in the right and top side of the hot arm. This confirms that the pressure driven flow on the top of the arms was limited in the low Knudsen number. In the space of the arms, two vortices are produced in the space due to non-uniform temperature distribution. In the followings, the effect of these vortices on the force generation on the cold arm will be comprehensively discussed.

In the high gap distance (Gap=50 μm), the pressure gradient becomes less and the formation of the small vortex close to the hot arm does not allow the main counterclockwise vortex to sense the temperature gradient and the clockwise small vortex further blocks the gas molecules flowing out of the gap. In addition, the pressure near the bottom of the gap is lower than the pressure on the top of the arms and this produces a big vortex inside the gap.

Since the main goal of this device (MIKRA) is to measure the force in various pressure conditions, the comparison of the force for the different gap sizes is significant. Figure 8 compares a generated force for different pressures and gap sizes..

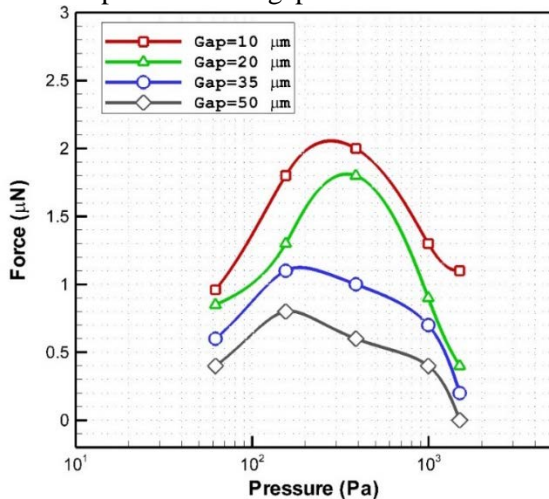


Fig. 8. Influence of the gap distance on the force production on the cold arm

The plot clearly shows that the Knudsen force increases when the gap size is decreased. In addition, it was found that the maximum force occurs at low pressure as the gap size is increased. Indeed, the presence of the vortex diminishes the force

production on the right side of the cold arm and does not allow the hot molecules to reach the surface of the cold arm

Effect of arm length (L)

In order to characterize the main mechanism of the operation of MIKRA, the length of the arms is varied to reveal the effect of this factor on the flow feature and Knudsen force generation on the actuator arm. Figure 9 compares the flow features inside the domain for three different values of length when thickness (50 μm) and pressure (P=387 pa) of the model remain constant. The contour shows that increasing the length of the arms divides the main circulations into two circulations.

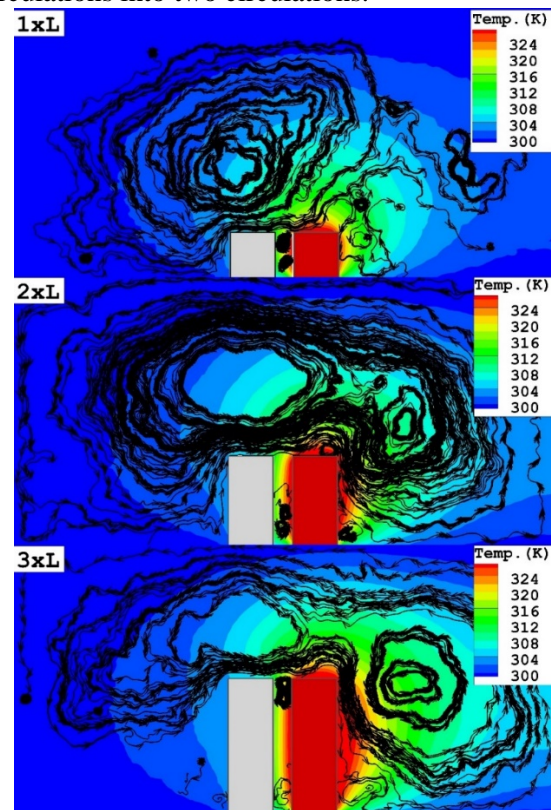


Fig. 9. Effect of the arm length (L) on flow pattern and temperature distribution inside the gas sensor (P=387 pa)

Moreover, the temperature gradient inside the domain significantly intensifies by increasing the length of arms. Figure 10 illustrates the variation of the force generation on the cold arm with various length values at various domain pressures. The induced Knudsen force noticeably increases as the length of the arms is raised. The value of maximum Knudsen force increases 366 percent by rising the length of arm from 1xL to 3xL. This shows that the rate of the induced force on the arms is more than the elongation rate. In addition, the maximum force is obtained at the same pressure for all arm lengths.

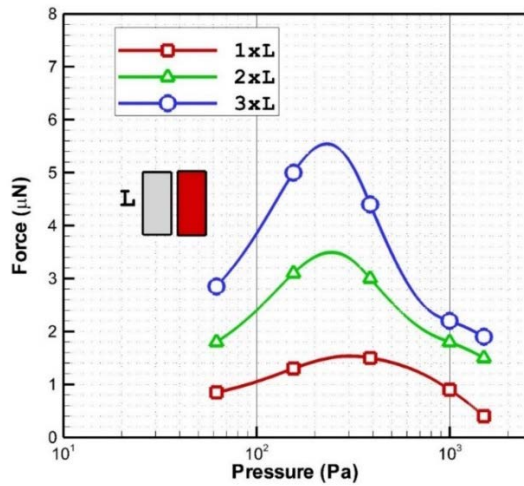


Fig. 10. Effect of the arm length on the Knudsen force generation

CONCLUSIONS

In this research, DSMC method was applied to simulate rarefied gas inside the MEMS device. This work focuses on the influence of ambient pressure on the flow features and force generation mechanism. The governing equation of the current problem is Boltzmann equation. DSMC approach was then applied to simulate the rarefied gas. The flow patterns and temperature distribution were compared for various values of pressure and gap size. Results showed that the gap size considerably influences the generated force, and the maximum force varied by the gap size. Our findings confirmed that the Knudsen force decreases when the pressure of the domain increases. Finally, the force distribution on the right side of the cold arm clearly confirms that the temperature gradient in the gap is significant for the force generation and plays a crucial role in the performance of this device.

REFERENCES

1. C. Liu, Ch.-Sh. Liu, X. Yan, *Physics Letters A*, **381**(12),1092 (2017)
2. A. Peyghan, F. R. Somayeh, L. N. Hadipour, *Phys. Lett. A* **378** (30), 2184 (2014).
3. S. K. Dadzie, J. M. Reese, *Phys. Lett. A* **376**, 967 (2012).

4. A. Hassanvand, M. B. Gerdroodbary, R. Moradi, Y. Amini. *Res. in Phys.* **9**, 351 (2018).
5. T. Goto, T. Itoh, T. Akamatsu, N. Izu, W. Shin, *Sens. and Actuat. B: Chemical*, **223**, 774 (2016).
6. G. Gregis, J.-B. Sanchez, I. Bezverkhy, G. Weber, F. Berger, V. Fierro, J.-P. Bellat, A. Celzard, *Sensors and Actuators B: Chemical*, **vol. 391** (2017).
7. A. Ketsdever, N. Gimelshein, S. Gimelshein, N. Selden, *Vacuum*, **86**, 1644 (2012).
8. W. Crookes, *Philos. Trans. R. Soc. London*, **164**, 501 (1874).
9. A. Passian, R. Warmack, T. Ferrell, T. Thundat, *Phys. Rev. Lett.* **90**, 124503 (2003).
10. A. Passian, A. Wig, F. Meriaudeau, T. L. Ferrell, T. Thundat, *J. Appl. Phys.*, **92**, 10 (2002)
11. A. Poozesh, M. Mirzaei, *J. Stat. Phys.* **166**, 354 (2017).
12. M. Barzegar Gerdroodbary, D. D. Ganji, I. Shiryanpour, R. Moradi. *J Nat Gas Sci Eng.*, **53**, 317 (2018):
13. M. B. Gerdroodbary, M. Mosavat, D.D. Ganji, M. Taeibi-Rahni, R. Moradi, *Vacuum*, **150**, 207 (2018)
14. M. B. Gerdroodbary, A. Anazadehseyd, A. Hassanvand, R. Moradi, *Int. J. Hydrog. Energy*, **43** (11), 5770 (2018)
15. M. B. Gerdroodbary, D. D. Ganji, M. Taeibi-Rahni, Shidvash Vakilipour, *Microsystem Technologies*, **24** (5), 2189 (2018),
16. A. Mahyari, M. Barzegar Gerdroodbary, M. Mosavat, D. D. Ganji. *Cas. Stud. in Therm. Eng.* **12**, 276, (2018).
17. A. D. Strongrich, A. J. Pikus, I. B. Sebastiao, D. Peroulis, A. A. Alexeenko, *IEEE 29th Int. Conf. on Micro Electro Mechanical Systems (MEMS)* (IEEE, 2016), p. 828.
18. A. Strongrich, A. Alexeenko, *Applied Physics Letters*, **107**, 193508 (2015).
19. M.B. Gerdroodbary, D.D. Ganji, M. Taeibi-Rahni, S. Vakilipour, *Europ. Phys. J. Plus*, **132** (7), 315 (2017)
20. G.A. Bird, *Oxford, Clarendon Press*; 1994.
21. OpenFOAM: the Open Source CFD Toolbox, User Guide, Version 1.6, (2009).
22. T. Zhu, W. Ye, *Physical Review E*, **82**, 036308 (2010).
23. S. McNamara, Y. B. Gianchandani, *J. Microelectromech. Syst.* **14**, 741 (2005).
24. T. Zhu, W. Ye, J. Zhang, *Physical Review E*, **84**, 056316 (2011).

ПРИЛОЖЕНИЕ НА ДИРЕКТНА МОНТЕ КАРЛО СИМУЛАЦИЯ ЗА РАЗРАБОТВАНЕ НА МИКРО ГАЗОВ СЕНЗОР

М.Б. Гердроодбари*¹, Д.Д. Ганджи¹, М. Таеиб-Рахни², Ш. Вакилипур³, Р. Моради⁴

¹ *Департамент по механоинженерство, Технологически университет на Бабол, Бабол, Иран*

² *Департамент по космическо инженерство, Шариф Технологичен университет, Техеран, Иран*

³ *Факултет по нови науки и технологии, Техерански Технологичен университет, Техеран, Иран*

⁴ *Катедра по химическо инженерство, Училище по инженерство и приложна наука, Казарския университет, Баку, Азербайджан*

Постъпила на 26 ноември 2017 г.; коригирана на 1 януари 2018 г.

(Резюме)

Разработването на нов микро газов сензор е съществено за анализа на излизащите газове от газоразделителни устройства. В настоящата статия е моделиран газов сензор за ниско налягане чрез директна Монте Карло симулация с цел изследване на влиянието на физичните параметри върху работата и основните характеристики на този вид устройства при различни условия на работа. Проведено е задълбочено параметрично изследване върху влиянието на атмосферното налягане, температурата и разстоянието между рамената на устройството. Установено е, че разстоянието има значително влияние върху характеристиките на потока и генерацията на сила в сензора.

Cloud point extraction combined with flame atomic absorption spectrometry for analysis of trace silver nanoparticles in environmental waters

H.Z. Wu^{1,2}, L.F. Meng^{2*}

¹ Faculty of Land Resources and Engineering, Kunming University of Science and Technology, Kunming 650224, China

² College of Mining Engineering, Guizhou University of Engineering Science, Bijie 551700, China

^{2*} College of Chemistry Engineering, Guizhou University of Engineering Science, Bijie 551700, China

Received January 8, 2018, Revised April 10, 2018

A cloud-point extraction (CPE) method using non-ionic surfactant Tergitol TMN-6 (TMN-6) is developed for the extraction and pre-concentration of silver nanoparticles (AgNPs). Effective separation of ionic silver species and AgNPs is achieved by using sodium thiosulfate ($\text{Na}_2\text{S}_2\text{O}_3$) as a masking agent. Addition of 1M $(\text{NH}_4)_2\text{SO}_4$ enhanced the phase separation and thus increased the extraction efficiency of AgNPs. An enrichment factor of 57 was obtained with 1% (v/v) TMN-6, and the recoveries of AgNPs spiked into environmental samples were in the range of 96.7% to 108%. A low limit of detection (LOD) of 6.5 $\mu\text{g/L}$ was achieved using flame atomic absorption spectrometry (FAAS) for quantification. The relative standard deviation (RSD) was 2.1% ($n=9$). This proposed method provides an efficient approach for the analysis and tracking of AgNPs in environmental water samples.

Key words: Silver nanoparticles, Cloud point extraction, Pre-concentration, Flame atomic absorption spectrometry, Tergitol TMN-6.

INTRODUCTION

Metallic nanoparticles are of high importance in current materials research, with potential applications in biomedicine, energy conversion, imaging, or as pigments [1,2]. Engineered nanomaterials (NMs) have already yielded a variety of commercially available products including cosmetics, antimicrobials, suntan lotions, paints, stain-resistant clothing and remediation products [3]. The rapid growth in the commercial use of AgNPs will inevitably increase silver exposure to the general population [4]. AgNPs may penetrate the skin [5] *via* textile or wound dressing contact, be inhaled from some spray medicines, or ingress into the female genital tract by incorporation from female hygienic products or medical implants [6]. It is also toxic to human cells [7-9]. Therefore, it is important from an analytical point of view to develop sensitive and economical methods for determination of trace silver nanoparticles.

A great deal of methods have been developed for characterization and quantitative analysis of NMs in simple matrices, as well as in natural NMs in a complex matrix such as environmental waters and soils [10,11]. In the case of AgNPs, the identification was usually conducted by the combination of scanning electron microscopy (SEM), transmission electron microscopy (TEM), energy dispersive spectroscopy (EDS), and UV-vis spectroscopy [12,13], whereas the quantification

was performed after oxidation of AgNPs to Ag^+ and detection with inductively coupled plasma mass spectrometry (ICP-MS) [14,15], graphite furnace atomic absorption spectrometry [16,17], inductively coupled plasma optical emission spectrometry (ICP-OES)[18], or chromogenic methods [19-21]. Due to the low concentration of analyte and matrix effects, often a suitable sample pretreatment step (pre-concentration and separation) is required.

Cloud-point extraction (CPE), which is based on the fact that most nonionic surfactants in aqueous solutions form micelles and become turbid when heated to the cloud point temperature or in the presence of an electrolyte. Above the cloud point, the micellar solution separates into a surfactant-rich phase with a small volume and a diluted aqueous phase [22]. To date, CPE has been successfully applied for the quantification of Au-NPs in water samples in combination with electrothermal atomic absorption spectrometry (ET-AAS) [23]. However, in ET-AAS measurements, due to large background absorption signals and sample inhomogeneity, the relative sensitivity and analytical precision are poor.

The typical surfactants used in CPE processes mostly include Triton series, Igepal series, PONPE series, etc. [24,25]. However, these surfactants contain alkyl phenyl groups in their hydrophobic moiety, leading to some environmental concerns [26]. Therefore, biodegradable surfactants are proposed such as ethoxylated alcohols without phenyl group and branched alkyl chains. Tergitol

* To whom all correspondence should be sent.
E-mail:1025588702@qq.com

series surfactants are polyethylene glycol trimethylnonyl ethers, non-ionic surfactants, with no aromatic group; with cloud-point temperature of 36°C, similar to that of Triton series. Therefore, the big potential of Tergitol TMN-6 in cloud point extraction will be taken advantage of.

In this study, the possibility of AgNPs enrichment by CPE based on TMN-6 as extractant was considered. A new microextraction method combined with flame atomic absorption spectrometry (FAAS) was developed for separation, enrichment and determination of AgNPs in environmental waters. Factors affecting the extraction efficiency, such as pH, concentration of extractant, extraction time, and nature of the extractant were studied and optimized.

EXPERIMENTAL

Chemicals and materials

All chemicals used were of analytical grade or better and all solutions were prepared in deionized water. Tannic acid, sodium carbonate, ammonium sulfate, hydrochloric acid, silver nitrate, ethanol, Tergitol TMN-6 and sodium thiosulphate, all were purchased from (Aladdin, China).

pH SJ-4A pH meter (Shanghai, China), vortex agitator (Shanghai, China), SK5210LHC ultrasonic instrument (Shanghai, China), centrifuge (Shanghai, China) and flame atomic absorption spectrometer (AA6300, Shimadzu, Japan) were used. Samples of waste water treatment plant (WWTP) were obtained from Chengong (Kunming, China), the river water sample was from Luo Long River (Kunming, China).

Nanoparticles synthesis

Preparation of AgNO₃ solution and tannic acid solution: 0.100 mol/L Na₂CO₃ solution in deionized water; 200 mL tannic acid solution were added to a three-mouth bottle in a thermostated water bath under stirring; 5mL of Na₂CO₃ solution was added for tannin reduction; after 10 min, a certain amount of AgNO₃ solution was dropwise added to the above mixture with a constant-pressure drop funnel. The color of the solution in the tree-mouth bottle gradually changed from colorless to light yellow, orange, red, and finally turned a deep red or red brown. The stirring and heating continued for 30 min more to obtain the AgNPs. The AgNPs concentration of the solution was determined by FAAS.

CPE of AgNPs

AgNPs sample solution (4 mL) was placed in a 10 mL long tapered glass centrifuge tube and pH was adjusted to 3.0 with dilute HCl. Then, 40 μL of 1M Na₂S₂O₃, 80 μL of 1% (v/v) TMN-6 and 40 μL of 1M (NH₄)₂SO₄ were added in sequence. The mixture was mixed and incubated at 36°C in a water bath for 15 min, and the tube was centrifuged at 3000 rpm at room temperature for 15 min to facilitate phase separation. The obtained TMN-6-rich phase (<100μL), which forms a viscous droplet was attached to the bottom of the tube. The supernatant aqueous phase can then easily be removed by decanting. The droplet was dissolved in 2 mL of ethanol and was submitted to FAAS measurement.

RESULTS AND DISCUSSION

Optimization of the CPE conditions

Parameters that commonly affect the CPE efficiency, such as salt content, surfactant concentration, temperature, pH, and incubation time, were optimized. pH plays an important role on metal chelate formation and subsequent extraction. To optimize the extraction conditions for the nanoparticles pH was varied between 1 and 7 using hydrochloric acid for pH adjustment while the other experimental variables remained constant. The highest extraction efficiency was achieved at pH 3.0 (Fig. 1) (number of replicates n=6). So, pH 3.0 was selected as the optimum pH value for further experiments.

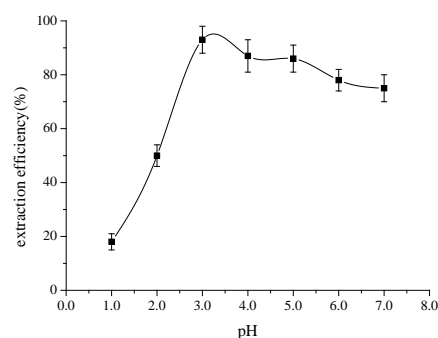


Fig. 1. Effect of pH on CPE of AgNPs

For the highest possible enrichment the final volume of the nanoparticle-rich phase should be as small as possible. On the other hand, the extraction efficiency of nanoparticles should not be decreased by the use of an insufficient amount of surfactant. Experiments with different amounts of TMN-6 at constant overall volume and nanoparticle concentration (Fig. 2) showed that for an aqueous sample of 4 mL 80μL of 1% TMN-6 solution are sufficient to meet the above criteria.

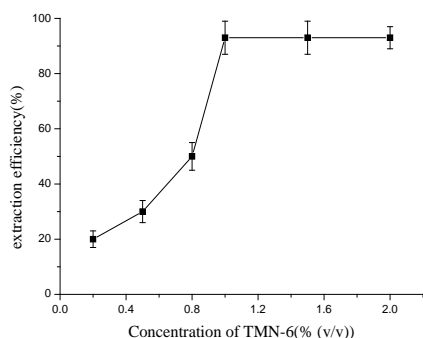


Fig. 2. Effect of TMN-6 concentration on the extraction efficiency

The CPE behavior was also affected by salt concentrations. Addition of salt can accelerate phase separation and lower the cloud point temperature of the surfactant solution. In this study, $(\text{NH}_4)_2\text{SO}_4$ was added as a salt to enhance the extraction of AgNPs, and $\text{Na}_2\text{S}_2\text{O}_3$ as a masking reagent to cover the interference of Ag^+ . When $\text{Na}_2\text{S}_2\text{O}_3$ was added, thiosulfate ions and silver ions generated thiosulfate (Fig. 3), which is soluble in water. In this way silver ions can be eliminated prior to the detection of AgNPs.

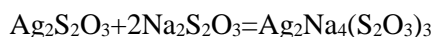
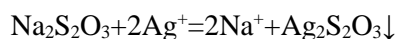


Fig. 3. The reaction of sodium thiosulfate with Ag^+

Fig. 4 shows the impact of $(\text{NH}_4)_2\text{SO}_4$ concentration on the extraction efficiency of AgNPs. The extraction efficiency increased with $(\text{NH}_4)_2\text{SO}_4$ concentration up to 1M while the other experimental variables remained constant. This effect may be due to increasing interactions between the analyte and salt in the sample solution with increasing salt concentration, due to the salting out effect of $(\text{NH}_4)_2\text{SO}_4$, and then remained constant up to 3M.

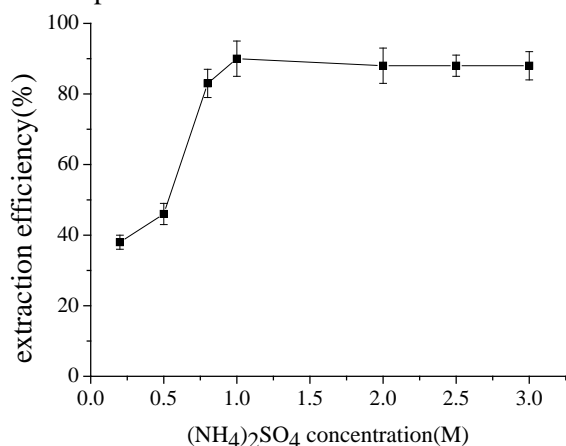


Fig. 4. Effect of $(\text{NH}_4)_2\text{SO}_4$ concentration on the extraction efficiency of AgNPs

To achieve easy phase separation, optimal equilibration temperature and incubation time are

necessary to complete extraction. The effects of equilibration temperature and time were studied within the ranges of 30–50 °C and 15–40 min, respectively while the other experimental variables remained constant. It was found that an equilibration temperature of 36 °C and a time of 15 min were adequate to achieve quantitative extraction.

In this work, the kinds of surfactant such as Triton X-114, Triton X-100, TMN-6, TMN-10 and Tween 20 were investigated. The results are illustrated in Fig. 5. It shows that the extraction efficiency was the highest with the use of TMN-6.

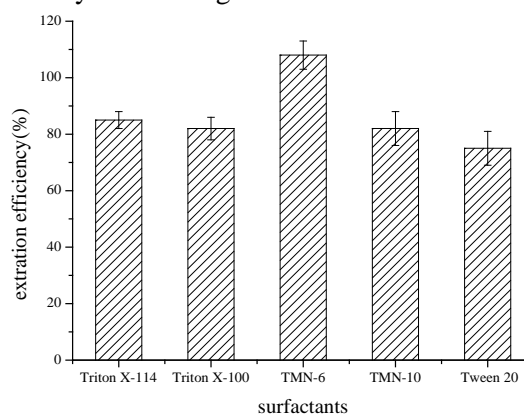


Fig. 5. Effect of surfactants on the extraction efficiency

The high viscosity of the so prepared surfactant-rich phase made it necessary to dissolve the sample prior to sample introduction to FAAS. Ethanol appeared to be a feasible solvent since it readily dissolves the surfactant-rich phase and prevents degradation of the enriched nanoparticles.

Evaluation of the preservation of the nanoparticle size distribution

To gain an insight in the size distribution of the nanoparticles in real samples it is necessary to know whether the size distribution of Ag-NPs is changing during the extraction procedure or not. This was studied using TEM for imaging of the particles before and after CPE. As shown, the size of the particles after the extraction process is more or less identical to the size before CPE treatment. Thereby we concluded that the size distribution is not affected by the present method. This supports the results of Yang *et al.* that studied CPE of metal nanoparticles [23]. This finding is particularly important because the size determination of nanoparticles is an important issue in the current research. CPE samples of Ag-NPs can therefore be used for $(\text{NH}_4)_2\text{SO}_4$ determination after pre-concentration.

The analytical characteristics of the method were evaluated under the optimum experimental conditions (Table 1).

Table 1. Analytical characteristics of the method

Parameter	Analytical feature
Linear range (µg/L)	10-1000
R ²	0.9999
Limit of detection (µg/L)	6.5
RSD(%) (n=9)	2.1
Enrichment factor	57
Pre-concentration time (min)	<10
Recovery (%)	96.7-108.0

Analytical features

The enrichment factor (EF), relative standard deviation (RSD) and limit of detection (LOD) are effective factors to evaluate a developed analytical method. With the optimized system, the calibration graph of AgNPs was linear over the range of 10-1000 µg/L. The calibration equation is $A=7.9 \times 10^{-2} + 0.003C$ with a correlation coefficient of 0.9999, where A is the absorbance and C is the Ag concentration in µg/L. The detection limit, defined as the concentration equivalent to three times the standard deviation of the reagent blank for AgNPs was 6.5µg/L. The relative standard deviation for AgNPs was 2.1% (n = 9). The relative recoveries of AgNPs in water samples at the spiking level of 3-20 µg/L ranged from 96.7% to 108%. The enhancement factor, defined as the ratio of slope of pre-concentrated samples to that obtained without pre-concentration, was 57 for AgNPs.

Effect of foreign ions

With regard to the high sensitivity of FAAS determination of Ag, the interferences connected with the CPE procedure were studied due to the fact that foreign cations may react with TMN-6 and lead to a decrease in extraction efficiency. 10 mL sample solution containing Ag⁺ and other ions was prepared and treated with the developed procedure. The tolerance limit was defined as the foreign ion concentration causing a change in the absorbance of less than ±5%. Table 2 shows the concentration of the interferent ions, the recovery is tolerable. No significant difference between recoveries for samples with or without filtration was observed, suggesting that the presence of natural particles in the samples had no significant effects on the CPE of AgNPs at a concentration of 20 µg/L. This result indicates that FAAS can be adopted to identify and quantify the AgNP content in environmental samples.

Analysis of real samples

To further evaluate the applicability of the proposed method, real environmental water samples were analyzed and the recoveries were determined by spiking 3-20 µg/L AgNPs. As shown in Table 3, the obtained recoveries of AgNPs were in the range of 96.7-108%, which was satisfactory with regard to the low spiking level.

Table 2. Effects of the matrix ions on the recoveries of the examined metal ions

Ions	Concentration (µg/L)	Recovery (%)	
		Pd	Ag
Na ⁺	10×10 ³	105.0	104.1
K ⁺	10×10 ³	104.2	104.8
Cl ⁻	10×10 ³	103.5	102.2
Ca ²⁺	10	99.1	101.1
Mg ²⁺	0.5	99.2	96.8
Cr ³⁺	0.5	100.7	98.8
Mn ²⁺	0.5	103.4	99.2
Zn ²⁺	0.5	102.2	100.1
Cd ²⁺	0.5	98.7	99.7
Ni ²⁺	0.5	99.6	100.8
Pb ²⁺	0.5	108.7	98.5
Cu ²⁺	0.5	102.6	99.9

Table 3. Determination and identification of AgNPs in environmental waters by the proposed method

Sample	AgNPs added (µg/L)	AgNPs found (µg/L)	Recovery (%)
River water	0	*ND	—
	5	4.9±0.3	98.0±0.6
	10	10.8±0.5	108.0±5.0
	20	20.5±0.6	102.5±3.0
WWTP	0	*ND	—
	3	2.9±0.5	96.7±16.7
	8	8.1±0.6	101.3±7.5
	15	15.8±0.7	105.3±4.6

Table 4. Comparison of proposed measurement with other measurements

Measurement	Sample volume (mL)	Detection time (min)	RSD (%) (n=9)	Injection volume (mL)	LOD ($\mu\text{g/L}$)	Reference
ICP-MS	9.5	> 10	5.6	5	0.006	[18]
ET-AAS	40	5	9.5	0.2	0.005	[24]
FAAS	5	< 2	2.1	0.2	6.5	This paper

Comparison with other measurements

Table 4 compares the characteristic data of the proposed method with those of other methods for AgNPs determination reported in literature. As it can be seen, the proposed method offers a better RSD and a lower detection time.

CONCLUSION

In this report, CPE based on TMN-6 was demonstrated to be an efficient approach for selective extraction and pre-concentration of trace AgNPs from environmental water samples. $\text{Na}_2\text{S}_2\text{O}_3$ was added to the extraction system as a masking reagent of Ag^+ to prevent its extraction into the TMN-6 rich phase and $(\text{NH}_4)_2\text{SO}_4$ was added as a salt to enhance the extraction of AgNPs. The TMN-6-rich phase can be directly determined by FAAS in small sample volumes with a high sensitivity and good reproducibility. In addition, the type of sample and matrix does not affect the detection of AgNPs. This proposed method provided a simple approach for quantification of AgNPs in environmental water samples.

Acknowledgements: Haizhi Wu, postdoctoral researcher, being engaged in mineralogy and fluid geochemistry. The work was greatly supported by the Key Disciplines of Guizhou Province (ZDXK[2016]13), Medical Neurobiology Key Laboratory of Kunming University of Science and Technology, the Analysis and Testing Foundation of Kunming University of Science and Technology (No. 2017121).

REFERENCES

1. S. Mohammad-Hosseini, K. Leila, *J. Chinese Chem. Soc.*, **57**, 1346 (2013).
2. T.G. Naemullah, F.Kazi, H.I. Shah, H.I. Afridi, J.A. Baig, A. S. Soomro, *J. AOAC Int.*, **96**, 447 (2013).
3. A. Khaligh, *Int. J. Environ. Anal. Chem.*, **95**, 16 (2015).
4. M. Mirzaei, A.K. Naeini, *J. Anal. Chem.*, **68**, 595 (2013).
5. M. Ghaedi, K. Niknam, K.S. Nasiri, M. Soylak, *Human & Exper. Toxicol.*, **32**, 504 (2013).
6. S. Procházková, R. Halko, *Analytical Lett.*, **49**, 1656 (2016).
7. N. Sirirat, K. Tetbuntad, A. Siripinyanond, *Pediatric Research*, **9**, 1 (2017).
8. M. Ghaedi, G. Karimipour, E. Alambarkat, A. Asfaram, M. Montazerzohori, *Int. J. Environ. Anal. Chem.*, **95**, 1030 (2015).
9. M. Habila, Y.E. Unsal, Z.A. Allothman, A. Shabaka, M. Tuzen, *Analytical Lett.*, **48**, 2258 (2015).
10. A. Nagy, E. Baranyi, A. Gaspar, *Microchem. J.*, **114**, 216 (2014).
11. N. Baghban, A. M. H. Shabani, Sh. Dadfarnia, *Int. J. Environ. Anal. Chem.*, **93**, 1367 (2013).
12. S.K. Mwilu, A.M.E. Badawy, K. Bradham, C. Nelson, D. Thomas, *Sci. Total Environ.*, **447**, 90 (2013).
13. A. Hebeish, M.H. El-Rafie, M.A. El-Sheikh, A.A. Seleem, M.E. El-Naggar, *Int. J. Biol. Macromol.*, **65**, 509 (2014).
14. K. Shameli, M.B. Ahmad, E.A.J. Al-Mulla, P. Shabanzadeh, S. Bagheri, *Res. Chem. Intermediates*, **41**, 251 (2015).
15. G.F. Prozorova, A.S. Pozdnyakov, N.P. Kuznetsova, S.A. Korzhova, A.I. Emel'yanov, *Int. J. Nanomedicine*, **9**, 1883 (2014).
16. S.J. Oh, H. Kim, Y. Liu, H.K. Han, K. Kwon, *Toxicol. Lett.*, **225**, 422 (2014).
17. T. Yin, H.W. Walker, D. Chen, Q. Yang, *J. Membrane Sci.*, **449**, 9 (2014).
18. G. Hartmann, C. Hutterer, M. Schuster, *J. Anal. Atomic Spectrometry*, **28**, 567 (2013).
19. S.M. Majedi, B.C. Kelly, H.K. Lee, *Anal. Chim. Acta*, **814**, 39 (2014).
20. T.K. Mudalige, H. Qu, S.W. Linder, *Anal. Chem.*, **87**, 7395 (2015).
21. S.M. Majedi, B.C. Kelly, H.K. Lee, *Environ. Sci. Poll. Res.*, **21**, 1811 (2014).
22. T. Tolessa, X.X. Zhou, M. Amde, J.F. Liu, *Talanta*, **169**, 91 (2017).
23. X. Yang, Z. Jia, X. Yang, G. Li, X. Liao, *Saudi J. Biol. Sci.*, **24**, 589 (2017).
24. G. Hartmann, M. Schuster, *Anal. Chim. Acta*, **761**, 27 (2013).
25. S.M. Majedi, B.C. Kelly, H.K. Lee, *Anal. Chim. Acta*, **789**, 47 (2013).
26. N. Altunay, R. Gürkan, U. Kır, *Anal. Methods*, **7**, 6629 (2015).

ЕКСТРАКЦИЯ ПРИ ТОЧКАТА НА ПОМЪТНЯВАНЕ В СЪЧЕТАНИЕ С
АТОМНОАБСОРБЦИОННА СПЕКТРОМЕТРИЯ ЗА АНАЛИЗ НА СЛЕДОВИ
КОЛИЧЕСТВА ОТ СРЕБЪРНИ НАНОЧАСТИЦИ В ОТПАДНИ И ПРИРОДНИ ВОДИ

Х.З. У^{1,2}, Л.Ф. Мън^{2*}

¹ Колеж по минно инженерство, Гуижоуски университет по инженерни науки, Биджие 551700, Китай

² Колеж по инженерна химия, Гуижоуски университет по инженерни науки, Биджие 551700, Китай

Постъпила на 8 януари 2018 г.; коригирана на 10 април 2018 г.

(Резюме)

Разработен е метод за екстракция при точката на помътняване (CPE) с използване на нейонното повърхностно активно вещество тергитол TMN-6 за извличане и концентриране на сребърни наночастици (AgNPs). Ефективно разделяне на йонните форми на среброто от AgNPs е постигнато с помощта на натриев тиосульфат ($\text{Na}_2\text{S}_2\text{O}_3$) като маскиращ реагент. Добавянето на 1M $(\text{NH}_4)_2\text{SO}_4$ подобрява разделянето на фазите и повишава степента на екстракция на AgNPs. Фактор на обогатяване от 57 е постигнат с 1% (v/v) TMN-6, като извличането на AgNPs, добавени към водите, е в границите от 96.7% до 108%. Границата на откриване (LOD) с пламъков атомноабсорбционен метод за количествено определяне е 6.5 $\mu\text{g/L}$. Относителното стандартно отклонение (RSD) е 2.1% (n=9). Разработеният метод предлага ефективен подход за определяне и проследяване съдържанието на AgNPs в природни води.

Selected papers presented at the 5th Asia-Pacific Conference on Engineering Technology (APCET 2017), May 27-30, 2017, Beijing, China.

Effects of sodium polyacrylate and potassium polymer on growth and physiological characteristics of different flue-cured tobaccos

W.X. Huang*, Z.Z. Wei, G.Y. Niu, Y.J. Zhang, H.F. Shao*

College of Tobacco Science, Henan Agricultural University, Zhengzhou, Henan, 450002, China

Received January 14, 2018; Accepted February 7, 2018

To investigate water retention effects and physiological regulation mechanism of water-retaining agents on the growth and development of different flue-cured tobacco varieties, a pot experiment was conducted using 'Yuyan 6' and 'Yuyan 10' to study the effects of sodium polyacrylate and potassium polymer on the agronomic characteristics, the root activity, the activity of antioxidant enzymes, the content of malondialdehyde (MDA) and proline in the leaves of flue-cured tobaccos. The results were as follows. (1) The application of water-retaining agents increased the plant height, the stem diameter, the number of effective leaves, the maximum leaf area and the root activity of flue-cured tobaccos and the effects were more significant for Yuyan 10 of relatively poor drought resistance. (2) The activity of SOD, POD and CAT of flue-cured tobaccos treated with water-retaining agents was reduced to different extents. (3) The application of water-retaining agents lowered the MDA content of flue-cured tobaccos but the effects were more significant for Yuyan 10 of relatively poor drought resistance. (4) The application of water-retaining agents decreased the proline content of flue-cured tobaccos under drought conditions, but the decrease of proline content in Yuyan 6 was larger than that in Yuyan 10. Yuyan 6 was highly drought-tolerant, so water-retaining agents could better promote the adaptability of Yuyan 10 to drought stress. Furthermore, water-retaining agent potassium polymer showed a stronger regulatory capability for the growth and physiological metabolism of flue-cured tobaccos than water-retaining agent sodium polyacrylate.

Keywords: Water-retaining agents; Flue-cured tobaccos; Growth; Physiological characteristics

INTRODUCTION

Tobacco is one of the important economic crops in China [1]. Moisture is a major consistent of tobacco plants, as well as an indispensable environmental factor in the growth and metabolism of tobacco [2]. At present, many soils of the world are rather short of water resources, especially in agricultural production [3]. The shortage of water resources in tobacco cultivation is intensified day by day. Drought stress gives rise to serious abnormal physiological and biochemical changes of tobacco plants and further decreases the output and quality of tobacco leaves [4]. Therefore, it is of great significance to develop drought-resistant and water-saving tobacco cultivation and achieve superior quality and stable output of flue-cured tobaccos.

In recent years, water-retaining agents, have been rapidly introduced in agricultural production as anti-drought chemical agents which can soon absorb moisture hundreds of times as much as their mass [5]. The role of water retaining agents has caught the attention of experts from the whole world [6]. Water-retaining agents can improve the infiltration rate of soil moisture and reduce direct

surface runoff [7-9], thus playing a key role in the response to drought stress [10]. Y.H. Yang *et al.* found that the application of water-retaining agents increased the soil moisture content in different growth stages of winter wheat, as well as the accumulation of dry matter [11]. D.H. Liu *et al.* also proved that water-retaining agents significantly promoted the photosynthetic productivity and the accumulation of biomass of potatoes [12]. Under drought conditions, the application of water-retaining agents is of importance in the growth of tobaccos [13-15]. In this paper, a pot experiment was conducted using 'Yuyan 6' of relatively good drought resistance and 'Yuyan 10' of relatively poor drought resistance [16] to study the effects of sodium polyacrylate $[(C_3H_3NaO_2)_n]$ and potassium polymer on the agronomic characteristics, the root activity, the activity of antioxidant enzymes, the contents of malondialdehyde ($C_3H_4O_2$) (MDA) and proline ($C_5H_9NO_2$) in tobacco leaves (see Fig. 1.), aiming to figure out the physiological regulation mechanism of different water-retaining agents in the growth of flue-cured tobaccos and provide theoretical references for water-saving tobacco cultivation.

* To whom all correspondence should be sent.

E-mail: : wxhuang@henau.edu.cn; shf.email@163.com

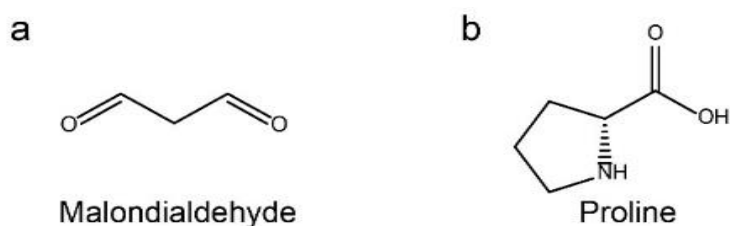


Fig. 1. a: Chemical structure of malondialdehyde; b: Chemical structure of proline.

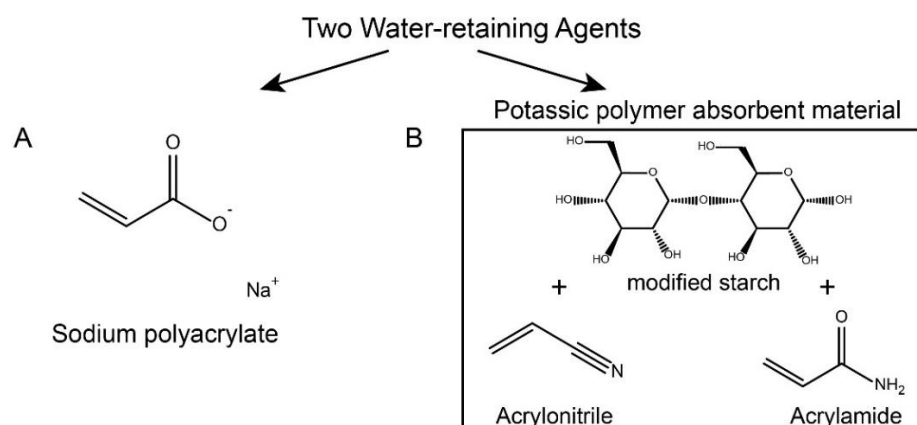


Fig. 2. Chemical structure of the effective components in two water retaining agents. A: Changhao anti-drought water-retaining agent; B: Shenghua water-retaining agent.

EXPERIMENTAL DETAILS

The pot experiment was conducted under a rainproof shelter in the agricultural experimental zone of the new campus of Henan University of Science & Technology in Luoyang in 2015. Two water-retaining agents were applied (Fig. 2.): A. Changhao anti-drought water-retaining agent, which was mainly composed of sodium polyacrylate $[(C_3H_3NaO_2)_n]$, white, granulated, crystalline, with a water absorption rate of 150 times, purchased from Changhao Environmental Science & Technology Co, Ltd; B. Shenghua water-retaining agent, which was a kind of potassium polymer absorbent material prepared with modified starch $[(C_6H_{10}O_5)_n]$, acrylonitrile (C_3H_3N) and acrylamide (C_3H_5NO), white powdered, with a water absorption rate of 200 times, provided by Changsha Shenghua Science & Technology Development Co., Ltd.

The flue-cured tobaccos for the experiment were ‘Yuyan 6’ and ‘Yuyan 10’ provided by

Luoyang’s Luoning tobacco workstation and cultivated in plastic pots with a row spacing of 100 cm×50 cm. Each plastic pot had a height of 35 cm, an inner diameter of 40 cm and was filled with 20.0 kg of cinnamon sandy soil which passed through a 0.5 cm×1 cm mesh sieve and contained organic matter 19.8 g/kg, available nitrogen 67.6 mg/kg, rapidly available phosphorous 14.5 mg/kg and rapidly available potassium 147.5 mg/kg, with a pH value of 7.45. In all treatments, NPK fertilizer and 5 g of pure nitrogen were applied to each pot. N:P₂O₅:K₂O=1:1.5:3. Where necessary, calcium phosphate and potassium sulfate were used to supplement inadequate phosphorus and potassium.

The flue-cured tobacco plants were transplanted on May 21, 2015. A total of six treatments were designed (Table 1) and 50 flue-cured tobacco plants were cultivated in 50 pots separately in each treatment, totaling 300 flue-cured tobacco plants. Before transplanting, water-retaining agents, NPK

Table 1. Experimental treatments

Treatments		Water Retaining Agents
Yuyan 10	CK	Without water retaining agents
Yuyan 10	T1	With water retaining agent A (sodium polyacrylate)
Yuyan 10	T2	With water retaining agent B (potassium polymer)
Yuyan 6	CK	Without water retaining agents
Yuyan 6	T1	With water retaining agent A (sodium polyacrylate)
Yuyan 6	T2	With water retaining agent B (potassium polymer)

fertilizer and soil were homogeneously blended and put into pots. Then, the flue-cured tobacco plants were watered with 2 L to resume growth and the watering volumes were equal in all treatments. Afterwards, the maximum field capacity was measured using the cutting-ring method [17], and TDR-100 soil moisture content analyzer (SPECTRUM, USA) was used to determine the soil moisture content. The flue-cured tobacco plants were subject to moderate water stress 10 d before sampling and measurement based on relative soil moisture contents at 50%, 70% and 60% of the maximum field capacity in the root extending stage, the vigorous growth stage and the maturity stage, respectively.

The plant height and the maximum leaf area of flue-cured tobaccos were measured using a tape of millimeter graduation, the stem diameter was measured with a vernier caliper and the number of effective leaves was recorded at the time [17], in which the maximum leaf area = the maximum leaf length \times the maximum leaf width \times 0.6345 (the leaf area index of flue-cured tobacco).

The sampling began 30 d after transplanting and later was conducted at 9:00 a.m. every 15 d. The top-down fifth fully-expanded leaves of three flue-cured tobacco plants were collected in each treatment each time. The fresh samples were placed in an ice tray and brought back to laboratory soon. The measurement of different indicators was repeated three times. The root activity was measured using the TTC method [18]; superoxide dismutase (SOD) activity was determined using the nitroblue tetrazolium reduction method [19]; peroxidase (POD) activity was measured with the guaiacol method [18]; catalase (CAT) activity was determined using the ultraviolet absorption method [19]; malonaldehyde (MDA) content was measured by the thiobarbituric acid method [18]; proline content was determined by the ninhydrin method.

RESULTS AND DISCUSSION

It can be seen from Table 2 that the plant height, the stem diameter, the number of effective leaves and the maximum leaf area of Yuyan 6 were larger than those of Yuyan 10 in CK treatment and that the application of water-retaining agents increased the plant height, the stem diameter, the number of effective leaves and the maximum leaf area of both Yuyan 6 and Yuyan 10 under drought stress. On the 30th d, 45th d and 75th d after transplanting, the plant height of Yuyan 10 in T2 treatment was

significantly above that in CK treatment by 31.9%, 25.2% and 18.4%, respectively; on the 30th d, 45th d and 60th d after transplanting, the maximum leaf area of Yuyan 10 in T2 treatment increased by 27.5%, 42.9% and 20.8% respectively in comparison with CK treatment; on the 60th d and 75th d after transplanting, the number of effective leaves of Yuyan 10 in T2 treatment was significantly higher than that in CK treatment by 10.0% and 13.5%, respectively. The plant height, the number of effective leaves and the maximum leaf area of Yuyan 6 were T2 > T1 > CK in different growth stages, but the differences were insignificant. Thus, it can be inferred that the application of water-retaining agents could promote the growth of flue-cured tobaccos but the promotional effects on Yuyan 10 of relatively poor drought resistance were more significant.

The root system is an important organ for adsorption of nutrients and moisture in soil and the root activity directly affects the drought resistance of crops [20-22]. As can be seen from Table 3, from the 30th d to the 75th d after transplanting, the root activity of flue-cured tobaccos increased at first, reached a maximum on the 60th d after transplanting and decreased from then on in different treatments. The root activity of Yuyan 6 was higher than that of Yuyan 10 in CK treatment and the application of water-retaining agents improved the root activities of both Yuyan 10 and Yuyan 6. On the 30th d after transplanting, the root activity of Yuan 10 in T1 and T2 treatments displayed significant differences from that in CK treatment; 45 d, 60 d and 75 d after transplanting, the root activity of Yuan 10 in T2 treatment was significantly different from those in T1 and CK treatments; what's more, on the 60th d after transplanting, the root activity of Yuyan 10 in T2 treatment was higher than those in T1 and CK treatments by 29.4

% and 25.0%, respectively. From 30 d to 60 d after transplanting, the root activity of Yuyan 6 had no significant differences; 75 d after transplanting, the root activity of Yuyan 6 in T2 and T1 treatments significantly differed from that in CK treatment and increased by 138.33 $\mu\text{g}/(\text{g}\cdot\text{h})$ and 249.44 $\mu\text{g}/(\text{g}\cdot\text{h})$, respectively. Therefore, it can be concluded that the application of water-retaining agents could enhance the root activity of flue-cured tobaccos and was favorable to the growth of the root system under drought conditions.

Table 2. Comparison of agronomic characteristics of flue-cured tobacco plants in different treatments

Indicators	Flue-cured Tobaccos	Treatments	Days after transplanting (d)			
			30	45	60	75
Plant height/cm	Yuyan 10	CK	15.67±1.53 b	47.67±7.02 b	70.00±3.46 ab	100.50±0.71 b
		T1	17.33±1.53 ab	53.67±1.53 ab	72.00±10.15 a	109.00±1.41 ab
		T2	20.67±2.08 a	59.67±4.04 a	78.67±6.66 a	119.00±9.90 a
	Yuyan 6	CK	20.33±2.31 a	55.33±1.53 a	76.00±5.57 a	117.50±10.61 a
		T1	22.33±1.53 a	54.33±6.03 a	79.67±11.93 a	120.00±19.80 a
		T2	24.33±2.31 a	58.67±0.58 a	87.67±14.64 a	127.50±3.54 a
Stem diameter/cm	Yuyan 10	CK	3.80±0.17 a	7.13±0.61 a	7.50±0.87 a	7.25±0.35 a
		T1	3.83±0.29 a	7.33±0.29 a	7.60±0.36 a	7.50±0.71 a
		T2	4.00±0.50 a	7.83±0.76 a	8.17±0.29 a	8.00±0.00 a
	Yuyan 6	CK	3.83±0.29 a	7.83±0.29 b	7.83±0.29 a	8.00±0.00 a
		T1	3.93±0.06 a	8.33±0.58 ab	8.00±0.00 a	8.25±1.06 a
		T2	4.00±0.00 a	9.00±0.50 a	8.17±0.76 a	8.25±0.35 a
Number of effective leaves	Yuyan 10	CK	9.33±1.15 a	13.00±0.00 a	16.67±0.58 b	18.50±0.71 b
		T1	9.67±0.58 a	13.33±0.58 a	18.00±0.00 a	20.50±0.71 a
		T2	10.00±1.00 a	13.33±1.15 a	18.33±0.58 a	21.00±0.00 a
	Yuyan 6	CK	10.00±1.00 a	14.67±0.58 a	17.00±1.00 a	19.00±1.41 a
		T1	11.00±1.73 a	15.00±1.00 a	17.33±1.53 a	20.00±1.41 a
		T2	10.67±0.58 a	15.33±0.58 a	19.00±1.00 a	21.50±0.71 a
Maximum leaf area/cm ²	Yuyan 10	CK	386.83±28.18 b	692.66±58.28 b	928.92±26.23 b	1054.68±134.80 a
		T1	432.94±32.50 b	870.27±51.76 ab	956.00±122.59 ab	1206.26±102.19 a
		T2	493.34±9.03 a	990.10±155.69 a	1122.43±101.14 a	1249.68±410.57 a
	Yuyan 6	CK	447.96±71.40 a	755.00±86.26 a	938.64±112.61 a	1355.50±68.59 a
		T1	499.25±32.10 a	913.77±215.12 a	1144.50±180.36 a	1452.00±69.30 a
		T2	526.00±42.99 a	941.15±114.95 a	1147.86±107.37 a	1472.25±113.49 a

Note: The data followed by different letters in each column are not significantly different at 0.05 level from each other according to Tukey Test. The same as below.

Table 3. Comparison of root activities of flue-cured tobaccos in different treatments, unit: µg/(g·h)

Flue-cured Tobaccos	Treatments	Days after transplanting (d)			
		30	45	60	75
Yuyan 10	CK	218.89±21.21b	458.89±19.64b	585.00±28.28b	130.00±30.64b
	T1	338.89±46.35a	514.72±57.75b	605.56±25.93b	239.44±25.14b
	T2	445.56±35.36a	650.00±25.93a	757.22±40.86a	387.22±45.57a
Yuyan 6	CK	290.56±7.86a	538.33±153.99a	646.11±50.28a	235.00±42.43b
	T1	377.22±66.00a	637.78±71.50a	701.11±62.07a	373.33±7.07a
	T2	375.56±76.21a	707.78±54.21a	704.44±40.07a	484.44±43.21a

Fig. 3 shows that the SOD activity declined in the whole growth stage in the different treatments. From 30 d to 75 d after transplanting, the SOD activities of Yuyan 10 in different treatments were T2<T1<CK and had significant differences. The SOD activity of Yuyan 10 in T2 treatment differed significantly from that in CK treatment and dropped by 45.7%, 33.1%, 50.3% and 39.2%, respectively; on the 75th d after transplanting, the SOD activities of Yuyan 10 in T1 and T2 treatments were significantly different from that in CK treatment and dropped by 42.1% and 43.5%, respectively. In CK treatment, the SOD activity of Yuyan 6 was higher than that of Yuyan 10. The flue-cured tobaccos differed in their responses of SOD activity to drought and the application of water-retaining agents could reduce the SOD activity of flue-cured tobaccos, but the reduction effects were diversified.

Fig. 4 shows that the POD activity increased from 30 d to 75 d after transplanting in different

treatments. The increase in the POD activity in the late growth stage was probably the result of physiological and biochemical reactions of flue-cured tobacco plants in the maturity and senescence stage, that is to say, POD converted carbohydrates in the tissues of flue-cured tobaccos into xylogen. In CK treatment, the POD activity of Yuyan 10 was higher than that of Yuyan 6 because the POD activity of tobacco leaves reflected not only the extent of stress but also the drought resistance, that is, the higher the POD activity, the weaker was the drought resistance of flue-cured tobaccos. 30 d, 60 d and 75 d after transplanting, the POD activities of Yuyan 10 in T2 treatment were significantly different from those in CK treatment and dropped by 50.8%, 32.8% and 40.1%, respectively. The POD activities of Yuyan 6 in the whole growth stage were T2<T1<CK and no significant differences were observed.

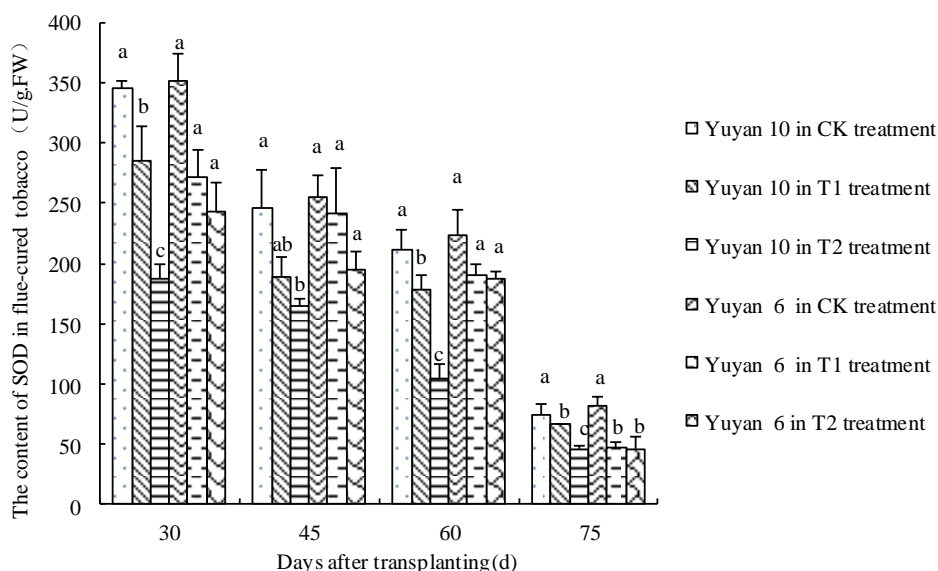


Fig. 3. Comparison of SOD activities of flue-cured tobacco leaves in different treatments

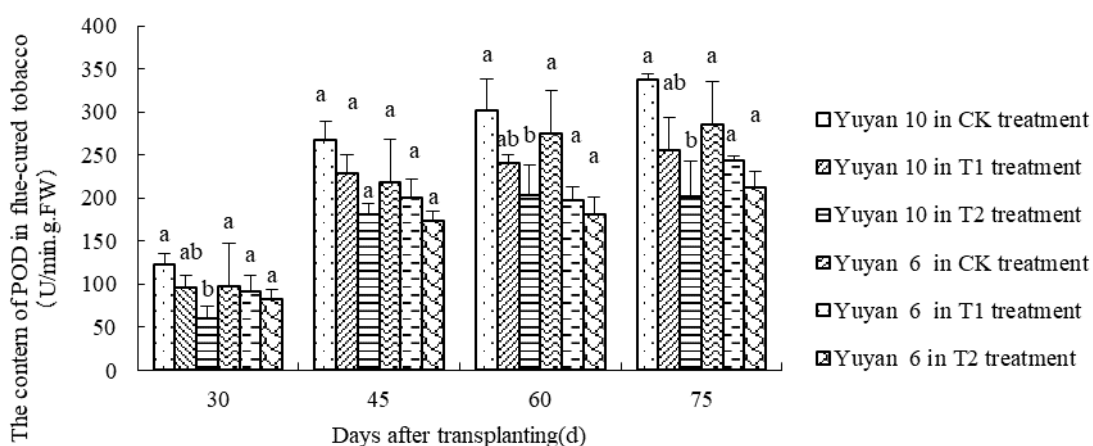


Fig. 4. Comparison of POD activities of flue-cured tobacco leaves in different treatments

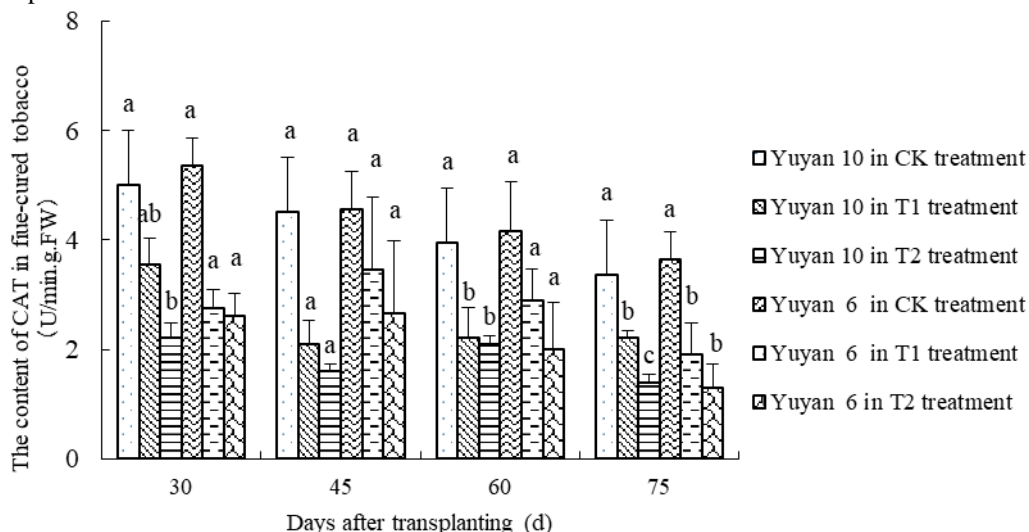


Fig. 5. Comparison of CAT activities of flue-cured tobacco leaves in different treatments

It can be seen from Fig. 5 that the CAT activity gradually decreased in the whole growth stage in the different treatments. 60 d and 75 d after transplanting, the CAT activities of Yuyan 10 treated with water retaining agents had significant differences from those in CK treatment; 60 d after

transplanting, the CAT activities of Yuyan 10 in T1 and T2 treatments dropped by 44.3% and 46.8 % in comparison with CK treatment; on the 75th d after transplanting, the CAT activities of Yuyan 10 in T1, T2 and CK treatments showed significant differences. The CAT activities of Yuyan 6 were

T2<T1<CK in different growth stages and the CAT activities of Yuyan 6 in T2 and T1 treatments were lower than that of CK treatment by 47.9% and 64.4% on the 75th days after transplanting.

Malonaldehyde (MDA) is a product of cellular membrane lipid peroxidation and the MDA content is a main indicator that reflects the extent of peroxidation damages of cellular membrane system of plants [23]. It can be seen from Table 4 that the MDA contents increased from the 30th d to the 75th d after transplanting in different treatments. The MDA contents were relatively low in the early growth stage but went up in the late growth stage, which was probably due to the physiological metabolism within flue-cured tobaccos in the maturity stage. In CK treatment, the MDA contents of Yuyan 6 were lower than those of Yuyan 10 in different growth stages, which suggested that Yuyan 6 was able to maintain a certain protective endoenzyme activity under drought stress, scavenge free radicals and reduce the extent of cellular membrane lipid peroxidation. Yuyan 10 of relatively poor drought resistance suffered from severe damages and could not resist adverse water stress. In the whole growth stage, the MDA contents of Yuyan 6 in different treatments were T2<T1<CK but had no significant differences. 30 d and 45 d after transplanting, the MDA contents of Yuyan 10 treated with water-retaining agents were

significantly different from those in CK treatment; from 30 d to 75 d after transplanting, the MDA contents of Yuyan 10 in T2 treatment had significant differences from those in CK treatment and dropped by 50.6%, 37.4%, 39.0% and 29.6%, respectively. Thus, it can be seen that the application of water-retaining agents could reduce the MDA contents of flue-cured tobaccos and the reduction effects on Yuyan 10 of relatively poor drought resistance were more significant.

The effects of different water-retaining agents on the proline contents of flue-cured tobacco leaves are shown in Fig. 6 and it can be seen that the proline contents of flue-cured tobaccos increased at first but dropped later from 30 d to 75 d after transplanting in different treatments. In the whole growth stage, the proline contents of Yuyan 10 in T2 treatment were lower than those in CK treatment by 46.4%, 51.7%, 51.1% and 36.5%, respectively. From 30 d to 60 d after transplanting, the proline contents of Yuyan 6 in T1 and T2 treatments significantly differed from those in CK treatment, that is, the proline contents of Yuyan 6 in T1 treatment dropped by 54.7%, 57.1% and 47.0% and the proline contents of Yuyan 6 in T2 treatment dropped by 75.6%, 67.9% and 49.7% in comparison with CK treatment. The decreases of proline content of Yuyan 6 between CK and T1, T2 treatments were larger than those of Yuyan 10.

Table 4. Comparison of MDA contents of flue-cured tobacco leaves in different treatments, unit: nmol/g

Flue-cured Tobaccos	Treatments	Days after transplanting (d)			
		30	45	60	75
Yuyan 10	CK	372.08±22.58a	518.05±45.21a	574.43±52.45a	659.87±27.90a
	T1	236.30±19.24b	412.58±28.42b	471.59±20.87ab	626.21±45.93a
	T2	183.67±9.47b	324.37±16.17b	350.63±48.26b	464.32±38.92b
Yuyan 6	CK	211.66±16.81a	422.28±24.50a	464.58±43.63a	521.94±13.36a
	T1	179.05±22.71a	410.40±59.14a	424.56±22.15a	491.90±47.37a
	T2	174.06±29.92a	314.50±71.96a	361.81±40.86a	449.21±75.63a

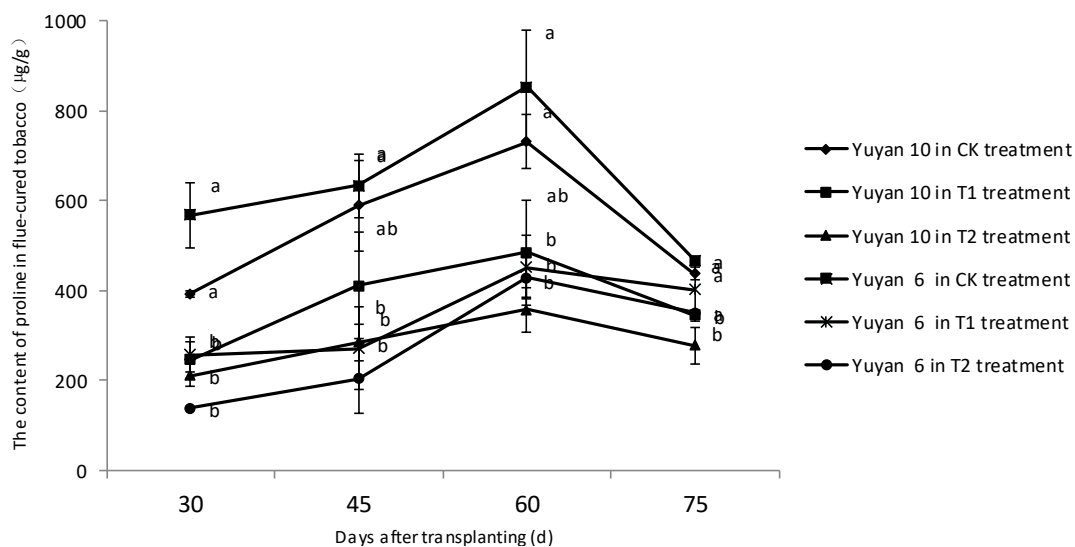


Fig. 6. Proline contents of flue-cured tobacco leaves in different treatments

Thus, it can be inferred that the application of water-retaining agents reduced the proline contents of both Yuyan 6 and Yuyan 10 under drought stress but the reduction effects on the former were larger than those on the latter.

CONCLUSIONS

The root system is the main organ for absorption of water and nutrients for tobacco plants and directly affects the growth of flue-cured tobaccos [24]. Apart from the genetic factors, the growth of the root system is mainly affected by the environmental factors like moisture content, nutrients in soil, etc. Therefore, the root activity is closely related to the soil moisture content. J. Zhang *et al.* [25] proved that the root activity of flue-cured tobaccos declined under drought stress. Our experimental results showed that the root activity of Yuyan 6 was higher than that of Yuyan 10 under drought conditions without applying water-retaining agents, so it can be inferred that the physiological metabolism of the root system of Yuyan 6 was more active. The application of water-retaining agent B (potassium polymer) enhanced the root activity of flue-cured tobaccos in the different growth stages. This is probably due to the application of a water-retaining agent which improves the soil aeration or a soil moisture sub-environment is formed around the root system and both water and nutrients are effectively conserved.

The production and scavenging of active oxygen in plants are in dynamic balance under normal conditions but a great deal of active oxygen will be accumulated under adverse stress, so the anti-oxidant enzymes like SOD, POD and CAT are of great importance to maintain the physiological functions of cells. According to relevant studies, the activity of anti-oxidant enzymes in plants generally shows an increasing tendency under drought conditions [26]. B.L. Xiao *et al.* [27] found that drought increased the SOD activity of flue-cured tobacco. In our experiment, it was found that the SOD and CAT activities of Yuyan 6 were higher than those of Yuyan 10 but the POD activity of Yuyan 10 was higher than that of Yuyan 6 under drought stress without applying water retaining agents. This was probably because the POD activity reflected the extent of stress damages and the higher the POD activity, the weaker was the drought resistance of flue-cured tobaccos. The application of water-retaining agents reduced the SOD, POD and CAT activities of flue-cured tobaccos but the reduction effects were diversified. It can be inferred that flue-cured tobaccos differed in their responses of anti-oxidant enzymes to drought.

The dynamic balance between production and scavenging of active oxygen in plants is broken under drought conditions so that a great deal of active oxygen is accumulated in plants, which leads to cellular membrane lipid peroxidation. MDA is the final product of the cellular membrane lipid peroxidation and the higher the MDA content, the greater damages plants suffer from [28]. Our experimental results showed that the application of water retaining agents reduced the MDA contents of flue-cured tobaccos and the reduction effects on Yuyan 10 of relatively poor drought resistance were more significant.

The MDA content in leaves of Yuyan 6 was significantly lower than that of Yuyan 10, which indicated that Yuyan 6 was able to reduce the cellular membrane lipid peroxidation under drought stress and the tissue membrane system of Yuyan 6 had a stronger drought-resistant ability. In comparison with Yuyan 10, Yuyan 6 could better adapt to the drought stress. When plants suffer from a drought, a great deal of osmotic regulation substances is accumulated within plants and the osmotic potential is reduced so as to adjust the cell turgor and maintain normal life activities [29]. In general, proline exists in plants in the free state and is an important osmotic regulation substance within plants. The proline content can reflect the stress degree for plants to some extent [30]. The proline content in plants is rather small (0.20~0.69 mg/g) under normal conditions but a great deal of proline is accumulated under drought conditions [31]. H.Y. Lu *et al.* [31] came to the conclusion that the application of water-retaining agents could decrease the contents of MDA and proline in leaves. Our experiment showed that the application of water-retaining agents reduced the proline content of tobacco leaves but water-retaining agent B (potassium polymer) had more significant reduction effects. Under drought conditions, the proline content of Yuyan 6 was largely increased, which was favorable to osmotic regulation, reduction of osmotic potential and improvement of drought-resistant ability, while the proline content of Yuyan 10 was slightly increased and the drought resistance of Yuyan 10 was poor.

It is reported that the constituents of water-retaining agents, the soil conditions of experimental fields, the crop species for experiment, as well as the experimental conditions like local climate may lead to differences in experimental results [32]. X.J. Guan *et al.* [33] showed that more than 90% of water conserved by high-quality water-retaining agents of good performance could be taken in by plants but about 1/3 of water conserved by water-retaining agents of poor performance could not be

absorbed by plants. Some relevant studies suggest that an overdose of sodium acrylate which participates in cross-linking polymerization may result in an impairment of plants and soil structure but the water retention performance and stability will be improved and water retaining agents will be conducive to the growth of plants and soil amelioration after degradation if potassium acrylate is put into use [34]. In our experiment, water retaining agent B (potassium polymer) is mainly composed of potassium acrylate and has a moderate water absorption rate, so its water retention ability and stability are better and promotional effects for the growth and physiological regulation capability of flue-cured tobaccos are more significant than those of water- retaining agent A (sodium polyacrylate). Instead, water-retaining agent A (sodium polyacrylate) is mainly composed of sodium acrylate and its effects on the growth of flue-cured tobaccos in different growth stages are weaker. Above all, the growth and physiological metabolism of flue-cured tobaccos can be improved as long as proper water-retaining agents are applied.

Acknowledgements: This work was supported by the program of the Education Department of Henan Province (17A210020).

REFERENCES

1. H.W. Niu, Z.C. Xu, H.F. Shao, L. Luo, R.R. Zhao, Y.X. Xiao, W.L. Yang, K.G. Wang, *Acta Tabacaria Sinica*, **5**, 39 (2012).
2. G.S. Liu, J.H. Chen, Beijing, *Science*, **3**, 1, 2012.
3. M.R. Islam, A.E. Eneji, C.Z. Ren, Y.G. Hu, G. Chen, X. Z. Xue, *J. Agric. Biotechnol.Ecol.*, **3**, 1 (2010).
4. B.W. Cui, Y.G. Lu, Z.Z. Zhang, K. Ren, *Chinese Tobacco Sci.*, **30**, 19 (2009)
5. Y. Shi, J. Li, J. Shao, S. Deng, R. Wang, N. Li, *Scientia Horticulturae*, **124**, 268 (2010)
6. M. Sadeghi, H. Hosseinzadeh, *Asian J. Chem.*, **22**, 6743 (2010)
7. A.R. Sepaskhah, A.R. Bazrafshan-Jahromi, *Biosys. Eng.*, **93**, 469 (2006)
8. W.J. Busscher, D.L. Bjorneberg, R.E. Sojka, *Soil Tillage Res.*, **104**, 215 (2009)
9. J. Akhter, K. Mahmood, K.A. Malik, A. Mardan, M. Ahmad, M.M. Iqbal, *Plant Soil & Environ.*, **50**, 463 (2004)
10. I.C. Dodd, in: *Advances in Plant Physiology* (A. Hemantarajan, editor), Springer Netherlands. Vol. **15**, **274**, p. 251 (2005)
11. Y.H. Yang, P.T. Wu, J.C. Wu, S.W. Zhao, X.N. Zhao, Z.B. Huang, *Trans. CSAE*, **26**, 19 (2010)
12. D.H. Liu, Z.B. Huang, L.J. Cai, Z.X. Wei, *Acta Agriculturae Boreali-occidentalis Sinica*. **17**, 266 (2008)
13. Q.D. Han, Y. Liu, Y.T. Han, L.X. Liu, M.J. Yang, B.D. Xie, *Chinese Tobacco Sci.*, **36**, 68 (2015)
14. Y. Li, H. Shen, Z.H. Jia, W.X. Pu, Z.J. Sun, Y.F. Wang, *Chinese Tobacco Sc.*, **3**, 10 (2013)
15. Z. Chen, J.Y. Xu, Y.K. Fan, W.X. Huang, P.W. Wang, X.Y. Wen, *Chinese J. Eco-Agric.*, **24**, 1508 (2016)
16. L. Wang, J.C. Zhang, X.Q. Zhang, L. Meng, L. Zhai, *J. Southwest Forestry Univ.*, **30**, 6 (2010)
17. X.H. Chen, S. Guo, G.S. Liu, L.Y. Qiu, M.D. Wang. *J. Xinyang Normal Univ.*, **1**, 47 (2014)
18. L.M. Lu, *Beijing Sci.*, **1**, 197 (2013)
19. Q. Sun, J.J. Hu. *Northwest Agric. Fores. Univ. Sci. Technol.*, **66**, 165 (2006)
20. S. Asseng, J.T. Ritchie, A.J.M. Smucker, *Plant and Soil*, **201**, 265 (1998)
21. R. Motzo, G. Attene, M. Deidda, *Euphytica*, **66**, 197 (1992)
22. Y.X. Xu, L.X. Bei, H. Zhang, G.B. Yu, K.J. Yang, C.J. Zhao, *Plant Physiol. J.*, **52**, 101 (2016)
23. L.B. Yang, H.F. Shao, X.J. Zhang, J.J. Yu, X.M. Ma, *Tobacco Science & Technology*, **10**, 45 (2002)
24. X.Y. Shang, H.B. Liu, X.Q. Zhang, J. Lin, W.J. Duan, *Acta Botanica Boreali-Occidentalia Sinica*, **30**, 357 (2010)
25. J. Zhang, H. Liu, X.P. Li, M. Lu, S.G. Sun, J.N. Su, *Agric. Res. Arid Areas*, **3**, 1 (2014)
26. Y.B. Yun, J.X. Li, F.Z. Ding, X.K. Su. *Chinese Tobacco Sci.*, **30**, 10 (2009)
27. B.L. Xiao, D.M. Li, L.X. Liu. *J. Henan Agric. Sci.*, **11**, 36 (2010)
28. H.L. Hu, J. Zhang, T.X. Hu, L.H. Tu, Y.X. Pan, F.M. Zeng, *Acta Botanica Boreali-Occidentalia Sinica*, **34**, 118 (2014)
29. J.Y. He, Y.F. Ren, Y.Y. Wang, Z.J. Li, *Acta Ecologica Sinica*, **31**, 522 (2011)
30. P. Qin, Y.J. Liu, F.H. Liu, *Chinese Tobacco Sci.*, **26**, 28 (2005)
31. H.Y. Lu, Y.Y. Liu, F.W. Gao, S.G. Luo, *J. Northeast Agric. Univ.*, **37**, 299 (2006)
32. Z.B. Huang, G.Z. Zhang, Y.Y. Li, M.D. Hao, Meni Ben-Hur, *Trans. CSAE*, **18**, 22 (2002)
33. X.J. Guan, J.C. Wu, *J. Henan Agri. Sci.*, **7**, 13 (2007)
34. W. Huang. J.H. Zhang, L.F. Zhang, Y.H. Liu, Y.H. Wang, *Chinese J. Ecol.*, **34**, 1910 (2015)

ВЛИЯНИЕ НА НАТРИЕВ ПОЛИАКРИЛАТ И КАЛИЕВ ПОЛИМЕР ВЪРХУ РАСТЕЖА И ФИЗИОЛОГИЧНИТЕ ПАРАМЕТРИ НА РАЗЛИЧНИ ОПУШЕНИ ТЮТЮНИ

У.Кс. Хуан*, З.З. Уей, Г.И. Ниу, И.Дж. Джан, Х.Ф. Шао*

Колеж по изучаване на тютюна, Хенански селскостопански университет, Женкжоу, Хенан, 450002, Китай

Постъпила на 14 януари, 2018 г.; коригирана на 7 февруари, 2018 г.

(Резюме)

За изучаване на задържането на водата и механизма на физиологичното регулиране на водозадържащи агенти върху растежа и развитието на различни сортове опушени тютюни е проведен експеримент в саксии със сортовете 'Yuuan 6' и 'Yuuan 10'. Изследвано е влиянието на натриев полиакрилат и калиев полимер върху агрономичните характеристики, кореновата активност, активността на антиоксидантните ензими, съдържанието на малонов дианхидрид (MDA) и пролин в листата на опушени тютюни. Установено е следното: (1) Използването на водозадържащи агенти води до повишаване на височината на растението, диаметъра на стъблото, броя на ефективните листа, максималната площ на листата и кореновата активност на опушените тютюни и влиянието е по-силно изразено при сорта Yuuan 10, характеризира се с по-малка издържливост на суша. (2) Активността на SOD, POD и CAT на опушените тютюни, третирани с водозадържащи агенти намалява в различна степен. (3) Прилагането на водозадържащи агенти понижава съдържанието на MDA, но ефектът е по-силно изразен при Yuuan 10. (4) Прилагането на водозадържащи агенти понижава съдържанието на пролин по-съществено при Yuuan 6, отколкото при Yuuan 10. Yuuan 6 е по-толерантен към суша, така че водозадържащите агенти стимулират по-добре адаптирането на Yuuan 10 към стрес от суша. Калиевият полимер демонстрира по-силен регулаторен капацитет върху растежа и физиологичния метаболизъм на опушени тютюни от натриевия полиакрилат.

Effects of deposition pressure on $\text{Cu}_2\text{ZnSnS}_4$ films prepared by one-step sputtering with quaternary target

H.G. Yang^{1,2,*}, J.D. Zhang², M.C. Li^{1*}, R.T. Hao³, G.L. Song²

¹ College of Renewable Energy, North China Electric Power University, Beijing 102206, China

² College of physics and materials scientific, Photovoltaic Materials Laboratory of Henan Province, Henan normal university, Xinxiang 453007, China

³ Solar Energy Research Institute of Yunnan Normal University, Kunming 650092, China

Received January 14, 2018; Accepted February 7, 2018

$\text{Cu}_2\text{ZnSnS}_4$ (CZTS) films were deposited from single-phase $\text{Cu}_2\text{ZnSnS}_4$ quaternary compound target by RF sputtering without post sulfurization process. The as-prepared CZTS films were annealed with 400°C in Ar atmosphere to obtain the single-phase kesterite structure. The influence of sputtering pressure on surface morphology, crystal structure, optical absorption coefficient, band gap, and the influence of the chemical composition of CZTS films was investigated. The diffraction peaks of (112) are sharp and the characteristic peaks of the kesterite-type structure such as (220) and (312) are clearly observed in X-Ray Diffraction patterns. The composition and optical properties of the samples were determined with energy dispersive X-ray spectroscopy (EDS) and UV-VIS-NIR spectrophotometer. While at the sputtering pressure of 0.2 Pa, an attractive Cu-poor and Zn-rich, large grain size and single-phase CZTS film can be obtained. Research result show that the CZTS films exhibit a high absorption coefficient of the order of 10^4 cm^{-1} , and an optical band gap of 1.49 eV.

Keywords: $\text{Cu}_2\text{ZnSnS}_4$ (CZTS) thin film, Crystal structure, Band gap, Magnetron sputtering, Sputtering pressure.

INTRODUCTION

Copper zinc tin sulfide ($\text{Cu}_2\text{ZnSnS}_4$, CZTS) quaternary semiconductor is emerging as a potential candidate that has several promising attributes for efficient, inexpensive solar cells made from abundant and nontoxic elements. CZTS compound is derived by replacing indium (In) and gallium (Ga) elements with zinc (Zn) and tin (Sn) elements in the chalcopyrite-type lattice of $\text{Cu}(\text{In,Ga})\text{Se}_2$ (CIGS). The band gap of CZTS has been reported to be about 1.5 eV, very close to the top absorbent layer band gap of the solar cell that results in a theoretical efficiency limit more than 32% [1-4]. The absorption coefficient of CZTS rises rapidly above the band gap energy and quickly reaches over 10^4 cm^{-1} so that a few microns thick film can absorb nearly all the solar radiation above the band gap. CZTS thin film solar cells have reached an efficiency of 8.6% and those based on a $\text{Cu}_2\text{ZnSn}(\text{S,Se})_4$ absorber layer have reached an efficiency of 11.6% [5,6], demonstrating the promising prospect of the CZTS technology. However, there are no detailed reports on the study of CZTS cells in the past years due to the lack of complete understanding of the parameters governing the low-efficiency performance.

To simplify the preparation procedure, a straightforward one-step deposition of CZTS films by magnetron sputtering without post-annealing

treatment has been explored. In this process, deposition parameters such as sputtering energy, substrate temperature and gas pressure could affect the film properties [7,8]. Sputtering pressure is one of the most important factors which affect the phase formation and morphology of the films by controlling the diffusion, aggregation and growth behaviors of deposited particles. In this work, polycrystalline CZTS films were deposited from single-phase $\text{Cu}_2\text{ZnSnS}_4$ quaternary compound target at different sputtering pressures by one-step radio frequency (RF) sputtering. The crystal structure, chemical composition, surface morphology and optical properties of CZTS films were examined.

EXPERIMENTAL DETAILS

$\text{Cu}_2\text{ZnSnS}_4$ thin films were directly deposited on glass substrates with a CZTS ceramic target by radio frequency magnetron sputtering process. The CZTS target used was composed of kesterite-structure $\text{Cu}_2\text{ZnSnS}_4$ powder through cold pressure method at 40MPa, the atomic ratios of the elements Cu, Zn, Sn, S was 2:1:1:4. Glass substrates were thoroughly cleaned with acetone and ethanol. Sputtering process was carried out in pure argon (99.99%) atmosphere with a substrate at room temperature. The distance between target and substrate was 15 cm and RF sputtering power was

* To whom all correspondence should be sent.
E-mail: : hgyang@htu.cn

70 W. Deposition pressure was maintained at 0.2 Pa, 0.3 Pa and 0.5 Pa, respectively. The total deposition time of the CZTS films was 60 min. The as-prepared CZTS films were annealed at 400°C in Ar atmosphere for 180 min.

The crystal structure of both target and thin films deposited on glass substrates were characterized by X-ray diffractometry (XRD, DX-2000). The surface morphology and composition of samples were determined by scanning electron microscopy (SEM, FEI Quanta FEG 250) and energy dispersive spectroscopy (EDS, FEI Quanta FEG 250). The optical reflectance and transmittance spectra were measured by UV-VIS-NIR spectrophotometry (Shimadzu UV-3600).

RESULTS AND DISCUSSION

Table 1 summarizes the chemical composition of CZTS thin films as a function of deposition pressure in the range from 0.2 to 0.5 Pa. The quaternary CZTS ceramic target used in this one-step sputtering process was a stable kesterite phase in which the sulfur element was well bonded to other elements. During the sputtering process, four elements were simultaneously sputtered by Ar ions and arrived on unheated substrates to directly form CZTS thin films. Energy dispersive spectroscopy (EDS) measurement results showed that all film compositions strongly depend on the sputtering pressure of the grown CZTS film. The spontaneously developed CZTS films on the unheated substrates by sputtering from a quaternary CZTS target provided a simple route to prepare CZTS absorbers with effective utilization of sulfur. It was found that the stoichiometry of quaternary CZTS films is easily controlled by the single-step sputtering deposition, and the composition of the as-grown films could be adjusted with changing the sputtering parameters [9-10]. The ratios of $Cu/(Zn+Sn)$ and Zn/Sn of the thin film fabricated at different sputtering pressures were in the range of 0.54–0.78 and 0.69–0.80, respectively. On decreasing the sputtering pressure, the proportion of copper was gradually reduced, but Zn and Sn ratio was gradually increased, which indicates that the sputtering pressure drop will exacerbate the loss of Cu element. For the efficient absorption of the CZTS thin film solar cell, the ratio of $[Cu]/([Zn]+[Sn])$ was between 0.7~1.0, and

$[Zn]/[Sn]$ - between 1.0~1.4, this would dominate the conversion efficiency of CZTS thin film solar cell [9,11,12]. It is believed that the increase in the proportion of S and Zn in the target material may bring the chemical composition of the samples close to the expected value.

Fig. 1 shows the XRD patterns of the CZTS targets and the CZTS thin film samples. The diffraction peaks of CZTS targets are consistent with the diffraction peak of kesterite structure of CZTS. The four diffraction peaks at $2\theta = 28.60^\circ$, 33.90° , 47.58° , and 56.36° of the samples (a)-(c) can be attributed to the diffraction of (112), (200), (220), (312), respectively. The peaks are specific to the kesterite structure of CZTS based upon JCPDS 26-0575 [13,14]. As the sputtering pressure decreases, the intensities of the (112), (220) and (312) preferred diffraction peaks become stronger. The peak intensity of the CZTS film increases due to the increase in the crystalline nature of the CZTS films. This is due to the decreased chance of sputtering target material particles to collide with gas molecules at low pressure, and higher energy reaches the substrate, which is propitious to produce large grains. Meanwhile it may be seen that diffraction peaks of the thin film samples (112), (220) and (312) become sharper as the sputtering pressure decreases, which shows that the lower sputtering pressure, the better will be thin film crystallinity. The optical characteristics of the CZTS films were evaluated in terms of the optical absorption coefficient and optical band gap. The optical transmittance and reflectance spectra of CZTS films were measured with UV-VIS-NIR spectrophotometer.

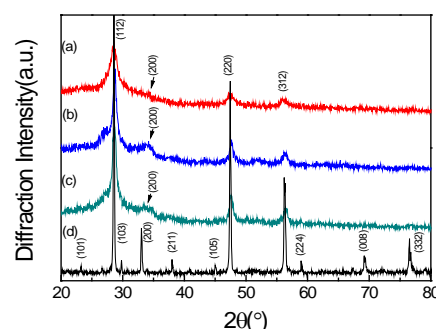


Fig. 1. XRD patterns of CZTS samples: (a), (b) and (c) correspond to their sputtering pressure, (a) 0.5Pa, (b) 0.3Pa and (c) 0.2Pa, (d) corresponds to target material.

Table 1. Chemical composition and compositional ratio of CZTS films

Deposition pressure	Cu (at%)	Zn (at%)	Sn (at%)	S (at%)	$Cu/(Zn+Sn)$	Zn/Sn
0.5 Pa	21.61	12.05	17.37	48.97	0.73	0.69
0.3 Pa	18.74	13.63	18.52	49.11	0.58	0.74
0.2 Pa	18.40	15.16	19.00	47.44	0.54	0.80

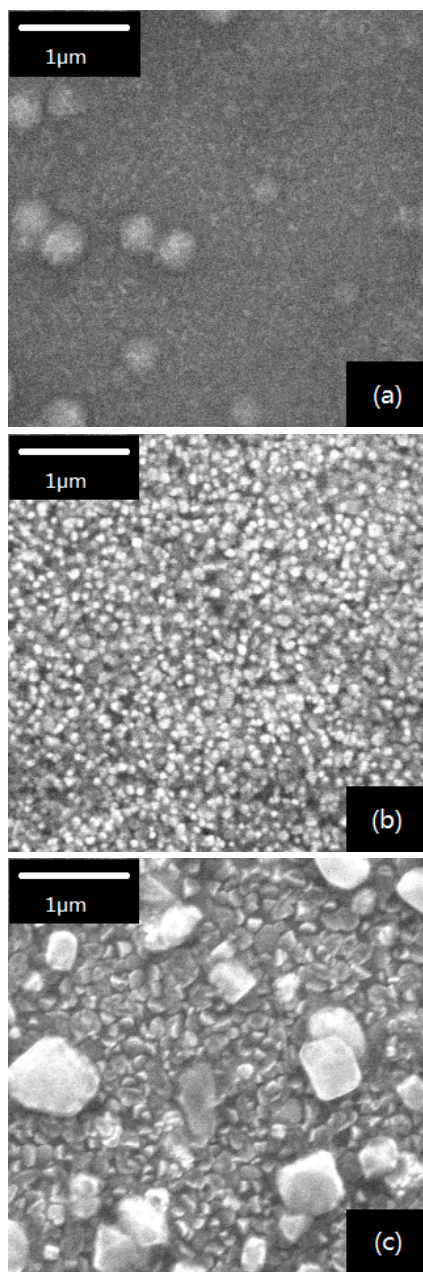


Fig. 2. SEM micrographs of the CZTS films at different sputtering pressures: (a) 0.5Pa, (b) 0.3Pa, (c) 0.2Pa.

Absorption coefficient α can be obtained by the transmittance and reflectance, α can be calculated by the following formula [10,17]:

$$\alpha = \frac{2 \ln(1-R) - \ln T}{d}$$

where d is the thickness of the thin films, T is the transmittance, and R is the reflectance of the thin film samples.

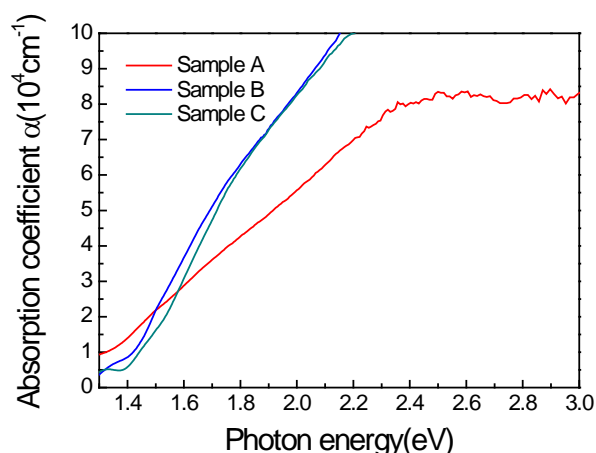


Fig. 3. Absorption coefficients of the CZTS films, the letters correspond to their sputtering pressure, A 0.5Pa, B 0.3Pa, C 0.2Pa.

Fig. 3 shows the plots of the absorption coefficient (α) versus photon energy ($h\nu$) for each CZTS film. A high absorption coefficient ($>10^4 \text{ cm}^{-1}$) is observed for all films in the visible region, and it shows a distinct absorption edge at about 1.40 eV. CZTS is a direct band gap semiconductor, so the band gap E_g can use extrapolation through $(\alpha h\nu)^2$ with photon energy $h\nu$ relationships obtained. Fig. 4, presents the band gap (E_g) estimated by extrapolating the linear region of the $(\alpha h\nu)^2$ plot. The single-phase CZTS film deposited at 0.5 Pa shows the smallest band gap (1.40eV), it is smaller than the reported experimental and theoretical values [18,19]. The Cu-rich and Zn-poor states of this film are probably responsible for the decrease of the band gap. The valence band maximum (VBM) of CZTS arises from antibonding of Cu 3d and S 3p orbitals. Therefore, excess Cu vacancies reduce the VBM so that the bandgap is blue shifted [19,20]. The larger E_g values of CZTS films deposited at 0.2 Pa may be attributed to the existence of Cu vacancies, which leads to a band gap of around 1.49eV [21].

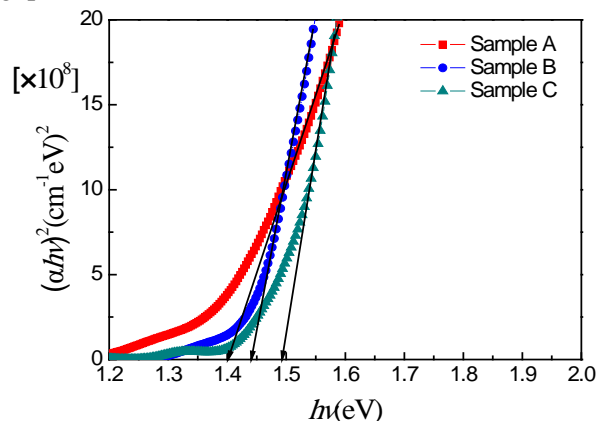


Fig. 4. Band gap energy of CZTS films: the letters correspond to their sputtering pressure, A 0.5Pa, B 0.3Pa, C 0.2Pa.

CONCLUSIONS

Cu₂ZnSnS₄ films with good crystallinity were successfully deposited using a single-phase kesterite-structure CZTS target material by RF magnetron sputtering method without sulfurization. The control of deposition pressure and film composition is considered to be crucial to obtain nearly stoichiometric single-phase films. The re-evaporation of volatile constituents during the sputtering process would lead to a deviation of film stoichiometry. CZTS films deposited at different deposition pressures show (112) preferred orientation and are poor in Cu and rich in Zn. A large fraction of Zn occurs in CZTS films deposited at pressure of 0.3 and 0.2 Pa, which is probably related to the enlargements of the band gaps ranging from 1.44 to 1.49 eV. The film deposited at 0.2 Pa has dominant single-phase structure, Cu-poor and Zn-rich state and large grain size. The CZTS thin films also exhibit high optical absorption ($>10^4$ cm⁻¹). These results suggest that quaternary CZTS would be a potential candidate for solar cell applications.

Acknowledgements: The work was supported by the National Nature Science Foundation of China (61176127, 61006085, 11474248), China Postdoctoral Science Foundation (2013M540908), Key Program for International S&T cooperation Projects of China (No. 2011DFA62380), Ph.D. Programs Foundation of Ministry of Education of China (No. 20105303120002) and Henan Province Education Department science and technology research projects (14B430027).

REFERENCES

1. T. K. Todorov, K. B. Reuter, D. B. Mitzi, *Advanced Materials*, **156**, 22 (2010).
2. K. Kim, I. Kim, Y. Oh, D. Lee, K. Woo, S. Jeong, *Green Chemistry*, **4323**, 16 (2014).
3. A. A. Barragan, H. Malekpour, S. Exarhos, A. A. Balandin, L. Mangolini, *ACS Appl. Mater. Interfaces*, **22971**, 8 (2016).
4. P. K. Nayak, J. Bisquert, D. Cahen, *Advanced Materials*, **2870**, 23 (2011).
5. S. Yazici, M. A. Olgar, F. G. Akca, A. Cantas, M. Kurt, G. Aygun, *Thin Solid Films*, **563**, 589 (2015).
6. S. L. Yun, T. Gershon, O. Gunawan, T. K. Todorov, T. Gokmen, Y. Virgus, *Advanced Energy Materials*, **7**, 5 (2015).
7. T. P. Dhakal, C. Peng, R. R. Tobias, R. Dasharathy, C. R. Westgate, *Solar Energy*, **23**, 100 (2014).
8. Y. Feng, T. K. Lau, G. Cheng, L. Yin, Z. Li, H. Luo, *Cryst. Eng. Comm.*, **1070**, 18 (2016).
9. A. I. Inamdar, S. Lee, K. Y. Jeon, H. L. Chong, S. M. Pawar, R. S. Kalubarme, *Solar Energy*, **196**, 91 (2013).
10. M. Xie, D. Zhuang, M. Zhao, B. Li, M. Cao, J. Song, *Vacuum*, **146**, 101 (2014).
11. D. B. Mitzi, O. Gunawan, T. K. Todorov, K. Wang, S. Guha, *Solar Energy Materials & Solar Cells*, **1421**, 95 (2011).
12. J. Tao, J. Liu, L. Chen, H. Cao, X. Meng, Y. B. Zhang, *Green Chemistry*, **550**, 18 (2016).
13. Y. P. Lin, Y. F. Chi, T. E. Hsieh, Y. C. Chen, K. P. Huang, *Journal of Alloys & Compounds*, **498**, 654 (2016).
14. R. Liu, M. Tan, L. Xu, X. Zhang, J. Chen, X. Tang, *Solar Energy Materials & Solar Cells*, **221**, 157 (2016).
15. T. Prabhakar, N. Jampana, *Solar Energy Materials & Solar Cells*, **1001**, 95 (2011).
16. C. J. Hages, M. J. Koeper, R. Agrawal, *Solar Energy Materials & Solar Cells*, **342**, 145 (2016).
17. J. Tauc, *Amorphous and Liquid Semiconductors*. Springer US, 159, 1974.
18. F. Liu, Y. Li, K. Zhang, B. Wang, C. Yan, Y. Lai, *Solar Energy Materials & Solar Cells*, **2431**, 94 (2010).
19. H. He, M. Xiao, Q. Zhong, Y. C. Fu, X. M. Shen, J. M. Zeng, *Ceramics International*, **13263**, 40 (2014).
20. S. Chen, A. Walsh, X. G. Gong, S. H. Wei, *Advanced Materials*, **1522**, 25 (2013).
21. H. Su, Y. Geng, H. Wei, M. Xu, L. Wei, Z. Yang, *Materials Letters*, **204**, 111 (2013).

ВЛИЯНИЕ НА НАЛЯГАНЕТО НА ОТЛАГАНЕ ВЪРХУ ФИЛМИ ОТ $\text{Cu}_2\text{ZnSnS}_4$, ПОЛУЧЕНИ ЧРЕЗ ЕДНОСТАДИЙНО РАЗПРАШАВАНЕ С ЧЕТВОРНА МИШЕНА

Х.Г. Ян^{1,2,*}, Дж.Д. Джан², М.Ц. Ли^{1*}, Р.Т. Хао³, Г.Л. Сун²

¹ Колеж по възобновяема енергия, Севернокитайски университет по електричеството, Пекин 102206, Китай

² Колеж по физика и материалознание, лаборатория по фотоволтаични материали на провинция Хенан, Университет на Хенан, Ксинксян 453007, Китай

³ Институт по изследване на слънчевата енергия, Университет на Юнан, Кунмин 650092, Китай

Постъпила на 14 януари, 2018 г.; коригирана на 7 февруари, 2018 г.

(Резюме)

$\text{Cu}_2\text{ZnSnS}_4$ (CZTS) филми са отложени от монофазова $\text{Cu}_2\text{ZnSnS}_4$ четворна мишена чрез RF разпрашаване без последваща сулфуризация. Получените CZTS филми са темперирани при 400°C в аргонова атмосфера за получаване на еднофазова кестеритна структура. Изследвано е влиянието на налягането на разпрашаване върху повърхностната морфология, кристалната структура, оптичния абсорбционен коефициент, разстоянието между ивиците, както и влиянието на химичния състав на CZTS филми. Дифракционните пикове на (112) са остри и характеристичните пикове на структури от кестеритов тип като (220) и (312) се наблюдават ясно в рентгеновите дифрактограми. Съставът и оптичните свойства на образците са определени с помощта на енергийно дисперсивна рентгенова спектроскопия (EDS) и UV-VIS-NIR спектрометрия. При налягане на разпрашаване от 0.2 Pa се получава перспективен беден на мед и богат на цинк монофазов CZTS филм с голям размер на зърната. Установено е, че CZTS филми проявяват висок абсорбционен коефициент от порядъка на 10^4 cm^{-1} и оптично разстояние между ивиците от 1.49 eV.

A novel all-thin-film electrochromic device for modulating optical transmittance

H.G. Yang^{1,2*}, R.T. Hao³, M.C. Li², G.L. Song¹

¹ College of Physics and Materials Scientific, Photovoltaic Materials Laboratory of Henan Province, Henan normal university, Xinxiang 453007, China

² College of Renewable Energy, North China Electric Power University, Beijing 102206, China

³ Solar Energy Research Institute of Yunnan Normal University, Kunming 650092, China

Received January 14, 2018; Revised February 7, 2018

An all-thin-film glass/ITO/WO₃/LiAlO₂/NiO_x/ITO device was successfully fabricated for electrochromic application, in which LiAlO₂ was used as the ion conducting layer material. The thin films were prepared by magnetron sputtering with a substrate temperature about -120 °C. The film structure was characterized by X-ray diffraction (XRD), and the film morphology was characterized by scanning electron microscopy (SEM). The electrochromic properties of the films and the device were measured with cyclic voltammetry and spectrophotometry. For the obtained electrochromic device, the average visible light transmittances of bleached and colored state can reach 73.4% and 32.8%, respectively, and the optical transmittance modulation can reach 40.6%. The results indicated that the LiAlO₂ thin film was a suitable ion conductor for the electrochromic device, and the monolithic system glass/ITO/WO₃/LiAlO₂/NiO_x/ITO has great potential to be applied in smart windows.

Keywords: Electrochromic device, WO₃, NiO_x, LiAlO₂, Magnetron sputtering.

INTRODUCTION

Over the past decades, increasing attention has been paid to the reduction of energy consumption in residential and commercial buildings. Windows are a critical component of the building envelope which can greatly improve energy efficiency of buildings. Electrochromic (EC) devices can be used to modulate the throughput of visible light and solar energy in windows, as well as for other applications. The ability to control the energy flows through windows by EC devices (ECD) can lead to saving of huge power by reducing the demand for air conditioning, and this technology can also create comfortable working and living conditions [1–4]. To achieve optical modulation, as it is well known, the electrochromic thin film needs to be incorporated into a multilayer structure with layers for conducting electrodes, ionic conductor and ion storage. When a voltage of the order of few volts is applied between transparent electrodes, ions can be exchanged between the ion storage film and the electrochromic film, and the electrons injected from the transparent conductors then alter the optical properties. The coloration also can be stopped at any intermediate level, and the device exhibits open-circuit memory [5,6]. For applications, all-solid-state ECD have unique advantages such as reliability and safety, compared to conventional liquid-based devices in which liquid electrolytes are used as the ion conductors. There are two types of all-solid-state ECDs, laminated devices and all-

thin-film devices. For a laminated device, the ion conductor is a polymeric electrolyte and the device consists of two half-cells laminated by the polymer. The polymeric electrolyte of a laminated device could have a degrading effect on the metal oxides, and produce problems like de-lamination and shrinkage. Compared to laminated devices, all-thin-film devices, in which the ion conductor is an inorganic film material, have received more attention because of their higher stability. A complementary ECD is a device containing two electrochromic layers, one of which is anodically colored while the other is cathodically colored, separated by an ion conducting layer.

In this study, a complementary all-thin-film transmittance-type EC device was successfully fabricated by a magnetron sputtering method, and its structure and performance were analyzed based on measurements. The device comprises a WO₃ film as the main cathodic electrochromic layer, a LiAlO₂ film as an inorganic ion conducting layer, a NiO_x film as a complementary anodic electrochromic layer, and a transparent conductive indium tin oxide (ITO) layer as the top and bottom electrode. The features of the ECD using LiAlO₂ film as ion conductor are low cost and high transmittance in bleached states.

EXPERIMENTAL DETAILS

All the films were prepared by a magnetron sputtering system. An ITO coated glass with a resistivity of 20Ω/m was used as the substrate. Sputtering took place from 6 cm diameter targets of

* To whom all correspondence should be sent:
E-mail: : hgyang@htu.cn

W, Ni, LiAlO₂, and ITO. The W and Ni targets were of 99.9% purity. The LiAlO₂ target was prepared by ourselves using LiOH·H₂O (99% purity) and Al₂O₃ (99% purity) with molar ratios 2:1 [7]. The ITO target was In₂O₃-SnO₂ ceramic (90:10 by weight). The NiO_x and WO₃ films were prepared by DC magnetron sputtering at 100 W in a 3 Pa environment consisting of Ar and O₂ (flow rate of 70:30). The LiAlO₂ film was prepared by RF magnetron sputtering at 70 W in a 1 Pa environment consisting of Ar and O₂ (90:10 in rate of flow). The ITO film was prepared by RF magnetron sputtering at 70 W in a 1 Pa environment consisting of Ar. The ECD consisting of glass/ITO/WO₃/LiAlO₂/NiO_x/ITO was obtained, and the films thicknesses were 150/600/300/300/300 nm. During the deposition, the substrate was cooled by liquid nitrogen, and the substrate temperature was about -120°C.

The X-ray diffraction data of WO₃, NiO_x and LiAlO₂ films were recorded using Cu K α radiation. The surface morphology of the WO₃ and NiO_x films was determined by scanning electron microscopy (SEM). The coloration characteristics of the ECD were characterized by spectrophotometry. The electrochemical properties of the WO₃ and NiO_x films were measured by cyclic voltammetry in a three-electrode electrochemical cell.

RESULTS AND DISCUSSION

Fig. 1 presents the XRD patterns of WO₃, LiAlO₂ and NiO_x films. We can see that the WO₃ and LiAlO₂ films are amorphous. Normally, amorphous and porous WO₃ films are more suitable than crystalline WO₃ films for EC applications, and the EC performance of the films is closely correlated with its structure and surface morphology [8-10]. Previous research suggested that amorphous ion conducting film is available as the solid electrolyte [11]. The amorphous LiAlO₂ thin film has very low Li⁺ diffusion along in-plane direction, and this amorphous thin film can accept Li⁺ intercalation and structural distortion. For the NiO_x film, a weak diffraction peak (200) was detected, and the peak at 43.36° was indexed as NiO [12]. Characteristic SEM images for the WO₃ and NiO_x films are shown in Fig. 2. It can be seen that the WO₃ particles are spheroidal, and their diameters are about 20 nm. The SEM micrographs indicated that WO₃ films exhibit fine particles and had an open porous surface structure. This character of the surface structure is crucial for the EC properties [9,13,14].

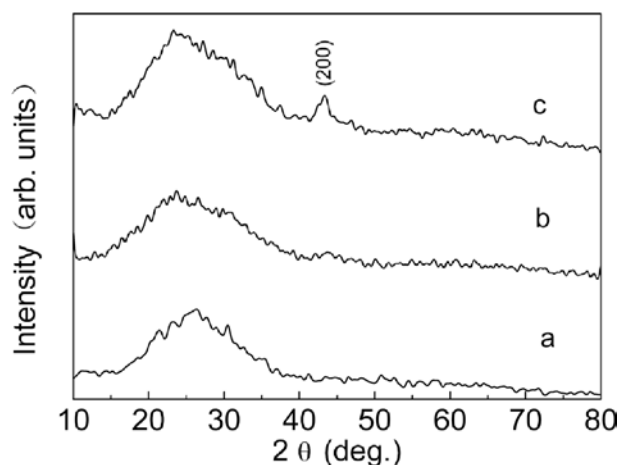


Fig. 1. XRD patterns of the as-deposited films: (a) WO₃, (b) LiAlO₂, (c) NiO_x.

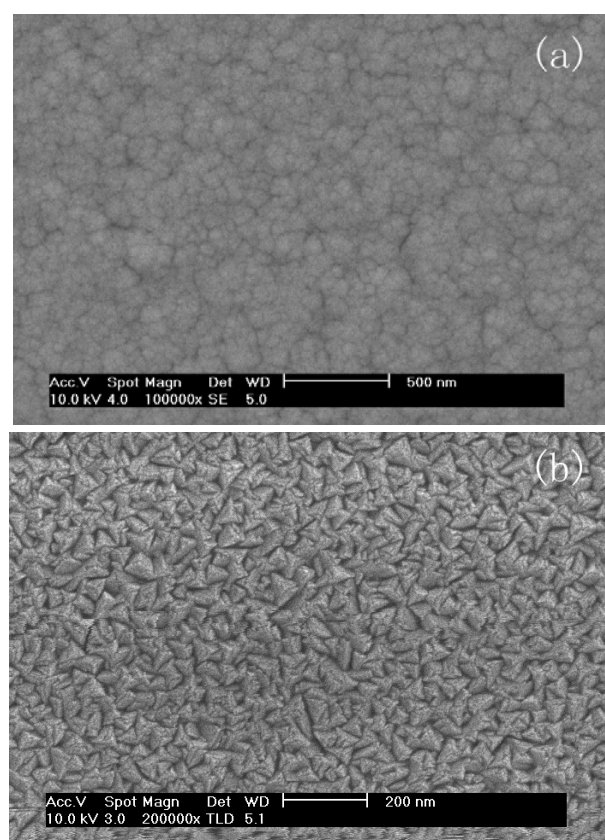


Fig. 2. Scanning electron microscopy surface images of films: (a) WO₃, (b) NiO_x.

The NiO_x is nano-crystalline, and the particle diameter is about 30 nm. Previous research showed that the electrochromic reaction occurred along the grain boundary of the NiO_x film, and small grain size would display a large surface to bulk ratio, which is important for high electrochromic activity [15].

The EC properties of the WO₃ and NiO_x films were mainly examined by cyclic voltammetry. The cyclic voltammograms of the films show the intrinsic shape of the electrochemical behavior and the charge densities related to continued Li⁺

intercalation and deintercalation of the films [9,15]. Fig. 3 (a) shows the cyclic voltammograms of the WO₃ film. During cathodic potential scan from +2 to -1.9 V, current remains almost zero up to 180 mV, and further sharply increases, resulting in deoxidation of W⁶⁺ to W⁵⁺ and causing dark-blue coloration of the film, when the Li⁺ ions and electrons flow into the film. Accordingly, the optical transmittance decays to reach a minimum at the voltammetric peak. Reversing the direction of the potential from -1.9 to 2 V, an anodic electric current is established and the film turns colorless when the Li⁺ ions and electrons flow out of the film.

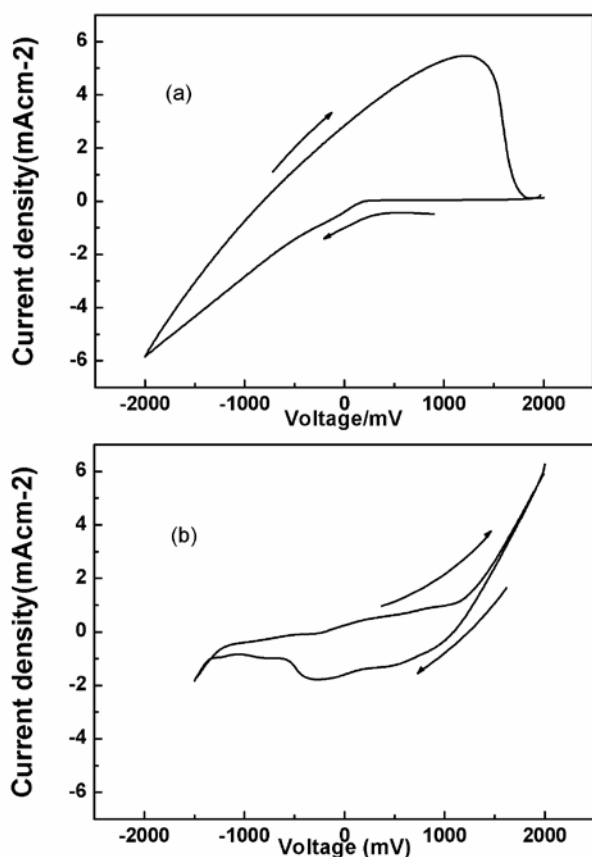


Fig. 3. Cyclic voltammograms of thin films: (a) WO₃, (b) NiO_x

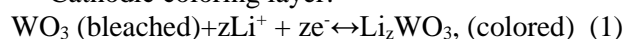
Fig. 3 (b) shows cyclic voltammetric curves obtained during continuous potential cyclings for NiO_x film. The most remarkable feature of the cyclic voltammetric curves of NiO_x films is that a clear cathodic peak (+1.9 mA cm⁻² at -345 mV) was observed in the cycle. The corresponding Li⁺ ions and electrons flow into the film. During anodic potential scan from -1.9 to 2V, current density slightly increases up to 1129 mV and further sharply increases resulting in oxidation of Ni²⁺ to Ni³⁺, consequently the color of the NiO_x film changes from transparent to brown. The slight

current increase was related to the Li⁺ ions and electrons flowing out of the film [16].

In order to examine EC property of the device, DC voltage of 5 V was applied at the top ITO electrode of the glass/ITO/WO₃/LiAlO₂/NiO_x/ITO stacked structure.

We propose the following mechanism for coloration of the EC device: The state of the ECD changes from as-deposited to colored when voltage is applied to the device such that the top ITO takes on a positive voltage. The state of the EC device changes to a bleached state after the applied voltage was switched off. The coloring and bleaching processes of the WO₃ and NiO_x films are due to the intercalation and deintercalation of Li⁺ ions and electrons in the films according to the reactions (1), (2), and (3):

Cathodic coloring layer:



Solid electrolyte layer:



Anodic coloring layer:

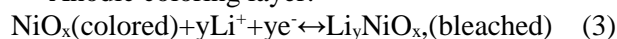


Fig. 4 shows the visible light transmittance (T_{vis}) of the as-deposited, colored and bleached glass/ITO/WO₃/LiAlO₂/NiO_x/ITO device before and after voltage application. An integral over the whole spectrum can be calculated to describe the total optical transmittance [17]. The average transmittance in the wavelengths from 400 nm to 800 nm was 56.8% through the whole structure before applying the voltage. The absorption of visible light means a lower Ni³⁺ content in the as-deposited NiO_x thin film, and the Ni³⁺ content in the film can be improved by adjusting deposition conditions. As can be seen from the figure, the transmittance (T_{vis}) in the visible light range increases up to 73.4% through the structure after applying -10V on the top ITO electrode. By changing the polarity, the device became colored and the value of T_{vis} decreased to 32.8%. The T_{vis} modulation over the colored and bleached state was 40.6%. This value is comparable to that of the devices using other ion conducting materials, such as Ta₂O₅ and LiNbO₃ [18-20]. These results suggest that the ECD has a potential application for smart windows.

The *in situ* transmittance studies at 550 nm measured with respect to coloring and bleaching were used to calculate the response time. Fig. 5 shows the switching characteristics of the glass/ITO/NiO_x/LiBSO/WO₃/ITO ECD on application of a potential of ±5 V for five cycles.

The time taken for the film to color and bleach was obtained from these characteristics.

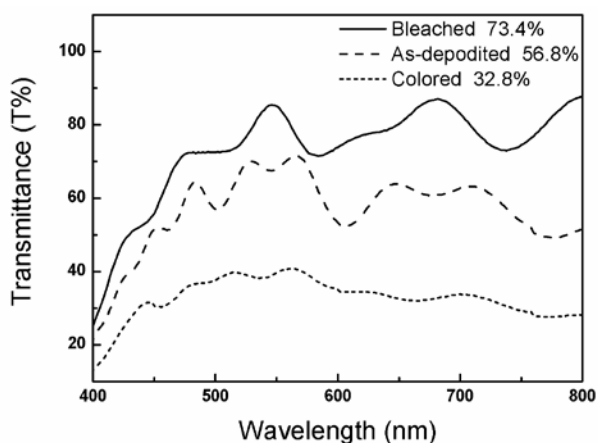


Fig. 4. Transmittance (T) of the glass/ITO/WO₃/LiAlO₂/NiO_x/ITO device

The coloration time is defined as the time required for the transmission of the film to decrease to 10% of the maximum transmittance value in the coloration cycle, and bleaching time is the time taken for the transmission to increase by 90% of the minimum value in the bleaching cycle. The maximum optical attenuation measured at 550 nm was 46%. Coloration time (T_c) and bleaching time (T_b) were found to be 20 s and 8 s, respectively, which are comparable to the other devices reported [21]. As the switching speed depends on the active area on which the material is deposited, the area was kept constant at 4 cm² for all measurements. The coloration time was longer than the bleaching time due to different color/bleach kinetics.

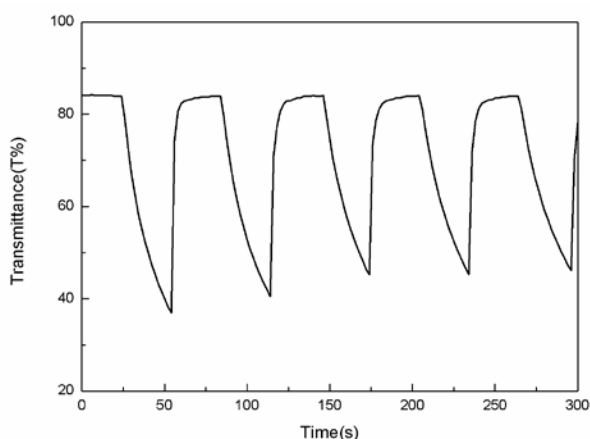


Fig. 5. Transmittance (at 550 nm) versus the response time of the device for five coloring and bleaching cycles.

CONCLUSIONS

In summary, a novel all-thin-film ECD employing WO₃ as the cathodically colored layer, NiO_x as the anodically colored layer, and LiAlO₂ as the ion conducting layer was fabricated by

magnetron sputtering on an ITO/glass substrate. The LiAlO₂ film is electrochemically stable and avoids the problems generally associated with delamination and shrinkage seen in laminated devices using polymeric electrolyte. In addition, the LiAlO₂ film can be prepared easily and inexpensively, which is of interest to researchers involved in the development of inexpensive ECDs. The experimental results from the glass/ITO/WO₃/LiAlO₂/NiO_x/ITO are as follows: The transmittance in the visible light range of the device changed from 73.4% to 32.8% with the transmittance change ($\Delta T\%$) of 40.6%. Our results demonstrated that amorphous LiAlO₂ is available as a thin film electrolyte, which is particularly suitable for the low-cost and high-transmittance all-thin-film ECD. Further studies on the physical and electrochemical behavior are under way, to improve $\Delta T\%$ values and cycle lifetime of ECDs.

Acknowledgements: The work was supported by National Nature Science Foundation of China (61176127, 61006085, 11474248), China Postdoctoral Science Foundation (2013M540908), Key Program for International S&T cooperation Projects of China (No. 2011DFA62380), Ph.D. Programs Foundation of Ministry of Education of China (No. 20105303120002) and Henan Province Education Department science and technology research projects (14B430027).

REFERENCES

1. C. G. Granqvist, *Solar Energy Mater. Solar Cells*, **1**, 99 (2012).
2. C. Baldassarri, A. Shehabi, F. Asdrubali, E. Masanet, *Solar Energy Mater. Solar Cells*, **170**, 156 (2016).
3. S. H. N. Lim, J. Isidorsson, L. Sun, B. L. Kwak, A. Anders, *Solar Energy Mater. Solar Cells*, **129**, 108 (2013).
4. L. M. Huang, C. W. Hu, H. C. Liu, C. Y. Hsu, C. H. Chen, K. C. Ho, *Solar Energy Mater. Solar Cells*, **154**, 99 (2012).
5. C. Faure, A. Guerfi, M. Dontigny, D. Clément, P. Hovington, U. Posset, *Electrochim. Acta*, **313**, 214 (2016).
6. P. Yang, P. Sun, W. Mai, *Materials Today*, **394**, 19 (2016).
7. C. Gang, *Chinese J. Inorg. Chem.*, **219**, 18 (2002).
8. C. P. Li, C. A. Wolden, A. C. Dillon, R. C. Tenent, *Solar Energy Mater. Solar Cells*, **50**, 99 (2012).
9. Z. Bi, S. Zhang, X. Xu, X. Hu, X. Li, X. Gao, *Mate. Lett.*, **186**, 160 (2015).
10. R. M. Fernández-Domene, R. Sánchez-Tovar, E. Segura-Sanchís, J. García-Antón, *Chem. Eng. J.*, **59**, 286 (2016).
11. A. I. Inamdar, Y. S. Kim, B. U. Jang, H. Im, W. Jung, D. Y. Kim, *Thin Solid Films*, **5367**, 520 (2012).

12. A. Karpinski, N. Ouldhamadouche, A. Ferrec, L. Cattin, M. Richardplouet, L. Brohan, *Thin Solid Films*, **5767**, 519 (2011).
13. Z. Jiao, J. Wang, L. Ke, X. Liu, H. V. Demir, M. F. Yang, *Electrochim. Acta*, **153**, 63 (2012).
14. H. Z. Li, J. M. Wang, Q. W. Shi, M. W. Zhang, C. Y. Hou, G. Y. Shi. *Appl. Surface Sci.*, **281**, 380 (2016).
15. S. V. Green, M. Watanabe, N. Oka, G. A. Niklasson, C. G. Granqvist, Y. Shigesato, *Thin Solid Films*, **3839**, 520 (2012).
16. Y. Abe, T. Suzuki, M. Kawamura, K. Sasaki, H. Itoh, *Solar Energy Mater. Solar Cells*, **38**, 99 (2012).
17. A. L. Larsson, G. A. Niklasson, *Solar Energy Mater. Solar Cells*, **351**, 84 (2004).
18. F. Mitsugi, A. Nakamura, Y. Kodama, T. Ohkubo, Y. Nomoto, *Thin Solid Films*, **4159**, 515 (2007).
19. D. A. A. D. Mello, M. R. S. Oliveira, L. C. S. D. Oliveira, S. C. D. Oliveira, *Solar Energy Mater. Solar Cells*, **17**, 103 (2012).
20. S. Y. Lin, Y. C. Chen, C. M. Wang, C. Y. Wen, T. Y. Shih, *Solid State Ionics*, **81**, 212 (2012).
21. D. Dong, W. Wang, G. Dong, F. Zhang, Y. He, H. Yu, *Appl. Surface Sci.*, **49**, 383 (2016).

НОВО ЕЛЕКТРОХИМИЧНО УСТРОЙСТВО ОТ ИЗЦЯЛО ТЪНЪК ФИЛМ ЗА МОДУЛИРАНЕ НА ОПТИЧНА ПРОПУСКЛИВОСТ

Х.Г. Ян^{1,2*}, Р.Т. Хао³, М.Ц. Ли², Г.Л. Сун¹

¹Колеж по физика и материалознание, лаборатория по фотоволтаични материали на провинция Хенан, Университет на Хенан, Ксинксян 453007, Китай

²Колеж по възобновяема енергия, Севернокитайски университет по електричеството, Пекин 102206, Китай

³Институт по изследване на слънчевата енергия на Университета в Юнан, Кунминг 650092, Китай

Постъпила на 14 януари, 2018 г.; коригирана на 7 февруари, 2018 г.

(Резюме)

Електрохимично устройство от изцяло тънък филм от стъкло/ITO/WO₃/LiAlO₂/NiO_x/ITO е произведено за електрохимично приложение, като LiAlO₂ е използван като йонно проводим слоест материал. Тънките филми са получени чрез магнетронно разпрашаване при температура на субстрата около -120 °C. Структурата на филмите е охарактеризирана чрез рентгенова дифракция (XRD), а морфологията им – чрез сканираща електронна микроскопия (SEM). Електрохромните свойства на устройството са измерени чрез циклична волтамметрия и спектрофотометрия. Средната пропускливост на видима светлина на избеленото състояние и цветното състояние може да достигне съответно 73.4% и 32.8%, а модулирането на оптичната пропускливост може да достигне 40.6%. Установено е, че тънкият филм от LiAlO₂ е подходящ йонен проводник за електрохимичното устройство, а монолитната система стъкло/ITO/WO₃/LiAlO₂/NiO_x/ITO има голям потенциал за приложение в „интелигентни“ прозорци.

Thickness dependence of internal stress in electrodeposited nano-twinned copper

S. Zhan¹, Y.L. Yang^{2,*}, W.Y. Peng^{1,*}, J.G. Chen³, Z.B. Li³, X.J. Hou², L. Feng², G.Q. Suo², Z.G. Chen⁴, J. Zou⁴, Y.D. Wang^{5,*}

¹ School of Materials Science and Engineering, Nanchang University, Nanchang, 330031, China

² School of Materials Science and Engineering, Shaanxi University of Science & Technology, Xi'an 710021, Shaanxi, China

³ Key Laboratory of Electromagnetic Processing of Materials, Ministry of Education, Northeastern University, Shenyang, 110004, China

⁴ Materials Engineering, The University of Queensland, Brisbane, QLD 4072, Australia

⁵ State Key Laboratory for Advanced Metals and Materials, University of Science and Technology Beijing, Beijing 100083, China

Received January 14, 2018; Accepted February 7, 2018

Electrodeposited pure copper with nano-scaled twins was proved to be a tradeoff for the contradiction of high mechanical strength and high electrical conductivity. In this work the internal stress of the nano-twinned copper was explored by means of X-ray diffraction analysis. The results show that the internal stress is associated with the deposition thickness. The macro-stress of the film is very small and constant. The type-II micro-stress (grain-orientation-dependent stress) is also small, while it becomes higher with the increase of deposition thickness.

Keywords: Electrodeposition; Nano-twin; Copper; Stress

INTRODUCTION

Electrodeposition has been proven to be a technologically and economically viable production route to synthesize various materials with different functions [1-4]. In the study of various metallic structures, electrodeposition has become well established as a cost-effective fabrication technique compared with physical or chemical vapor deposition techniques [5]. Although there are some drawbacks associated with the electrodeposition process, such as the relatively limited number of elements that can be deposited from aqueous electrolytes and the need for a conducting substrate, electrodeposition does offer the clear benefits of high growth rates and the use of very simple apparatus. These benefits are as applicable to the fabrication of structures that are patterned in the growth plane.

A thorough understanding of the relationship between the electrodeposition parameters, the microstructure and the performance of electrodeposited films is required in order to tailor their microstructure and thereby design their properties and performance. Grain size, grain shape, dislocation density and inclusion content in electrodeposited layers markedly affect the properties of the deposit. Moreover, electrodeposited films are often crystallographically textured because of preferred growth of particular

grain orientations. As a result, anisotropy of the elastic properties of the deposited films is anticipated [6].

Conventional methods for materials strengthening usually cause an obvious decrease in electrical conductivity. A reasonable explanation is that all of the strengthening methods, such as solid solution, second phase strengthening, and strain hardening, always introduce various kinds of defects, which at the same time increase the scattering of conducting electrons at these defects, and thus decrease the electrical conductivity. It is a contradiction for strengthened conducting materials. An ideal microstructure, twin, has been proved as a tradeoff, which could effectively block dislocation motion and greatly minimize the scattering of conducting electrons [7]. Lu *et al.* [8] have synthesized high-purity copper with high density of nanoscale grown twins using a pulse electrodeposition technique, which demonstrates ultrahigh strength and ultrahigh electrical conductivity. However, the thickness of the deposited copper film always has a limit of several or tens of micrometers because of the deteriorating surface with the increase in deposition duration. Moreover, some details in the process of twin formation through pulse electrodeposition are not fully understood. It is of significance to study the development of microstructure in such an electrodeposition process both for the structure design on nanometer scale in electronic industry and studies of the performance and lifetime of components used in microelectronics, tribological,

* To whom all correspondence should be sent.

E-mail: yanling_yang@126.com

The first two authors contributed equally to this paper.

mechanical, and electrochemical applications [9]. In this paper we studied the internal stress of nano-twinned copper by means of X-ray diffraction analysis, in the hope of obtaining a deeper understanding of the deposition process of nano-twinned copper.

A postulation is that the generation of the twins could be due to the stress in the deposited films [10]. Regardless of the method of deposition, it is well known that internal stress will be developed in thin films [11]. The close relationship between stress behavior and morphology of thin films is expected to facilitate the detailed description of thin film growth from analysis of stress development. Among existing methods to investigate strain in coatings, X-ray diffraction (XRD) is a powerful tool due to its capability to measure the full strain or stress and provide complementary information on crystallographic phase non-destructively [12].

EXPERIMENTAL DETAILS

A series of samples deposited at different durations were used for the study of stress evolution as a time-dependent process. The samples were prepared with a cathode of Ni-P amorphous film deposited on pure Fe and with the pulsed electrodeposition parameters as reported by Lu *et al.* [8]. The standard sample (copper powder) is commercially available and was annealed in vacuum at 190°C for 10 min to remove the residual stress. Generally, there should be only instrumental broadening in the diffraction pattern of the standard sample and physical broadening was discarded.

The X-ray diffraction measurements were carried out using a ω diffractometer and a ψ diffractometer. Generally, a specific hkl reflection was scanned at several specimen tilts and possible rotation angles. The measured peak positions were used to calculate the lattice spacing and the lattice strain at every tilt and rotation angle. The samples were tilted around Eulerian cradle axis from 0 to 80° with an interval to get $\text{Sin}^2\psi$ equally split, which facilitates the data processing. For every ψ , a certain plane was scanned for the corresponding 2θ with interval of 0.05°. The classical stress analysis was done with the $\text{sin}^2\psi$ method. The general formula for the bi-axial case is:

$$\varepsilon_\psi = \frac{d_\psi - d_0}{d_0} = \frac{1+\nu}{E} \sigma_\phi \text{sin}^2\psi - \frac{\nu}{E} (\sigma_1 + \sigma_2) \quad (1)$$

where E is the Young's modulus of the deposited film, ν the Poisson's ratio of the film, σ_ϕ the in-plane residual stress, σ_1 and σ_2 the in-plane major stress respectively. Derivate ε_ψ by $\text{sin}^2\psi$, it gives:

$$\sigma_\phi = \frac{E}{1+\nu} \cdot \frac{\partial \varepsilon_\psi}{\partial \text{sin}^2\psi} \quad (2)$$

In our case we plotted micro-strain *vs.* $\text{sin}^2\psi$, from the slope of which the macro-stress σ_ϕ could

be estimated. What is more, this method is adapted for assessment of average lattice distortion (strain) with increase of $\text{sin}^2\psi$, while the detailed strain distribution needs to be studied according to physical broadening obtained by a Fourier convolution method.

Generally speaking, the stress-free d-spacing should be calculated from the standard sample, or can be calculated from a corresponding $\text{sin}^2\psi$ strain-free value by interpolation *via* the linear fitting in the d-spacing (ψ) *vs.* $\text{sin}^2\psi$ plot. In this case, the stress-free d-spacing (d_0) is an average one of d-spacings obtained at different tilt ψ for the standard sample.

RESULTS AND DISCUSSION

Fig. 1 shows the high-resolution TEM image of nano-twinned copper deposited for 24 h. A homogeneous microstructure with nano-scaled twins was obtained with lamella thickness of about 5 nm. The micro-strain *vs.* $\text{sin}^2\psi$ plots are given in Fig. 2. Before studying the graphs, one more thing should be considered. The self-annealing characteristic [13] of electrodeposited copper allows recrystallization at room temperature because of a high defect density that lowers the activation energy. Thus internal stress (σ) also evolves in the film; the decrease of σ starts immediately after plating, and then stops after a much shorter time.

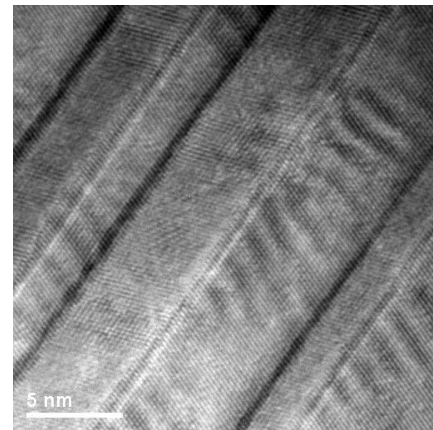


Fig. 1. High-resolution TEM image of nano-twinned copper deposited for 24 h

Although part of the stress is relaxed on open circuit at room temperature, there is still something that could be taken into consideration. The stress release tends to be stronger when the layer is thinner (with a shorter deposition duration), which is indicated by the average magnitude of the micro-strain of samples deposited for different durations or different deposited thickness. To account for these observations, it is believed that the diffusion would be much easier in the areas close to the surface, leading to an almost complete stress release for the thinnest layers while a larger stress would remain for thicker films.

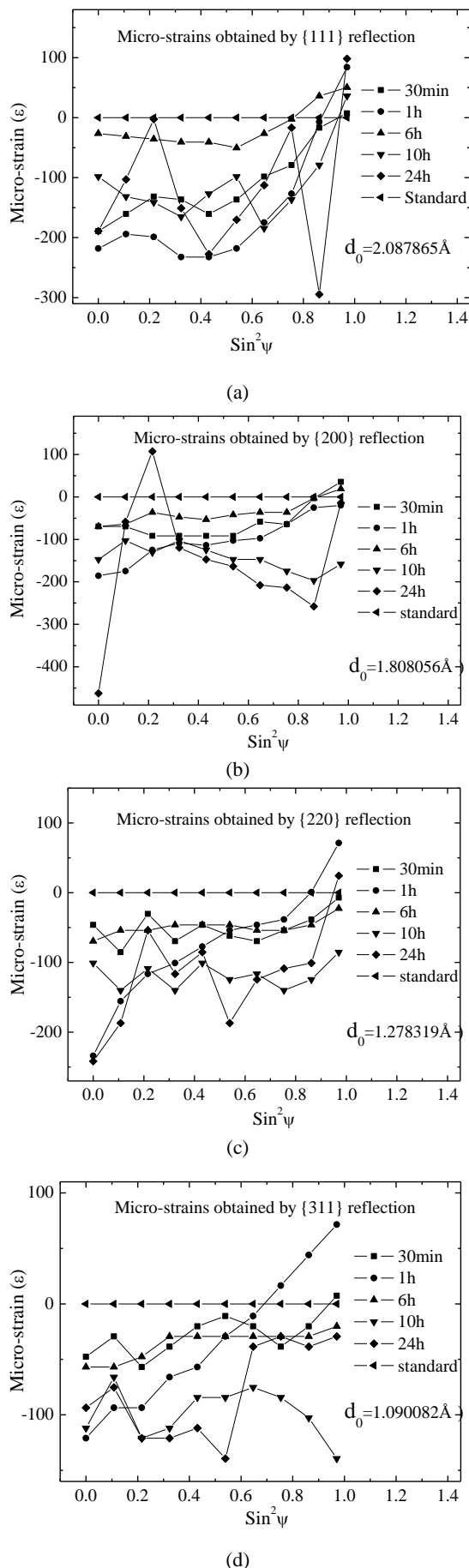


Fig. 2. Micro-strains obtained by {111}, {200}, {220} and {311} reflections

As shown in Fig. 2, the macro-stress is very small (less than 30 MPa), which is estimated from the slope of strain distribution for the (311) peak. People usually think that the linear relationship is very good for (311) and the macro-stress evaluation is accurate by using this one. The type II stress (grain-orientation-dependent stress) is also not big. However, the type-II stress becomes higher with the increase in deposition duration up to 24 h. The sawtooth-like figure may be described as at about the point a maximum in the tensile stress in the pole is reached which is then followed by the film stress turning compressive.

Anyway, it is not very big compared to the deposited Fe [9]. The measured accuracy in lattice strain using the lab X-ray was within 100 micro-strains. If the lattice strains with about over 700 micro-strains, it can only be believed that the type II stress is larger. Generally, the mechanism of stress-raising conditions may be classified as follows: crystallite-joining theory, hydrogen theory, excess energy theory and lattice-defect theory. Comparison made between pulse and direct plating indicated that with direct plating, higher stress values were obtained [14]. This is explained by the proposed crystallite-joining theory. As the current density increases, the residual stress increases when using conventional direct deposition. This is due to increased nucleation rate caused by an increase in overpotential, leading to a greater crystal boundary volume [15]. The intrinsic stress of the electrodeposited film is related to the number of grain boundaries that are formed when the individual crystallites grow together. It means that the tensile stress is proportional to the total twin boundary area, and therefore increases with the decrease in average thickness of twin lamella.

Unlike conventional electrodeposition in which the internal stress may come from the escaping hydrogen-induced shrinkage in the dendrites [9], there is little possibility that the internal stress in the nano-twinned copper film would come from the release of molecular hydrogen. Because in the pulse electrodeposition process, the actual growth process is controlled by the on-time/off-time ratio, there is little possibility that the deposits would grow into dendrites.

Another postulation is that the stress may come from the lattice mismatch. In the initial process of electrodeposition, the level of internal stress of the copper deposits may be attributed to the lattice misfit between deposit and substrate under conditions of assumed epitaxy (i.e. the deposit continues the structure of the substrate) or the two layers are deposited closely with different dimensions. The greater this mismatch or misfit between the lattice parameters of the deposit and substrate, or the dimension difference between the two layers deposited closely, the greater is the

associated strain energy. Tensile stress can be considered to be due to deposits being dimensionally less than substrate or the previously laid down layer while compressive stress is supposed to be the contrary. However, the model has to be modified to allow for the relaxation processes associated with pulse on-time and off-time. Even in conventional electroplating, it was found that the lattice strains weakly depend on depth [9], which means that if thick enough, the coating will minimize the influence of stress gradients. What's more, the cathode used is pure iron coated with Ni-P amorphous alloy, for which the epitaxial growth of the substrate could almost be discarded.

Vacancies can be also created during domain growth and this lattice defect may result in lattice distortion or increase of crystal volume which is indirectly represented by the tensile stress [16].

The diffraction intensity was measured as a function of the tilt angle, Ψ , with respect to the surface normal and the rotation angle Φ (in the plane perpendicular to the surface normal) at 2θ angles corresponding to the Bragg diffraction angle of the {111}, {200} and {220} reflections. The background intensities for the investigated {hkl} reflections were estimated from the intensity distribution experimentally and were determined as a function of Ψ and Φ .

CONCLUSION

The internal stress of nano-twinned copper was explored by means of X-ray diffraction analysis. It is found that the macro-stress is very small and constant. The type II micro-stress (grain-orientation-dependent stress) is also small, while it becomes higher with the increase of deposition thickness.

Acknowledgements: The present work is financially supported by the National Natural Science Foundation of China (Grant Nos.: 51464020, 51101076, 51704188 and 51702199),

Jiangxi Natural Science Foundation (Grant No.: 20161BAB206164) and Jiangxi Key Research and Development Plan of China (Grant No.: 20161BBH80062).

REFERENCES

1. I. Gurrappa, L. Binder, *Sci. Technol. Adv. Mat.*, **9**, 43 (2008).
2. U.S. Mohanty, *J. Appl. Electrochem.*, **41**, 257 (2011).
3. U. Erb, A.M. El-Sherik, G. Palumbo, K.T. Aust, *Nanostruct. Mater.*, **2**, 383 (1993).
4. M. Nath, A. Govindaraj, C.N.R. Rao, *Adv. Mater.*, **13**, 283 (2001).
5. A. Brenner, *Electrodeposition of Alloys*, Academic Press, New York (1963).
6. E. Budevski, G. Staikov, W.L. Lorenz, *Electrochim. Acta*, **45**, 2559 (2000).
7. J.W. Christian, S. Mahajan, *Prog. Mater. Sci.*, **39**, 1 (1995).
8. L. Lu, Y.F. Shen, X.H. Chen, L.H. Qian, K. Lu, *Science*, **304**, 422 (2004).
9. Y.D. Wang, R.L. Peng, J. Almer, M. Oden, Y.D. Liu, J.N. Deng, C.S. He, L. Chen, Q.L. Li, L. Zuo, *Adv. Mater.*, **17**, 1221 (2005).
10. A.U. Mane, S.A. Shivashankar, *J. Cryst. Growth*, **275**, 1253 (2005).
11. B.D. Cullity, S.R. Stock, *Elements of X-ray Diffraction*, 3rd ed., Prentice Hall, 2001.
12. L. Qiu, Y.H. Hu, *X-ray diffraction technology and equipment*, Metallurgical Industry Press, Beijing, 1998.
13. S. Lagrange, S.H. Brongersma, M. Judelewicz, A. Saerens, I. Vervoort, E. Richard, R. Palmans, K. Maex, *Microelectron. Eng.*, **50**, 449 (2000).
14. S.E. Hadian, D.R. Gabe, *Surf. Coat. Tech.*, **122**, 118 (1999).
15. T.A. Tochitskii, G.A. Jones, H.J. Blythe, V.M. Fedosyuk, J. Castro, *J. Magn. Magn. Mater.*, **224**, 221 (2001).
16. X.W. Zhou, H.N.G. Wadley, *Acta. Mater.*, **47**, 1063 (1999).

**ЗАВИСИМОСТ НА ВЪТРЕШНОТО НАПРЕЖЕНИЕ ОТ ДЕБЕЛИНАТА НА
ЕЛЕКТРООТЛОЖЕНИ ДВОЙНИ МЕДНИ КРИСТАЛИ**

С. Джан¹, И.Л. Ян^{2*}, У. И. Пън¹, Дж.Г. Чън³, З.Б. Ли³, Кс.Дж. Хоу², Л. Фън², Г.К. Суо², З.Г. Чен⁴,
Дж. Зоу⁴, И.Д. Уан⁵

¹ Училище по материалознание и инженерство, Университет в Нанчан, Нанчан 330031и, Китай

² Училище по материалознание и инженерство, Университет по наука и технология на Шаанкси, Ксиан
710021, Шаанкси, Китай

³ Лаборатория по електромагнитна обработка на материали, Министерство на образованието,
Североизточен университет, Шенянг 110004, Китай

⁴ Материалознание, Университет на Куинсланд, Брисбейн, QLD 4072, Австралия

⁵ Държавна лаборатория по нови метали и материали, Пекински университет по наука и технология, Пекин
100083, Китай

Постъпила на 14 януари, 2018 г.; коригирана на 7 февруари, 2018 г.

(Резюме)

Установено е, че електроотложена чиста мед с наноразмерни двойни кристали е компромис между противоречащите си висока механична якост и висока електропроводимост. В настоящата статия е изследвано вътрешното напрежение на мед с наноразмерни двойни кристали с помощта на рентгенов дифракционен анализ и е установено, че вътрешното напрежение е свързано с дебелината на филма. Макро-напрежението е много малко, напрежението от тип II (зависещо от ориентацията на зърната) е също малко, но нараства с увеличаване на времето на отлагане.

ERRATUM

To the paper:

Chemical profile of *Artemisia annua* from the region of Sliven, Bulgaria. A preliminary NMR study

V. Kurteva*, A. Trendafilova, S. Simova

Institute of Organic Chemistry with Centre of Phytochemistry, Bulgarian Academy of Sciences, Acad. G. Bonchev street, bl. 9, 1113 Sofia, Bulgaria

Published in *Bulg. Chem. Commun.*, **49**, Special Edition D, 209–214 (2017)

Incorrect structure of the reference compound used for the semi-quantitative NMR analysis necessitates correction of the concentrations in the experimental part and estimated quantity of artemisinin in results and discussion. The correct structure of “Salophen” used is 4-acetamidophenyl 2-hydroxybenzoate, and figure 2 has to be replaced.

The correct data are as follows:

NMR Spectra: For estimation of the artemisinin quantity to a solution of 16 mg artemisinin containing fraction in 0.5 ml in CDCl_3 1.6 mg salophene (5.9×10^{-3} mmol) was added. In the proton spectrum of the mixture the integral of the artemisinin signal at 3.4 ppm amounted 0.31 as compared to the salophene hydroxyl proton at 10.5 ppm (equal to 1) providing estimation for the

quantity of artemisinin as 0.516 mg (1.83×10^{-3} mmol, 31% in respect to salophene).

Results and Discussion: The amount of artemisinin was roughly estimated by comparison with salophen as an internal standard (Fig. 2). The integral intensity of the signal at 3.4 ppm was determined as 0.31 to the salophene hydroxyl proton, which represents 3.23 wt.% of the fraction, 0.17 wt.% of the total extract, and 0.00086 wt.% of the dry plant.

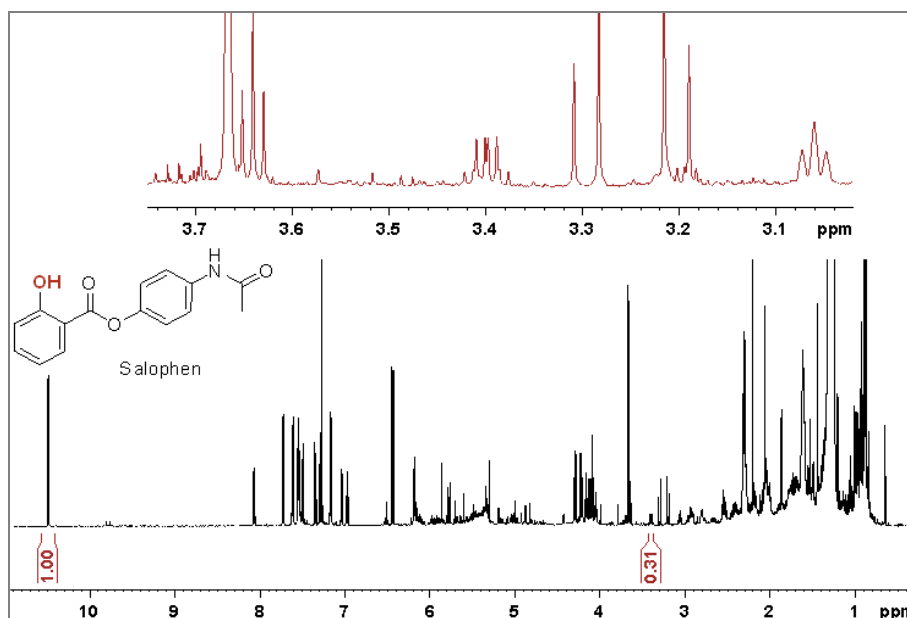


Fig. 2. ^1H NMR spectrum of artemisinin containing fraction with addition of salophene.

The corrected manuscript is supplied as electronic supplementary data available [here](#).

Instructions about Preparation of Manuscripts

General remarks: Manuscripts are submitted in English by e-mail. The text must be typed on A4 format paper using Times New Roman font size 11, normal character spacing. The manuscript should not exceed 15 pages (about 3500 words), including photographs, tables, drawings, formulae, etc. Authors are requested to use margins of 2 cm on all sides.

Manuscripts should be subdivided into labelled sections, e.g. **Introduction, Experimental, Results and Discussion**, etc. **The title page** comprises headline, author's names and affiliations, abstract and key words. Attention is drawn to the following:

a) **The title** of the manuscript should reflect concisely the purpose and findings of the work. Abbreviations, symbols, chemical formulas, references and footnotes should be avoided. If indispensable, abbreviations and formulas should be given in parentheses immediately after the respective full form.

b) **The author's** first and middle name initials and family name in full should be given, followed by the address (or addresses) of the contributing laboratory (laboratories). **The affiliation** of the author(s) should be listed in detail by numbers (no abbreviations!). The author to whom correspondence and/or inquiries should be sent should be indicated by asterisk (*) with e-mail address.

The abstract should be self-explanatory and intelligible without any references to the text and containing not more than 250 words. It should be followed by key words (not more than six).

References should be numbered sequentially in the order, in which they are cited in the text. The numbers in the text should be enclosed in brackets [2], [5, 6], [9–12], etc., set on the text line. References are to be listed in numerical order on a separate sheet. All references are to be given in Latin letters. The names of the authors are given without inversion. Titles of journals must be abbreviated according to Chemical Abstracts and given in italics, the volume is typed in bold, the initial page is given and the year in parentheses. Attention is drawn to the following conventions: a) The names of all authors of a certain publication should be given. The use of “*et al.*” in the list of references is not acceptable. b) Only the initials of the first and middle names should be given. In the manuscripts, the reference to author(s) of cited works should be made without giving initials, e.g. “Bush and Smith [7] pioneered...”. If the reference carries the names of three or more authors it should be quoted as “Bush *et al.* [7]”, if Bush is the first author, or as “Bush and co-workers [7]”, if Bush is the senior author.

Footnotes should be reduced to a minimum. Each footnote should be typed double-spaced at the bottom of the page, on which its subject is first mentioned. **Tables** are numbered with Arabic numerals on the left-hand top. Each table should be referred to in the text. Column headings should be as short as possible but they must define units unambiguously. The units are to be separated from the preceding symbols by a comma or brackets. Note: The following format should be used when figures, equations, etc. are referred to the text (followed by the respective numbers): Fig., Eqns., Table, Scheme.

Schemes and figures. Each manuscript should contain or be accompanied by the respective illustrative material as well as by the respective figure captions in a separate file (sheet). As far as presentation of units is concerned, SI units are to be used. However, some non-SI units are also acceptable, such as °C, ml, l, etc. The author(s) name(s), the title of the manuscript, the number of drawings, photographs, diagrams, etc., should be written in black pencil on the back of the illustrative material (hard copies) in accordance with the list enclosed. Avoid using more than 6 (12 for reviews, respectively) figures in the manuscript. Since most of the illustrative materials are to be presented as 8-cm wide pictures, attention should be paid that all axis titles, numerals, legend(s) and texts are legible.

The authors are required to submit the text with a list of three individuals and their e-mail addresses that can be considered by the Editors as potential reviewers. Please, note that the reviewers should be outside the authors' own institution or organization. The Editorial Board of the journal is not obliged to accept these proposals.

The authors are asked to submit **the final text** (after the manuscript has been accepted for publication) in electronic form by e-mail. The main text, list of references, tables and figure captions should be saved in separate files (as *.rtf or *.doc) with clearly identifiable file names. It is essential that the name and version of the word-processing program and the format of the text files is clearly indicated. It is recommended that the pictures are presented in *.tif, *.jpg, *.cdr or *.bmp format.

The equations are written using "Equation Editor" and chemical reaction schemes are written using ISIS Draw or ChemDraw programme.

EXAMPLES FOR PRESENTATION OF REFERENCES

REFERENCES

1. D. S. Newsome, *Catal. Rev.–Sci. Eng.*, **21**, 275 (1980).
2. C.-H. Lin, C.-Y. Hsu, *J. Chem. Soc. Chem. Commun.*, 1479 (1992).
3. R. G. Parr, W. Yang, *Density Functional Theory of Atoms and Molecules*, Oxford Univ. Press, New York, 1989.
4. V. Ponec, G. C. Bond, *Catalysis by Metals and Alloys (Stud. Surf. Sci. Catal., vol. 95)*, Elsevier, Amsterdam, 1995.
5. G. Kadinov, S. Todorova, A. Palazov, in: *New Frontiers in Catalysis (Proc. 10th Int. Congr. Catal., Budapest, (1992), L. Guzzi, F. Solymosi, P. Tetenyi (eds.), Akademiai Kiado, Budapest, 1993, Part C, p. 2817.*
6. G. L. C. Maire, F. Garin, in: *Catalysis. Science and Technology*, J. R. Anderson, M. Boudart (eds), vol. 6, SpringerVerlag, Berlin, 1984, p. 161.
7. D. Pocknell, *GB Patent 2 207 355* (1949).
8. G. Angelov, PhD Thesis, UCTM, Sofia, 2001, pp. 121-126.
- 9 JCPDS International Center for Diffraction Data, *Power Diffraction File*, Swarthmore, PA, 1991.
10. CA **127**, 184 762q (1998).
11. P. Hou, H. Wise, *J. Catal.*, in press.
12. M. Sinev, private communication.
13. <http://www.chemweb.com/alchem/articles/1051611477211.html>.

Texts with references which do not match these requirements will not be considered for publication!!!

CONTENTS

<i>S. Fiorito, F. Epifano, F. Prezioso, V. A. Taddeo, S. Genovese</i> , Waste waters of milk and cheese processing as an efficient promoter for the synthesis of 1,8-dioxo-octahydroxanthenes	189
<i>M. Khaleghdadi, A. Hassanabadi</i> , One-pot three-component synthesis of 3-[(aryl)-arylsulfanyl-methyl]-4-hydroxy-6-methylpyran-2-one	194
<i>H. M. Rageh, M. M. Abou-Krishna, A. M. Abo-Bakr, M. Abd-ElSabour</i> , Detection limit and electrochemical behavior of maleic acid on a platinum electrode	198
<i>I. Kara</i> , Chemical analysis of components in burned and unburned propellant powders	204
<i>F.A.I. Al-Khodir</i> , New chelation products of thorium(IV) and cerium(III) with diclofenac and paracetamol analgesic drugs: Synthesis, spectroscopic, thermal stability, antimicrobial activities investigations	208
<i>E. Menteşe, F. Yılmaz, B. Kahveci</i> , A new green protocol for the synthesis of 2-substituted perimidines from hydrazones under catalyst- and solvent-free conditions	218
<i>Al. S. Chanachev, S. S. Simeonova, P. D. Georgiev, Tz. N. Ivanova, S. D. Petrova, K. T. Balashev</i> , Characterization by atomic force microscopy of gold nanoparticles functionalized with azocasein for protease colorimetric enzyme assay	223
<i>Sh. Yao, L. Xu, G. Feng, L. Tang</i> , Optimization scheme for a typical longitudinal three-level Rankine cycle cold energy power generation system for recycling liquid gas	228
<i>N. S. Krstić, R. S. Nikolić, V. D. Dimitrijević, D. M. Đorđević, M. N. Stanković, I. M. Krstić, M. G. Nikolić</i> , Lactic acid and M(II) d-metals (Cu, Co, Mn, Cd) milli- and micro- quantities interaction: FTIR and ESI-MS analysis ..	237
<i>L.M. Takić, B.Ž. Todorović, A.S. Zdravković, N.M. Elezović, N.V. Živković</i> , Correlation analysis of physicochemical parameters of the ecological status: a case study of Ibar River (Serbia)	243
<i>T.N. Rizov, S.S. Paneva</i> , Determination of fluoride in toothpaste and in mouthwash products by GC/FID/HS	250
<i>M. Ur-Rehman, M.Sh. Khurram, S. Rafiq, Sh.A. Memon, M. Ghauri, F. Jamil, M. H. Jaffery, M. Gh. Doggar</i> , Modeling of organic Rankine cycle for suitable working fluid in HYSYS for power generation in Pakistan	254
<i>G. Gergov, A. Alin, P. Katsarov, V. Simeonov, D. Yankov, Y. Al-Degs</i> , Net analyte signal-based methods for the simultaneous determination of paracetamol, propyphenazone and caffeine by UV spectrophotometry	265
<i>S.I. Lavrova-Popova, Z.L. Yaneva, B.K. Koumanova</i> , Study on copper ions adsorption from aqueous solution by Emeraldine	274
<i>H. Hristov, M. Nedyalkova, V. Simeonov</i> , Insight into polymer-borate hybrid films - structural approach	281
<i>B. Parvizi, A. Khanlarkhani, Y. Palizdar</i> , Nonlinear predictive control based on artificial neural network model for pilot reformer plant: Approach for ratio control	286
<i>M. Canlica</i> , Co, Ni, Cu phthalocyanines with tetra substituted bisbenzimidazole	294
<i>M.B. Gerdoodbary, D. D. Ganji, M. Taeibi-Rahni, Sh. Vakili-pour, R. Moradi</i> , Application of direct simulation Monte Carlo for development of micro gas sensor	298
<i>H.Z. Wu, L.F. Meng</i> , Cloud point extraction combined with flame atomic absorption spectrometry for analysis of trace silver nanoparticles in environmental waters	306
<i>The 5th Asia-Pacific Conference on Engineering Technology (APCET 2017)</i>	313
<i>W.X. Huang, Z.Z. Wei, G.Y. Niu, Y.J. Zhang, H.F. Shao</i> , Effects of sodium polyacrylate and potassium polymer on growth and physiological characteristics of different flue-cured tobaccos	315
<i>H.G. Yang, J.D. Zhang, M.C. Li, R.T. Hao, G.L. Song</i> , Effects of deposition pressure on Cu ₂ ZnSnS ₄ films prepared by one-step sputtering with quaternary target	324
<i>H.G. Yang, R.T. Hao, M.C. Li, G.L. Song</i> , A novel all-thin-film electrochromic device for modulating optical transmittance	329
<i>S. Zhan, Y.L. Yang, W.Y. Peng, J.G. Chen, Z.B. Li, X.J. Hou, L. Feng, G.Q. Suo, Z.G. Chen, J. Zou, Y.D. Wang</i> , Thickness dependence of internal stress in electrodeposited nano-twinned copper	334
ERRATUM	339
INSTRUCTIONS TO THE AUTHORS	341

СЪДЪРЖАНИЕ

<i>С. Фиорито, Ф. Епифано, Ф. Прециузо, В. А. Тадео, С. Дженовезе</i> , Отпадъчни води от производството на мляко и сирене като ефективен промотор за синтеза на 1,8-диоксо-октахидроксантиени	193
<i>М. Калегати, А. Хасанабади</i> , Едностадийн трикомпонентен синтез на 3-[(арил)-арилсулфанил-метил]-4-хидрокси-6-метилпиран-2-он	197
<i>Х.М. Радех, М. М. Абу-Криша, А. М. Або-Бакр, М. Абд-Елсабур</i> , Граница на откриване и електрохимично отнасяне на малеинова киселина върху платинов електрод	203
<i>И. Кара</i> , Химичен анализ на компонентите в изгорели и недоизгорели горивни прахове	207
<i>Ф.А.И. Ал-Кодир</i> , Нови хелатни продукти на торий(IV) и церий(III) с аналгетичните лекарства диклофенак и парацетамол: синтез и изследване на спектроскопските характеристики, термичната стабилност и антимикробиалната активност	217
<i>Е. Ментеше, Ф. Йълмаз, Б. Кахведжи</i> , Нов "зелен" протокол за синтез на 2-заместени перимидини от хидразони в отсъствие на катализатор и разтворител	222
<i>Ал. Чаначев, С. Симеонова, П. Георгиев, Св. Петрова, Цв. Иванова, К. Балашев</i> , Охарактеризиране на златни наночастици, функционализирани с азоказеин с помощта на атомно-силова микроскопия (AFM) и приложението им за колориметрични ензимни тестове на протеаза	227
<i>Ш. Яо, Л. Сю, Г. Фън, Л. Тан</i> , Оптимизационна схема на типична надлъжна система с Ранкинов цикъл на три нива, използваща студена енергия, за генериране на енергия за рециклиране на течен газ	236
<i>Н.С. Кръстич, Р.С. Николич, В.Д. Димитриевич, Д.М. Джорджевич, М.Н.Станкович, И.М. Кръстич, М.Г. Николич</i> , Изследване на взаимодействието между млечна киселина и М(II) d-метали (Cu, Co, Mn, Cd) на милиграмово и микрограмово ниво чрез FTIR и ESI-MS анализ	242
<i>Л.М. Такич, Б.Ж. Тодорович, А. С. Здравкович, Н. М. Елезович, Н.В. Живкович</i> , Орелационен АНАЛИЗ на физикохимичните параметри на екологичния статус: пример с река Ибар (Сърбия)	249
<i>Т.Н. Ризов, С.С. Панева</i> , Определяне на флуорид в паста за зъби и продукти за орална хигиена с използване на газова хроматография с пламъков йонизационен детектор и автоматично устройство за внасяне на проби (GC/FID/HS)	253
<i>М. Ур-Рехман, М.Ш. Хурам, С.Рафик, Ш.А. Мемон, М. Гаури, Ф. Джамил, М.Х. Джафери, М.Г. Догар</i> , Моделиране на органичен Rankine цикъл за подходящ работен флуид чрез HYSYS за производство на енергия в Пакистан	264
<i>Г. Гергов, А. Алин, П. Кацаров, В. Симеонов, Д. Янков, И. Ал-Дегс</i> , Методи, основаващи се на нетния сигнал на анализа за едновременно определяне на парацетамол, пропифеназон и кафеин чрез УВ спектروفотометрия	273
<i>С. И. Лаврова-Попова, З. Л. Янева, Г. И. Хлебаров, Б. К. Куманова</i> , Изследване на адсорбцията на медни йони от воден разтвор с използване на Емералдин	280
<i>Хр. Христов, М. Недялкова, В. Симеонов</i> , Поглед към хибридни полимер-боратни филми – структурен подход	285
<i>Б. Парвизи, А. Ханлархани, И. Пализдар</i> , Нелинеен предсказващ контрол на основата на изкуствен модел на невронна мрежа за пилотна установка: подход за контрол на съотношенията	293
<i>М. Джанлъджа</i> , Фталоцианини на Co, Ni и Cu с тетразаместен бисбензимида	297
<i>М.Б. Гердроодбари, Д.Д. Ганджи, М. Таеиб-Рахни, Ш. Вакилтур, Р. Моради</i> , Приложение на директна Монте Карло симулация за разработване на микро газов сензор	305
<i>Х.З. У, Л.Ф. Мън</i> , Екстракция при точката на помътняване в съчетание с атомноабсорбционна спектроскопия за анализ на следови количества от сребърни наночастици в отпадни и природни води	311
<i>5-та конференция на Азиатско-тихоокеанския регион по инженерна технология (APCET 2017)</i>	313
<i>У.Кс. Хуан, З.З. Уей, Г.И. Нуу, И.Дж. Джан, Х.Ф. Шао</i> , Влияние на натриев полиакрилат и калиев полимер върху растежа и физиологичните параметри на различни опушени тютюни	323
<i>Х.Г. Ян, Дж.Д. Джан, М.Ц. Ли, Р.Т. Хао, Г.Л. Сун</i> , Влияние на налягането на отлагане върху филми от Cu_2ZnSnS_4 , получени чрез едностадийно разпръскване с четворна мишена	328
<i>Х.Г. Ян, Р.Т. Хао, М.Ц. Ли, Г.Л. Сун</i> , Ново електрохимично устройство от изцяло тънък филм за модулиране на оптична пропускливост	333
<i>С. Джан, И.Л. Ян, У. И. Пън, Дж.Г. Чън, З.Б. Ли, Кс.Дж. Хоу, Л. Фън, Г.К. Суо, З.Г. Чен, Дж. Зоу, И.Д. Уан</i> , Зависимост на вътрешното напрежение от дебелината на електроотложени двойни медни кристали	338
<i>ИНСТРУКЦИЯ ЗА АВТОРИТЕ</i>	343